Master Thesis 2011-2012 EMSD

Energy Efficient Control of an Induction Machine for an Electric Vehicle

By:

Thomas Christensen
Bjørn Bøge
Niels Balzer Sørensen

Aalborg University

Aalborg University
Study Board of Industry and Global Business Development
Fibigerstraede 16
DK - 9220 Aalborg East
Phone +45 99 40 93 09
http://www.industri.aau.dk/

Title:
Energy Efficient Control of an Induction Machine for an Electrical Vehicle

Semester:
3rd – 4th EMSD

Semester Theme:
Industrial Development

Project period:
1. September 2011 - 1. June 2012

ECTS:
60

Project group:
EMSD4-B

Group members:

Thomas Christensen

Niels Balzer Sørensen

Bjørn Bøge

Supervisor(s):
Søren Juhl Andreasen &
Michael Møller Bech

Number printed: 6

Pages: 197

Enclosed: Appendix and CD

Synopsis:

One of the main disadvantages possessed by electric vehicles (EV) compared to internal combustion engine vehicles is short range per charge. The focus of this report is on increasing the range of an EV by maximizing the efficiency of an induction machine and inverter implemented in an EV. The case study EV used in this project is a called a *Kewet* EV.
For controlling the induction machine a field oriented control strategy is developed including current controllers and rotor flux estimation. In order to maximize the efficiency a mapping algorithm for the induction machine is developed. The mapping determines the efficiency at various operating points (torque and velocities) when varying the magnetizing current. From the results of the mapping a least square optimization algorithm is utilized for estimation of loss equations. From the loss equations the energy optimal magnetizing currents at all operating points are determined.
Finally implementation strategies for the energy optimal magnetizing currents are tested by simulation of a standard urban drive cycle. The most promising strategy provides an efficiency of 72%. Utilizing optimal magnetizing currents provides 4 %-point better efficiency than when using nominal magnetizing current. By using new components in the EV and by applying the developed implementation strategy the energy per range for the Kewet is 0.144 $^{kWh}/_{km}$ which is 10.6 % less than for the original Kewet.

By signing this document, each member of the group confirms participation on equal terms in the process of writing the project. Thus, each member of the group is responsible for the all contents in the project.

PREFACE

This Master Thesis is written on 3rd-4th semester at Aalborg University by a group of students enrolled on the master study program; Electro-Mechanical System Design. The theme for this project is 'Industrial development'.

The report consists of a main report and an appendix. The main report can be read independently of the appendix.

References are setup by the Chicago method meaning that a reference is stated as [Author, year] or [Author, year, page/chapter]. If referring to slides used in a course the reference is stated as [Author, year, MM], where MM refers to a specific mini module. In the bibliography references are stated as: Author. (Year). *Title*. URL / ISBN.

Tables and figures are numbered sequentially with chapter numbers and figure numbers in the concerning chapter - for instance 'Table 4.7' refers to the seventh table in chapter four.
The chapters and references in the appendix are numbered alphabetic starting from A.
A CD-ROM is enclosed containing various files such as appendix and report in PDF format, simulation models, experimental results, Matlab algorithms etc.

RESUMÉ

Denne rapport omhandler energieffektiv styring af en induktionsmaskine i en el-bil. En af de største problemstillinger ved el-biler i forhold til biler med forbrændingsmotor er dårlig rækkevidde per opladning. Fokus er i denne rapport på at maksimere virkningsgraden af en induktionsmaskine samt en inverter i en el-bil, for på den måde at øge rækkevidden af el-bilen. Som case study bliver der brugt en el-bil kaldet Kewet model 5. For at teste udviklede styringsstrategier er der i projektet blevet bygget en test opstilling. Opbygningen af test opstillingen kan ses på figur 1.

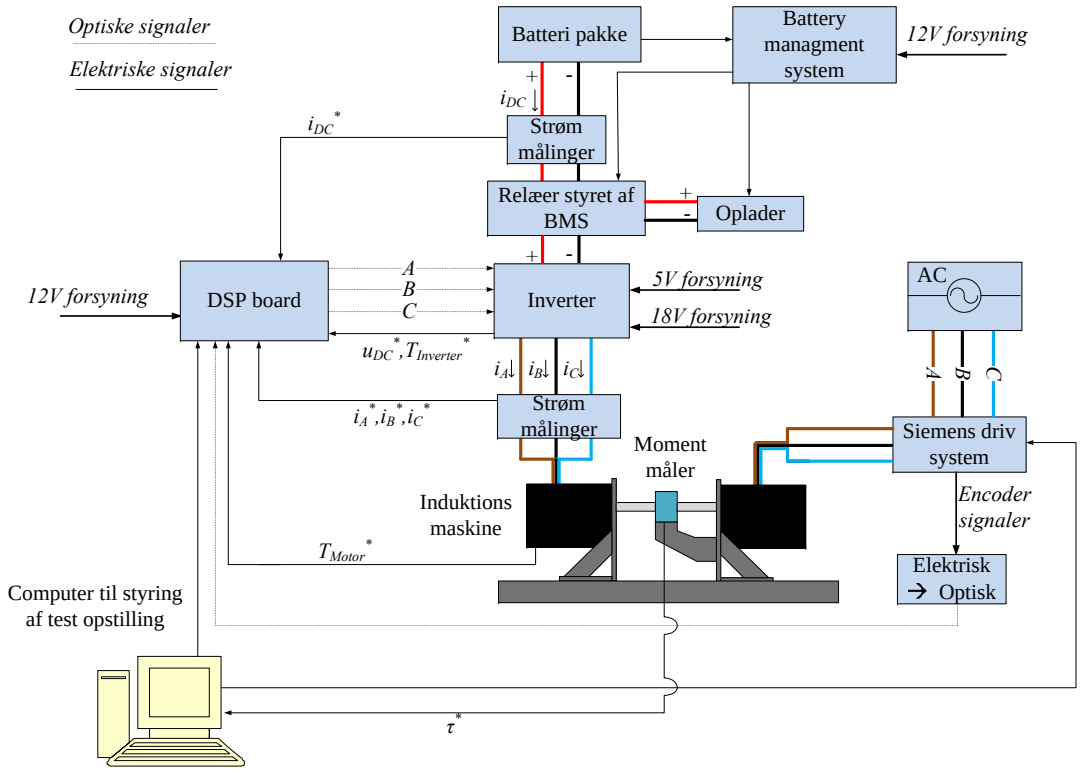

Figure 1: *Opbygning af teststand.*

For at udvikle styringsstrategier er transmissionssystemet blevet modelleret i Simulink. Der er udviklet en felt orienteret styring til systemet der gør brug af en udbygget indirekte flux estimering.

Et moment fra en induktionsmaskine kan opnås ved forskellige kombinationer af q og d stator strømme. For at bestemme den mest energi effektive kombination i alle arbejdspunkter er der blevet lavet en mapping af motoren hvor virkningsgraden for motoren er bestemt i forskellige arbejdspunkter (momenter og hastigheder) og ved forskellige magnetiseringsstrømme. Ud fra resultaterne af mappingen er ubekendte konstanter i tabs-ligningerne for systemet blevet estimeret ved brug af en optimeringsalgoritme. De estimerede tabs-ligninger er efterfølgende blevet brugt til at bestemme energioptimal magnetiseringsstrøm i alle arbejdspunkter. Den opnåelige effekt i hele arbejdsområdet ved brug af optimal magnetiseringsstrøm kan ses på figur 2.

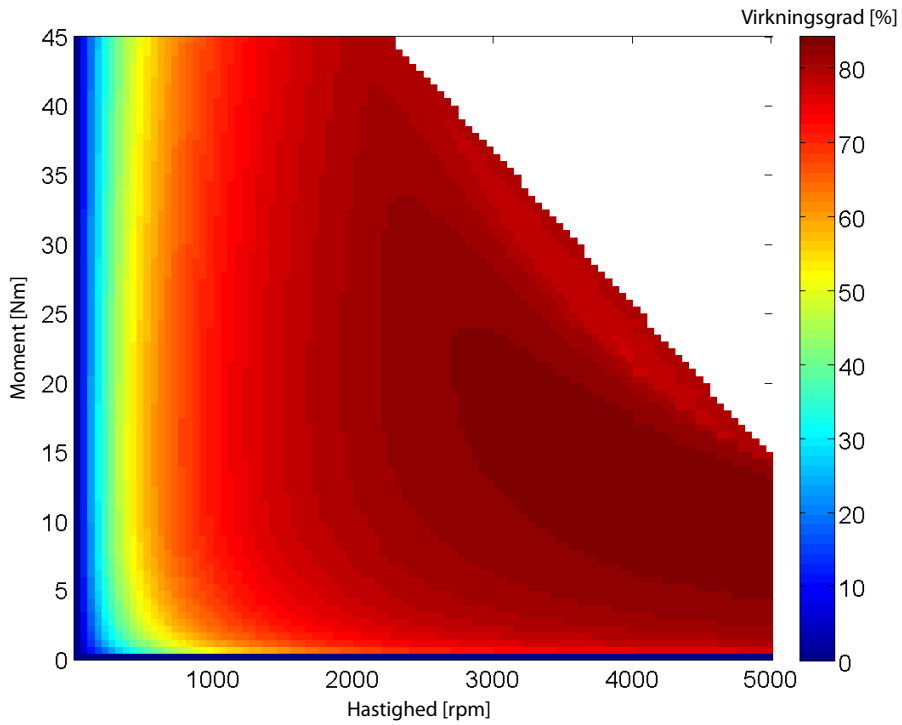

Figure 2: *Opnåelig virkningsgrad ved brug af energioptimal magnetiseringsstrøm.*

Når magnetiseringsstrømmen varieres for hurtigt kan induktionsmaskinens ydeevne forværres. Der er derfor blevet udviklet forskellige implementeringsstrategier af den energi effektive styring der hver er et kompromis mellem ydeevne og virkningsgrad. Strategierne er blevet testet ud fra en simulering af en standard kørselscyklus for bykørsel. Strategierne er blevet evalueret ud fra performance og virkningsgrad i simuleringen. Den mest lovende strategi giver en virkningsgrad på 72%. Med nye komponenter i elbilens powertrain samt energioptimal styring kan der opnåes en energi pr km på $0.144^{kWh}/_{km}$ hvilket er 10.6% lavere end den oprindelige Kewet. Mapping algoritmen samt optimeringsalgoritmerne er lavet i Matlab. Algoritmerne kan også benyttes til at bestemme energioptimale magnetiseringsstrømme på andre induktionsmaskiner.

CONTENTS

CHAPTER 1

INTRODUCTION

The modern society is highly dependent on personal transportation. A large marked within this area is the passenger car. In 2008 approximately 53 million cars was produced worldwide [Worldometers]. The main type of passenger cars is the internal combustion engine vehicle (ICEV). The increasing number of ICEVs worldwide entails an increase in pollution of the environment and contributes to the depletion of the oil resources [Ehsani et al., 2010]. As a result the prize of crude oil has increased from 20 $\$/barrel$ in 2002 [OECD, 2004, p. 2] to 125 $\$/barrel$ in 2012 [Oil-price.net] corresponding to an increase of 625 % in ten years. This makes fuel efficiency an important benchmark for the car companies and encourages them to invest in research and development of more efficient vehicles making transportation cheaper for the consumer. Another way to reduce the fuel cost per kilometer is to use alternatives to fossil fuels. One alternative is to use electricity instead of gas as an energy source for the vehicle. For an ICEV with a fuel efficiency of 25 km/l and a gas prize of 12.5 DKK/l, the fuel cost is 0.50 DKK/km. For an electric vehicle (EV) announced in 2008 the prize was 0.20 DKK/km [JP.dk].
Most car companies have announced new electric vehicles within recent years [Nissan] [Honda] [Peugeot] [Citroën]. The EV technology is still new compared to the ICEV. This yields good potential for improvement within the area of EV technology. EVs have a lot of benefits compared to the ICEV including absence of emissions, high efficiency, and quiet and smooth operation [Ehsani et al., 2010], but the range per charge and the charge time of the EV remains a disadvantage compared to ICEV. This is due to much lower energy density of the batteries than gasoline [Ehsani et al., 2010, p. 123] and to the limited charge rate of the batteries. The range of the EV Renault Fluence Z.E. is estimated to be 185 km using NEDC (New European Driving

Cycle) [Bil.guide.dk]. A similar size ICEV Renault Megane has a fuel consumption of 18.9 km/l using NEDC [Renault, c], and a fuel tank of 60 l [Renault, d]. This combined yields 1132 km per refueling or more than six times longer range than the fully charged Renault Fluence Z.E.. Furthermore the refueling of an ICEV only takes a few minutes while fully charging the Renault Fluence Z.E. takes six to eight hours [Renault, a].

The relatively low range per charge leads to the following initial problem:

How can the range of an electric vehicle be improved?

CHAPTER 2

PROBLEM ANALYSIS

In this chapter the factors which limits the range of an EV is discussed. First a mechanical analysis of the car is presented to yield an overview of the forces which in connection with the velocity limits the range of the EV. The powertrain propelling the EV is then presented and measures to improve the efficiency of it are discussed. A vehicle used as a case for the project is presented and finally an area of focus for improvement of the range of the vehicle is chosen.

2.1 Mechanical Analysis of an Electric Vehicle

In this section a mechanical analysis of an EV is presented to determine the forces acting on it when driving. The analysis also applies for an ICEV.

In figure 2.1 a diagram displaying the forces acting on a rear-wheel driven EV driving uphill is seen. The forces acting against the direction of motion of the EV are the gravity ($m_e \cdot g \cdot \sin(\theta_{road})$), the aerodynamic drag F_w and the rolling resistance force F_r. The force acting in direction of the motion is the traction force F_t.

The aerodynamic drag is given by equation (2.1) [Ehsani et al., 2010, p. 24]. In this equation the aerodynamic drag coefficient C_D is used. C_D is determined by the shape of the EV and varies between 0.15 for optimized streamlined design to 0.7 [Ehsani et al., 2010, p. 25].

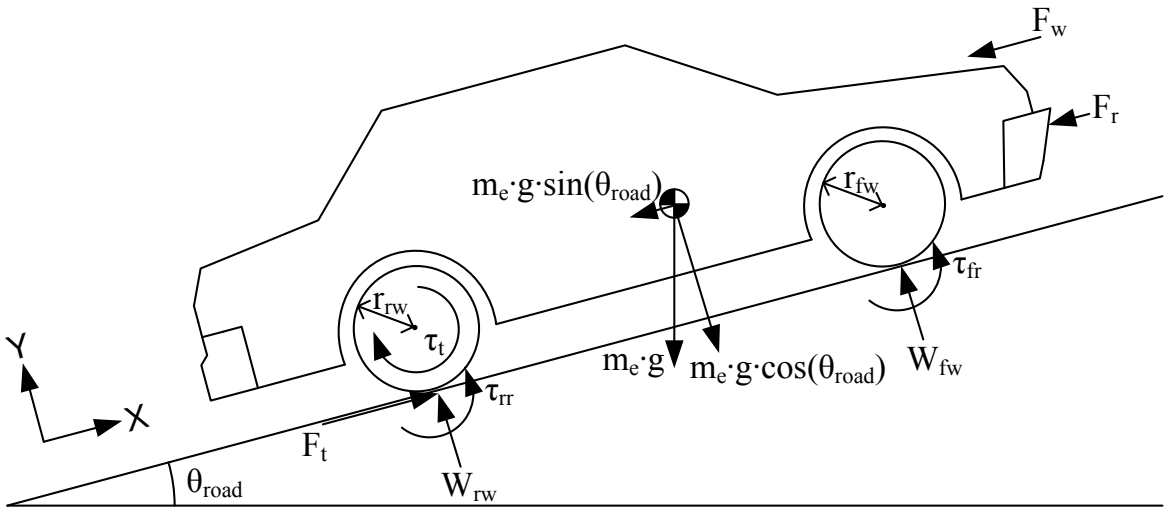

Figure 2.1: *Forces acting on a rear-wheel driven EV driving uphill.*

$$F_w = \frac{1}{2} \cdot \rho \cdot A_f \cdot C_D \cdot (\dot{x}_{EV} - V_w)^2 \tag{2.1}$$

where:

	F_w	Aerodynamic drag $[kN]$
	ρ	Density of air $[kg/m^3]$
	A_f	Frontal area of the EV $[m^2]$
	C_D	Aerodynamic drag coefficient $[-]$
	$\dot{x}_{EV}$	Velocity of the EV $[m/s]$
	V_w	Velocity of the wind blowing in the moving direction of the EV $[m/s]$

The rolling resistance force is primarily caused by hysteresis in the tire material when driving on a hard road surface. In figure 2.2 the pressure distribution of the contact area between the tires and the road is seen at standstill on a leveled road.

Figure 2.3 shows the force acting on the rear wheel tires W_{rw} versus the deformation in loading and unloading. From this it is seen that for a given weight on the tires, W_{rw}, the deformation Δr_{rw} is determined by whether the tires had just been loaded or unloaded. If the tires are loaded from zero force to $W_{rw.max}$ and back to zero, the energy lost due to hysteresis is proportional to the grey area of figure 2.3. The energy lost due to hysteresis is converted into heat which is dissipated in the tire material.

In figure 2.4 the pressure distribution of the contact area between the tires and the road when moving on a leveled hard road surface is seen. In this figure the right part of the contact area is in loading condition while the left part of the contact area is in unloading condition, causing an asymmetric pressure distribution due to hysteresis [Ehsani et al., 2010, p. 20].

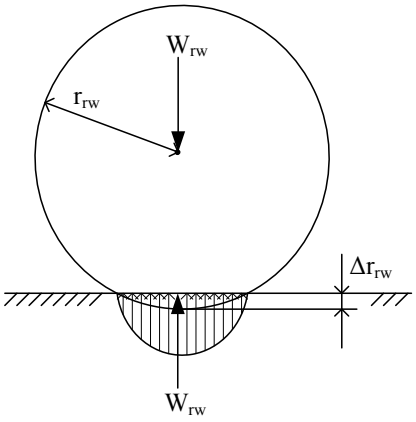

Figure 2.2: *The pressure distribution of the contact area between tire and road at standstill on a leveled hard road surface [Ehsani et al., 2010, p. 21] (modified).*

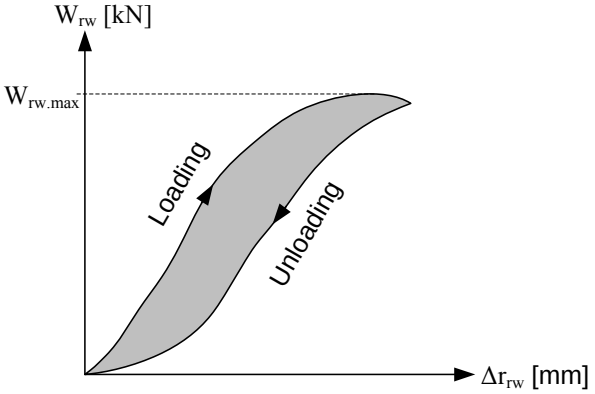

Figure 2.3: *Force W_{rw} acting on the rear wheel tires versus deformation in loading and unloading [Ehsani et al., 2010, p. 21] (modified).*

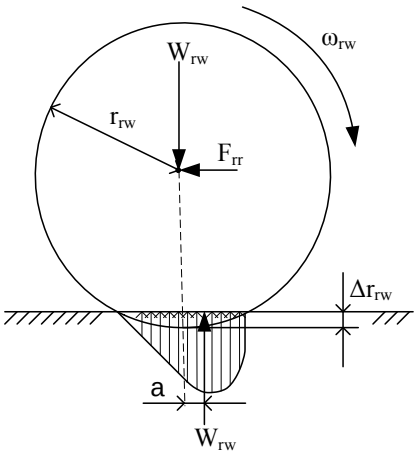

Figure 2.4: *Pressure distribution of the contact area between tires and road when moving on a leveled hard road surface [Ehsani et al., 2010, p. 22] (modified).*

The center of force in the pressure distribution of figure 2.4 is shifted to the right by a distance a, causing a torque of τ_{rr} given by equation (2.2) opposing the movement of the wheels.

$$\tau_{rr} = W_{rw} \cdot a \tag{2.2}$$

where:	τ_{rr}	Rolling resistance torque of the rear wheels of the EV $[Nm]$
	W_{rw}	Gravity force acting on the rear wheels $[kN]$
	a	Force displacement due to hysteresis of the tire $[mm]$

The force contribution to the center of the wheel is given by equation (2.3).

$$\begin{aligned} F_{rr} &= \frac{\tau_{rr}}{r_{rw} - \Delta r_{rw}} \\ &= \frac{W_{rw} \cdot a}{r_{rw} - \Delta r_{rw}} \\ &= W_{rw} \cdot f_r \end{aligned} \tag{2.3}$$

where:	F_{rr}	Rolling resistance force of the rear wheels of the EV $[kN]$
	r_{rw}	Radius of the rear wheel tires $[mm]$
	Δr_{rw}	Displacement of the rear wheel tires $[mm]$
	f_r	Rolling resistance coefficient $[-]$

In this equation the rolling resistance coefficient is a variable depending on the velocity of the vehicle and the inflation pressure of the tires. For the most common range of inflation pressures equation (2.4) is used to determine the value of the rolling resistance coefficient [Ehsani et al., 2010, p. 23].

$$f_r = 0.01 \cdot \left(1 + \frac{\dot{x}_{EV}}{160}\right) \tag{2.4}$$

If the weight of the vehicle is assumed to be equally distributed on all four wheels, the entire rolling resistance force is found using equation (2.3) by applying the entire weight of the vehicle ($m_e \cdot g \cdot cos(\theta_{road})$) instead of just the weight on the rear wheels. Utilizing Newtons second law, the acceleration of the vehicle is given by equation (2.5).

$$
\begin{aligned}
m_{EV} \cdot \ddot{x}_{EV} &= F_t - m_{EV} \cdot g \cdot \sin(\theta_{road}) - F_w - F_r \\
&\Downarrow \\
\ddot{x}_{EV} &= \frac{1}{m_{EV}} (F_t - m_{EV} \cdot g \cdot \sin(\theta_{road}) - F_w - F_r)
\end{aligned}
\tag{2.5}
$$

where:

	$\ddot{x}_{EV}$	Acceleration of the EV $[m/s^2]$
	m_{EV}	Mass of EV $[kg]$
	F_t	Traction force $[N]$
	g	Gravitational acceleration constant $[m/s^2]$
	θ_{road}	Gradient of the road $[rad]$
	F_r	Rolling resistance of the wheels $[kN]$

From this equation it is seen that the force contributing to a positive acceleration is the traction force. The traction force is given by equation (2.6) when neglecting the displacement of the tires due to gravity.

$$
F_t = \frac{\tau_t}{r_{rw}} \tag{2.6}
$$

where:

	τ_t	Traction torque acting on the center of the rear wheels of the EV $[Nm]$

From equation (2.6) and equation (2.5) it is evident that in order to achieve a good acceleration and maximum velocity of the EV it is important to actuate the wheels of the EV with a sufficient traction torque τ_t. In section 6.4 the mechanical equations is used to assess the performance of a practical application. The following section describes the configuration of the EV which among other things includes the powertrain that generates the traction torque.

2.2 Configuration of an Electric Vehicle

In figure 2.5 an example of an EV configuration is seen. It consists of three subsystems. The electric propulsion system which converts the electric power from the battery to a mechanical power on the wheels. The energy source subsystem which handles charging and energy distribution of the batteries. Finally the auxiliary subsystem handles functions like power steering, climate control, lighting etc.

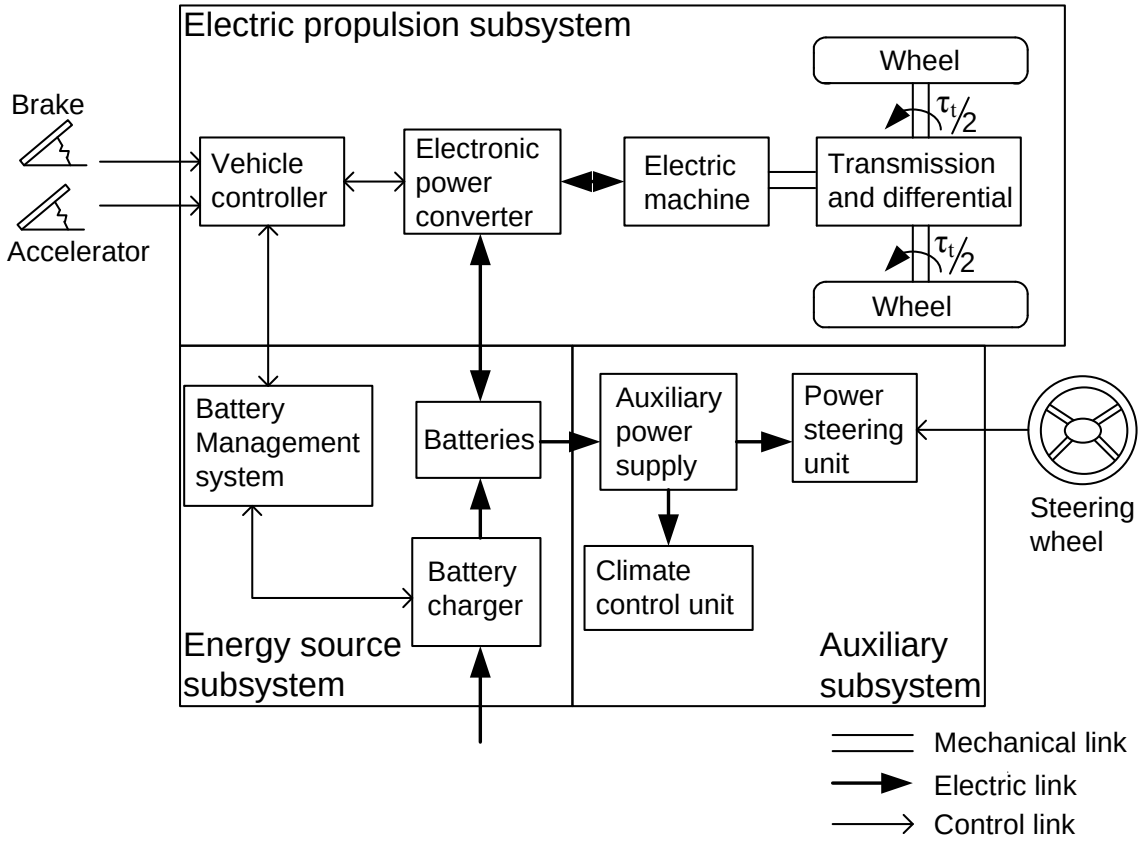

Figure 2.5: *EV configuration example [Ehsani et al., 2010, p. 106] (modified).*

In this system the powertrain is the main component that delivers power to the wheels. It consists of: Batteries, electronic power converter, electric machine, transmission and differential. The whole system is controlled by a driver using steering wheel, brake and accelerator.
In the following section possibilities for extension of the range of the EV is examined.

2.3 Improvement of Range of an Electric Vehicle

The following describes how the range of an EV can be improved. In general the range of an EV is determined by the energy delivered to the wheels by the powertrain and the energy lost due to aerodynamic drag, rolling resistance and intentional friction of the brakes.

The aerodynamic drag can be reduced by optimizing the body of the EV. This improvement has especially good potential to increase the range of the vehicle at high velocities since the power loss due to aerodynamic drag is proportional to the velocity raised to the third power $\dot{x}_{EV}^3$ according to equation (2.1).
The rolling resistance of the car can be reduced by using low resistance tires. According to Ehsani et al. [2010] the rolling resistance coefficient of equation (2.3) can be reduced from 13 $\cdot 10^{-3}$ to less than 10 $\cdot 10^{-3}$ or more than 23 %.
Some of the energy lost when braking can be reduced by using the electric machine in generator mode. In figure 2.5 the unidirectional power flow between batteries and electric machine is indicated by the double-sided arrows.

Improving the efficiency of the components in the powertrain can also improve the range of the EV.
In general the transmission and differential consists of a series of gear systems. For a single helical gear transmission the efficiency is 98 % to 99 % for gear ratios of 1:1 to 1:6 [Roymech]. Since the power output for an electrical machine is constant in a large speed range the transmission may only contain one gearing ratio [Ehsani et al., 2010, p. 108]. A differential has three different gear meshes from the transmission to the wheels yielding an efficiency of 94 % to 97 % [Pearlman]. The energy loss in theese gear systems is primarily associated with gear tooth friction and lubrication churning losses [Roymech].

The efficiency of the electric machine is varying depending on the type of machine and its characteristics. When choosing an electric machine for an EV it is not only the efficiency that matters other factors such as cost, reliability etc. are important as well. The various types of electric machines used for EVs can be divided into two groups commutator machines and commutatorless machines. The commutator machines are primarily the DC machines. The DC machines needs commutator and brushes to feed current to the armature. The brushes are worn

over time and this makes DC machines more maintenance heavy than other electric machines. The other group of electric machines is as mentioned the commutatorless machines. Two of the most used commutatatorless machines are the induction machine (IM) and the permanent magnet synchronous machine (PMSM). The benefit of using IMs is low cost, high reliability and maintenance free operation [Ehsani et al., 2010, p. 152]. Compared to the DC machine, the IM has additional advantages such as light weight nature, small volume and high efficiency [Ehsani et al., 2010, p. 168]. The benefit of using PMSM is its high efficiency and high power density. However the PMSM also suffers from some disadvantages such as cost because of the price of rare-earth magnets, safety in case of wreck and possibility of magnet demagnetization because of temperature or control failure [Ehsani et al., 2010, p. 202]. The losses of an electric machine primarily originate from conduction -and core losses. These losses are elaborated in section 6.5.2. In addition to the electric losses there are also mechanical losses due to e.g. friction in the bearings of the machine.

There are various kinds of electronic power converters depending on the machine it has to power. An example is the three phase inverter. The efficiency of this kind of electronic power converter is load dependent but can be about 90 % or more in the power range of 30 % to 100 % of rated output [Saiful Islam and Nijs]. According to [Abrahamsen, 2000] the losses in inverters can be divided into conduction losses and switching losses. These losses are elaborated in section 6.5.1.

The efficiency of the batteries is dependent on whether the battery is being charged or discharged. It also depends on the amount of energy left in the battery which is given by the state of charge (SOC). The SOC is 100 % for a fully charged battery and 0 % for a completely discharged battery. In discharge mode the efficiency of the battery is highest at high values of SOC while the efficiency in charge mode is highest at low values of SOC. The efficiency of a lead-acid battery in discharge mode is about 94 % at a SOC of approximately 80 % SOC. It decreases to below 82 % for SOC's below 20 % [Ehsani et al., 2010, p. 385].

Besides improving the efficiency of the components in the powertrain the range can be extended by altering the composition of the powertrain. Increasing the amount of cells in the battery pack would extend the range of the EV at the cost of higher vehicle weight and charging time. The

weight of the EV Renault Fluence Z.E. is 1610 kg [Renault, b] or about 25 % more than a similar size Renault Megane weighing 1290 kg [Renault, d]. Furthermore the volume of the batteries would limit the vehicle space at the users disposal. In a review of Renault Fluence Z.E. it is pointed out that it has limited trunk compartment space due to a large battery pack [Bil.guide.dk].
The EV Renault Fluence Z.E. features high capacity Lithium-ion batteries [Better place] which has a specific energy of 155 $^{Wh}/_{kg}$ [Ehsani et al., 2010, p. 389]. If the EV used i.e. Nickel-metal hydride batteries which has a specific energy of 65 $^{Wh}/_{kg}$ [Ehsani et al., 2010, p. 388] the battery package weight and probably also volume would increase or the range of the EV would be reduced.

Another way of extending the range of the EV is to convert it into a hybrid electric vehicle. This is done by adding a separate energy source to the powertrain. There are various ways of doing this. For example the batteries and the battery charger unit in figure 2.5 could be supplemented with an electric machine (in generator mode) connected to an internal combustion engine with a fuel tank [Ehsani et al., 2010, p. 127]. This principle is illustrated in figure 2.6. If the batteries are drained the internal combustion engine can supply power to the powertrain eliminating the range problem, since the range of the vehicle is highly increased and the gas station infrastructure in general is well developed. Introducing these extra components limits the space for the batteries and may affect the weight of the vehicle.

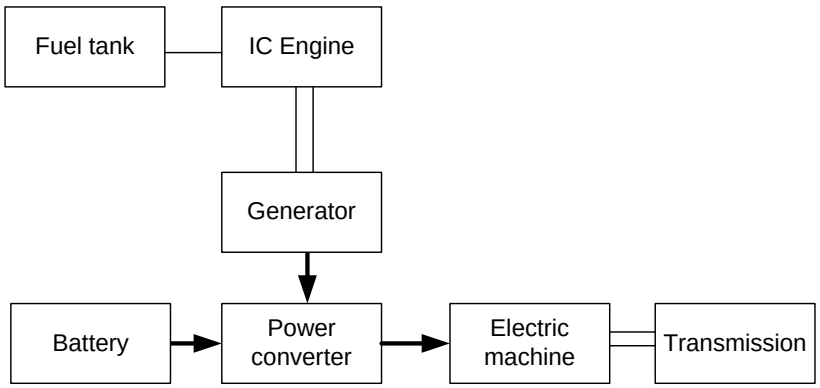

Figure 2.6: *Example of a hybrid vehicle configuration.*

All improvements whether installing high efficiency components in the powertrain, adding extra batteries or converting the EV into a hybrid comes at a cost that adds to the total prize per kilometer when including write-off on a car loan and maintenance expenses.
The following price example is based on the Danish registration and pollution tax rates. The

prize of the EV Renault Fluence Z.E. is 206,900 DKK [Renault, b] which is about the same as Renault Megane costing 218,900 DKK [Renault, d] including registration tax. It should be kept in mind that the registration tax on a ICEV may represent more than half the price of the vehicle [Skatteministeriet, b], while it is zero for the EV [Skatteministeriet, a]. Furthermore the pollution tax for the Renault Megane is 1080 DKK per year [FDM] while it is zero for Renault Fluence Z.E. [Skatteministeriet, a]. The fact that EV technology is relatively new may reduce the production cost of future generations of EVs, but other factors such as the absence of future tax benefits may counteract the decrease purchase cost for the consumer.
The maintenance expenses may be lower for an EV compared to an ICEV since it has 70 % fewer moving parts [Western Lithium].
An electric vehicle is at the project group's disposal to use as a practical application for range improvement of an EV. The following section contains a description of the EV and the range extending improvements which are implemented.

2.4 Kewet EV

The electric vehicle used in this project is called Kewet model 5. The newest model of the Kewet is called Buddy and is produced by the Norwegian company Pure Mobility [Puremobility.com]. The Buddy has about the same specifications as the Kewet used in this project [Kewetmuseum]. The specifications for the Kewet are:

Electric machine: Brushed 12 kW DC machine.
Transmission: 1:7 constant gear ratio.
Maximum velocity: 80 km/h.
Driving range on fully charged battery: 80-100 km.
Battery package size: 12 blocks of 10 cells (1.2 V). The package is coupled in 2 parallel strings each consisting of 6 blocks.
Battery package voltage: 72 V.
Battery package capacity: 200 Ah (14.4 kWh).
Battery type: Nickel-metal hydride (NiMH).
Heating plant: 1.6 kW.
Weight without driver: 719 kg.
Prize: 150,000 DKK.

The Buddy EV is equipped with a 13 kW DC machine and is able to accelerate from 0 to 50 $^{km}/_{h}$ in 7 seconds. The acceleration time from 0 to 50 $^{km}/_{h}$ for the Kewet used in this project may therefore be a bit more than 7 seconds, since the DC machine of this vehicle is only 12 kW. The Kewet is seen in figure 2.7.

Figure 2.7: *Kewet EV used in this project.*

As seen in the figure the EV has "Hywet" written on its side. The label is placed on the car in connection with a project where fuel cells are implemented into the vehicle [Andreasen, 2009]. The fuel cells are removed from the EV, since this is not the focus for this project.
The configuration of the EV is seen in figure 2.8. It is a more specific version of the general EV configuration is seen in figure 2.5. For the Kewet: The electric machine is a 12 kW DC machine, the electronic power converter is a DC/DC converter, the battery type is nickel-metal hydride and the climate control unit is a 1.6 kW electric heater. The Kewet does not feature a power steering unit. The following section describes the changes made to its powertrain in order to attempt to obtain a longer range of the vehicle.

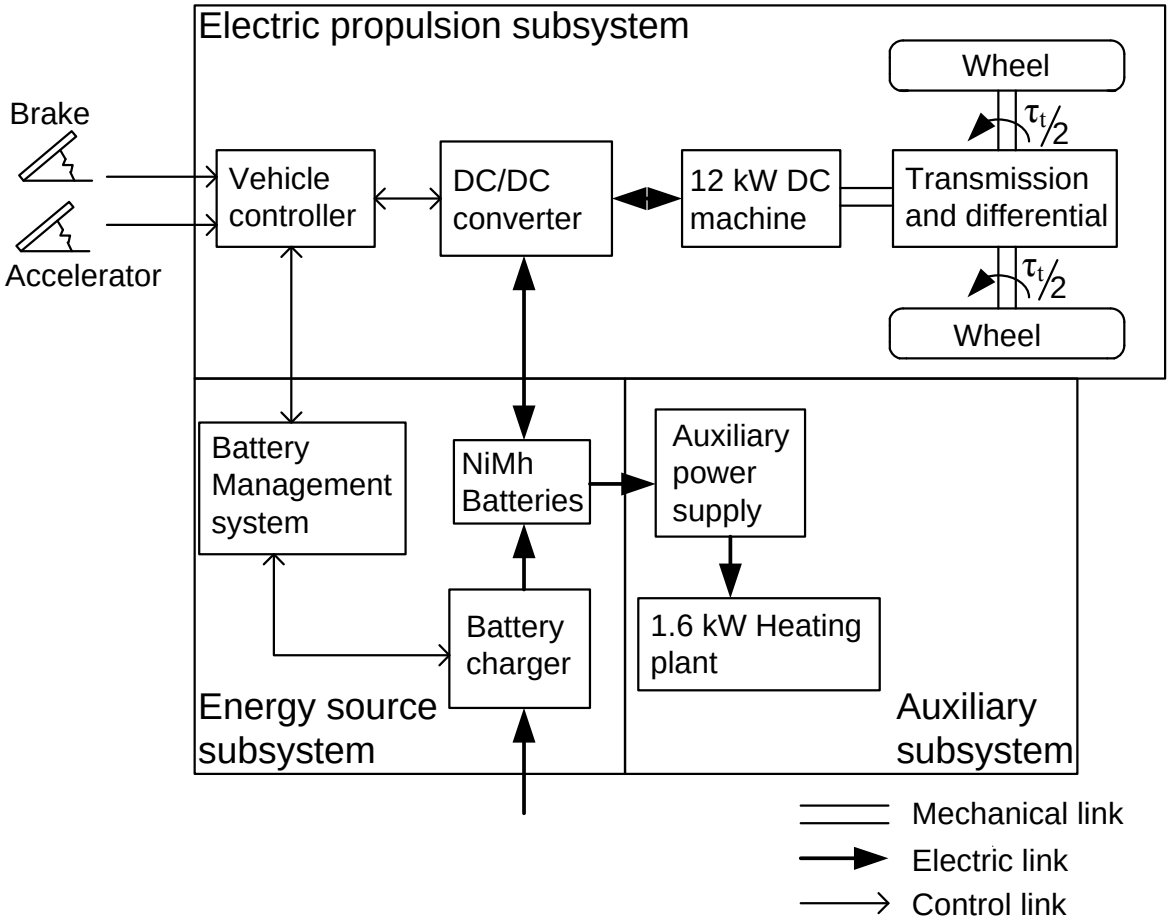

Figure 2.8: *Original configuration of the Kewet EV.*

2.4.1 New Components in the Vehicle

In order to attempt to increase the range of the EV, components from the Kewets powertrain is replaced. In figure 2.9 the new vehicle configuration of the Kewet EV is seen.
The DC machine is replaced by an induction machine. The DC/DC converter is replaced by a 3-phase inverter. The NiMH (nickel-metal hydride) batteries are replaced by Li-ion (Lithium-ion) batteries. Finally the vehicle controller is replaced by a DSP (digital signal processor).

The efficiency of the original DC machine is unknown, but as earlier mentioned the efficiency of induction machines is better than DC machines in general [Ehsani et al., 2010, p. 168]. Furthermore induction machines have lower weight, volume and prize for a similar power DC machine [Ehsani et al., 2010, p. 168]. The maintenance expenses are also lower for induction machines since it has no commutator brunches which require maintenance and replacement over time [Oriental motor].

The 3-phase inverter powers the induction machine using MOSFET's (Metal-Oxide Semiconductor Field-Effect Transistor) supplying PWM (Pulse-Width Modulated) voltage to the terminals of the induction machine.
It is unknown which type of DC/DC converter is used in the original vehicle configuration of figure 2.8. One solution may be a chopper [Ehsani et al., 2010, p. 158]. For a separately excited DC machine the chopper supplies PWM voltages to the stator- and rotor circuit. The chopper supplies the PWM voltages using a transistor i.e. a MOSFET [Ehsani et al., 2010, p. 159]. Since the 3-phase inverter and the chopper may use the same type of components in switch mode it might be reasonable to assume that they approximately have the same efficiency. It is unknown whether it is a chopper type of DC/DC converter used in the original configuration ruling out efficiency comparison of the power electronic converters.

The specific energy of the original NiMH batteries is listed to be 65 $^{Wh}/_{kg}$ [Ehsani et al., 2010, p. 388]. The Li-ion based batteries used in the new configuration has a nominal voltage of 3.2 V and a nominal capacity of 160 Ah [ThunderSky] yielding a nominal energy of 512 Wh. The weight of one cell is 5.6 kg resulting in a specific energy of 91.4 $^{Wh}/_{kg}$, 40.6 % larger than the original batteries. The general specific energy of a Li-ion battery is listed to be 155 $^{Wh}/_{kg}$ [Ehsani et al., 2010, p. 389]. The 41.0 % lower value for the specific energy calculated from datasheet values may result from i.e. the weight contribution of the robust battery casing.
In the following chapter a problem is formulated based on range improvement of the configured Kewet EV.

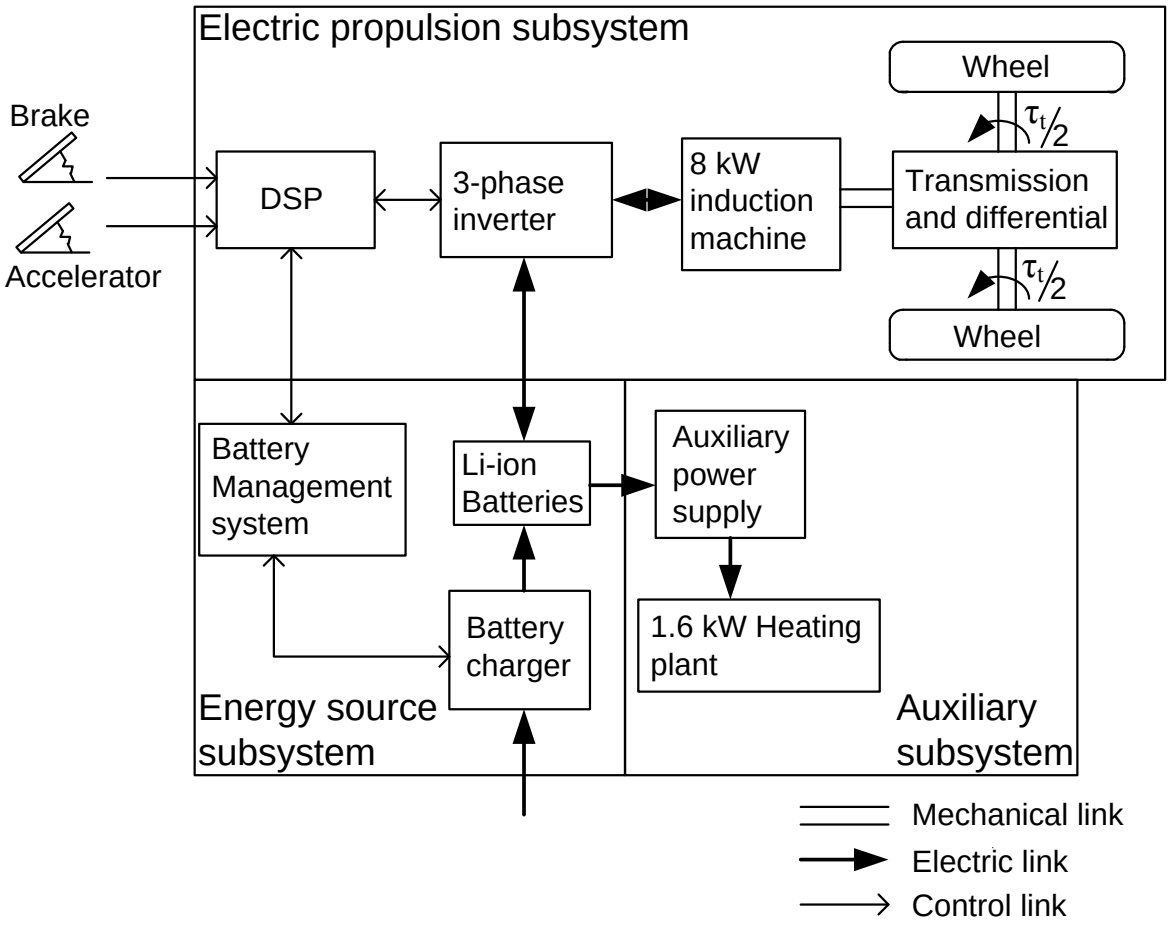

Figure 2.9: *New configuration of the Kewet EV.*

CHAPTER 3

PROBLEM FORMULATION

As oil prices are rising due to depletion of oil resources the EV is becoming a more viable alternative to the internal combustion engine vehicle. Two of the main disadvantages of the EV is the range per charge and the charge time. In order to obtain a larger range per charge it is desired to increase the efficiency of the components in the powertrain of the EV. In the problem analysis the forces counteracting the propulsion of the electric vehicle was analyzed. The general configuration of an EV was described and the case study EV for this project was presented. The case study is a Kewet EV. In order to improve the range of the EV some of the components in the powertrain of the EV are replaced. The new parts in the powertrain are Li-ion batteries, a three phase inverter and an 8 kW induction machine.
The focus of this project is developing a control strategy for the induction machine in order to obtain good energy efficiency and hereby improving the range of the electric vehicle. It is hereby desirable to develop a control strategy which provides the best possible efficiency of the induction machine and the inverter, without compromising the performance of the electric vehicle. This leads to the following formulation:

How can the efficiency of an induction machine and an inverter for an electric vehicle be maximized by implementing energy efficient control without compromising the performance of the electric vehicle?

In order to determine an energy efficient control strategy it is desirable to develop an algorithm for determination of energy optimal magnetizing flux throughout the entire operating area of the induction machine. The algorithm is to map the induction machine, determine loss equation parameters and determine energy optimal magnetizing flux. The algorithm is intended to also be applicable in other induction machine applications.

3.1 Demand Specification

In order to evaluate the developed control strategy it is important to specify the demands for the solution.

Implementation in Kewet EV

The control strategy must be applicable in the Kewet EV. The implementation in the electric vehicle must therefore be considered when developing control strategies and building test setups throughout the project.

Correspondence to Urban Drive Cycle

In order to evaluate the developed control strategy a standard drive cycle for light weight urban vehicles are simulated using a developed simulation model. The drive cycle is seen in figure 3.1. The velocity of the electric vehicle throughout the drive cycle must have proper correspondence with the drive cycle. Proper correspondence is considered as a maximum error of 5 $^{km}/_{h}$.

Maximum Velocity of Electric Vehicle

The speed limit on highways in Denmark is 80 $^{km}/_{h}$. The electric vehicle is considered to be an urban vehicle however it is desirable that the vehicle can drive on highways as well. It is therefore considered as a demand for the performance of the electric vehicle to be able to reach a velocity of 80 $^{km}/_{h}$.
Since the original electric machine of the Kewet EV was a 12 kW DC machine and the maximum velocity of it was 80 $^{km}/_{h}$ it is highly unlikely that the 8 kW induction machine is able to provide a similar maximum velocity. The Kewet EV however functions as a case study. The considerations described throughout this report are also applicable for other EVs with larger induction machines.

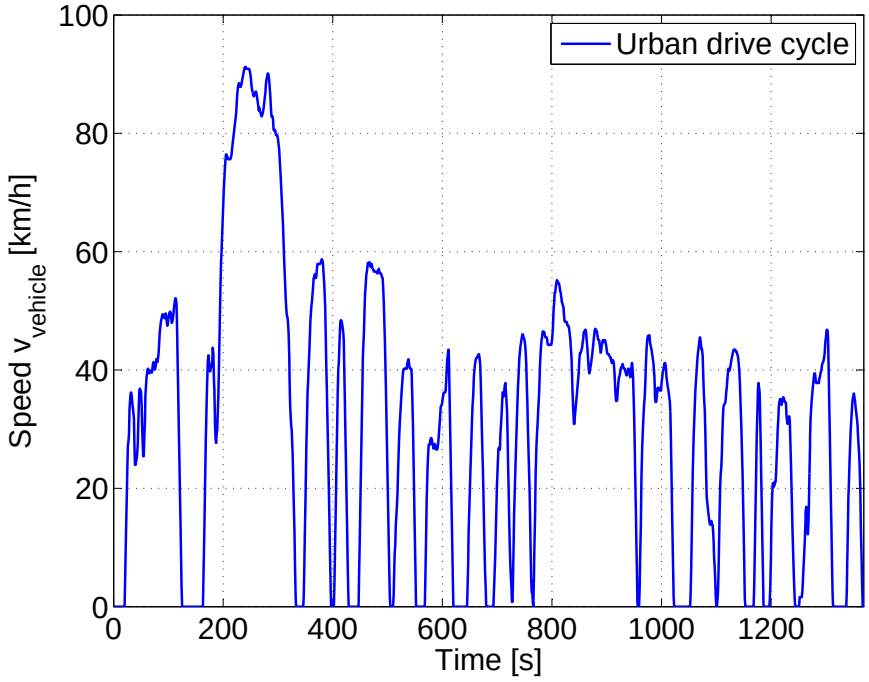

Figure 3.1: *Urban drive cycle.*

Energy per Range

From section 2.4 the energy per km is calculated. Assuming a range per charge of 100 km the energy per range is calculated to 0.144 $^{kWh}/_{km}$. For the implementation of the induction machine, inverter and batteries to be justifiable the energy per range must be decreased at least 10 %.

CHAPTER 4

SOLUTION STRATEGY

According to the problem formulation an energy efficient control strategy for an induction machine in an electric vehicle (EV) is to be developed. This chapter contains a description of the strategy for developing an energy efficient control method. The structure of the rest of this report is seen in the following listing:

- Description of test setup and implementation strategy for EV (Chapter 5).
- Modeling of powertrain in EV (Chapter 6).
- Development of control strategy for EV (Chapter 7).
- Description of DSP (Digital Signal Processor) program for controlling the induction machine (Chapter 8).
- Mapping of induction machine (Chapter 9).
- Determination of loss equations (Chapter 10).
- Determination of energy optimal magnetizing currents for the induction machine (Chapter 11).
- Implementation strategies for energy optimal control of EV (Chapter 12).

In order to test developed control strategies a test setup is designed in the laboratory. The test setup is used to test control strategies before the actual implementation in the electric vehicle.

The design of the test setup and choosing an appropriate induction machine is done with respect to easy implementation in the electric vehicle. The test setup and implementation strategy is described in the proceeding chapter.
Since most modern vehicles are designed to deliver a torque corresponding to an acceleration pedal position [Bosch, 2007, p. 610] a torque control strategy is to be implemented on the induction machine. The control scheme chosen for the induction machine is field oriented control (FOC). This control scheme provides a good dynamic torque response [Rasmussen, 2010] which is important for an electrical vehicle. In order to develop control strategies a simulation model of the powertrain is constructed for testing potential control strategies. The modeling of the powertrain is presented in chapter 6 and the development of a control strategy is presented in chapter 7. The control strategy is implemented and tested on a DSP connected to the test setup. The program for the DSP is presented in chapter 8.
When using FOC for an induction machine the magnitude of the rotor flux can be controlled. In order to obtain energy efficient control of the electric vehicle it is desirable to vary the magnitude of the rotor flux to obtain the highest possible efficiency at all possible velocity -and torque combinations.
A mapping of the machine is therefore performed in chapter 9 measuring the combined efficiency of inverter and machine at various velocities, torque and rotor flux magnitudes.
After mapping the machine an optimization algorithm is used to determine parameters in equations describing the losses in the system (chapter 10). These equations are used to determine optimal rotor flux magnitudes at various velocities and torque with respect to energy efficiency (chapter 11).
Variation of the rotor flux magnitude induces undesirable dynamics in the torque control. Varying the magnitude of the rotor flux is therefore a compromise between performance and energy efficiency of the machine. Three control strategies involving compromises between energy efficiency and performance are developed and tested in chapter 12 and finally it is concluded which strategy for implementation of energy efficient control in an EV is most promising.

CHAPTER 5

SYSTEM DESCRIPTION

As stated in the problem formulation an energy efficient control strategy is to be developed for an induction machine supplied by an inverter. This chapter contains a description of how the machine, inverter and control system is to be implemented in the vehicle.
In order to test control strategies a test setup was designed. The test setup is described in this chapter.

5.1 Implementation in Kewet Electric Vehicle

The design of various components and choosing an appropriate induction machine is done with respect to easy implementation in the electric vehicle. This means that the components designed and assembled for the test setup can be directly implemented in the EV.
As stated in the problem analysis section 2.4 the original DC motor is removed from the motor compartment of the electric vehicle. In figure 5.1a it is seen where the induction machine is to be mounted in the motor compartment. This mounting sets some demands for the dimensions and shaft type of the induction machine. These demands are further explained in section 5.2.3.

The control system including inverter, signal electronics and battery management system is to be placed on top of the motor compartment as illustrated in figure 5.1b. The battery pack is to be placed under the seats.

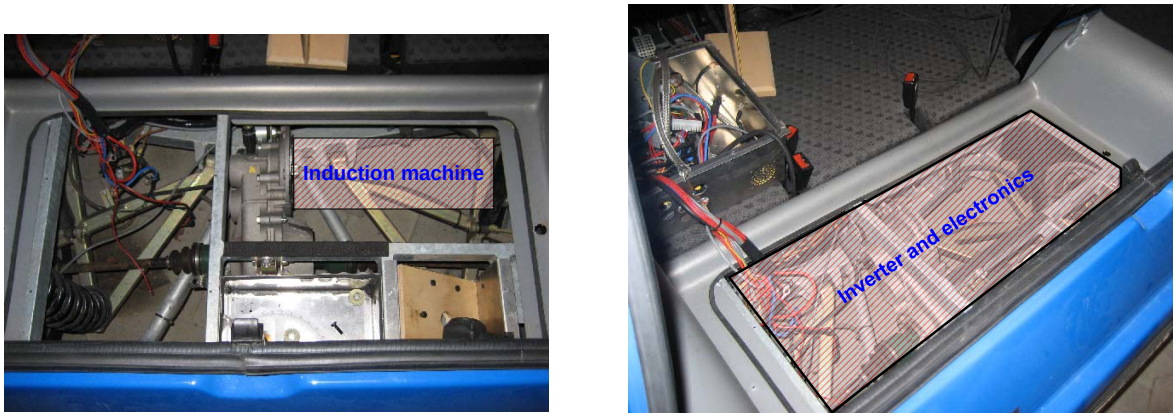

(a) *Motor compartment of the electric vehicle.*

(b) *Top of the motor compartment of the electric vehicle.*

Figure 5.1: *Implementation of induction machine, inverter and control system in the electric vehicle.*

5.2 Test Setup

This section contains a description of the test setup that was designed in order to test control strategies for the electric vehicle. The test setup is illustrated in figure 5.2.

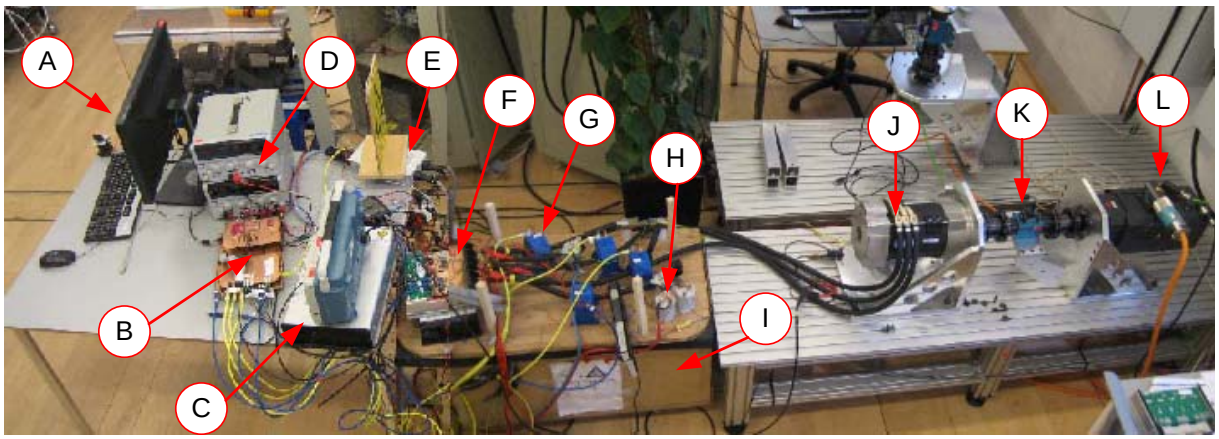

Figure 5.2: *Overview of the test setup.*

The parts numerated in figure 5.2 are explained in the following:

(A) Computer for control of the entire test setup.

(B) Control boards for test setup including DSP, optical in- and output ports, RJ45 ports and DC/DC converters.

(C) Charger for the battery pack.

(D) Laboratory power supplies for test setup.

(E) Battery management system (BMS) for monitoring and controlling the battery pack.

(F) Inverter.

(G) LEM current transducers.

(H) Relays controlled by BMS for connecting the battery pack to the inverter and for connecting the charger to the battery pack when charging.

(I) Battery pack.

(J) Induction machine.

(K) Torque transducer.

(L) Siemens drive system.

A schematic of the test setup is seen in figure 5.3.

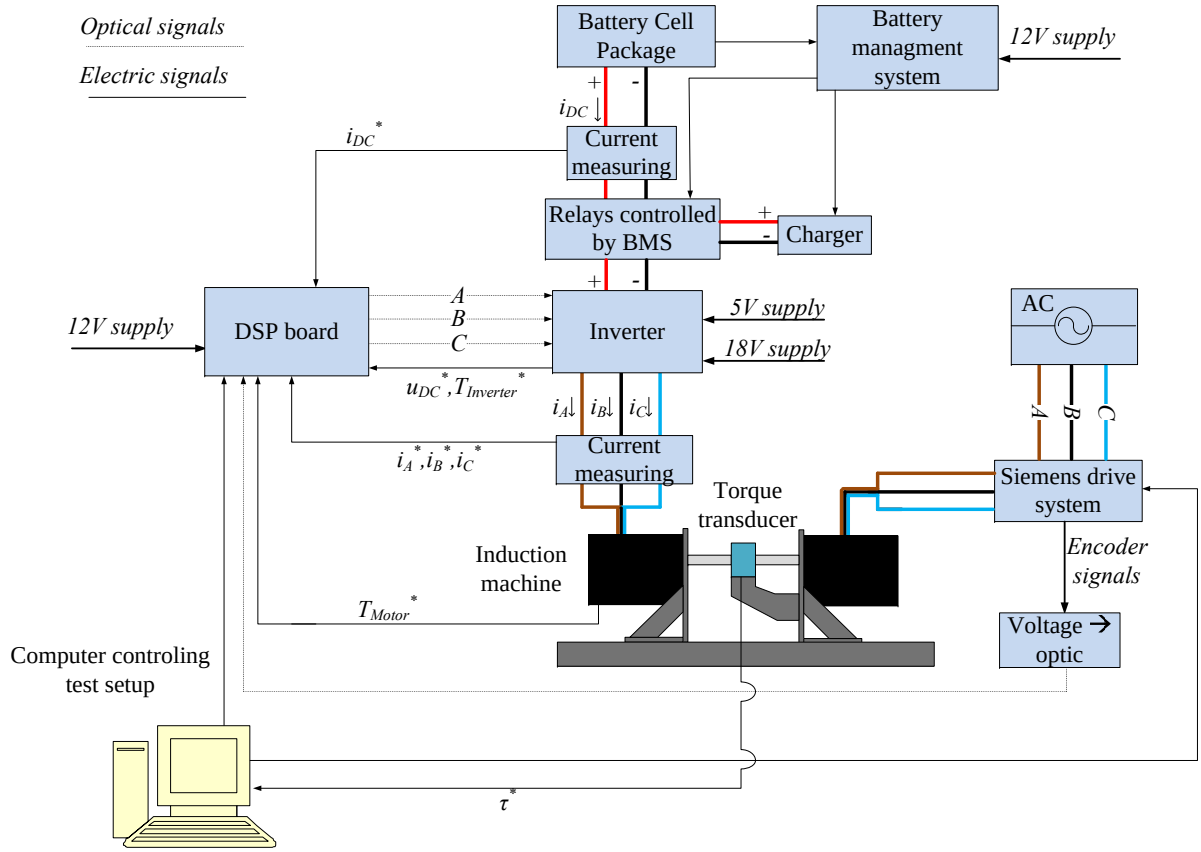

Figure 5.3: *Schematic of test setup.*

The test setup is divided into six parts and explained further throughout the rest of this section.

5.2.1 Battery Pack including BMS and Charger

The battery pack consists of 20 Thunder Sky battery cells. One of the battery cells is seen in figure 5.4a. Specifications for the battery cells is seen in table 5.1.

Thunder Sky battery cell	
Model number	TS-LFP160AHA
Nominal capacity	160Ah
Operational voltage	2.5V - 4.25V
Nominal voltage	3.2V
Max charge current	$\leq$3CA
Max discharge current (continuous)	$\leq$3CA
Max discharge current (impulse)	$\leq$20CA
Standard charge/discharge current	0.5CA
Operating temperature	-45°C $\sim$ 85°C
Self-discharge rate	$\leq$3% (monthly)
Weight	5.6 kg $\pm$ 100g

Table 5.1: *Specifications for battery cells (1CA=160A. [ThunderSky]).*

The 20 battery cells are coupled in two parallel strings each consisting of ten cells. This connection type is illustrated in figure 5.4b. As seen in figure 5.2 the battery pack is placed in a wooden box underneath the inverter. As stated in section 5.1 the battery pack is to be implemented underneath the front seats of the electric vehicle and the wooden box is therefore a temporary container only to be used in the test setup.

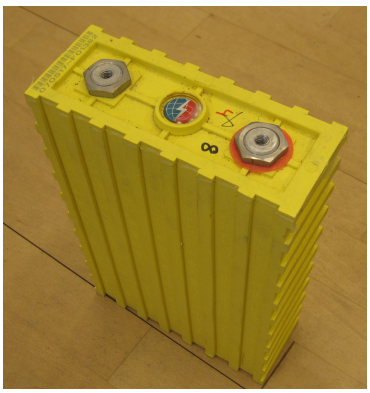

(a) *Thunder Sky battery cell.*

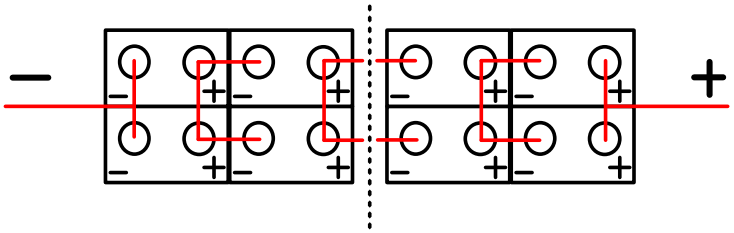

(b) *Connection of cells in battery pack. The dotted line implies that the pack consists of more cells than the eight cells in the figure. The total battery pack consists of 20 cells.*

Figure 5.4: *Single battery cell and battery pack schematic.*

Battery Management System

The battery management system (BMS) is produced by Lithium Balance. The function of the BMS is to protect the battery pack. The BMS can be set in three modes: charge, discharge or idle. The mode is controlled by a manual switch next to the computer controlling the test setup. The relays and the switch are seen in figure 5.5.

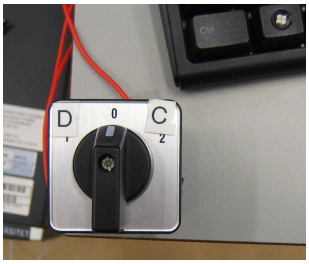

(a) Manual switch for BMS system.

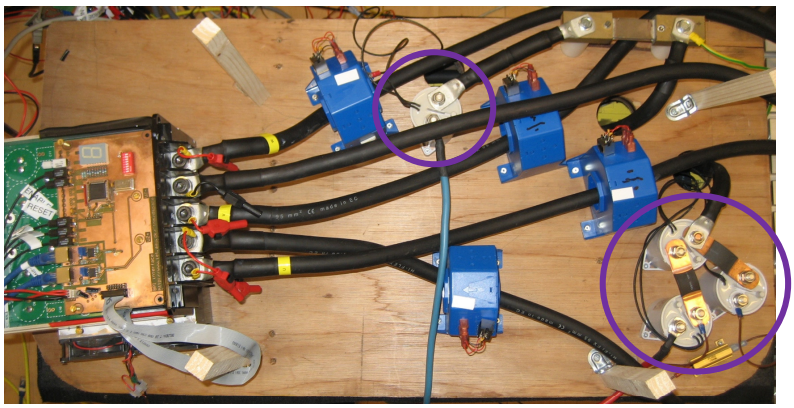

(b) Relays controlled by BMS. The relays are marked by purple circles.

Figure 5.5: *Manual switch controlling the BMS and relays controlled by the BMS.*

The relay settings for each of the three modes are illustrated in figure 5.6. As seen in the figure the circuit contains a pre-charge resistor. This is activated as the manual switch is set to charge or discharge. The resistor limits the current entering the capacitor bank of the inverter until the voltage difference between the battery pack and the capacitor bank is sufficiently small. The resistor is thereafter disconnected from the circuit. The shunt resistor is used by the BMS system to measure the charge/discharge current.

The BMS monitors the voltage of each cell, the temperature of the battery pack and the charge/discharge current. Restraints as e.g. minimum and maximum cell voltage, maximum temperature and maximum discharge/charge current are set in the BMS software. If a restraint is violated the BMS will open the relays disconnecting the battery pack.

When charging the battery pack using the charger the BMS controls the charge current. In the BMS software the maximum voltage difference between the cells is set. If this restraint is violated during charging the BMS will even out the difference by discharging the cell at the highest potential. This is called bleeding.

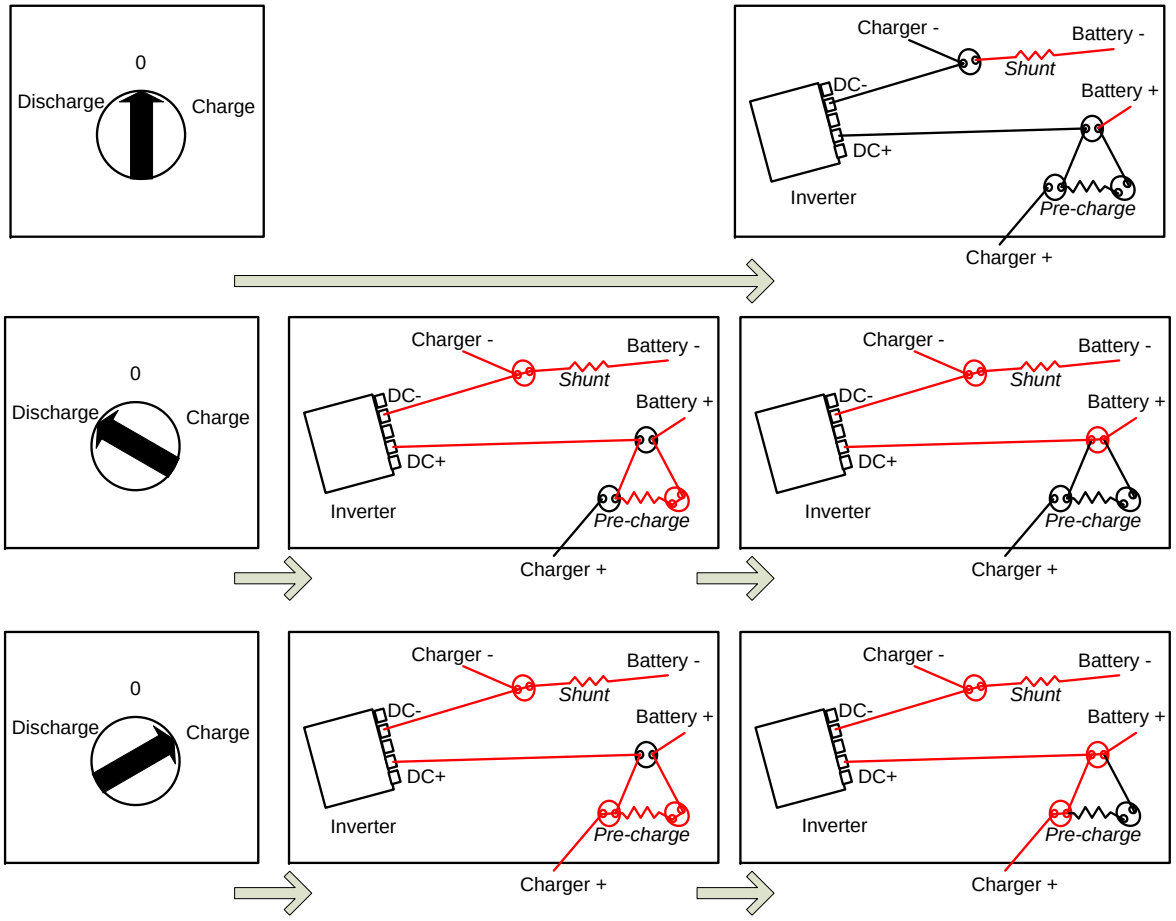

Figure 5.6: *Relay settings for idle, discharge and charge. Red lines marks connection to the battery terminals. A red relay marks that the relay is closed.*

5.2.2 Inverter

The inverter is produced by Sauer Danfoss and is seen in figure 5.7. Specifications for the inverter is seen in table 5.2. The inverter is placed on the wooden board on top of the battery pack as seen in figure 5.4b. When implementing the system in the EV the wooden board is to be placed on top of the motor compartment according to figure 5.1b.

Sauer Danfoss battery powered inverter	
Model number	BPI 5435
Input DC voltage	48V (-35%/+20%)
Output RMS current	0-350A

Table 5.2: *Specifications for Sauer Danfoss inverter.*

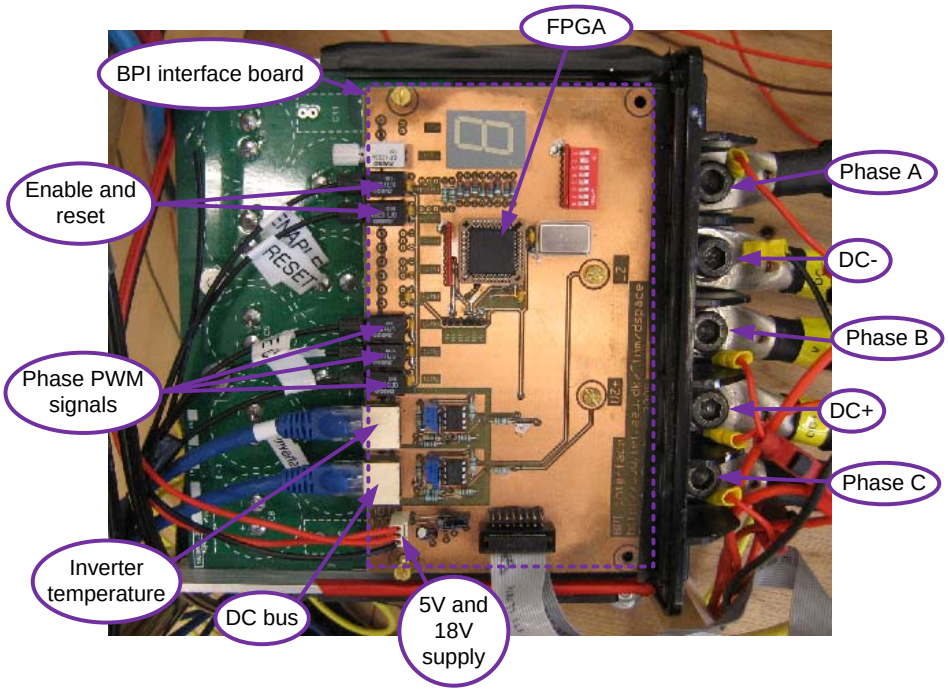

Figure 5.7: *Sauer Danfoss inverter.*

A BPI interface board controlling the inverter is placed on top of the inverter, as seen in figure 5.7. The inverter needs a 5 V -and an 18 V supply to function. The BPI interface board receives optical PWM signals from the DSP described later in this chapter. The PWM signals are send to a FPGA (Field Programmable Gate Array) on the BPI interface board which calculates when to open and close the transistors of the inverter. The FPGA also includes dead time which can be adjusted by the user on the BPI interface board. The DC bus and inverter temperature are measured and send to the DSP through RJ45 ports. The schematics and a more detailed description of the BPI interface board is found in appendix H.

The inverter has two input and three output terminals. The input terminals are for $DC+$ and $DC-$ and the three output terminals are for the three phases A, B and C.

5.2.3 Induction Machine

As stated in section 5.1 the induction machine is to be mounted in the motor compartment. Since there is a limited amount of space in the motor compartment some demands must be set for the dimensions of the induction machine. Furthermore the shaft and the interface of the induction machine must correspond with the shaft and interface of the differential in the electric vehicle or at least some adapter must be produced. The shaft end of the differential is a spline and is seen in figure 5.8. The rear right wheel is also marked in the figure to give a sense of orientation.

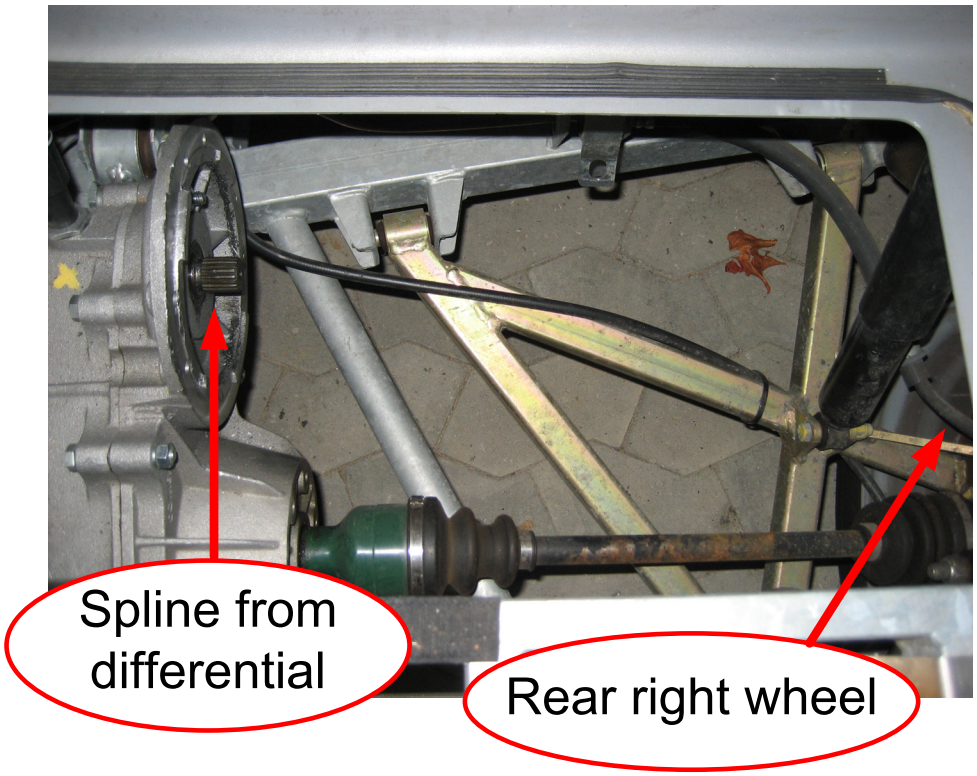

Figure 5.8: *Motor compartment.*

The induction machine chosen for the electric vehicle is from the German company ABM Greiffenberger. The machine has an internal spline corresponding to the external spline on the differential in the electrical vehicle. The machine however only has one end shield. Therefore another end shield must be designed and produced. Machine specifications are seen in table 5.3.

ABM induction machine	
Model number	DLGF 112200 - 4
Nominal speed	2000 rpm
Nominal torque	45 Nm
Nominal RMS voltage line-line	28 V
Nominal RMS current	304 A
Nominal frequency	69 Hz
Maximum speed	5000 rpm
Number of poles	4
Stator winding connection	Δ
Winding temperature class	F (155°C continuous)
Temperature sensor	KTY84
Protection class	IP 20
Mounting type	B9

Table 5.3: *Specifications for ABM induction machine.*

Torque, power, voltage and current characteristics for the induction machine are seen in figure 5.9. Furthermore torque -slip curves at various synchronous frequencies F_{syn} is seen in figure 5.10. The torque slip curves is created using a steady state model which is presented in appendix D and IM parameters determined in section 6.3.1. Furthermore magnetic saturation which is an issue for the torque -slip curve at a synchronous frequency of 69 Hz is taken into account. The magnetic saturation compensation is described in section 7.3.3. The torque -slip curve at 69 Hz has a peak motor mode torque of 85 Nm. The stator RMS current level at this operating point is 675 A limiting the time of operation considerably.
The performance of the induction machine when implemented in the electric vehicle is considered in the proceeding subsection *Machine Performance in Electrical Vehicle.*

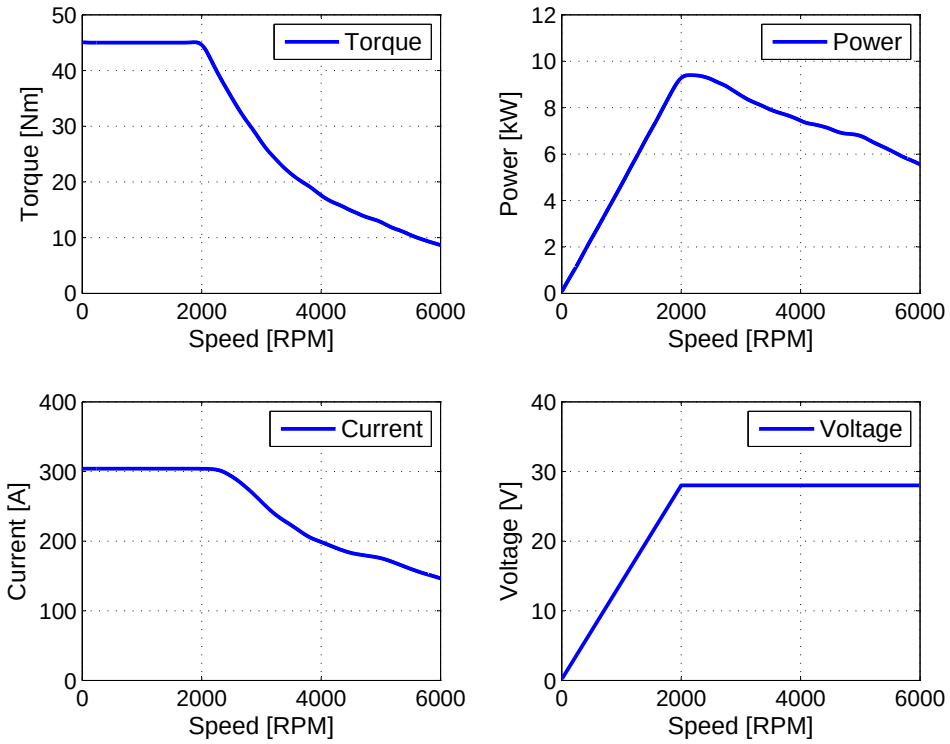

Figure 5.9: *Torque, power, voltage and current characteristics at various angular velocities [ABM].*

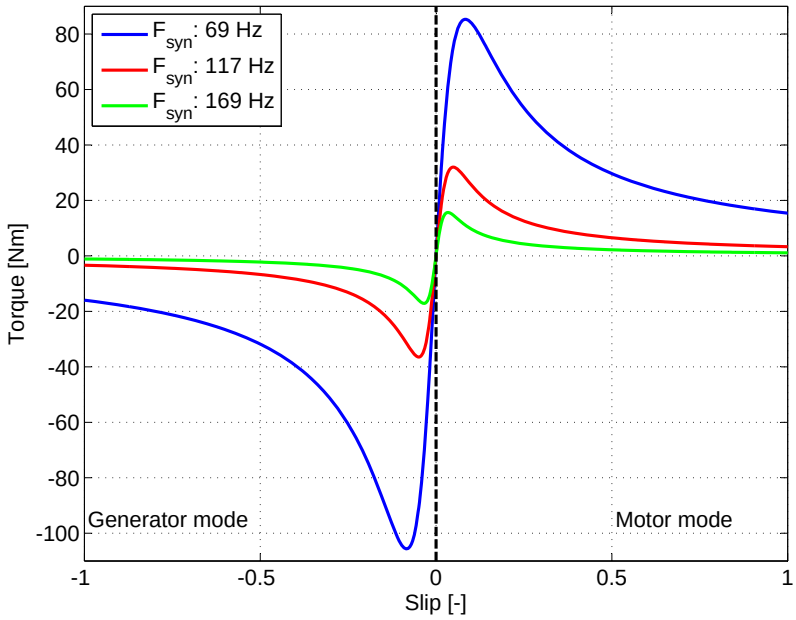

Figure 5.10: *Torque -slip curves at various synchronous frequencies F_{syn}.*

As mentioned earlier an end shied must be designed for the induction machine. A 3D model of the induction machine including a mounted end shield is seen in figure 5.11a. The induction machine mounted on the differential of the electric vehicle is seen in figure 5.11b.

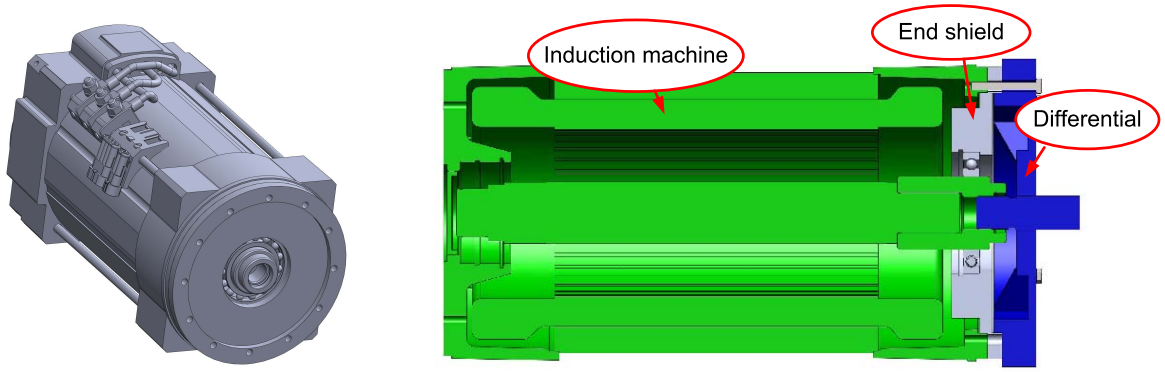

(a) *Induction machine including end shield.*

(b) *Cut through view of the induction machine mounted on the differential in the electric vehicle.*

Figure 5.11: *Induction machine.*

A closer view of the end shield is seen in figure 5.12.

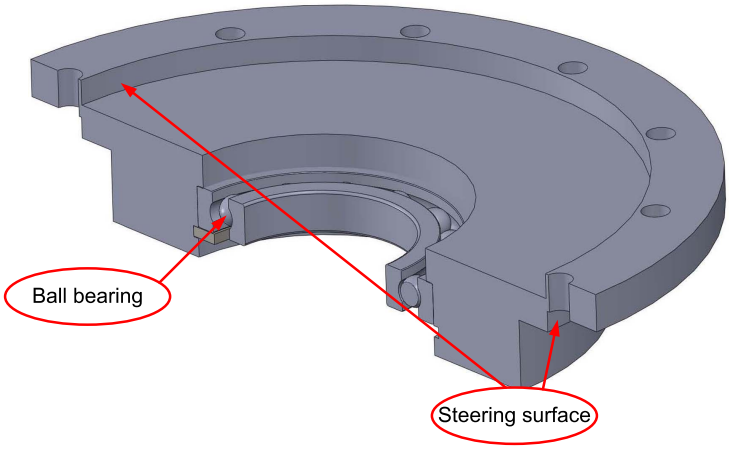

Figure 5.12: *Cut through view of end shield.*

When using the designed end shield the engagement of the spline connection is about 1/3 of the full length. With this engagement the connection is able to transmit 153 % of the maximum torque of the induction machine, calculations is found in appendix G. A transmissible torque of at least twice the maximum torque of the induction machine is desired, and the engagement of the connection must therefore be increased. The internal spline module is mounted on the rotor shaft using an interference fit. To increase the engagement of the spline, the module is heated in an attempt to pull it closer to the differential. However during this attempt the spline module

is destroyed.Therefore a new internal spline is developed for the induction machine. The new internal spline is illustrated in figure 5.13. The new internal spline is dimensioned to provide full engagement of the spline connection (18.5 mm). This connection provides a transmissible torque of 456 % of the maximum torque of the induction machine.
The new internal spline is to be mounted on the induction machine using an interference fit. The designed fit provides a transmissible torque of 313 % of the maximum torque of the induction machine. The calculations for the interference fit is seen in appendix G.

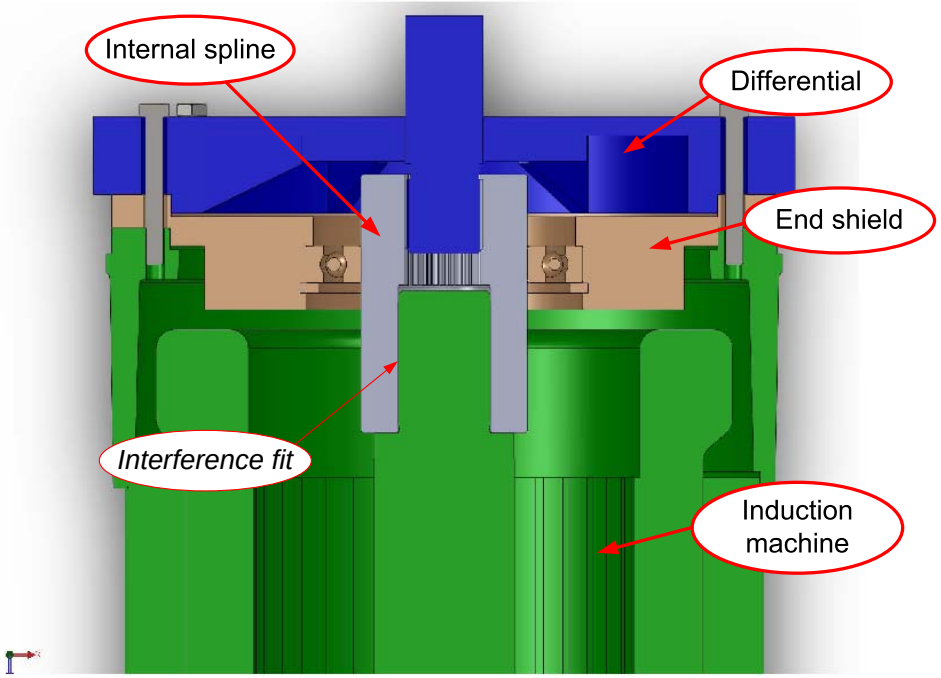

Figure 5.13: *Cut through view of internal spline mounted on rotor shaft.*

The induction machine is mounted in the test setup as seen in figure 5.2. The shaft is connected to a torque transducer which is connected to the Siemens drive system described later in this chapter. The induction machine, torque transducer and servo motor from the Siemens drive system is seen in figure 5.14.
The three phase terminals of the machine are connected to the inverter described in the previous section. The motor is equipped with a thermal sensor and an encoder. The thermal sensor is used to estimate the stator winding temperature. The encoder can be used to determine the angular position of the shaft. The Siemens drive system also offers encoder signals that can be used to determine the shaft position, as described later in this chapter. The Siemens drive

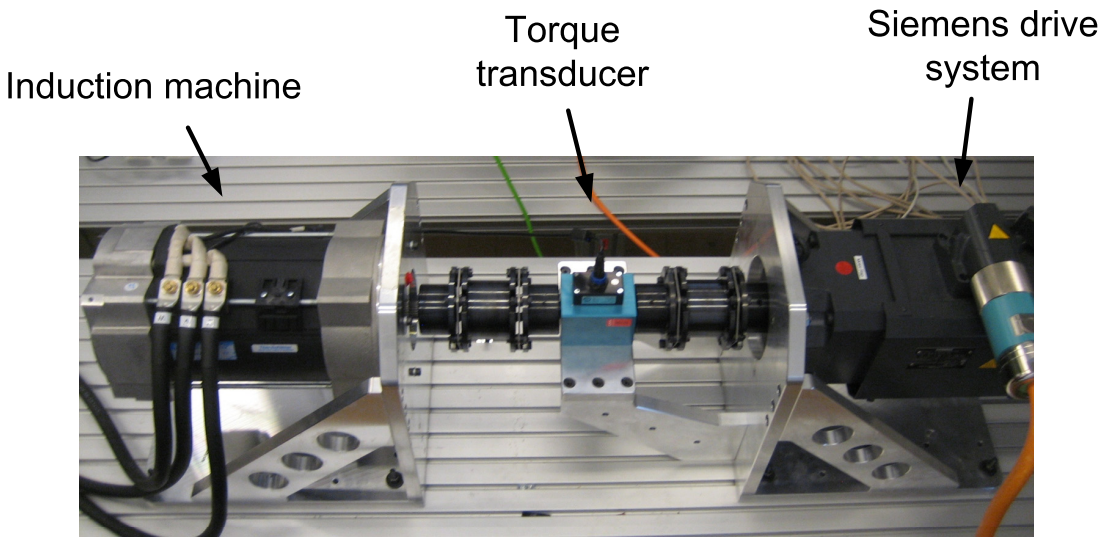

Figure 5.14: *Induction machine connected to torque transducer and servo motor from Siemens drive system.*

encoder signals has a better resolution than the encoder of the induction machine. Therefore the encoder signals from the Siemens drive system is used instead.

Machine Performance in Electrical Vehicle

In order to determine whether the induction machine is a reasonable choice for the electrical vehicle the performance of the induction machine when implemented in the electrical vehicle must be considered.
As seen in figure 5.9 the induction machine is able to provide a constant high torque at low velocities. This is beneficial since it is desirable to be able to obtain high acceleration from low velocities. At higher velocities the obtainable torque drops but when the EV has obtained a high velocity a high acceleration is not as crucial. The general torque characteristic of the induction machine is hereby suitable for the EV. As a comparison vehicles using internal combustion engines are equipped with several gear settings in order to obtain a similar good torque characteristic [Chan and Chau, 2001, p. 34].

In order to evaluate the performance of the induction machine further, the torque required of the induction machine in order to provide predefined accelerations and velocities of the electric vehicle must be determined. In section 6.4.2 the torque equation for the induction machine when implemented in the electrical vehicle is derived (equation (6.20)). In this equation the angular velocity of the induction machine can be simulated using torque and time as inputs.

The equation is rewritten in order to determine the translational velocity of the electric vehicle as function of the applied torque of the induction machine. For convenience the torque equation is also seen in equation (5.1).

$$\begin{aligned}\dot{\omega}_m \cdot \frac{m_{EV}}{7^2} \cdot r_w^2 &= \left(\tau_e - \tau_{\mu-IM}\right) \cdot \mu_{differential} \cdot \mu_{gear} \\ &\quad -m_{EV} \cdot g \cdot \sin\left(\theta_{road}\right) \cdot \frac{r_w}{7} - \frac{1}{2} \cdot \rho \cdot A_f \cdot C_D \cdot \left(\frac{\omega_m}{7} \cdot r_w - V_w\right)^2 \cdot \frac{r_w}{7} \\ &\quad -g \cdot \cos\left(\theta_{road}\right) \cdot 0.01 \cdot \left(1 + \frac{\frac{\omega_m}{7} \cdot r_w}{160}\right) \cdot \frac{r_w}{7} \end{aligned} \tag{5.1}$$

where:

	ω_m	Angular velocity of shaft $[rad/s]$
	m_{EV}	Mass of EV $[kg]$
	r_w	Radius of wheels in electric vehicle $[m]$
	τ_e	Torque of induction machine $[Nm]$
	$\tau_{\mu-IM}$	Friction of bearings in induction machine $[Nm]$
	$\mu_{differential}$	Efficiency of differential in electric vehicle $[-]$
	μ_{gear}	Efficiency of gear in electric vehicle $[-]$
	θ_{road}	Gradient of road $[rad]$
	ρ	Density of air $[kg/m^3]$
	A_f	Frontal area of the EV $[m^2]$
	C_D	Aerodynamic drag coefficient $[-]$
	V_w	Velocity of the wind blowing in the moving direction of the EV $[m/s]$

The angular velocity of the shaft is directly transformed to translational velocity of the electric vehicle as described in section 6.4.2.

From equation (5.1) it is possible to calculate the torque needed to obtain a constant velocity of the electric vehicle or an acceleration of the electric vehicle at a given torque. Some of the factors in the equation are dependent on driving conditions. These factors are the gradient of the road (θ_{road}) and velocity of the wind (V_w). It is desirable to inspect the performance of the induction machine in the electric vehicle when varying these driving conditions. This is done in the preceding.

The constants in equation (5.1) are seen in table 5.4. The friction of the induction machine is a function of the rotor velocity and is seen in section 6.4.1. The friction is close to 1 Nm at most velocities and is therefore set constant at 1Nm in these calculations.

Constant	Value
m_{EV}	800 kg
r_w	0.2665 m
$\tau_{\mu-IM}$	1 Nm
$\mu_{differential}$	0.94
μ_{gear}	0.98
ρ	1.3 kg/m^3
A_f	1.785 m^2
C_d	0.5

Table 5.4: *Constants used in torque equation.*

It is now possible to evaluate the performance of the induction machine at various driving conditions. The performance at zero wind velocity ($V_w = 0$) and zero gradient of the road ($\theta_{road} = 0$) is illustrated in figure 5.15. As seen in the figure the maximum velocity of the electric vehicle is about 69 km/h. As expected in the demand specification (section 3.1) the maximum velocity of the EV, with the 8 kW induction machine implemented, does not meet the demand for maximum velocity of 80 km/h. The Kewet EV however serves as a case study for any electric vehicle equipped with an induction machine as the considerations regarding energy optimal control are applicable for any induction machine.
The performance when varying the wind velocity and gradient of the road is evaluated in the proceeding.
The effect of wind velocity is dependent on whether the wind is positive (tailwind) of negative (headwind). As seen in figure 5.16 increasing the headwind decreases the maximum velocity of the electric vehicle due to the increase in drag force. The drag force equation is seen in section 2.1. The magnitude of the force is proportional to the drag coefficient C_d. C_d is set to 0.5 but it may vary between 0.15 to 0.7 depending on the shape of the vehicle. If the actual drag coefficient of the EV is lower than 0.5 the maximum velocity of the EV is increased however since the maximum velocity of the induction machine is 5000 rpm (corresponding to a translational velocity of 71.7 km/h) the performance is still not acceptable according to the demand specification, section 3.1.
The effect of varying the gradient of the road is dependent on whether the gradient is positive (uphill) or negative (downhill). When the gradient is positive the maximum velocity decreases. This is seen in figure 5.17. The maximum gradient that the EV is able to start from is about 7.1°. As a comparison the steepest road in Denmark is 13.5° [Danskebjerge.dk].

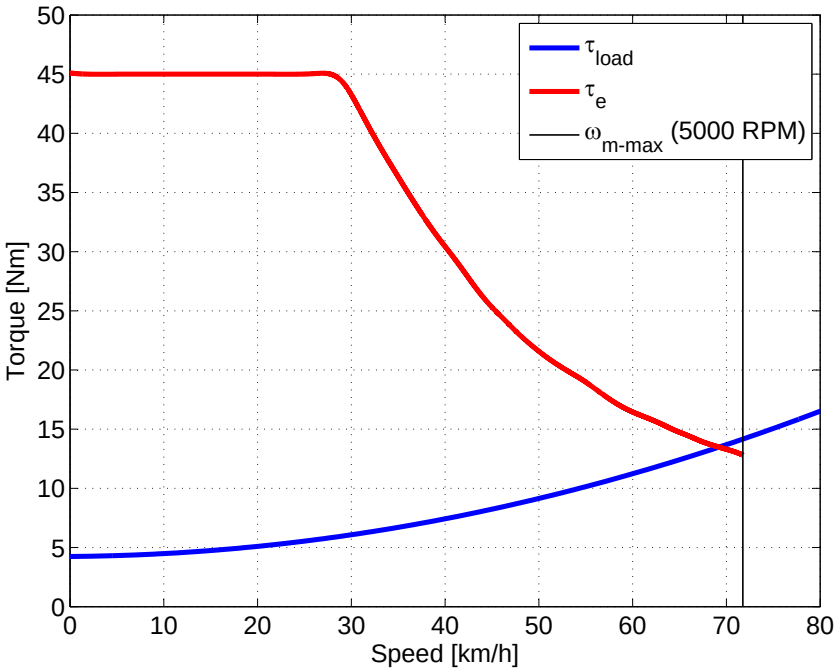

Figure 5.15: *Performance evaluation of induction machine at zero wind and zero gradient of road. τ_e is the maximum torque provided by the induction machine and τ_{load} is the sum of the torque counteracting τ_e according to equation* (5.1).

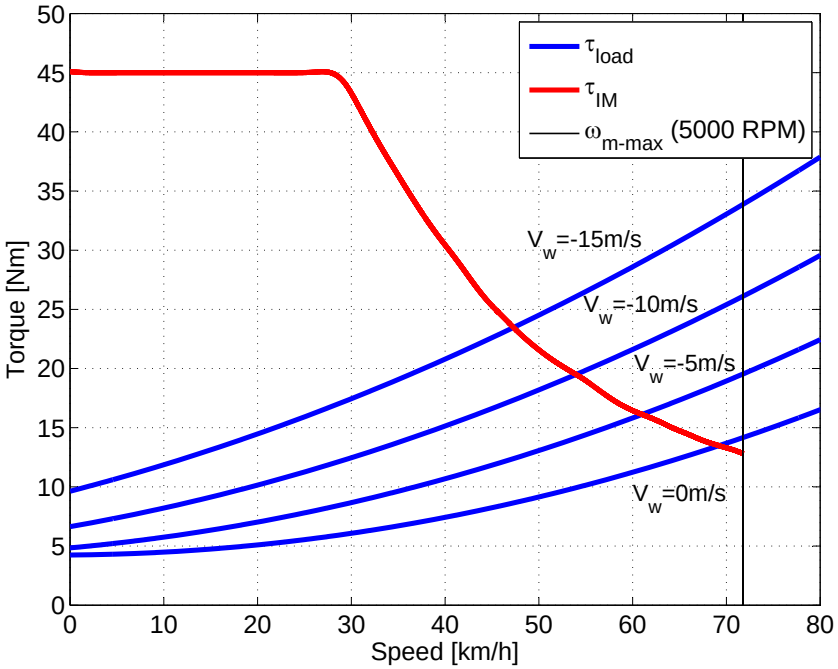

Figure 5.16: *Performance evaluation of induction machine when varying the wind velocity.*

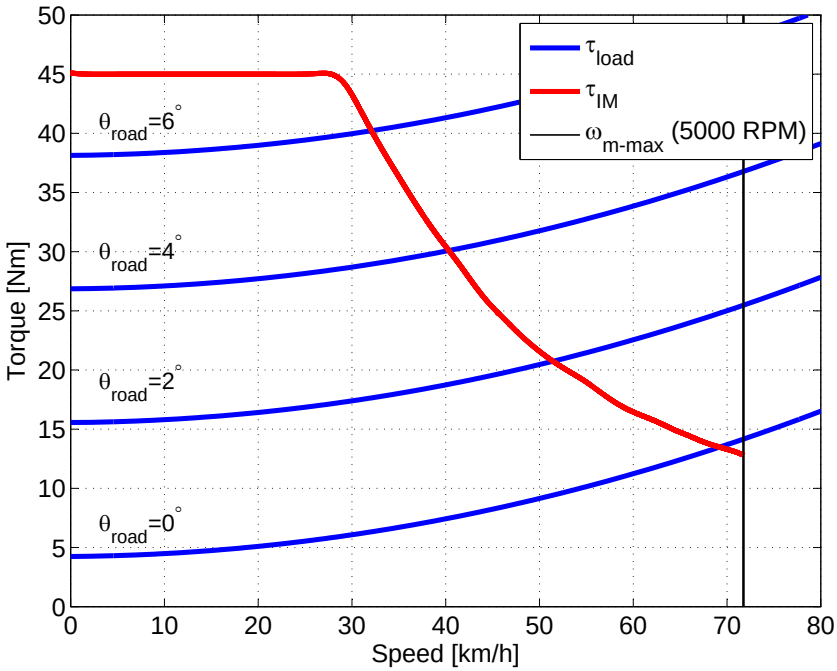

Figure 5.17: *Performance evaluation of induction machine when varying the gradient of the road.*

The velocity of the EV during maximum acceleration is seen in figure 5.18. The wind velocity and road gradient are both set to zero. As seen in the figure the electric vehicle reaches 50 $^{km}/_{h}$ in about 12 seconds. This is 5 seconds more than the Kewet Buddy presented in the problem analysis. Since the Kewet Buddy has a 13 kW DC machine implemented it seems reasonable that the Kewet EV with an 8 kW induction machine implemented has a lower acceleration.

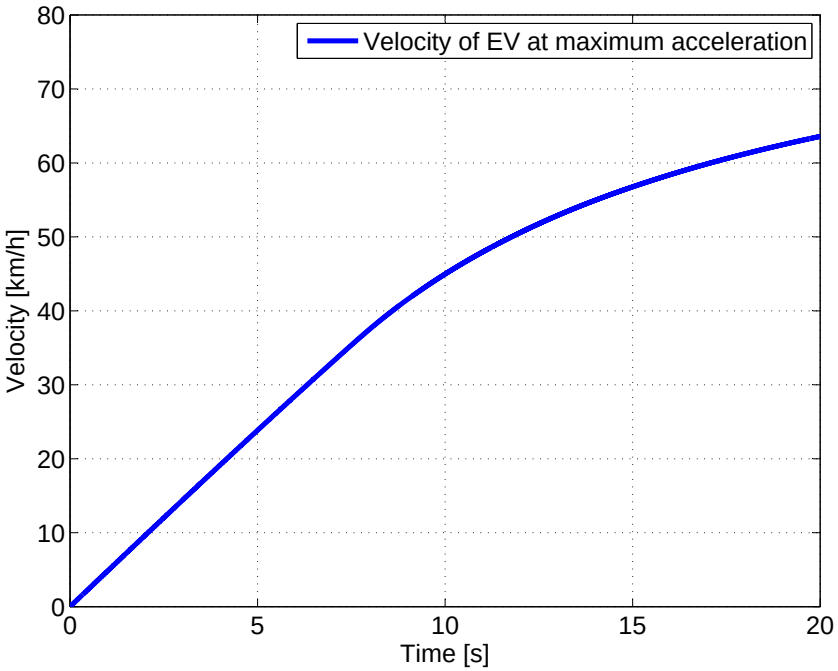

Figure 5.18: *Velocity of electric vehicle at maximum acceleration.*

5.2.4 Digital Signal Processor

The DSP used in this project is embedded on a experimental kit called the TMS320F28335. The processor on the DSP is a 32 bit floating point processor. On the kit different peripheral devices are included such as PWM modulator, ADC channels, interrupts and an encoder module. General specifications of the DSP are listed in table 5.5. The bit tolerance of ADC channels is calculated in equation (5.2). In the following section the signal electronics connected to the DSP is described.

$$u_{bit-DSP} = \frac{3.0V}{2^{12}} = 732.4\mu V \tag{5.2}$$

Characteristic	Value
Maximum clock frequency	150 [MHz]
Maximum input voltage	3.0 [V]
Output voltage	3.3 [V]
ADC resolution	12 [bits]
ADC maximum conversion rate	12.5 [MHz]
ADC conversion time	80 [ns]
RAM memory available	34000 x 16 bit
Number of external interrupts	8
Supply voltage	5 [V]

Table 5.5: *Specifications of the DSP.*

5.2.5 Signal Electronics

In order to obtain proper control of the inverter and the induction machine signal electronics must be designed and implemented. The signal electronics involves measurements of current, voltage, angular position and temperatures. It also involves transmitting the correct signals to the inverter.

The system is controlled by a digital signal processor (DSP), see figure 5.19. Schematics and more detailed information about the boards are found in appendix H.

The DSP sends digital PWM signals to the optical output ports which are connected to the inverter. The DSP receives optical encoder signals from the Siemens drive system described in the proceeding section. The encoder signals are used to determine the angular position of the shaft.

The currents in the three phases and in the DC bus are measured by LEM current transducers, see more about the LEM transducers in section 5.2.7. The signals are send from the LEM transducers to the DSP through RJ45 cables. Besides transferring signals from the LEM transducers the RJ45 cables also transfers supply voltage from the DSP board to the LEM modules.

As described in the previous section the machine is equipped with a thermal sensor estimating the temperature of the stator windings. The thermal sensor circuit is described in section 5.2.7. The measurement signal from the sensor is transferred to the DSP through a RJ45 cable.

The temperature of the inverter and the DC bus voltage are measured by the inverter BPI interface board and send to the DSP, also through RJ45 cables.

The signals send from the LEM transducers and the inverter are all current signals. On the DSP board the currents are transformed into voltages, using resistances of appropriate sizes, see section 5.2.7, for the DSP to measure. Using current signals in the RJ45 cables instead of voltage

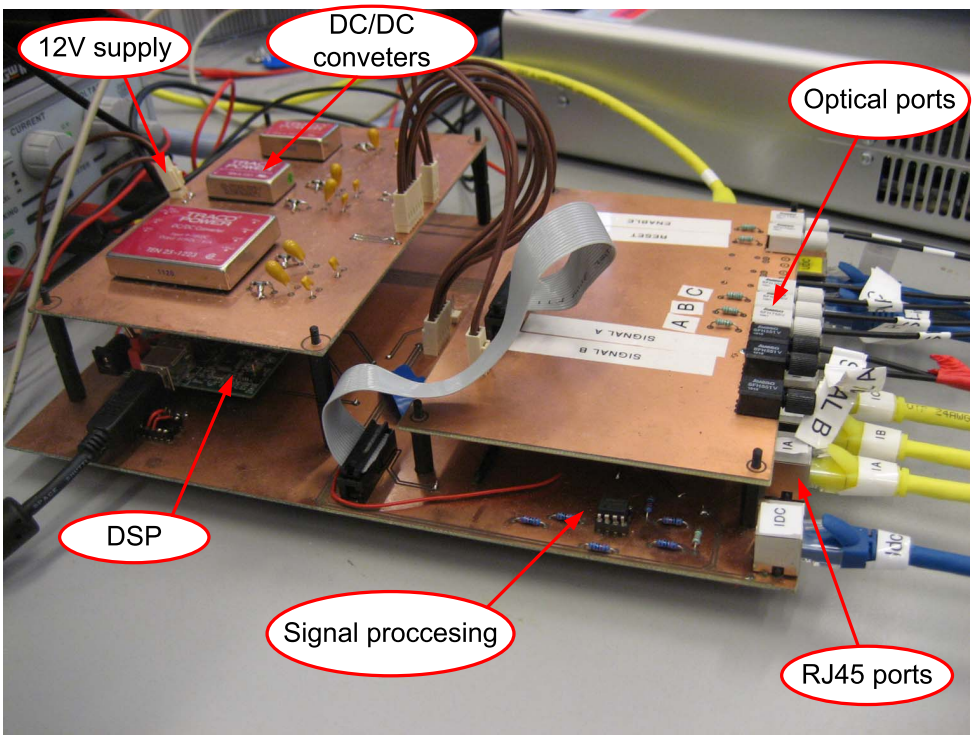

Figure 5.19: *Signal electronics.*

signals decreases the amount of electrical noise in the signal.
In the electric vehicle a 12 V battery is available to supply the DC/DC converters. The DC/DC converters ensure correct supply voltages for the signal electronics. The DC/DC converters must be able to deliver the following voltage potentials for the signal electronics:

Voltage transformation	Electronics
$12V \rightarrow \pm 15V$	Operational amplifiers/LEM modules
$12V \rightarrow \pm 5V$	DSP / Operational amplifiers / Inverter
$12V \rightarrow 18V$	Inverter
$12V \rightarrow 12V$	BMS

Table 5.6: *Supply voltages for signal electronics.*

The DSP is controlled using Code Composer Studio on the computer of the test setup, see figure 5.2. Code Composer Studio can be controlled through Matlab making it possible to control the entire test setup, including Siemens drive system, through Matlab.
The torque transducer sends signals to the computer through a USB cable, see more about the torque transducer in section 5.2.7. The computer has software installed making it possible to read out the torque values in Matlab.

5.2.6 Siemens Drive System

The Siemens drive system consists of a permanent magnet synchronous machine, a frequency converter and an embedded control system. Specifications for the Siemens drive system is seen in table 5.7. The permanent magnet synchronous machine for the Siemens drive system is seen in figure 5.14.

Siemens drive system	
Motor model number	1FT6086-8SH71-1DAO
Nominal torque	27 Nm
Maximum torque	35 Nm
Nominal speed	4500 min^{-1}
Maximum speed	7900 min^{-1}
Nominal current	32A
Maximum current	38A
Nominal voltage	261V
Temperature class	Th.Cl.155(F) (max 155°)
Encoder	IC22DQ B25 (22bit resolution)

Table 5.7: *Specifications for Siemens drive system.*

The frequency converter is able to supply energy to the grid making it possible for the drive to function as a generator without a brake chopper. The drive has a preprogrammed control algorithm implemented. The velocity or torque of the drive can be set in Matlab. The drive is controlled through an OPC server. The code used for controlling the drive is found on the enclosed CD. In the Matlab code it is possible to set maximum velocity, maximum torque, maximum power and read out temperatures, velocities and estimated air gap torque. It is also possible to use ramp functions if velocity control is used.
Encoder signals are available for the user through three output ports. The resolution of the encoder signals can be varied in the software for the drive system. The encoder signals are send to the DSP through optical cables and used to determine the angular position of the shaft. The Siemens drive is mainly used as a load drive in constant velocity mode.

5.2.7 Transducers

In this section the various transducers are described and tested to verify that the hardware and software affiliated with the transducers are working. The verified transducers are the current transducers, the temperature transducer and the torque transducer. The boards designed for the transducers connected to the DSP can be found in appendix H.

Current Transducer

Four current transducers are used for measuring the three phase currents i_A, i_B, i_C and the DC current i_{DC}, see figure 5.3. In this section the current transducer transfer function is derived and verified, and the tolerance of the transducers is analyzed. The current transducers are placed on the wooden board on top of the batteries. The current transducers are seen in figure 5.20.

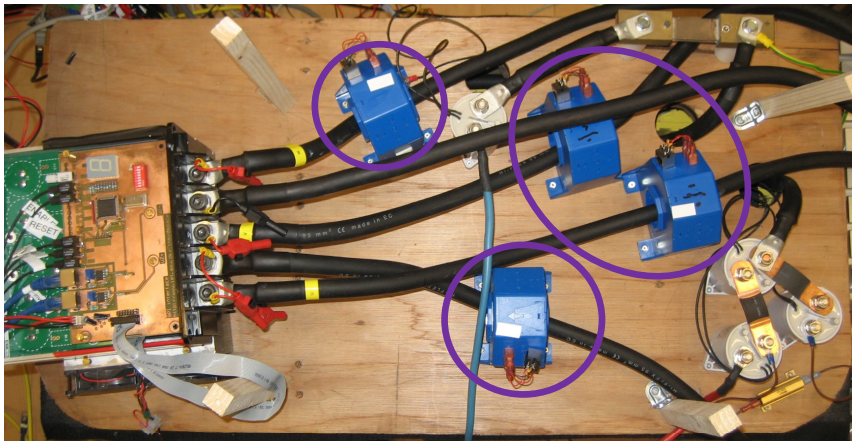

Figure 5.20: *Top of wooden board. The current transducers are marked with purple circles.*

The current transducers utilized are the model LT 505-S from the company LEM. When a current I_P flows through a phase cable the transducer generates a current I_S which is proportional with the current I_P with a conversion ratio of $K_N = \frac{1}{5000}$ see equation (5.3), and figure 5.21.

$$I_S = K_N \cdot I_P \tag{5.3}$$

where:	I_S	Secondary current $[A]$
	K_N	Conversion ratio $[-]$
	I_P	Primary current $[A]$

In the datasheet there is a recommended connection diagram see figure 5.21. The DSP's ADC channel is measuring the voltage drop $u_{current}$ over the measurement resistance R_m. To measure both positive and negative current a voltage offset circuit is implemented since the DSP's ADC channels only measures positive voltages. The circuit is designed so that a phase current of 0 A results in a potential of 1.5 V at the DSP's ADC channel. This corresponds to half of its maximum measurement voltage. R_m for the phase current measurements is chosen from a maximum desired current measurement consideration. According to the IM datasheet the maximum RMS current is 304 A which equals 430 A in amplitude. At the test bench the

Siemens load drive is only able to deliver 27 Nm continues torque and 35 Nm peak torque. Because of the limitations of the torque at the test bench a maximum current measurement of 380 A is considered appropriate. When the IM is put into the EV R_m should be replaced by a smaller resistor enabling measurement of larger current amplitudes. Furthermore the DSP code should be updated to ensure correct readouts. The value of R_m is calculated in equation (5.4).

$$R_{m.ph} = \frac{V_{DSP-max}}{K_N \cdot I_{max.ph}} = \frac{1.5\ V}{\frac{1}{5000} \cdot 380\ A} = 19.7\ \Omega \tag{5.4}$$

where:

$R_{m.ph}$	Measurement resistance for the phase current $i_{max.ph}$ $[\Omega]$.
$V_{DSP-max}$	Maximum voltage difference measured by the DSP $[V]$.
$I_{max.ph}$	Maximum measurable phase current amplitude $[A]$.

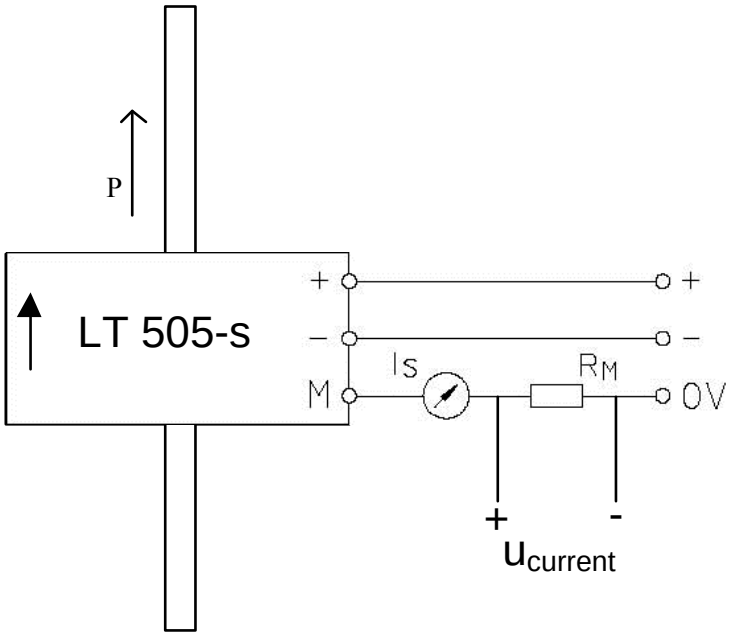

Figure 5.21: *Connection diagram for LT 505-S.*

Since there is no resistor with a resistance of 19.7 Ω available a resistor with a resistance of 19.5 Ω is chosen. The measurement resistance R_{m-DC} for the i_{DC} measurement is calculated from a maximum DC current I_{DC-max}= 300 A, see equation (5.5).

$$R_{m-DC} = \frac{V_{DSP-max}}{K_N \cdot I_{max.DC}} = \frac{1.5\ V}{\frac{1}{5000} \cdot 300\ A} = 25\ \Omega \tag{5.5}$$

where: R_{m-DC} Measurement resistance for the DC current i_{DC} $[\Omega]$.

$I_{max.DC}$ Maximum measurable DC-link current amplitude $[A]$.

Since there is no resistor with a resistance of 25.0 Ω available a resistor with a resistance of 24.0 Ω is chosen.
The electric circuits for the current measurements are seen in figure H.10 in appendix H.
The DSP ADC channels have a 12 bit resolution and is able to measure between 0.0 V and 3.0 V which gives a bit tolerance of 732.4 μV see section 5.2.4. The relationship between the measured voltage $u_{current}$ and the secondary current I_S is seen in equation (5.8).

$$u_{current} = R_m \cdot I_S + 1.5\ V \tag{5.6}$$

$$\Downarrow \tag{5.7}$$

$$I_s = \frac{(u_{current} - 1.5\ V)}{R_m} \tag{5.8}$$

where: $u_{current}$ Measured voltage drop over the resistance R_m $[V]$.

Combining equation (5.3) and equation (5.8) and solving for I_P yields:

$$I_P = \frac{u_{current} - 1.5\ V}{R_m \cdot K_N} \tag{5.9}$$

The transfer function used in the DSP code to calculate the current amplitude using a sampled bit value is seen in equation (5.10).

$$I_P = \frac{\left(bit_{u-current} \cdot \frac{3.0\ V}{4096}\right) - 1.5\ V}{R_m \cdot K_N} \tag{5.10}$$

where: $bit_{u-current}$ Bit value of the voltage drop $u_{current}$ measured by the DSP $[-]$.

The effect of the bit tolerance is seen in equation (5.11). The bit value 2049 is utilized because a bit value of 2048 is equal to 0 A so a bit value of 2049 gives a bit increment of 1.

$$\Delta I_{P-bit} = \frac{\left(2049 \cdot \frac{3.0\ V}{4096}\right) - 1.5\ V}{R_m \cdot K_N} = \frac{\left(2049 \cdot \frac{3.0\ V}{4096}\right) - 1.5\ V}{19.5\ \Omega \cdot \frac{1}{5000}} = 0.19\ A \tag{5.11}$$

where: ΔI_{P-bit} Bit tolerance of the measured primary current $[A]$.

In the datasheet for the current transducer an overall accuracy of $\pm$ 0.6% is given. The maximum measured current is 380 A which gives the worst case accuracy seen in equation (5.12).

$$I_{accuracy} = \pm 6.0 \cdot 10^{-3} \cdot 380A = \pm 2.28A \tag{5.12}$$

where: $I_{accuracy}$ Current accuracy for maximum measured primary current $[A]$.

An experiment is conducted to verify that the LEM LT 505-S, the electrical circuit and the DSP code is functioning as expected. The experiment is conducted at a mechanical speed of 2940 rpm and an electrical speed of 100 Hz. The voltage amplitude is set to 19.5 V. Besides using the LEM modules to measure the phase currents a current probe connected to an oscilloscope is used to verify the current measurements. The results of the experiment are seen in figure 5.22. There is good coherence between the results from the current probe and the DSP's measurements. Furthermore it is seen in figure 5.22 that sampling of the current measurements is performed in the middle of the current ripple. A more detailed description of the current sampling is done in chapter 8.

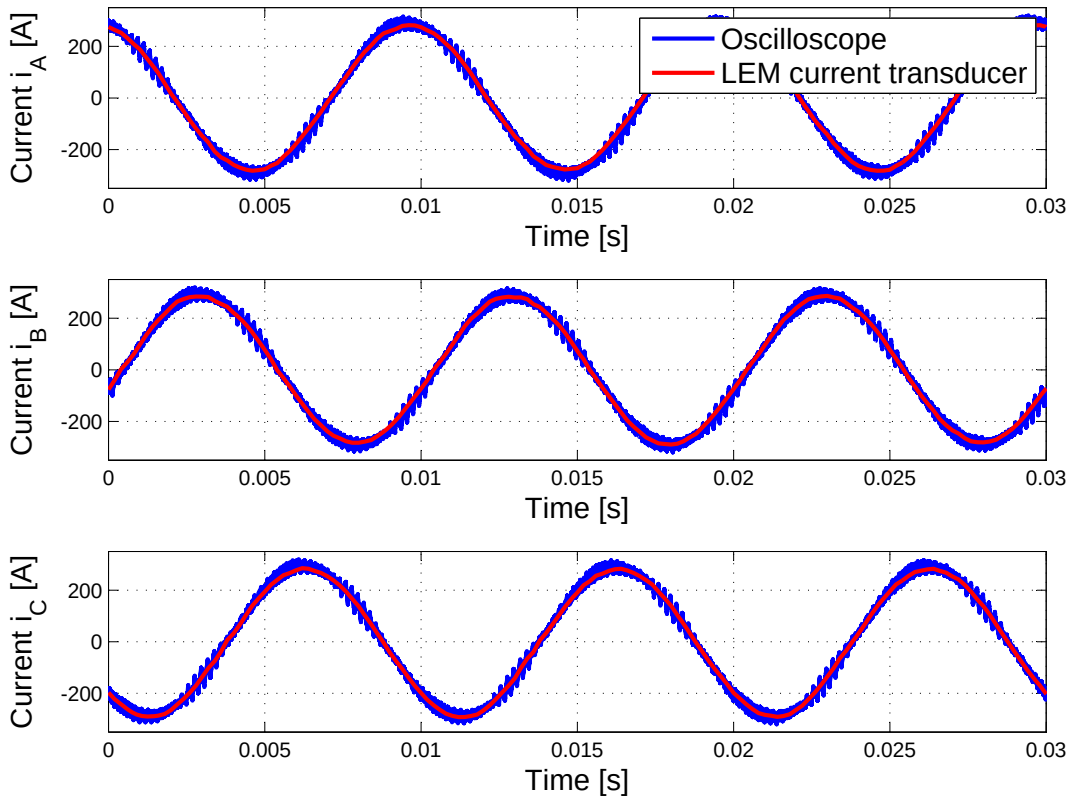

Figure 5.22: *Measured currents from oscilloscope and current transducer.*

Thermal sensor

The purpose of the thermal sensor is to ensure that the heat dissipated in the stator windings due to losses does not increase the temperature of the lamination to a critical level where it melts causing short circuit. In addition the temperature measurement is used to estimate the stator and rotor resistance in a control algorithm presented in section 7.3.3.

The temperature measurement is conducted using a silicon temperature sensor (type: KTY84-130). The sensors internal resistance varies as a function of the ambient temperature. The basic principle is to estimate the resistance of the sensor to approximate the temperature. In figure 5.23 the thermal sensor circuit is seen. In this $R_T(T)$ represents the internal resistance of the sensor, R_M is a resistor used to generate a reasonable amplitude of the measured voltage u_M. Finally the voltage source U_{DSP} supplies 3.3 V to the circuit using the DSP. The low voltage supply is used in order to limit the current flowing through the sensor. If the current passing through the sensor is to high, the sensor may become warmer than the ambient temperature

resulting in a faulty temperature reading.

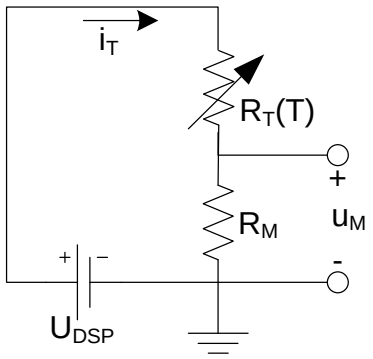

Figure 5.23: *Thermal sensor circuit.*

The voltage u_M in figure 5.23 is calculated using the voltage divider rule in equation (5.13). In equation (5.14) the resistance representing the thermal sensor is isolated.

$$u_M = U_{DSP} \cdot \frac{R_M}{R_M + R_T(T)} \tag{5.13}$$

$$\Downarrow$$

$$R_T(T) = R_M \cdot \left(\frac{U_{DSP}}{u_M} - 1 \right) \tag{5.14}$$

where:	u_M	Voltage measured by the DSP $[V]$
	U_{DSP}	Voltage provided by the DSP $[V]$
	R_M	Measurement resistor $[\Omega]$
	$R_T(T)$	Internal resistance of the thermal sensor $[\Omega]$

According to the datasheet [Philips, p. 3], the sensor has an almost linear temperature-resistance characteristic. The temperature range it primarily is going to measure within in the laboratory is assumed to be 20 $^\circ C$ to 150 $^\circ C$. In the datasheet the sensor average resistance is listed to be 581 Ω at 20 $^\circ C$ increasing to 1334 Ω at 150 $^\circ C$. Combining these data points yields an expression of the temperature as a function of the sensor resistance (equation (5.15)). Inserting equation (5.14) into equation (5.15) yields equation (5.16) which is implemented into the DSP-code enabling online estimation of the stator temperature.

$$T = 172.6 \cdot 10^{-3} \cdot R_T(T) - 80.31 \tag{5.15}$$

$$= 172.6 \cdot 10^{-3} \cdot \left(R_M \cdot \left(\frac{U_{DSP}}{u_M} - 1 \right) \right) - 80.31 \tag{5.16}$$

where: T Temperature of the stator $[^\circ C]$

To determine the optimum size of the measurement resistor R_M, the difference between the maximum measured voltage $u_{M.max}$ and the minimum measured voltage $u_{M.min}$ denoted Δu_M (equation (5.17)) is evaluated. The maximum measured voltage is achieved when the value of R_T is at its lowest value. Correspondingly the minimum measured voltage is achieved when the value of R_T is at its highest value. Equation (5.13) is inserted into equation (5.17) with the corresponding values of the thermal sensor resistance yielding equation (5.18).

$$\Delta u_M = u_{M.max} - u_{M.min} \tag{5.17}$$

$$= \left(U_{DSP} \cdot \frac{R_M}{R_M + R_T(20^\circ C)} \right) - \left(U_{DSP} \cdot \frac{R_M}{R_M + R_T(150^\circ C)} \right)$$

$$= \left(3.3\ V \cdot \frac{R_M}{R_M + 581\Omega} \right) - \left(3.3V \cdot \frac{R_M}{R_M + 1334\ \Omega} \right) \tag{5.18}$$

where: Δu_M Voltage difference $[V]$

$u_{M.max}$ Maximum voltage measured by the DSP $[V]$

$u_{M.max}$ Minimum voltage measured by the DSP $[V]$

In figure 5.24 the potential difference Δu_M is plotted as a function of the measurement resistor size R_M. From this plot it is seen that the maximum potential differential is achieved when the measurement resistor R_M has a value of about 900 Ω. The resistor size is chosen to be the standard value of 909 Ω. Under this condition the maximum current flowing through the circuit is 2.22 mA cf. equation (5.19). In the datasheet a sensor current of 2 mA is recommended for ambient temperatures above 200 $^\circ C$. The 10 % to high sensor current is assessed to be acceptable, since the limit is only exceeded at low temperatures where accurate temperature readings are not crucial to ensure safe operation of the IM. The DSP is able to measure voltages between 0 V and 3 V. In equation (5.22) it is shown that the maximum measured voltage is 2.01 V, well below the 3 V saturation limit.

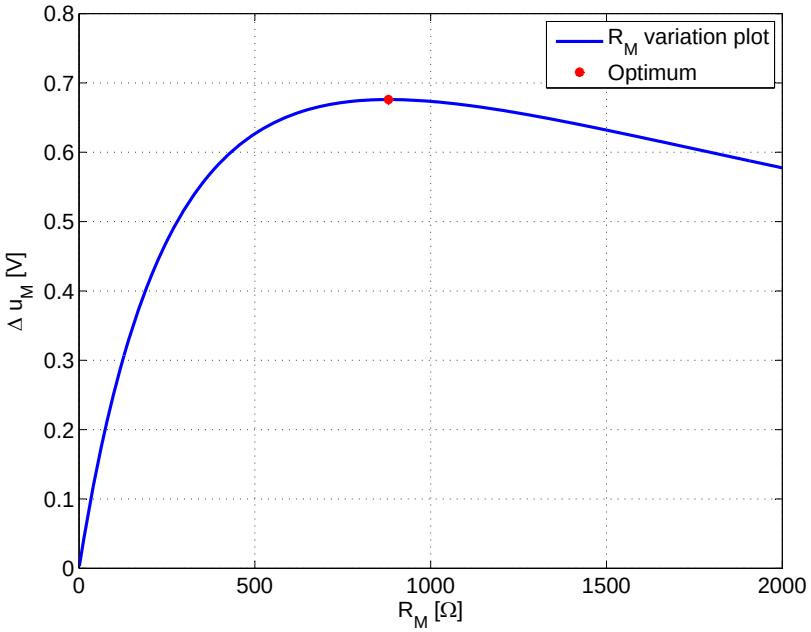

Figure 5.24: *Maximum difference between the maximum and minimum measured voltage.*

$$i_{T.max} = \frac{U_{DSP}}{R_T(20°) + R_M} \tag{5.19}$$

$$= \frac{3.3\ V}{581\ \Omega + 909\ \Omega} \tag{5.20}$$

$$= 2.22\ mA \tag{5.21}$$

where: $i_{T.max}$ Maximum current in the thermal resistor circuit $[A]$

$$u_{M.max} = U_{DSP} \cdot \frac{R_M}{R_M + R_T(20°)} \tag{5.22}$$

$$= 3.3\ V \cdot \frac{909\ \Omega}{909\ \Omega + 581\ \Omega} \tag{5.23}$$

$$= 2.01\ V \tag{5.24}$$

The main factors contributing to the tolerance of the temperature measurement are the bit tolerance of the analog to digital conversion of the DSP and the tolerance of the temperature sensor. The bit tolerance of the DSP is calculated to be 732.4 μV in section 5.2.4. In equation (5.25) equation (5.14) is differentiated with respect to u_M to determine the area where the measured voltage is most sensitive with respect to bit tolerance. According to equation (5.25) it is when u_M is small that the derivative is large. This results in the property that an increment in u_M

will give a large deviation in the estimated sensor resistance at high temperatures compared to low temperatures. The measured voltage at 150 $^{\circ}C$ is calculated in equation (5.26). In equation (5.29) this result is used in connection with the bit voltage tolerance Δu_{bit} to determine the thermal resistance variation due to the bit tolerance. Finally in equation (5.30) this is converted into a temperature tolerance of 0.21 $^{\circ}C$.

$$\frac{\partial R_T(T)}{\partial u_M} = \frac{-R_M \cdot U_{DSP}}{u_M^2} \tag{5.25}$$

$$\begin{aligned} u_{M.min} &= U_{DSP} \cdot \frac{R_M}{R_M + R_T(150^{\circ}C)} && (5.26)\\ &= 3.3\ V \cdot \frac{909\ \Omega}{909\ \Omega + 1334\ \Omega} && (5.27)\\ &= 1.337\ V && (5.28) \end{aligned}$$

$$\begin{aligned} \Delta R_{T.bit.tol} &= R_T(150^{\circ}) - R_M \cdot \left(\frac{U_{DSP}}{u_{M.min} + \Delta u_{bit}} - 1 \right) && (5.29)\\ &= 1334\Omega\ - 909\ \Omega \cdot \left(\frac{3.3\ V}{1.3373607\ V + 0.0007324\ V} - 1 \right) \\ &= 1.23\ \Omega \end{aligned}$$

where: $\Delta R_{T.bit.tol}$ Estimated resistance bit tolerance $[\Omega]$

$$\begin{aligned} \Delta T_{bit.tol} &= 172.6 \cdot 10^{-3} \cdot \Delta R_{T.bit.tol} && (5.30)\\ &= 0.21\ ^{\circ}C \end{aligned}$$

where: $\Delta R_{T.bit.tol}$ Estimated temperature bit tolerance $[^{\circ}C]$

According to the datasheet, the tolerance of the temperature sensor is $\pm 7.1^{\circ}C$ at worst in the considered temperature range. Adding the bit tolerance with this yields an overall tolerance of about $\pm 7.3^{\circ}C$.

The temperature measurement is calibrated using a digital thermometer where the IM has not been operating for more than 16 hours. The calibration is performed by adjusting the constant contribution of -80.31 in equation (5.15) to -80.03.

Torque Transducer

The torque transducer used in the test bench is a Lorenz DR-3000-111237. The maximum measurable torque is 100 Nm. The transducer conducts up to 2500 $^{\text{measurements}}/_{\text{s}}$. It is a 16 bit transducer with gives a bit tolerance of 0.002 Nm. The transducer has an accuracy of 0.1 % of the nominal torque which corresponds with an accuracy of 0.1 Nm. The torque transducer is seen in figure 5.14. The transducer is connected to a PC using a USB interface. Lorenz has its own software for data logging but it is not utilized. Instead measurements from the transducer are sent directly to Matlab, using protocols provided by Lorenz.
To verify the transducer and the Matlab collecting loop an experiment is conducted. The experiment is conducted by setting a constant speed on the Siemens load drive and applying a torque with the IM. The measured torque from the torque transducer is collected together with the approximated air gap torque of the Siemens drive. The sampling frequency is set to 100 Hz. The Siemens drive air gap torque is updated with a frequency of 10 Hz. Data logging is performed over 1 second. In figure 5.25 the results of an experiment performed at 1000 rpm and an applied torque of 11.0 Nm is seen.

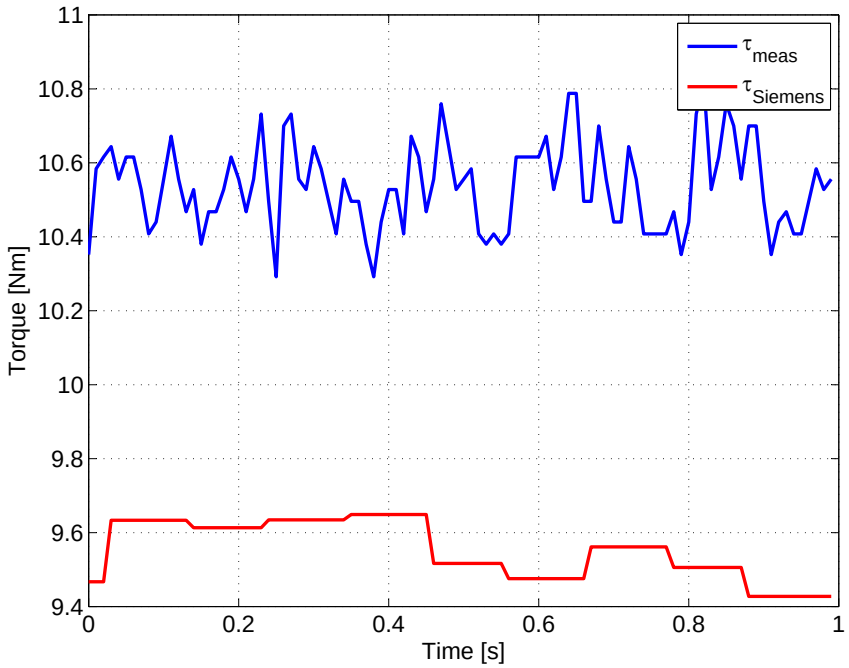

Figure 5.25: *Torque measured by torque transducer and torque estimated by Siemens drive system. The velocity is set to 1000 rpm and a torque of 11 Nm is applied by the IM.*

The sign of $\tau_{Siemens}$ is in accordance with figure 6.9. τ_{meas} is in this experiment defined as seen in equation (5.31).

$$\tau_{meas} = \tau_{Siemens} + \tau_{\mu-Siemens} \tag{5.31}$$

It is assumed that the air gap torque calculated by the Siemens drive is correct, and can be used to verify that the torque transducer is measuring correct. From the results in figure 5.25 the mean values of τ_{meas} and $\tau_{siemens}$ is found in equation (5.32) and (5.33).

$$\underline{\tau}_{meas} = \frac{1}{100} \cdot \sum_{i=1}^{100} \tau_{meas,i} = 10.54Nm \tag{5.32}$$

$$\underline{\tau}_{Siemens} = \frac{1}{100} \cdot \sum_{i=1}^{100} \tau_{Siemens,i} = 9.55Nm \tag{5.33}$$

From equation (5.31):

$$\underline{\tau}_{\mu-Siemens} = \underline{\tau}_{meas} - \underline{\tau}_{Siemens} = 10.54Nm - 9.55Nm = 0.99Nm \tag{5.34}$$

A friction of 0.99 Nm at 1000 rpm is considered realistic and therefore the Lorenz DR-3000 torque transducer is measuring correctly. In table 5.8 results from experiments where the torque transducer is tested for consistency is seen. Two different operating points are tested. At each point the air gap torque $\tau_{Siemens}$ and measured torque τ_{meas} is collected like in the experiment mentioned above. Each operating point is repeated three times.

Results from torque transducer experiments				
Torque [Nm]	Speed [rpm]	$\underline{\tau}_{meas,1}$ [Nm]	$\underline{\tau}_{meas,2}$ [Nm]	$\underline{\tau}_{meas,3}$ [Nm]
11.0	1000	10.54	10.53	10.54
21.5	2000	19.67	19.74	19.77

Table 5.8: *Results from torque transducer experiments.*

From figure 5.25 it is seen that the measured torque τ_{meas} is varying from 10.29 Nm to 10.82 Nm. Since the mean torque, see table 5.8, is very consistent the mean torque is considered applicable for estimation of steady state torque. A collection of 100 measurements with a sampling frequency of 100 Hz is considered acceptable for estimation of steady state torque.
The test setup is now presented. In the next chapter a simulation model of the powertrain is developed.

CHAPTER 6

MODELING

In order to test control strategies for performance, stability and energy efficiency it is desirable to set up a model describing the powertrain. A general overview of this model is seen in figure 6.1.

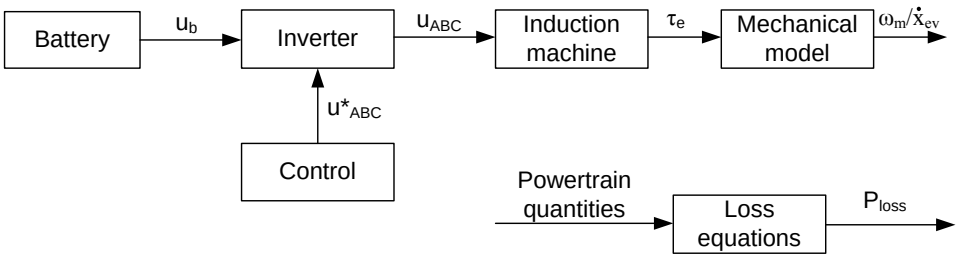

Figure 6.1: *General model of powertrain.*

As seen in figure 6.1 the model is divided into six parts. The battery is the energy source for the powertrain. The battery supplies a DC voltage, u_b, to the inverter. Using the DC voltage from the battery and signals from the controller the inverter supplies phase voltages, u_{ABC}, to the induction machine. When applying voltages to the induction machine an electric torque, τ_e, is created which, depending on the mechanical model, results in a rotational velocity of the rotor shaft, ω_m, or a translational velocity of the electric vehicle, $\dot{x}_{ev}$ (depending on whether the IM is implemented in the test setup or the electric vehicle).
In order to evaluate the energy efficiency of potential control strategies the losses in the powertrain is calculated from powertrain quantities.

In this chapter the modeling of the battery, inverter, induction machine, mechanical model and losses are described. The control strategy is described in the proceeding chapter.

6.1 Battery

The battery package is the power source of the powertrain. The terminal voltage of the battery, u_b, varies depending on the current flowing from the battery package. The terminal voltage is also dependent on the energy remaining in the battery.
In the simulation model used to determine performance, stability and energy efficiency for potential control strategies, the battery package is modeled as having a constant terminal voltage.
In appendix A a model describing the terminal voltage as function of current flowing from the battery and remaining energy in the battery is presented. This model is used to gain an understanding of the dynamics and characteristics of the battery pack.
The model has several potentials not utilized in this project. The model can be used to determine the varying terminal voltage throughout a driving cycle for the electric vehicle. Furthermore the range of the electric vehicle can be estimated. From the range estimation it may be evaluated whether the battery pack has a sufficient capacity. The model may also be implemented into the electric vehicle in order to inform the driver about remaining energy in the batteries.

6.2 Inverter

The inverter is as mentioned in the previous chapter a three phase Sauer Danfoss battery powered inverter. The function of the inverter is to convert the DC voltage from the battery to controlled phase voltages for the induction machine. In order to obtain a predictable torque from the induction machine the phase voltages should ideally be three 120° phase-shifted sinusoidal voltages. The inverter however does not produce pure sinusoidal phase voltages. The inverter instead converts the DC voltage from the battery pack into pulse width modulated (PWM) signals. Since the three phases in the induction machine consist of inductances, the resulting phase currents are still sinusoidal but contain a high frequency current ripple.
The inverter consists of six MOSFET transistors and six diodes. The diodes inhibit the current from flowing reverse biased through the transistors and thereby preventing damaging the transistors. A scheme of the electric circuit is depicted in figure 6.2.
Terminal voltage of each phase is controlled by controlling the transistors in each branch.
Since the inverter uses PWM modulation to generate voltage the actual phase voltages are as

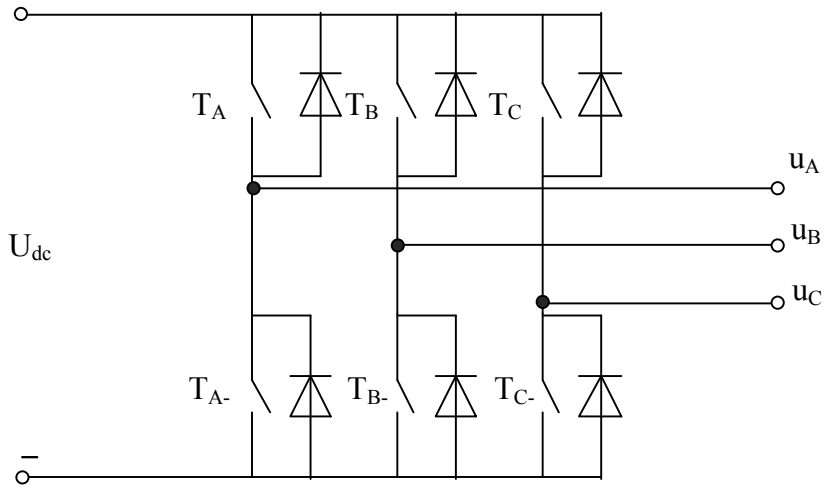

Figure 6.2: *Electrical circuit of the three phase inverter.*

mentioned earlier not sinusoidal. The inverter is however modeled as being a sinusoidal voltage source. This simplification reduces the complexity of the model significantly and hereby reduces simulation time. The error in the model induced by this simplification is considered in appendix B. Modulation strategies are also considered in appendix B.

6.3 Induction Machine

The induction machine (IM) used in this project is a 3-phase squirrel cage induction machine. The IM hereby has three phases, *A*, *B* and *C*. In order to obtain a torque acting on the rotor shaft the induction machine must ideally be fed sinusoidal phase shifted voltages. Due to inductances in the phases PWM voltages may however also be applied on the phases in order to obtain torque on the rotor shaft.

As described in the previous section the inverter is modeled as being a ideal sinusoidal voltage source. In this section the voltage equations and torque equations describing the torque acting on the rotor as function of the phase voltages are presented. A detailed description derivation of the equations is found in appendix C.

The stator is delta coupled but can be considered as wye-connected as described in appendix C. When considering the stator as wye-connected the electrical stator and rotor phases in the IM are illustrated as in figure 6.3.

Rotor and stator phase quantities are illustrated as in figure 6.4. θ_r is the angle between phase *A* in the stator and phase *A* in the rotor.

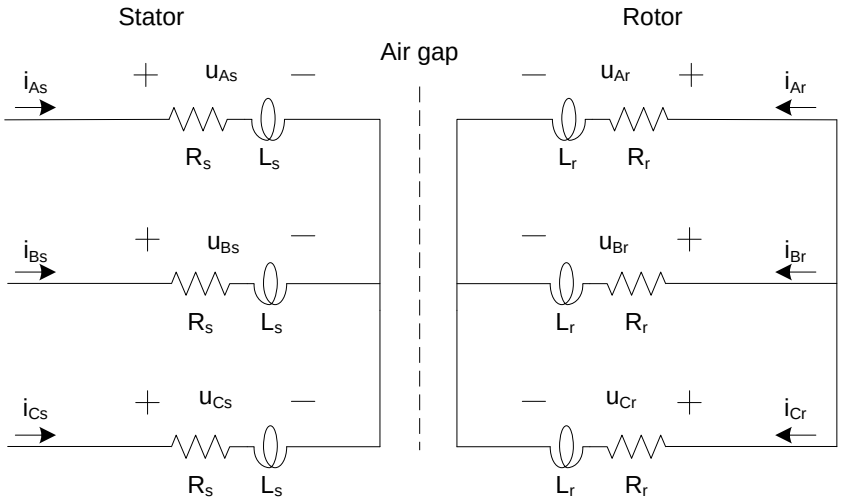

Figure 6.3: *Electrical equivalent diagram of the wye connected, squirrel cage induction machine.*

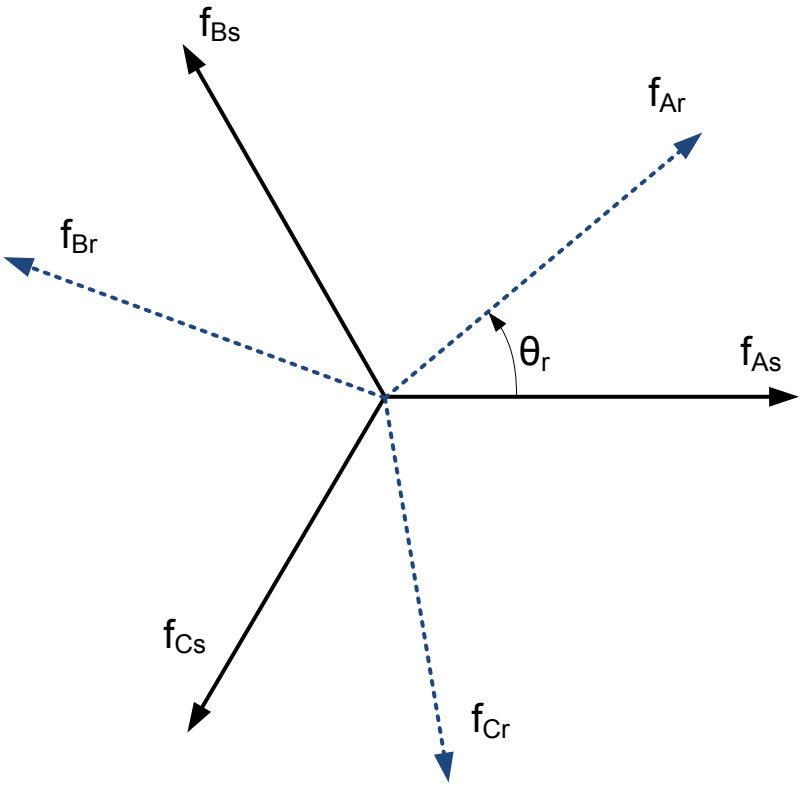

Figure 6.4: *Illustration of rotor and stator phase quantities.*

The voltage equations in phase quantities are written as in equation (6.1).

$$\begin{bmatrix} \bar{u}_{ABCs} \\ \bar{u}'_{ABCr} \end{bmatrix} = \begin{bmatrix} \bar{R}_s + p \cdot \bar{L}_s & p \cdot \bar{L}'_{sr} \\ p \cdot (\bar{L}'_{sr})^T & \bar{R}'_r + p \cdot \bar{L}'_r \end{bmatrix} \cdot \begin{bmatrix} \bar{i}_{ABCs} \\ \bar{i}'_{ABCr} \end{bmatrix} \tag{6.1}$$

where:	$\bar{u}_{ABCs}$	Stator voltages $[V]$
	$\bar{u}'_{ABCr}$	Rotor voltages referred to stator $[V]$
	$\bar{R}_s$	Stator winding resistance matrix $[\Omega]$
	$\bar{R}'_r$	Rotor winding resistance matrix referred to stator $[\Omega]$
	p	Differential operator $[-]$
	$\bar{L}_s$	Stator inductance matrix $[H]$
	$\bar{L}'_r$	Rotor inductance matrix referred to stator $[H]$
	$\bar{L}'_{sr}$	Mutual inductance matrix referred to stator $[H]$
	$\bar{i}_{ABCs}$	Stator currents $[A]$
	$\bar{i}'_{ABCr}$	Rotor currents referred to stator $[A]$

In order to control the torque using field oriented control it is desirable to express the voltage equations in an arbitrary $qd0$ reference frame. The phase quantities in an arbitrary reference frame is illustrated in figure 6.5 where θ_{rf} is the angle between phase A in the stator and the q axis in the rotating $qd0$ reference frame. The 0 axis in the $qd0$ reference-frame is normal to the d,q plane.

The velocities ω_{rf} and ω_r are the velocity of the arbitrary reference-frame and the electric velocity of the rotor shaft respectively. The angle β is the angle between the rotor shaft and the reference frame.

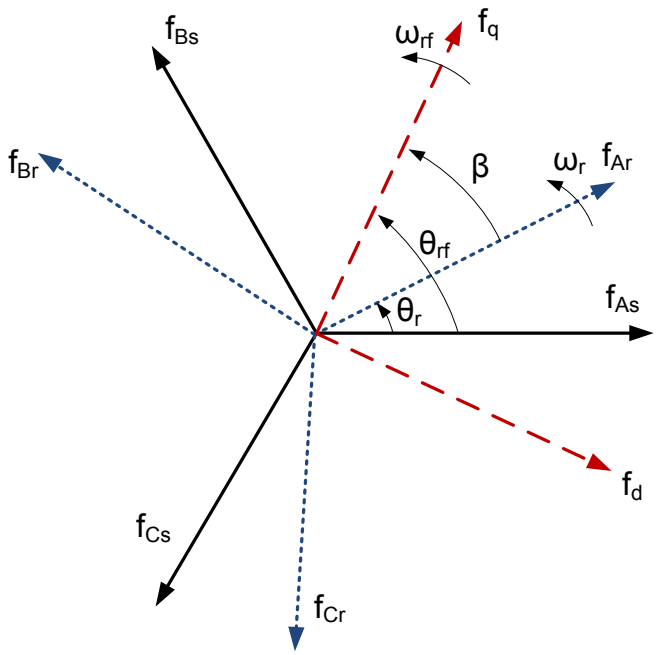

Figure 6.5: *Relation between 3-phase ABC reference-frame and arbitrary rotating qd0 reference-frame*

The voltage equations in the arbitrary $qd0$ reference frame are expressed as:

$$u_{qs} = R_s \cdot i_{qs} + \omega_{rf} \cdot \lambda_{ds} + p \cdot \lambda_{qs} \tag{6.2}$$

$$u_{ds} = R_s \cdot i_{ds} - \omega_{rf} \cdot \lambda_{qs} + p \cdot \lambda_{ds} \tag{6.3}$$

$$u'_{qr} = R'_r \cdot i'_{qr} + (\omega_{rf} - \omega_r) \cdot \lambda'_{dr} + p \cdot \lambda'_{qr} \tag{6.4}$$

$$u'_{dr} = R'_r \cdot i'_{dr} - (\omega_{rf} - \omega_r) \cdot \lambda'_{qr} + p \cdot \lambda'_{dr} \tag{6.5}$$

where:

u_{qs}	Stator voltage in q-axis direction $[V]$
u_{ds}	Stator voltage in d-axis direction $[V]$
u'_{qr}	Rotor voltage in q-axis direction referred to stator $[V]$
u'_{dr}	Rotor voltage in d-axis direction referred to stator $[V]$
i_{qs}	Stator current in q-axis direction $[A]$
i_{ds}	Stator current in d-axis direction $[A]$
i'_{qr}	Rotor current in q-axis direction referred to stator $[A]$
i'_{dr}	Rotor current in d-axis direction referred to stator $[A]$
ω_{rf}	Velocity of arbitrary reference frame $[rad/s]$
ω_r	Electrical velocity of rotor shaft $[rad/s]$
λ_{qs}	Stator flux linkage in q-axis direction $[Wb]$
λ_{ds}	Stator flux linkage in d-axis direction $[Wb]$
λ'_{qr}	Rotor flux linkage in q-axis direction referred to stator $[Wb]$
λ'_{dr}	Rotor flux linkage in d-axis direction referred to stator $[Wb]$

The flux linkages are expressed as:

$$\lambda_{qs} = L_{ls} \cdot i_{qs} + L_M \cdot (i_{qs} + i'_{qr}) \tag{6.6}$$

$$\lambda_{ds} = L_{ls} \cdot i_{ds} + L_M \cdot (i_{ds} + i'_{dr}) \tag{6.7}$$

$$\lambda'_{qr} = L'_{lr} \cdot i'_{qr} + L_M \cdot (i_{qs} + i'_{qr}) \tag{6.8}$$

$$\lambda'_{dr} = L'_{lr} \cdot i'_{dr} + L_M \cdot (i_{ds} + i'_{dr}) \tag{6.9}$$

where:

L_{ls}	Stator leakage inductance $[H]$
L'_{lr}	Rotor leakage inductance referred to stator $[H]$
L_M	Magnetising inductance $[H]$

The torque equation in the $dq0$ reference frame is expressed as:

$$\tau_e = \frac{3}{2} \cdot \frac{P}{2} \cdot L_M \cdot \left(i_{qs} \cdot i'_{dr} - i_{ds} \cdot i'_{qr} \right) \tag{6.10}$$

where: τ_e Electromagnetic torque $[Nm]$

P Number of poles $[-]$

In the simulation model the voltage equations are expressed in the stationary reference frame. Expressing the equations in the stationary reference frame simplifies the equations as the velocity of the reference frame is zero. The voltage equations in the stationary reference frame are seen in appendix C.
The voltage and torque equations for the induction machine are now determined. The parameters in the equations are determined in the proceeding section.

6.3.1 Motor Parameters

In this section the parameters used in the modeling of the induction machine are found by experiments and data analysis. The theory for the experiments are described in more detail in appendix D.1. The experiments conducted to find the motor parameters are described in detail in appendix E. The model used to find these parameters is a steady state model described in appendix D. The electrical circuit for the steady state model is seen in figure 6.6.

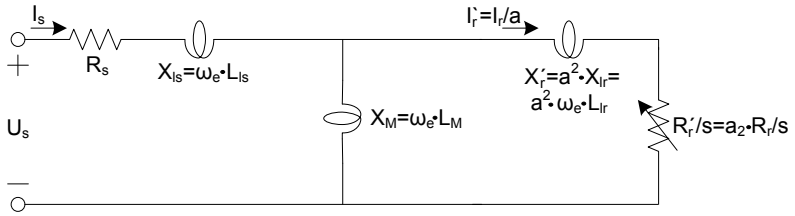

Figure 6.6: *Simplified electrical circuit model of the induction machine.*

The experiments conducted to find the motor parameters are: DC test, no load test and a load test. The DC test is a simple experiment where the stator resistance R_s is found. The experiment is conducted by connecting a DC supply to two phases and measure the voltage and current to find the resistance R_s. A more detailed description of the theory behind the experiment is found in appendix D.1.1 and the experiment itself and the data analysis is found in appendix E.1.
The next experiment conducted is a no load test where the motor is operated at zero slip using an AC source and the Siemens drive system. In this experiment $I'_r = 0$ see figure 6.6 so the sum of the two reactances X_{ls} and X_M is found using impedance relations. A more detailed description

of the theory behind the experiment is found in appendix D.1.2. A detailed description of the conducted experiment and the data analysis is found in appendix E.2.
The last experiment conducted is a load test, where the slip is different from zero. The theory for this experiment is used to set up a relationship between rotor resistance R'_r and the reactances X_M and X_{ls}.
This relationship combined with the no load test makes it possible to calculate all parameters as a function of one variable X_M. X_M is determined in an iterative process of fitting the parameters to the results from the load test. A more detailed description of the theory for this experiment is found in appendix D.1.3. A more detailed description of the conducted load experiment is found in appendix E.2.
When the fitting of parameters is satisfactory the inductances are calculated from the reactances. The results from the parameter determination is seen in table 6.1. In appendix E.3 the parameter fitting is described in more detail. In figure 6.7 results from the load experiment is compared to a simulation using the parameters from table 6.1. The parameters are inserted into the voltage -and torque equations described in the preceding sections and the output of the equations are compared to an experiment. This is done in the proceeding section.

ABM induction machine parameters	
Stator resistance R_s	1.627 $m\Omega$
Phase cable resistance R_{cable}	0.415 $m\Omega$
Rotor resistance R'_r	1.364 $m\Omega$
Stator leakage inductance L_{ls}	19.42 μH
Rotor leakage inductance L'_{lr}	19.42 μH
Magnetizing inductance L_M	320 μH

Table 6.1: *Parameters for ABM induction machine.*

6.3.2 Dynamic Verification of machine parameters

In this section the machine parameters found in the preceding section are inserted in the machine equations and the equations are verified dynamically. The experiment conducted to verify the machine parameters and equations is a step on the load torque. The induction machine is controlled with a V/Hz control where the voltage amplitude and frequency is set. When the induction machine is in steady state a step on the torque is performed by the load drive (Siemens drive system), see appendix F.3 for more information. The current in phase A i_A is measured before, during and after the torque step which is compared to a phase current in the model. The torque, voltage and rotor speed is measured before and after the torque step. The current is mea-

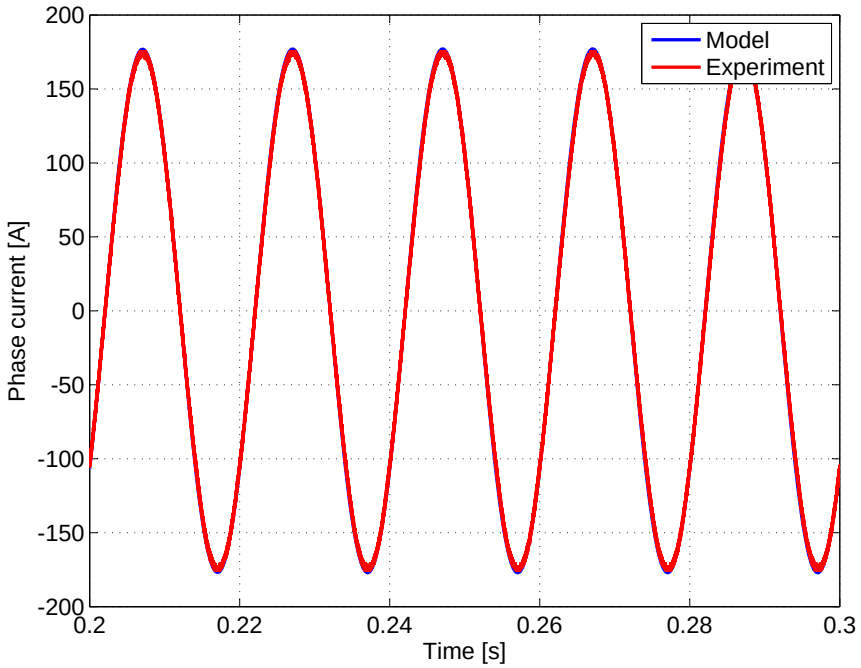

Figure 6.7: *Comparison between results from experiment and the simulation model with fitted machine parameters.*

sured by a current probe connected to an oscilloscope to get the desired collection frequency and time span. The torque step is applied at a random time meaning that the step time in the model is fitted to get a good comparison between measured and modeled currents.

The steady state values responses before and after the torque step are firstly considered. Steady state results for the experiment is seen in table 6.2. The simulated model results is seen in table 6.3. The measured and simulated steady state values coincide satisfactory. The voltage difference between before and after the step is explained by the non-ideal phenomenas described in appendix B.

Steady state measurements from experiment		
	Before torque step	After torque step
Rotor velocity	1796 rpm	1734 rpm
Phase voltage amplitude	11 V	10.15 V
Phase voltage frequency	60 Hz	60 Hz
Load Torque	0.7 Nm	15.3 Nm
Phase current amplitude	85 A	245 A

Table 6.2: *Steady state measurements from experiment before and after the torque step.*

Steady state values from model		
	Before torque step	After torque step
Rotor velocity	1798 rpm	1736 rpm
Phase voltage amplitude (input to model)	11 V	10.15 V
Phase voltage frequency (input to model)	60 Hz	60 Hz
Load torque (input to model)	0.7 Nm	15.3 Nm
Phase current amplitude	86 A	247 A

Table 6.3: *Steady state values from model before and after the torque step.*

The dynamic response when applying the torque step is seen in figure 6.8. It should be noted that the model voltage amplitude input is constant at 10.15 V before, during and after the torque step. An attempt to implement the change in voltage amplitude during the step into the model seemed to do more harm than good and is therefore not implemented. The consequence of this is that the conditions in the simulation before and sometime during the torque step will differ from the experiment. The comparison is accomplished with above-mentioned in mind. It is seen from figure 6.8 that the frequency, phase and amplitude of the current is coinciding for the experiment and the model. The small differences could be caused by: errors in parameters, time of torque step and the voltage drop that occurs during the step. The differences between simulation and experiment are however so small that the dynamic performance of the machine equations with determined machine parameters is considered satisfactory and the model is considered as verified.

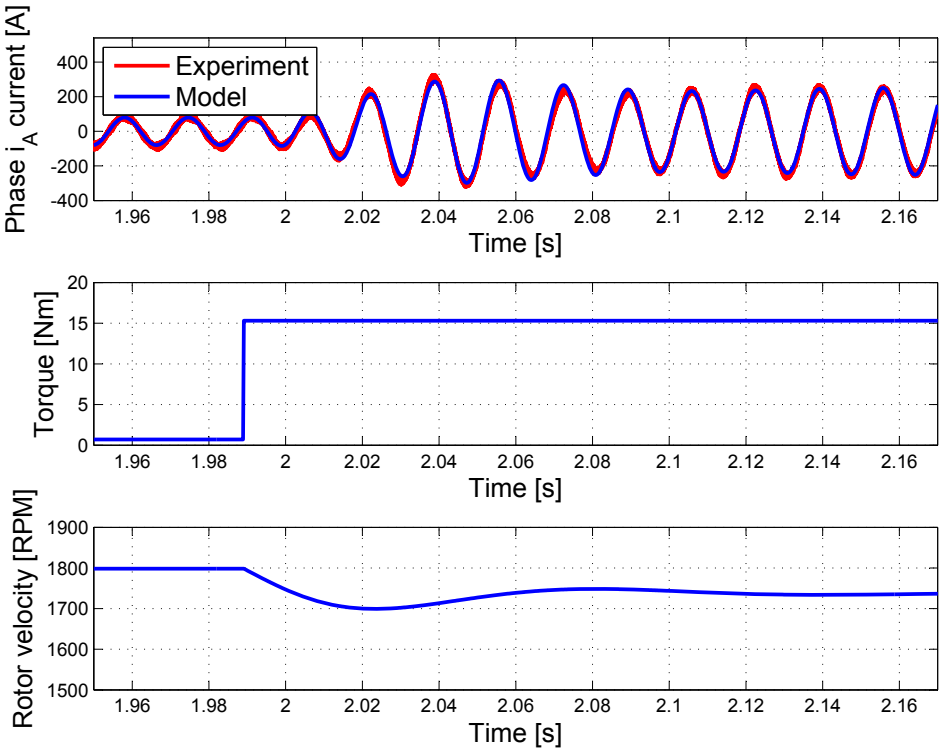

Figure 6.8: *Dynamic verification of machine equations and parameters.*

6.4 Mechanical Modeling

When the torque from the induction machine is calculated using the equations described in the previous section the resulting acceleration of the machine must be determined. The acceleration is dependent on other torques acting on the shaft. The source and size of torque are dependent on whether the induction machine is implemented in the vehicle or in the test setup and so is the moment of inertia. This section contains a description of the torque acting on the shaft and the moment of inertia for implementation in electric vehicle and implementation in test setup.

6.4.1 Implementation in Test Setup

When the induction machine is implemented in the test setup the torque acting on the shaft besides the torque from the induction machine are coulomb- and viscous frictions and the torque from the Siemens drive system. The torque are illustrated in figure 6.9. As seen in the figure the torque are divided into five where τ_e is the torque from the induction machine, $\tau_{Siemens}$ is the torque from the Siemens drive system, $\tau_{\mu-IM}$ is the friction of the bearings and viscous friction of the induction machine, $\tau_{\mu-tt}$ is the friction from the bearings in the torque transducer and

$\tau_{\mu-Siemens}$ is the friction from the bearings and viscous friction in the Siemens machine.

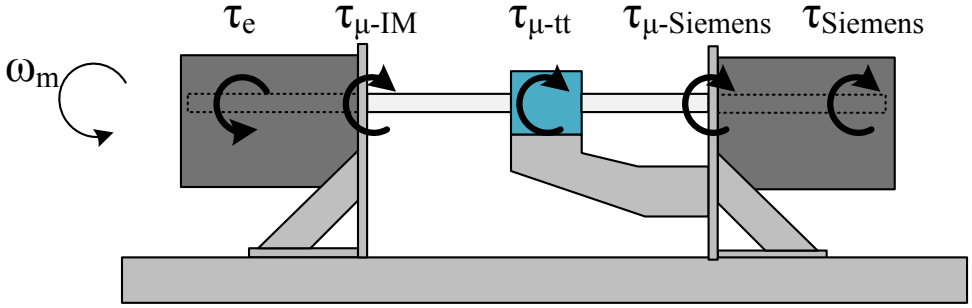

Figure 6.9: *Torque acting on the shaft.*

Newtons second law is applied in order to determine the angular velocity of the shaft, ω_m, as in equation (6.11).

$$J_{test-setup} \cdot \dot{\omega}_m = \tau_e - \tau_{Siemens} - \tau_{\mu-IM} - \tau_{\mu-tt} - \tau_{\mu-Siemens} \tag{6.11}$$

where:

$J_{test-setup}$	Moment of inertia for test setup $[kg \cdot m^2]$
$\tau_{Siemens}$	Torque from Siemens drive system $[Nm]$
$\tau_{\mu-IM}$	Friction of induction machine $[Nm]$
$\tau_{\mu-tt}$	Friction of torque transducer $[Nm]$
$\tau_{\mu-Siemens}$	Friction of Siemens machine $[Nm]$

The angular velocity of the shaft is expressed as in equation (6.12) when the machine has two pole pairs:

$$\omega_m = \frac{\omega_r}{2} \tag{6.12}$$

where:

ω_r	Electric angular velocity of rotor shaft $[^{rad}/_s]$

When applying a constant velocity of the shaft the angular acceleration is zero. The measured torque from the torque transducer, τ_{meas}, may at a constant velocity be expressed as:

$$\tau_{meas} = \tau_e - \tau_{\mu-IM} - \tau^*_{\mu-tt} \tag{6.13}$$

where:

τ_{meas}	Measured torque from torque transducer $[Nm]$
$\tau^*_{\mu-tt}$	Friction from bearings in the torque transducer measured by the transducer$[Nm]$

The * in $\tau^*_{\mu-tt}$ indicates that not all friction in bearings in the torque transducer is measured. The friction measured by the torque transducer ($\tau_{\mu-IM} + \tau^*_{\mu-tt}$) is determined by applying a constant velocity of the shaft using the Siemens drive system and applying no torque from the induction machine (τ_e=0). The experiment is further described in appendix F.4. The friction as a function of rotor velocity is seen in figure 6.10.

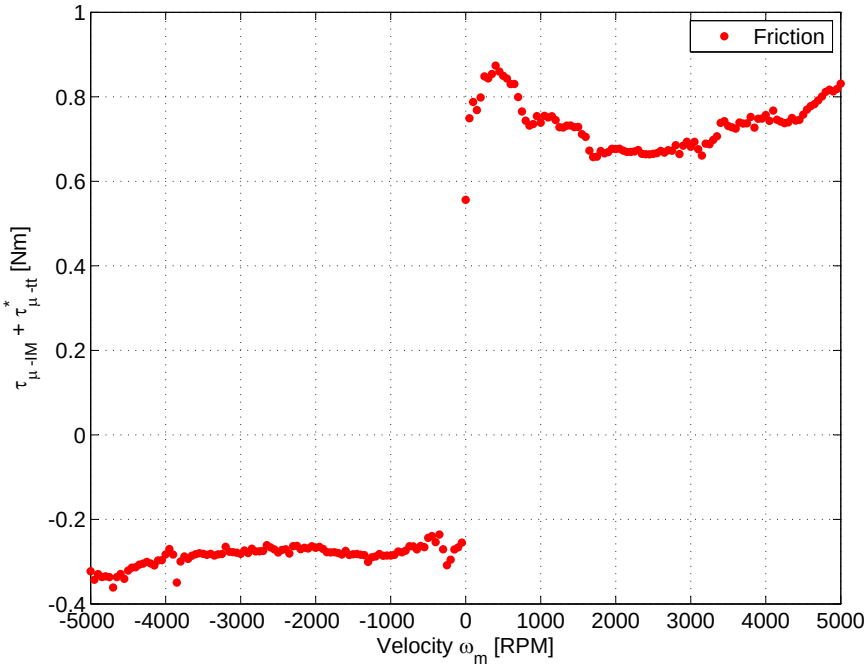

Figure 6.10: *Friction measured by torque transducer as function of rotor velocity.*

The friction depicted in figure 6.10 is a combination of coulomb friction (static friction) and viscous friction (dynamic friction). The static friction is expected to provide a constant torque against the direction of rotation independent on the velocity. The dynamic friction is expected to provide a torque proportional to the velocity also against the direction of rotation. As seen in the figure this is not the case. The friction seems to be close to constant all over the operating velocity range only depending on the sign of the velocity. This characteristic can be explained by an increase of lubrication in bearings at high velocities.

As seen in the figure the friction at 0 rpm is not 0 Nm. This is considered as a calibration error in the torque transducer.

When performing the mapping of the motor the friction is considered as an offset in the measured torque. If e.g. the torque transducer is measuring τ_{meas} equal to 10 Nm at 2000 rpm and the friction ($\tau_{\mu-IM} + \tau*_{\mu-tt}$) is 0.7 Nm at 2000 rpm, as seen in figure 6.10, the torque provided by the induction machine τ_e is 10.7 Nm according to equation (6.13).

The moment of inertia for the induction machine when implemented in the test setup includes the rotor of the induction machine, the rotor of the Siemens drive system and the shaft between them. The moment of inertia is calculated from an experiment where a constant acceleration is applied to the rotor by the Siemens drive system and the torque applied by the induction machine is zero. The moment of inertia is expressed utilizing equation (6.11). The moment of inertia is calculated using equation (6.14).

$$\begin{aligned} J_{test-setup} \cdot \alpha_m &= -\tau_{Siemens} - \tau_{\mu-IM} - \tau_{\mu-tt} - \tau_{\mu-Siemens} \\ &\Downarrow \\ J_{test-setup} &= \frac{-\tau_{Siemens} - \tau_{\mu-IM} - \tau_{\mu-tt} - \tau_{\mu-Siemens}}{\alpha_m} \end{aligned} \tag{6.14}$$

α_m Angular acceleration of shaft $[rad/s^2]$

The experiment for determination of moment of inertia is described in appendix F.5. The result is a moment of inertia of 0.030 $kg \cdot m^2$.

6.4.2 Implementation in Electric Vehicle

When the induction machine is implemented in the electric vehicle Newtons second law is applied in order to determine the translational velocity of the vehicle as described in section 2.1. For convenience the force equation is repeated in equation (6.15).

$$m_{EV} \cdot \ddot{x}_{EV} = F_t - m_{EV} \cdot g \cdot \sin(\theta_{road}) - F_w - F_r \tag{6.15}$$

where:
- m_{EV} Mass of EV $[kg]$
- $\ddot{x}_{EV}$ Acceleration of the EV $[m/s^2]$
- F_t Traction force $[N]$
- g Gravitational acceleration constant $[m/s^2]$
- θ_{road} Gradient of the road $[rad]$
- F_w Dynamic drag $[kN]$
- F_r Rolling resistance of the wheels $[kN]$

The traction force in equation (6.15) is the propelling force of the electric vehicle. It can be expressed as a function of the torque of the induction machine as described in the proceeding. First the power of the shaft of the induction machine is expressed as in equation (6.16).

$$P_{IM} = \left(\tau_e - \tau_{\mu-IM}\right) \cdot \omega_m \tag{6.16}$$

where: P_{IM} Shaft power of induction machine $[W]$

The friction in the induction machine is estimated from figure 6.10 if the friction in the torque transducer($\tau^*_{\mu-tt}$) is assumed to be zero.
The power of the shaft is now multiplied by typical efficiencies of the differential and gear in the electric vehicle in order to determine the power transferred to the wheels:

$$P_{wheel} = P_{IM} \cdot \eta_{differential} \cdot \eta_{gear} \tag{6.17}$$

where: P_{Wheel} Power of the wheels of electric vehicle $[W]$
$\eta_{differential}$ Efficiency of differential in electric vehicle $[-]$
η_{gear} Efficiency of gear in electric vehicle $[-]$

The traction force may now be expressed as in equation (6.18).

$$\begin{aligned} F_t &= \frac{P_{wheel}}{\omega_{wheel} \cdot r_w} \\ &\Downarrow \\ F_t &= \frac{\left(\tau_e - \tau_{\mu-IM}\right) \cdot \omega_m \cdot \eta_{differential} \cdot \eta_{gear}}{\omega_{wheel} \cdot r_w} \end{aligned} \tag{6.18}$$

where: r_w Radius of wheels in electric vehicle $[m]$
ω_{wheel} Angular velocity of wheels $[rad/s]$

As mentioned in section 2.4 the gear ratio for the electric vehicle is 1:7. This means that $\omega_m = 7 \cdot \omega_{wheel}$. The velocity of the vehicle may hereby be expressed as in equation (6.19).

$$\dot{x}_{EV} = \omega_{wheel} \cdot r_w = \frac{\omega_m}{7} \cdot r_w \tag{6.19}$$

Using equation (6.15), (6.18), (6.19) and the forces described in section 2.1 it is now possible to rewrite the force equation to a torque equation for torque acting on the rotor shaft of the induction machine.

$$
\begin{aligned}
m_{EV} \cdot \ddot{x}_{EV} &= F_t - m_{EV} \cdot g \cdot \sin(\theta_{road}) - F_w - F_r \\
&\Downarrow \\
m_{EV} \cdot \frac{\dot{\omega}_m}{7} \cdot r_w &= \frac{\left(\tau_e - \tau_{\mu-IM}\right) \cdot \omega_m \cdot \eta_{differential} \cdot \eta_{gear}}{\frac{\omega_m}{7} \cdot r_w} \\
&\quad - m_{EV} \cdot g \cdot \sin(\theta_{road}) - \frac{1}{2} \cdot \rho \cdot A_f \cdot C_D \cdot \left(\frac{\omega_m}{7} \cdot r_w - V_w\right)^2 \\
&\quad - g \cdot m_{EV} \cdot \cos(\theta_{road}) \cdot 0.01 \cdot \left(1 + \frac{\frac{\omega_m}{7} \cdot r_w}{160}\right) \\
&\Downarrow \\
\dot{\omega}_m \cdot \frac{m_{EV}}{7} \cdot r_w &= \frac{\left(\tau_e - \tau_{\mu-IM}\right) \cdot \eta_{differential} \cdot \eta_{gear} \cdot 7}{r_w} \\
&\quad - m_{EV} \cdot g \cdot \sin(\theta_{road}) - \frac{1}{2} \cdot \rho \cdot A_f \cdot C_D \cdot \left(\frac{\omega_m}{7} \cdot r_w - V_w\right)^2 \\
&\quad - g \cdot m_{EV} \cdot \cos(\theta_{road}) \cdot 0.01 \cdot \left(1 + \frac{\frac{\omega_m}{7} \cdot r_w}{160}\right) \\
&\Downarrow \\
\dot{\omega}_m \cdot \frac{m_{EV}}{7^2} \cdot r_w^2 &= \left(\tau_e - \tau_{\mu-IM}\right) \cdot \eta_{differential} \cdot \eta_{gear} \\
&\quad - m_{EV} \cdot g \cdot \sin(\theta_{road}) \cdot \frac{r_w}{7} - \frac{1}{2} \cdot \rho \cdot A_f \cdot C_D \cdot \left(\frac{\omega_m}{7} \cdot r_w - V_w\right)^2 \cdot \frac{r_w}{7} \\
&\quad - g \cdot m_{EV} \cdot \cos(\theta_{road}) \cdot 0.01 \cdot \left(1 + \frac{\frac{\omega_m}{7} \cdot r_w}{160}\right) \cdot \frac{r_w}{7} \\
&\Downarrow \\
\dot{\omega}_m \cdot J_{EV} &= \sum \tau_{shaft}
\end{aligned}
\tag{6.20}
$$

where:

	ρ	Density of air $[\mathrm{kg/m^3}]$
	A_f	Frontal area of the EV $[m^2]$
	C_D	Aerodynamic drag coefficient $[-]$
	V_w	Velocity of the wind blowing in the EV moving direction $[\mathrm{m/s}]$
	θ_{road}	Gradient of road $[rad]$
	J_{EV}	Moment of inertia for electric vehicle $[kg \cdot m^2]$
	τ_{shaft}	Torque acting on rotor shaft of induction machine $[Nm]$

The moment of inertia for the electrical vehicle can now be expressed as:

$$
J_{EV} = m_{EV} \cdot \left(\frac{r_w}{7}\right)^2 \tag{6.21}
$$

As seen in equation (6.20) the dynamics of the electric vehicle is dependent on driving conditions (gradient of the road and velocity of wind). The variation of these conditions and their effect on the performance of the electrical vehicle is discussed in section 5.2.3.

6.5 Losses in Powertrain

A model describing the quantities in the powertrain is constructed from the four preceding sections. When testing potential control strategies for the electric vehicle it is however also interesting to estimate the losses in the powertrain during driving cycles. It is therefore desirable to find equations describing the losses.
As described in the problem formulation the focus of this project is on energy efficient control of the induction machine in the electric vehicle using an inverter. Therefore only inverter and motor losses are considered. The loss equations originates from [Abrahamsen, 2000].

6.5.1 Losses in Inverter

The losses in the inverter can be divided into conduction losses and switching losses. The conduction losses for the transistors and diodes in each branch is expressed as in equation (6.22) and (6.23) respectively. These conduction loss equations are valid when using third order harmonic injection in the PWM modulation for the inverter. In this project space vector modulation is utilized and the equations are therefore assumed to be valid as the line-line voltage when using third harmonic injection is similar to when using space vector.

$$P_{con,T} = \frac{V_{0,T} \cdot I_s \cdot \sqrt{2}}{\pi} + \frac{I_s \cdot V_{0,T} \cdot m_i \cdot cos(\phi)}{\sqrt{6}} + \frac{R_{0,T} \cdot I_s^2}{2} + \frac{R_{0,T} \cdot I_s^2 \cdot m_i}{\sqrt{3} \cdot cos(\phi) \cdot 6 \cdot \pi} - \frac{4 \cdot R_{0,T} \cdot I_s^2 \cdot m_i \cdot cos(3 \cdot \phi)}{45 \cdot \pi \cdot \sqrt{3}} \quad (6.22)$$

$$P_{con,D} = \frac{V_{0,D} \cdot I_s \cdot \sqrt{2}}{\pi} - \frac{I_s \cdot V_{0,D} \cdot m_i \cdot cos(\phi)}{\sqrt{6}} + \frac{R_{0,D} \cdot I_s^2}{2} - \frac{R_{0,D} \cdot I_s^2 \cdot m_i}{\sqrt{3} \cdot cos(\phi) \cdot 6 \cdot \pi} + \frac{4 \cdot R_{0,D} \cdot I_s^2 \cdot m_i \cdot cos(3 \cdot \phi)}{45 \cdot \pi \cdot \sqrt{3}} \quad (6.23)$$

where:	$P_{con,T}$	Conduction loss from transistors in each branch $[W]$
	$P_{con,D}$	Conduction loss from diodes in each branch $[W]$
	$V_{0,T}$	On voltage for transistor $[V]$
	$V_{0,D}$	On voltage for diode $[V]$
	I_s	Stator RMS current $[A]$
	m_i	Modulation index $[-]$
	ϕ	Phase shift angle $[rad]$
	$R_{0,T}$	Resistance for transistor $[\Omega]$
	$R_{0,D}$	Resistance for diode $[\Omega]$

The switching losses are expressed as in equation (6.24).

$$P_{sw} = K_{sw} \cdot I_s \cdot f_{sw} \quad (6.24)$$

where:	P_{sw}	Switching loss in inverter $[W]$
	K_{sw}	Empirically determined constant $[V \cdot s]$
	f_{sw}	Switching frequency $[Hz]$

The total inverter losses are expressed as:

$$P_{loss,inv} = 3 \cdot (P_{con,T} + P_{con,D}) + P_{sw} \quad (6.25)$$

where:	$P_{loss,inv}$	Total loss in inverter $[W]$

The parameters for these equation are found in chapter 10.

6.5.2 Losses in induction machine

In this section equations describing the losses of the induction machine are presented. The induction machine steady state model presented in section 6.3 is repeated in figure 6.11 for convenience. From this it is seen that the losses are caused by stator and rotor conduction loss represented by R_s and R'_r respectively and core loss (Eddie and hysteresis) by R_c. Harmonic losses are not included in the loss equations for the induction machine. The following sections describes the conduction -and core losses.

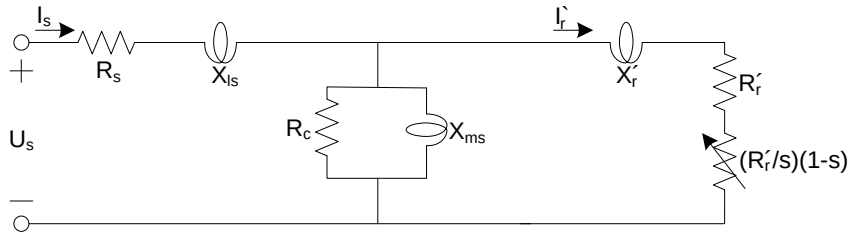

Figure 6.11: *Steady state induction machine circuit.*

Conduction losses

The stator conduction losses are given by equation (6.26). As seen in this equation the stator resistance is dependent on temperature. The stator resistance is given by equation (6.27).

$$P_{con,S} = 3 \cdot R_s(T_s) \cdot I_s^2 \tag{6.26}$$

where:
- $P_{con,S}$ — Conduction loss in the stator windings $[W]$.
- $R_s(T_s)$ — Temperature dependent stator resistance $[\Omega]$.

$$R_s(T_s) = (1 + \alpha_s \cdot (T_s - T_{Room})) \cdot R_{s0} \tag{6.27}$$

where:
- α_s — Coefficient of electrical stator resistance variation with temperature $[1/^\circ C]$
- T_s — Temperature of stator windings $[^\circ C]$
- T_{Room} — Room temperature $[^\circ C]$
- R_{s0} — Stator resistance at room temperature $[\Omega]$

The rotor conduction losses may be expressed using the same equations.

$$P_{con,R} = 3 \cdot R'_r(T_r) \cdot I_r^2 \tag{6.28}$$

where:
- $P_{con,R}$ Conduction loss in the rotor windings $[W]$
- $R'_r(R_r)$ Temperature dependent rotor resistance $[\Omega]$
- I_r Rotor RMS current $[A]$.

$$R'_r(T_r) = (1 + \alpha_r \cdot (T_r - T_{Room})) \cdot R'_{r0} \tag{6.29}$$

where:
- α_r Coefficient of electrical rotor resistance variation with temperature $[1/^\circ C]$
- T_r Temperature of rotor windings $[^\circ C]$
- R'_{r0} Rotor resistance at room temperature $[\Omega]$

Core losses

The core losses are given by equation (6.30).

$$P_{core} = \left(1 + s \cdot \frac{m_r}{m_s}\right) \cdot k_{h.s} \cdot \lambda_m^{\nu} \cdot f_s + \left(1 + s^2 \cdot \frac{m_r}{m_s}\right) \cdot k_{e.s} \cdot \lambda_m^2 \cdot f_s^2 \tag{6.30}$$

where:
- P_{core} Total core loss $[W]$
- s Slip $[-]$
- m_r Mass of rotor $[kg]$
- m_r Mass of stator $[kg]$
- $k_{h.s}$ Hysteresis coefficient $[1/H]$
- $k_{e.s}$ Eddie coefficient $[1/\Omega]$
- λ_m Magnetizing flux linkage $[Wb.]$
- ν Coefficient that depends on the magnetic material $[-]$
- f_s Stator frequency $[rad/s]$

The total losses for the induction machine and inverter may hereby be expressed as:

$$P_{loss,total} = P_{loss,inv} + P_{con,S} + P_{con,R} + P_{core} \tag{6.31}$$

where:
- $P_{loss,total}$ Total losses in inverter and induction machine $[W]$.

6.6 Final Model Structure

When modeling the powertrain as described in this chapter the final model structure can be depicted as in figure 6.12. The model is build up in the Matlab extension Simulink.

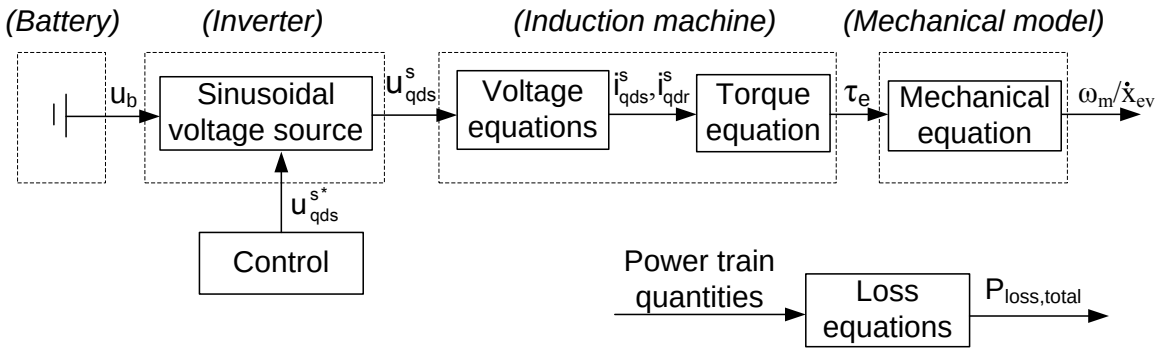

Figure 6.12: *Structure of final simulation model.*

In the next chapter the control strategy for the powertrain is considered.

CHAPTER 7

CONTROL STRATEGY

In this section the control strategy for the induction machine is presented. For combustion engine vehicles the accelerator pedal gives a torque reference for the engine [Bosch, 2007, p. 610]. Torque control for induction machines can be achieved by a control algorithm called field-oriented control [Krause et al., 2002, p. 540]. There are two types of field-oriented control for an induction machine, indirect and direct control. Indirect control is based on steady state considerations whereas direct control is based on measured machine quantities [Novotny and Lipo, 1996, p. 264]. In this section the basic principles of field-oriented control is presented and the choice of direct vs. indirect control is considered.

7.1 Field-Oriented Control

The basic premise of field-oriented control is seen in the torque equation for the induction machine, equation (6.10). The torque equation is rewritten inserting the flux linkage equations (6.8) and (6.9):

$$\tau_e = \frac{3}{2} \cdot \frac{P}{2} \cdot \left(\lambda'_{qr} \cdot i'_{dr} - \lambda'_{dr} \cdot i'_{qr} \right) \tag{7.1}$$

The quantities in equation (7.1) is illustrated in figure 7.1. Equation (7.1) is rewritten as:

$$\tau_e = -\frac{3}{2} \cdot \frac{P}{2} \cdot \left| \bar{\lambda}'_{qdr} \right| \cdot \left| \bar{i}'_{qdr} \right| \cdot sin\left(\theta\right) \tag{7.2}$$

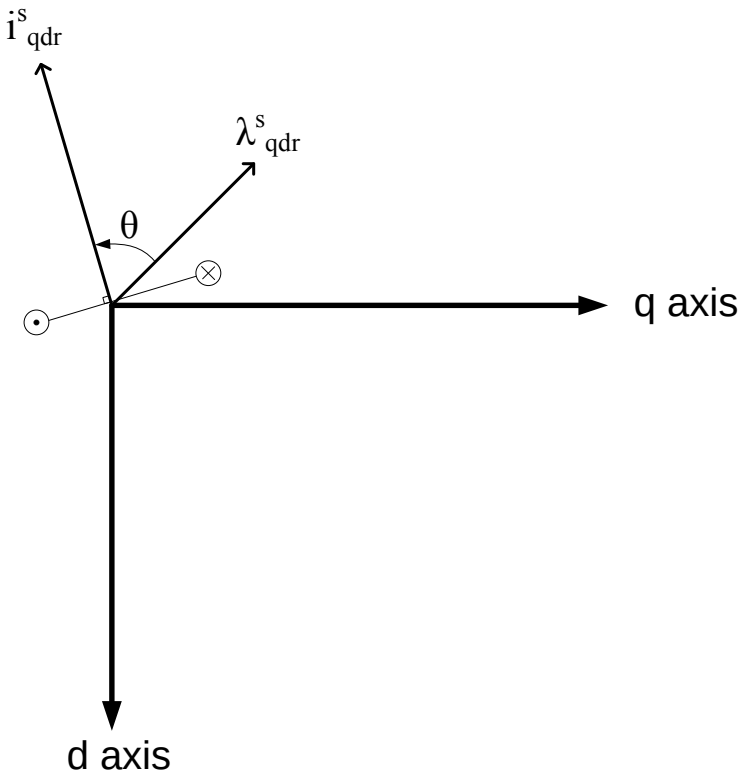

Figure 7.1: *Quantities for the torque equation [Krause et al., 2002, p. 541].*

Equation (7.2) is derived using equation (7.3) which is the cross product of the two vectors:

$$\bar{\lambda}'_{qdr} \times \vec{i}'_{qdr} = -\left|\bar{\lambda}'_{qdr}\right| \cdot \left|\vec{i}'_{qdr}\right| \cdot sin(\theta) \tag{7.3}$$

The minus sign in equation (7.3) is because the d-axis is defined positive in the downward direction see figure 7.1.
From equation (7.2) it is seen that for a given magnitude of the two vectors $\bar{\lambda}'_{qdr}$ and $\vec{i}'_{qdr}$ the torque is maximized when the two vectors are perpendicular. In steady state the rotor flux linkage vector and rotor current vector are always perpendicular. This applies to all singly fed induction machines [Krause et al., 2002, p. 541]. The orthogonal steady state property is seen from the rotor voltage equations (6.4) and (6.5). If the rotor part of the IM is a short circuited squirrel cage and the IM is operated in steady state the equations is simplified to:

$$0 = R'_r \cdot i'_{qr} + \left(\omega_{rf} - \omega_r\right) \cdot \lambda'_{dr} \tag{7.4}$$

$$0 = R'_r \cdot i'_{dr} - \left(\omega_{rf} - \omega_r\right) \cdot \lambda'_{qr} \tag{7.5}$$

Isolating the two currents:

$$i_{qr}^{'} = -\frac{1}{R_r'} \cdot \left(\omega_{rf} - \omega_r\right) \cdot \lambda_{dr}^{'} \tag{7.6}$$

$$i_{dr}' = \frac{1}{R_r'} \cdot \left(\omega_{rf} - \omega_r\right) \cdot \lambda_{qr}' \tag{7.7}$$

The dot product between the rotor flux linkage vector and the rotor current vector is written as:

$$\bar{\lambda}_{qdr}' \cdot \vec{i}_{qdr}' = \lambda_{qr}' \cdot i_{qr}' + \lambda_{dr}' \cdot i_{dr}' \tag{7.8}$$

Inserting equation (7.6) and (7.7) into equation (7.8):

$$\begin{aligned} \bar{\lambda}_{qdr}' \cdot \vec{i}_{qdr}' &= \lambda_{qr}' \cdot \left(-\frac{1}{R_r'} \cdot \left(\omega_{rf} - \omega_r\right) \cdot \lambda_{dr}'\right) + \lambda_{dr}' \cdot \left(\frac{1}{R_r'} \cdot \left(\omega_{rf} - \omega_r\right) \cdot \lambda_{qr}'\right) \\ &= 0 \end{aligned} \tag{7.9}$$

Since the two expressions in the dot product are identical except for the signs the dot product between the rotor current and rotor flux is always zero. This means that the rotor current and rotor flux are always perpendicular in steady state.
In field-oriented control the goal is to keep the rotor flux linkage vector and the rotor current vector perpendicular during transient conditions. From equation (7.8) it is seen that there are many possibilities to make the dot product zero. In field-oriented control the strategy of keeping the rotor flux linkage vector and the rotor current vector perpendicular is twofold. First part of the strategy is to ensure that:

$$\lambda_{qr}' = 0 \tag{7.10}$$

The second is to ensure that:

$$i_{dr}' = 0 \tag{7.11}$$

It is seen from equation (7.8) that if equation (7.10) and (7.11) are fulfilled in transient conditions the rotor flux linkage vector and the rotor current vector are always perpendicular.
The next step in field-oriented control is to find out how equation (7.10) and (7.11) are satisfied. Equation (7.10) is satisfied by ensuring that the reference frame always points in the same direction as the rotor flux.

Equation (7.11) is satisfied by keeping i_{ds} constant. This is seen from the d-axis voltage equation for the rotor (equation (6.5)) where $\lambda_{qr}^{'} = 0$:

$$0 = R'_r \cdot i'_{dr} + p \cdot \lambda'_{dr} \tag{7.12}$$

Inserting equation (6.9) into equation (7.12):

$$\begin{aligned} 0 &= R'_r \cdot i'_{dr} + p\left(L'_{lr} \cdot i'_{dr} + L_M \cdot \left(i_{ds} + i'_{dr}\right)\right) && (7.13)\\ &= R'_r \cdot i'_{dr} + p \cdot i'_{dr} \cdot (L_{lr} + L_M) + p \cdot L_M \cdot i_{ds} && (7.14) \end{aligned}$$

The stator referred rotor inductance is defined as:

$$L'_r = L'_{lr} + L_M \tag{7.15}$$

Combining (7.14) and (7.15):

$$0 = R'_r \cdot i'_{dr} + p \cdot i'_{dr} \cdot L'_r + p \cdot L_M \cdot i_{ds} \tag{7.16}$$

Isolating $p \cdot i'_{dr}$:

$$p \cdot i'_{dr} = -\frac{R'_r}{L'_r} \cdot i'_{dr} - \frac{L_M}{L'_r} \cdot p \cdot i_{ds} \tag{7.17}$$

Equation (7.17) is a stable first order differential equation describing i'_{dr} with $p \cdot i_{ds}$ as input. If i_{ds} is constant, $p \cdot i_{ds}$ is zero and i'_{dr} will go towards and stay at zero regardless of other transients in the system.
Inserting equation (7.11) into (6.9) yields equation (7.18) showing that it is possible to control the d-axis rotor flux linkage with the stator d-axis current.

$$\begin{aligned} \lambda'_{dr} &= L'_{lr} \cdot i'_{dr} + L_M \cdot \left(i_{ds} + i'_{dr}\right) \\ &= L_M \cdot i_{ds} && (7.18) \end{aligned}$$

Inserting equation (7.10) into (7.1) yields equation (7.19).

$$\begin{aligned} \tau_e &= \frac{3}{2} \cdot \frac{P}{2} \cdot \left(\lambda'_{qr} \cdot i'_{dr} - \lambda'_{dr} \cdot i'_{qr}\right) \\ &= -\frac{3}{2} \cdot \frac{P}{2} \cdot \left(\lambda'_{dr} \cdot i'_{qr}\right) && (7.19) \end{aligned}$$

Inserting equation (6.8) into (7.10) and utilizing the inductance relation of equation (7.15) yields an expression for the rotor q-axis current as a function of the stator q-axis current given by equation (7.20).

$$\begin{aligned} \lambda'_{qr} &= L'_{lr} \cdot i'_{qr} + L_M \cdot \left(i_{qs} + i'_{qr}\right) \\ &\Downarrow \\ 0 &= = L_M \cdot i_{qs} + L_r \cdot i'_{qr} \\ &\Downarrow \\ i'_{qr} &= -\frac{L_M}{L_r} \cdot i_{qs} \end{aligned} \tag{7.20}$$

Inserting equation (7.20) into (7.19) yields:

$$\tau_e = \frac{3}{2} \cdot \frac{P}{2} \cdot \frac{L_M}{L'_r} \cdot \lambda'_{dr} \cdot i_{qs} \tag{7.21}$$

Inserting equation (7.18) into (7.21) yields:

$$\tau_e = \frac{3}{2} \cdot \frac{P}{2} \cdot \frac{L_M^2}{L'_r} \cdot i_{ds} \cdot i_{qs} \tag{7.22}$$

Equation (7.22) shows that a given torque can be obtained using various combinations of d- and q-axis currents. According to the problem formulation the efficiency of the IM is to be maximized. The combination of d- and q-axis currents must therefore be chosen on basis of minimizing the losses. Minimizing the stator currents minimizes the conduction losses in the stator however depending on core loss in the IM and switching losses in the inverter the most energy efficient combination may not be when the stator current is at its minimum. In order to determine the most energy efficient combination the loss equations for the induction machine and inverter must be determined. This is done by performing a mapping of the IM in chapter 9 and from this mapping determining the loss equations using optimization in chapter 10.
Controlling the d- and q-axis currents for obtaining energy efficient control requires an estimation of the angular position of the rotor flux. In the following section two methods for flux estimation are presented.

7.2 Rotor Flux Estimator

In order to control the torque of the IM using stator currents the position of the rotor flux, and hereby the d-axis of the reference frame, must be known. The position can be determined in

several ways. In general there are two types of rotor flux estimation: Indirect and direct. Indirect control is based on steady state considerations whereas direct control is based on measured machine quantities [Novotny and Lipo, 1996, p. 264]. Direct control can be based on measurements of e.g. air gap flux (using hall sensors) or phase currents.
One direct and one indirect method are considered. The indirect method was first implemented in the test setup but its parameter sensitivity made it favorable to consider using a direct method. In this section the basic principles and some advantages/disadvantages of the two methods are described. Furthermore some of the problems encountered using the indirect flux estimation are also described in this section.

7.2.1 Indirect Flux Estimator

As mentioned in the preceding indirect field oriented control is based on steady state considerations. The rotor flux angle is determined by deriving an expression for the rotor flux velocity and integrate it with respect to the time. To determine the rotor flux velocity equation (6.4) is applied along with relations that the rotor q-axis flux is zero (equation (7.10)) and that the rotor voltage is zero. The expression for the rotor flux velocity is seen in equation (7.24).

$$0 = R'_r \cdot i'_{qr} + \left(\omega_{rf} - \omega_r\right) \cdot \lambda'_{dr} \tag{7.23}$$

$$\Downarrow$$

$$\omega_{rf} = \omega_r - R'_r \cdot \frac{i'_{qr}}{\lambda'_{dr}} \tag{7.24}$$

Inserting equation (7.20) and (7.18) into equation (7.24) yields:

$$\omega_{rf} = \omega_r + \frac{R'_r}{L'_r} \cdot \frac{i_{qs}}{i_{ds}} \tag{7.25}$$

$$\tau_r = \frac{L'_r}{R'_r} \tag{7.26}$$

$$\Downarrow$$

$$\omega_{rf} = \omega_r + \frac{1}{\tau_r} \cdot \frac{i_{qs}}{i_{ds}} \tag{7.27}$$

$$= \omega_r + \omega_s \tag{7.28}$$

where: ω_s Slip velocity $[^{rad}/_s]$.
τ_r Rotor time constant $[^H/_\Omega]$.

The inputs to the indirect field-oriented control strategy are a torque -and rotor flux reference from which a q-axis stator current reference is calculated. This is done by isolating i_{qs} in equation (7.21) resulting in the following expression:

$$i_{qs} = \frac{2}{3} \cdot \frac{2}{P} \cdot \frac{L'_r}{L_M} \cdot \frac{\tau_e}{\lambda_{dr}} \tag{7.29}$$

Figure 7.2 shows the indirect field-oriented control in diagram form, it is based upon equation (7.29) and (7.27). Instead of calculating the frequency of the rotor flux (ω_{rf}) the rotor flux angle (θ_{rf}) is directly calculated from the sum of the rotor position (θ_r) and the integral of slip velocity ($\int \omega_s dt$).

The control strategy has two reference signals τ_{e-ref} and λ'_{dr-ref} which is converted to reference stator currents i_{qs-ref} and i_{ds-ref}. These reference currents together with the estimation of the rotor flux angle θ_{rf} and the measured currents $\bar{i}_{ABC}$ are sent into the current control box, see figure 7.2. The current control transforms the reference currents and the measured currents into the same reference frame using the rotor flux angle θ_{rf}. The errors between commanded -and measured currents are then calculated and are transformed into voltages by controllers. Finally the voltages are then transformed to duty cycles and send to the inverter.

The indirect flux estimator has some limitations. As seen in equation (7.27) the estimator depends on the rotor time constant and hereby the rotor resistance. The rotor temperature is not constant during operation of the IM due to losses. This results in an estimation error during

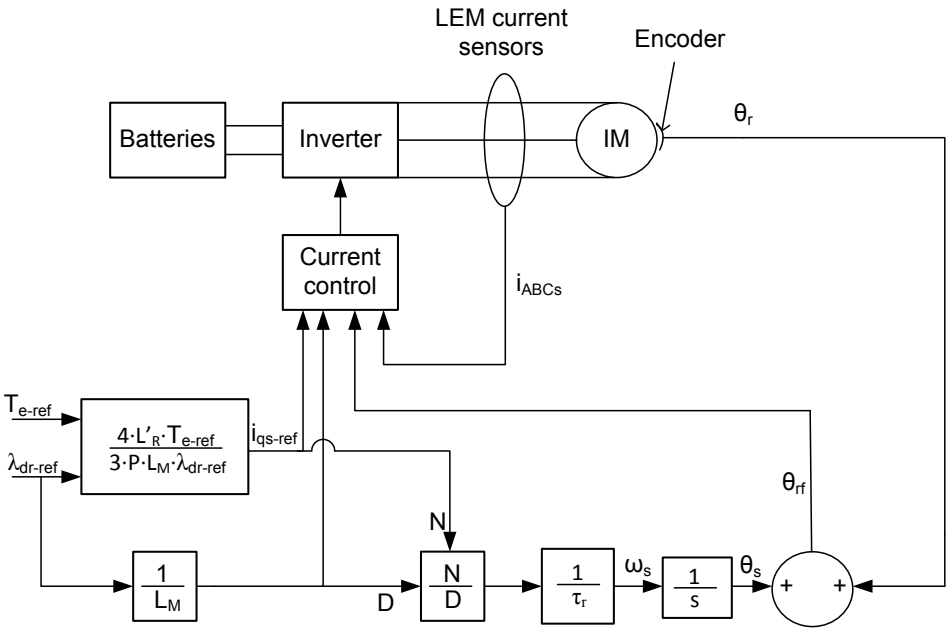

Figure 7.2: *Standard indirect field-oriented control strategy.*

operation which is temperature dependent. The indirect flux observer does not take magnetic saturation and the dynamic response of the rotor flux into account. In section 7.3.3 the effect of these limitations and possible ways to compensate them is examined. In the following section the direct flux estimator is presented.

7.2.2 Direct Flux Estimator

As described in the previous section the indirect flux estimation has the disadvantage of being sensitive to changes in rotor temperature.This section contains a description of a direct flux estimator that is less sensitive to rotor temperature.The estimator is based on Jansen et al. [1994] and is illustrated in diagram form in figure 7.3.
The direct flux estimator uses measured stator currents, rotor position and calculated voltage outputs of the inverter to estimate the rotor flux. Besides estimating the angle of the flux its magnitude is also estimated. The magnitude can be utilized in order to obtain a desired rotor flux level. The transient torque response can also be improved using the rotor flux magnitude. The two sub-components "'flux estimation"' and "'flux control and torque compensation"' are explained in the following.

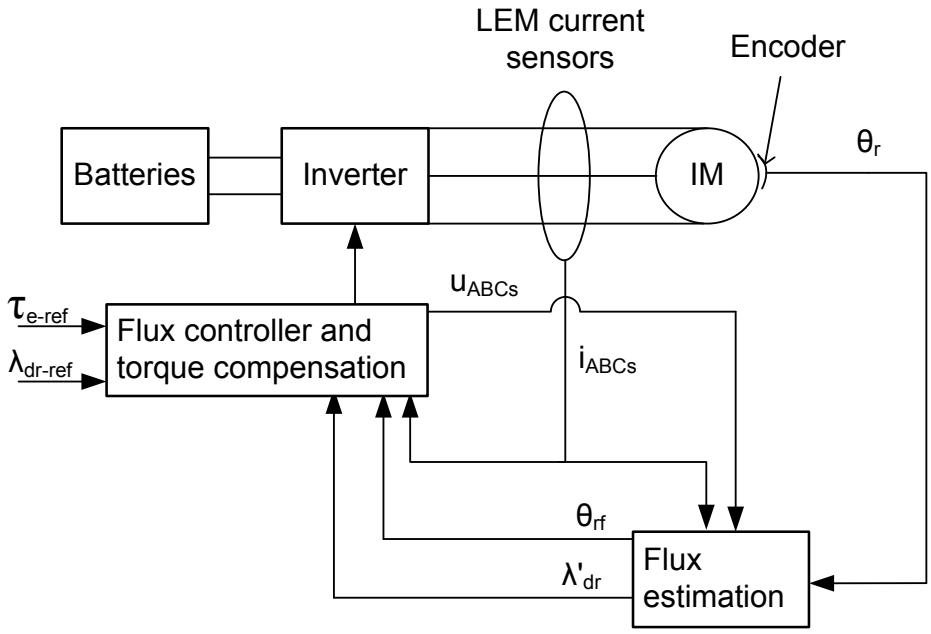

Figure 7.3: *Direct flux estimator.*

The flux estimation sub-component (seen in figure 7.3) is illustrated in figure 7.4. As seen in the figure the flux estimator can be divided into a current model and a voltage model. Both models

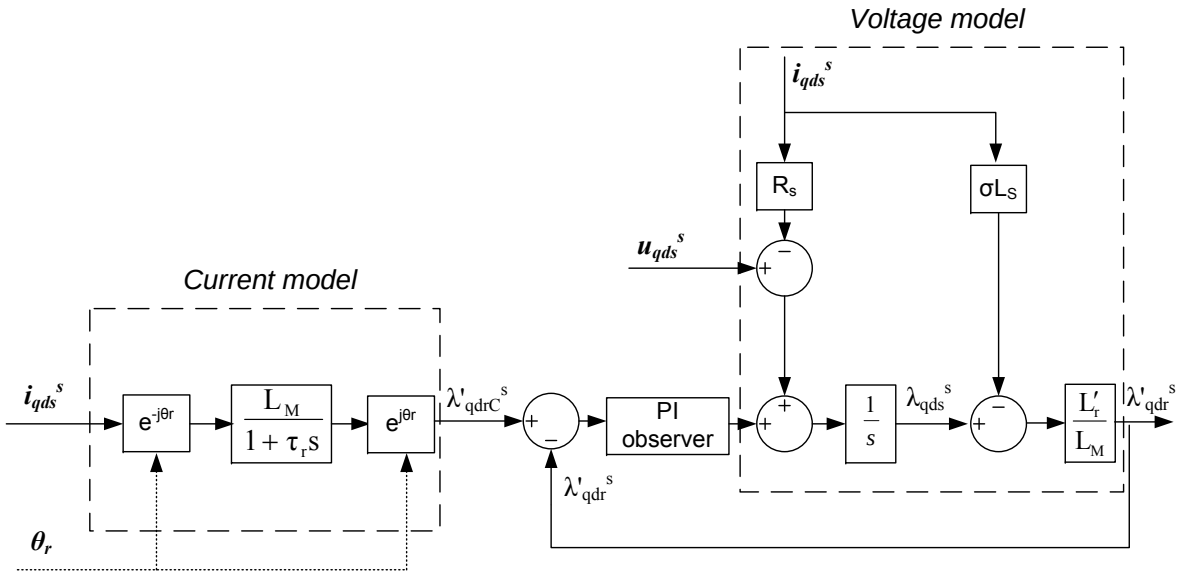

Figure 7.4: *Flux estimator sub-component.*

are based on equations presented in section 6.3. The *s* in superscripts implies that the quantity is in the stationary reference frame. The current model is based on equation (6.4), (6.5), (6.8) and (6.9). For convenience these equations are repeated in equation (7.30) to (7.33).

$$u'_{qr} = R'_r \cdot i'_{qr} + (\omega_{rf} - \omega_r) \cdot \lambda'_{dr} + p \cdot \lambda'_{qr} \tag{7.30}$$

$$u'_{dr} = R'_r \cdot i'_{dr} - (\omega_{rf} - \omega_r) \cdot \lambda'_{qr} + p \cdot \lambda'_{dr} \tag{7.31}$$

$$\lambda'_{qr} = L'_{lr} \cdot i'_{qr} + L_M \cdot (i_{qs} + i'_{qr}) \tag{7.32}$$

$$\lambda'_{dr} = L'_{lr} \cdot i'_{dr} + L_M \cdot (i_{ds} + i'_{dr}) \tag{7.33}$$

As seen in figure 7.4 the measured stator currents are first transferred to the physical rotor reference frame using the mechanical angle from the encoder. This removes all cross couplings between the currents. This is seen by inserting the mechanical velocity ω_r as the reference frame velocity ω_{rf} in equation (7.30) and (7.31). Since the rotor is a short circuited squirrel cage the rotor voltage is set to zero and equation (7.30) and (7.31) is rewritten as:

$$0 = R'_r \cdot i'^{r}_{qr} + p \cdot \lambda'^{r}_{qr} \tag{7.34}$$

$$0 = R'_r \cdot i'^{r}_{dr} + p \cdot \lambda'^{r}_{dr} \tag{7.35}$$

The superscript *r* indicates that the quantities are in the physical rotor reference frame. From equation (7.32) and (7.33) i'_{qr} and i'_{dr} are isolated and inserted into equation (7.34) and (7.35). The rotor fluxes are now expressed as:

$$\lambda'^{r}_{qr} = \frac{L_M}{1+p\cdot\tau_r}\cdot i^r_{qs} \tag{7.36}$$

$$\lambda'^{r}_{dr} = \frac{L_M}{1+p\cdot\tau_r}\cdot i^r_{ds} \tag{7.37}$$

After calculating the rotor fluxes in the rotating reference frame the fluxes are transferred back to the stationary reference frame using the mechanical angle of the encoder.

The voltage model is based on equation (6.2), (6.3), (6.6), (6.7), (6.8) and (6.9). For convenience these equations are repeated here:

$$u_{qs} = R_s\cdot i_{qs} + \omega_{rf}\cdot\lambda_{ds} + p\cdot\lambda_{qs} \tag{7.38}$$

$$u_{ds} = R_s\cdot i_{ds} - \omega_{rf}\cdot\lambda_{qs} + p\cdot\lambda_{ds} \tag{7.39}$$

$$\lambda_{qs} = L_{ls}\cdot i_{qs} + L_M\cdot(i_{qs}+i'_{qr}) \tag{7.40}$$

$$\lambda_{ds} = L_{ls}\cdot i_{ds} + L_M\cdot(i_{ds}+i'_{dr}) \tag{7.41}$$

$$\lambda'_{qr} = L'_{lr}\cdot i'_{qr} + L_M\cdot(i_{qs}+i'_{qr}) \tag{7.42}$$

$$\lambda'_{dr} = L'_{lr}\cdot i'_{dr} + L_M\cdot(i_{ds}+i'_{dr}) \tag{7.43}$$

In the stationary reference frame $\omega_{rf}=0$. Equation (7.38) and (7.39) are rewritten in order to express the stator fluxes:

$$\lambda^s_{qs} = \left(u^s_{qs} - R_s\cdot i^s_{qs}\right)\cdot\frac{1}{p} \tag{7.44}$$

$$\lambda^s_{ds} = (u^s_{ds} - R_s\cdot i^s_{ds})\cdot\frac{1}{p} \tag{7.45}$$

i'_{qr} and i'_{dr} are isolated in equation (7.40) and (7.41) and inserted into equation (7.42) and (7.43) yielding the following expression for the rotor flux:

$$\lambda'^{s}_{qr} = \left(\lambda^s_{qs} - \sigma\cdot L_s\cdot i^s_{qs}\right)\cdot\frac{L'_r}{L_M} \tag{7.46}$$

$$\lambda'^{s}_{dr} = (\lambda^s_{ds} - \sigma\cdot L_s\cdot i^s_{ds})\cdot\frac{L'_r}{L_M} \tag{7.47}$$

Where $\sigma\cdot L_s = L_s - \frac{{L_M}^2}{L'_r}$.

The two models of the flux estimator are both flux observers estimating the flux. If there are no errors in measurements or motor parameters the two models should have the same output. This is most likely not the case when implemented since there are measurement disturbances, parameter variations and voltage drops in the inverter. The current model uses the motor parameters L_M, L'_r and R_r to estimate the flux. If the temperature of the rotor changes the rotor resistance also changes, as described in the indirect flux control. The current model therefore poses similar temperature sensitivity as the indirect flux estimator. The voltage model uses the motor parameters L_M, L'_r, L_s and R_s. It is hereby not dependent on the rotor resistance. It is dependent on stator resistance but since the stator temperature is measured, the actual stator resistance can be estimated. The voltage model therefore possesses a much better robustness against variations in the rotor resistance compared to the current model and compared to the indirect flux estimator. The voltage model is therefore desirable to use when estimating the rotor flux. As described in the following the voltage model however does possess some weaknesses making the current model more desirable in some operating points.
When using the voltage model as flux estimator the precision of the flux estimation is low at low frequencies. This is due to the fact that the voltage model uses phase voltages and currents to estimate the flux. Since the phase voltage is a PWM signal it cannot be measured and used in the voltage model. Instead the output of the current controllers is used to estimate the phase voltages. Due to the fact that the inverter is not ideal as described in appendix B the actual phase voltage differs from what is used in the flux estimator. The sensitivity with respect to errors in output voltage of the inverter is most significant at low frequencies since the back EMF is low. This enlarged sensitivity at low frequencies makes it desirable to apply the current model at low frequencies since the current model only uses measured phase currents when estimating the rotor flux. The minimum frequency at which the voltage model produces acceptable flux estimation is dependent on the application. It therefore must be determined experimentally or by performing simulations.

When a minimum frequency for the voltage model is determined the transition between the two models must be considered. As seen in figure 7.4 a PI controller is applied between the two models. The PI ensures a continuous transition between the two models.

Flux Control

The output of the flux observer sub-component is a complex vector which is converted into a rotor flux angle -and magnitude. The magnitude can be utilized in the flux control for the system. The flux control (seen in figure 7.3) is illustrated in figure 7.5.

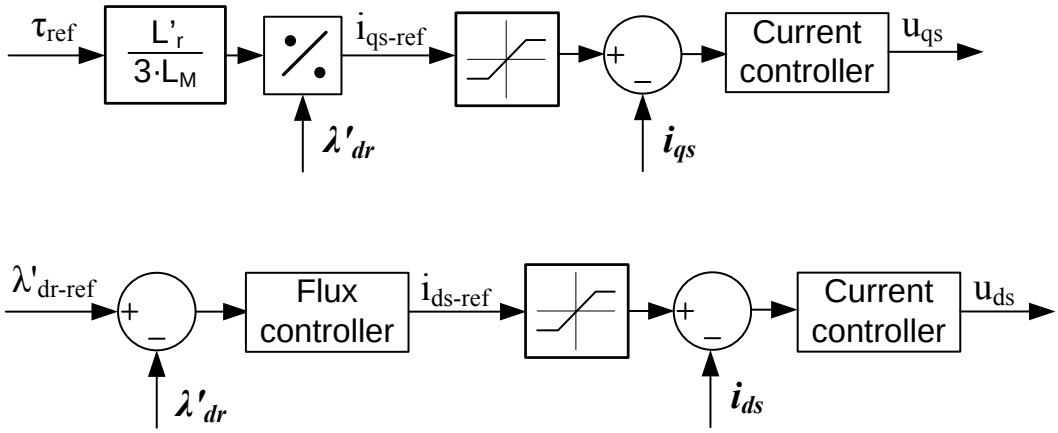

Figure 7.5: *Flux control sub-component of the flux estimator.*

As seen in the figure the input references for the control system is a torque reference τ_{ref} and a rotor flux reference λ'_{dr-ref}. The d-axis current reference (i_{ds-ref}) is calculated by using the magnitude of the estimated rotor flux. The use of this compensation improves the transient response of the rotor flux. The d-axis of the reference frame is defined as the direction of the rotor flux. This means that the rotor flux in the stationary reference frame λ'^{s}_{qdr} is converted into a d-axis rotor flux amplitude λ'_{dr} and angle θ_{rf}. The rotor flux magnitude is part of the inputs to the flux control sub-component.

The flux controller seen in figure 7.5 can be a simple PI controller. The output of the controller sets the current reference for i_{ds}. The current reference i_{qs-ref} is calculated from a desired torque τ_{ref} and the rotor flux λ'_{dr}. Saturation functions are added to the current references to limit the maximum current reference entering the current controllers. This safety feature is especially relevant for the upper branch of the diagram see figure 7.5 since the rotor flux is small at startup. In connection to this a startup sequence should be considered before implementing the direct flux control.

Utilizing the rotor flux controller provides a better transient torque response as explained in the following. The time constant for the rotor flux when applying a magnetizing current in the d-direction is much higher than the time constant for the stator currents (The derivation of time constants is performed in section 7.3.1). If the rotor flux has not yet reached a desired flux reference the q-axis current is increased in order to obtain a desired torque, τ_{ref}, faster. When the rotor flux reaches the desired λ'_{r-ref} the q-axis current decreases to a steady state. At the same time when building up a rotor flux λ'_{dr} the flux controller speeds up the time it takes to build up a steady state rotor flux.

Due to increased robustness against changes in rotor temperature the direct flux estimator is more favorable than the indirect flux estimator.
In the following sections controllers for the direct flux estimator is developed.

7.3 Development, Implementation and Improvement of Control Strategy

This section contains a description of the development and implementation of current controllers and flux estimator. The current controllers are presented first. Next the direct flux estimation is presented. It turns out that the direct flux estimator must be discarded due to technical difficulties and an improved indirect flux estimator is therefore used instead. The improved indirect flux estimator is described and finally the implementation of the control strategy, involving current control and flux estimation, is evaluated.

7.3.1 Development of Current Controllers

In order to control the q- and d-axis currents to obtain a desired torque, as described in section 7, current controllers must be developed. The current controllers are illustrated as in figure 7.6.

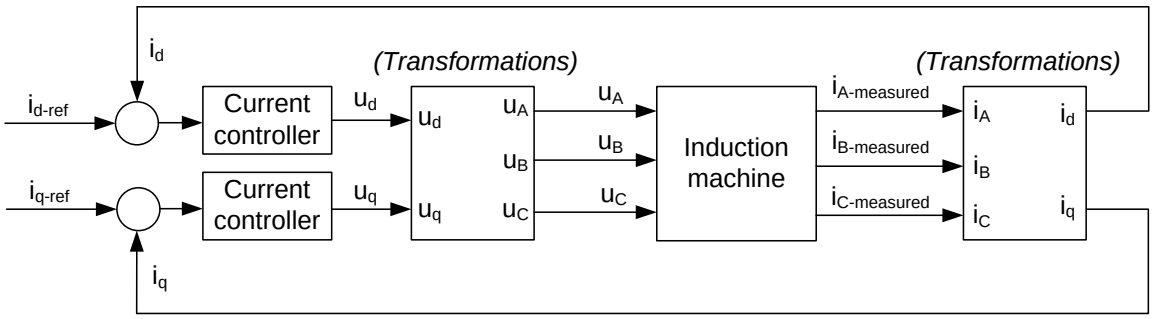

Figure 7.6: *Current controllers for i_{qs} and i_{ds}.*

In order to develop suitable current controllers the voltage equations for the q- and d-axis must be studied. The voltage equations are derived in section 6.3. For convenience the voltage equations are repeated here:

$$
\begin{aligned}
u_{qs} &= R_s \cdot i_{qs} + \omega_{rf} \cdot \lambda_{ds} + p \cdot \lambda_{qs} && (7.48)\\
u_{ds} &= R_s \cdot i_{ds} - \omega_{rf} \cdot \lambda_{qs} + p \cdot \lambda_{ds} && (7.49)\\
u'_{qr} &= R'_r \cdot i'_{qr} + (\omega_{rf} - \omega_r) \cdot \lambda'_{dr} + p \cdot \lambda'_{qr} && (7.50)\\
u'_{dr} &= R'_r \cdot i'_{dr} - (\omega_{rf} - \omega_r) \cdot \lambda'_{qr} + p \cdot \lambda'_{dr} && (7.51)\\
\lambda_{qs} &= L_{ls} \cdot i_{qs} + L_M \cdot (i_{qs} + i'_{qr}) && (7.52)\\
\lambda_{ds} &= L_{ls} \cdot i_{ds} + L_M \cdot (i_{ds} + i'_{dr}) && (7.53)\\
\lambda'_{qr} &= L'_{lr} \cdot i'_{qr} + L_M \cdot (i_{qs} + i'_{qr}) && (7.54)\\
\lambda'_{dr} &= L'_{lr} \cdot i'_{dr} + L_M \cdot (i_{ds} + i'_{dr}) && (7.55)
\end{aligned}
$$

The flux linkages are now inserted into the stator voltage equations:

$$
\begin{aligned}
u_{qs} &= R_s \cdot i_{qs} + \omega_{rf} \cdot \left(L_{ls} \cdot i_{ds} + L_M \cdot (i_{ds} + i'_{dr})\right) + p \cdot \left(L_{ls} \cdot i_{qs} + L_M \cdot (i_{qs} + i'_{qr})\right)\\
&\downarrow\\
u_{qs} &= R_s \cdot i_{qs} + \omega_{rf} \cdot \left(L_s \cdot i_{ds} + L_M \cdot i'_{dr}\right) + p \cdot \left(L_s \cdot i_{qs} + L_M \cdot i'_{qr}\right) && (7.56)
\end{aligned}
$$

$$
\begin{aligned}
u_{ds} &= R_s \cdot i_{ds} - \omega_{rf} \cdot \left(L_{ls} \cdot i_{qs} + L_M \cdot (i_{qs} + i'_{qr})\right) + p \cdot \left(L_{ls} \cdot i_{ds} + L_M \cdot (i_{ds} + i'_{dr})\right)\\
&\downarrow\\
u_{ds} &= R_s \cdot i_{ds} - \omega_{rf} \cdot \left(L_s \cdot i_{qs} + L_M \cdot i'_{qr}\right) + p \cdot \left(L_s \cdot i_{ds} + L_M \cdot i'_{dr}\right) && (7.57)
\end{aligned}
$$

Where:

$$
L_s = L_{ls} + L_M \qquad (7.58)
$$

The rotor currents are isolated in equation (7.54) and (7.55):

$$
\begin{aligned}
\lambda'_{qr} &= L'_{lr} \cdot i'_{qr} + L_M \cdot (i_{qs} + i'_{qr})\\
&\downarrow\\
\lambda'_{qr} &= L'_r \cdot i'_{qr} + L_M \cdot i_{qs}\\
&\downarrow\\
i'_{qr} &= \frac{\lambda'_{qr} - L_M \cdot i_{qs}}{L'_r} && (7.59)
\end{aligned}
$$

$$\begin{aligned}
\lambda'_{dr} &= L'_{lr} \cdot i'_{dr} + L_M \cdot (i_{ds} + i'_{dr}) \\
&\downarrow \\
\lambda'_{dr} &= L'_r \cdot i'_{dr} + L_M \cdot i_{ds} \\
&\downarrow \\
i'_{dr} &= \frac{\lambda'_{dr} - L_M \cdot i_{ds}}{L'_r}
\end{aligned} \tag{7.60}$$

Where:

$$L'_r = L'_{lr} + L_M \tag{7.61}$$

The rotor currents can now be inserted in the stator voltage equations:

$$\begin{aligned}
u_{qs} &= R_s \cdot i_{qs} + \omega_{rf} \cdot \left(L_s \cdot i_{ds} + L_M \cdot \left(\frac{\lambda'_{dr} - L_M \cdot i_{ds}}{L'_r} \right) \right) \\
&\quad + p \cdot \left(L_s \cdot i_{qs} + L_M \cdot \left(\frac{\lambda'_{qr} - L_M \cdot i_{qs}}{L'_r} \right) \right) \\
&\downarrow \\
u_{qs} &= \left(R_s + p \left(L_s - \frac{L_M^2}{L'_r} \right) \right) \cdot i_{qs} + \omega_{rf} \cdot \left(L_s - \frac{L_M^2}{L'_r} \right) \cdot i_{ds} \\
&\quad + \omega_{rf} \cdot \frac{L_M}{L'_r} \cdot \lambda'_{dr} + \omega_{rf} \cdot \frac{L_M}{L'_r} \cdot \lambda'_{qr}
\end{aligned} \tag{7.62}$$

$$\begin{aligned}
u_{ds} &= R_s \cdot i_{ds} - \omega_{rf} \cdot \left(L_s \cdot i_{qs} + L_M \left(\frac{\lambda'_{qr} - L_M \cdot i_{qs}}{L'_r} \right) \right) \\
&\quad + p \cdot \left(L_s \cdot i_{ds} + L_M \cdot \left(\frac{\lambda'_{dr} - L_M \cdot i_{ds}}{L'_r} \right) \right) \\
&\downarrow \\
u_{ds} &= \left(R_s + p \left(L_s - \frac{L_M^2}{L'_r} \right) \right) \cdot i_{ds} - \omega_{rf} \cdot \left(L_s - \frac{L_M^2}{L'_r} \right) \cdot i_{qs} \\
&\quad + p \cdot \frac{L_M}{L'_r} \cdot \lambda'_{dr} - \omega_{rf} \cdot \frac{L_M}{L'_r} \cdot \lambda'_{qr}
\end{aligned} \tag{7.63}$$

According to section 7.1 $\lambda'_{qr} = 0$. The voltage equations both consist of three parts (when $\lambda'_{qr} = 0$). In the q-axis voltage equation the first part is a first order transfer function describing the dynamics between u_{ds} and i_{ds}. The second part is the coupling between q-axis voltage and d-axis current. The third part contains the rotor flux in the d-direction and the flux velocity. The rotor flux in the d-direction has a large time constant compared to i_{ds}, this is shown in the proceeding.

The rotor flux in the d-direction (λ'_{dr}) is expressed as function of i_{ds} using equation (7.50) and (7.60):

$$\begin{aligned} u'_{dr} &= R'_r \cdot i'_{dr} - (\omega_{rf} - \omega_r) \cdot \lambda'_{qr} + p \cdot \lambda'_{dr} \\ &\downarrow \\ 0 &= R'_r \cdot i'_{dr} + p \cdot \lambda'_{dr} \\ &\downarrow \\ i'_{dr} &= \frac{-p \cdot \lambda'_{dr}}{R'_r} \end{aligned} \tag{7.64}$$

$$\begin{aligned} \lambda'_{dr} &= L_r \cdot i'_{dr} + L_M \cdot i_{ds} \\ &\downarrow \\ \lambda'_{dr} &= -L_r \frac{p \cdot \lambda'_{dr}}{R'_r} + L_M \cdot i_{ds} \\ &\downarrow \\ \lambda'_{dr} &= \frac{L_M}{1 + \frac{L'_r}{R'_r} \cdot p} \cdot i_{ds} \end{aligned} \tag{7.65}$$

The time constant for i_{ds} is seen in the first order system (first part of the q-axis voltage equation) as $\left(L_s - \frac{L_M^2}{L'_r}\right) \cdot \frac{1}{R_s}$. The time constants for the current and the flux are calculated as $\tau_i = \left(L_s - \frac{L_M^2}{L'_r}\right) \cdot \frac{1}{R_s}$=0.02 s and $\tau_\lambda = \frac{L'_r}{R'_r}$=0.20 s respectively. Since τ_λ is 10 times larger than τ_i the d-axis current can change much faster than the rotor flux in the d-direction.
The velocity of the rotor flux (ω_{rf}) is approximately the same as the electrical mechanical velocity of the rotor shaft (ω_r) as the slip usually is low (<5%) [Sen, 1997, p. 225]. The mechanical velocity of the rotor shaft also has a high time constant compared to i_{ds}. This is seen from the general transfer function for the mechanical system:

$$\begin{aligned} J \cdot \dot{\omega}_m &= \tau_{shaft} - B \cdot \omega - \tau_{static} \\ &\downarrow \\ \tau_{shaft} &= \omega_m \cdot (B + J \cdot \cdot s) \\ &\downarrow \\ \omega_m &= \frac{1/B}{1 + J/B \cdot s} \cdot \tau_{shaft} \end{aligned} \tag{7.66}$$

where:

	τ_{shaft}	Torque applied on rotor shaft $[Nm]$
	J	Moment of inertia $[kg \cdot m^2]$
	B	Damping $[Nm \cdot s/rad]$
	τ_{static}	Static friction $[Nm]$

The moment of inertia is calculated in section 6.4. As seen in section 6.4 the induction machine does not have a dynamic friction proportional to velocity and the damping B is therefore not determined. Using a linear fitting between the two points in the friction curve that provide the largest damping, the damping is estimated to $0.07 Nm \cdot s/rad$. The mechanical time constant can now be estimated as 0.4 s. The mechanical time constant is hereby 20 times higher than the electrical. The third part in the q-axis voltage equation may hereby be considered as a reject able disturbance to the first order system as the time constants of the mechanical system and the rotor flux are much higher than the time constant for the electrical system. The third part of the q-axis voltage equation is hereby neglected.

The third part of the d-axis voltage equation is proportional to the change in rotor flux. In the induction machine the rotor flux is to be changed in order to obtain energy efficient control. Depending on how the rotor flux is changed the third part of d-axis voltage equation results in a disturbance for the current control. For now the part is neglected. The effect of the change in rotor flux is evaluated in chapter 12.

The remaining parts of the voltage equations are seen in equation (7.67) and (7.68). The equations now consist of a first order system and a cross coupling.

$$u_{qs} = \left(R_s + p \cdot \left(L_s - \frac{L_M^2}{L_r'}\right)\right) \cdot i_{qs} + \omega_{rf} \cdot \left(L_s - \frac{L_M^2}{L_r'}\right) \cdot i_{ds} \tag{7.67}$$

$$u_{ds} = \left(R_s + p \cdot \left(L_s - \frac{L_M^2}{L_r'}\right)\right) \cdot i_{ds} - \omega_{rf} \cdot \left(L_s - \frac{L_M^2}{L_r'}\right) \cdot i_{qs} \tag{7.68}$$

The cross couplings in the voltage equations are proportional to the frequency of the rotor flux. The cross coupling is therefore more pronounced at high rotor velocities. When varying the ro-

tor flux in order to obtain energy efficient control the cross coupling becomes more pronounced. This might cause an undesirable torque response. In order to develop controllers for the currents the cross couplings are for now considered as reject able disturbances. Later in this section a feed forward compensation is considered in order to accommodate the cross couplings. When neglecting the cross couplings the voltage equations only consist of first order systems as seen in equation (7.69) and (7.70).

$$\begin{aligned} u_{qs} &= \left(R_s + p \cdot \left(L_s - \frac{L_M^2}{L_r'}\right)\right) \cdot i_{qs} \\ &\downarrow \\ G_q &= \frac{i_{qs}}{u_{qs}} = \frac{{}^1/_{R_s}}{1 + p \cdot \left(L_s - \frac{L_M^2}{L_r'}\right) \cdot \frac{1}{R_s}} \end{aligned} \tag{7.69}$$

$$\begin{aligned} u_{ds} &= \left(R_s + p \cdot \left(L_s - \frac{L_M^2}{L_r'}\right)\right) \cdot i_{ds} \\ &\downarrow \\ G_d &= \frac{i_{ds}}{u_{ds}} = \frac{{}^1/_{R_s}}{1 + p \cdot \left(L_s - \frac{L_M^2}{L_r'}\right) \cdot \frac{1}{R_s}} \end{aligned} \tag{7.70}$$

where: G_q Transfer function for i_{qs} $[-]$

G_d Transfer function for i_{ds} $[-]$

The two first order systems are identical and the current controllers for each of the currents are therefore also identical.

The time constant for the first order systems is rewritten as in equation (7.71)

$$\begin{aligned} \tau_i &= \left(L_s - \frac{L_M^2}{L_r'}\right) \cdot \frac{1}{R_s} \\ &\downarrow \\ \tau_i &= \left(L_M + L_{ls} - \frac{L_M^2}{L_M + L_{lr}'}\right) \cdot \frac{1}{R_s} \\ &\downarrow \\ \tau_i &= \frac{L_{lr}' + L_{ls}}{R_s} - \frac{L_{lr}'^2}{(L_M + L_{lr}') \cdot R_s} \end{aligned} \tag{7.71}$$

Since $\frac{L_{lr}' + L_{ls}}{R_s} \gg \frac{L_{lr}'^2}{(L_M + L_{lr}') \cdot R_s}$ $(1.9 \cdot 10^{-2} \gg 0.05 \cdot 10^{-2})$ the second part of the time constant $\left(\frac{L_{lr}'^2}{(L_M + L_{lr}') \cdot R_s}\right)$ can be neglected. The time constant may therefore be considered as a function of the leakage inductances and the stator resistance.

The controllers used for the currents are PI controllers. A PI controller eliminates steady state errors in the current resulting in the current reaching the desired reference. The PI controller consists of a proportional part and an integrator part as seen in equation (7.72).

$$G_c = k_p + \frac{k_i}{s} \tag{7.72}$$

where:	G_c	Transfer function for PI controller $[-]$
	k_p	Proportional gain $[-]$
	k_i	Integrator gain $[-]$

The cut-off frequency of the PI controller is determined by the relation between the integrator part and the proportional part ($\omega_{cut} = \frac{k_i}{k_p}$).
A PI controller is developed. The proportional part of the controller is $k_p = 0.006$ and the cut-off frequency is $\omega_{cut} = 150\ ^{rad}/_{s}$. The integrator part is hereby $k_i = 0.9$. This controller provides a bandwidth of 249 Hz for the closed loop system. In order to minimize the discretization effects of the controller the bandwidth should be <20 times the sampling frequency [Franklin et al., 1998, p. 453]. The controller fulfills this rule of thumb as the sampling frequency is 5000 Hz.
A root locus plot for the system $G_q \cdot G_c$ is seen in figure 7.7. A bode plot for the system is seen in figure 7.8.
As seen in the root locus the system has closed loop poles in $-107 \pm 112j$. The relative stability margins for the system are considered as acceptable as the phase never crosses -180° and the minimum margin from -180° is 62° as seen in the bode plot.
The closed loop step response for $G_q \cdot G_c$ without any cross couplings is seen in figure 7.9. The step has an overshoot of 13%.
As seen in equation (7.68) the cross couplings from the currents are proportional to the frequency of the reference frame. The cross coupling effect is therefore more pronounced at large rotor velocities. This is seen when stepping on i_{qs} at various velocities as in figure 7.10 or when stepping on i_{ds} at various velocities as in figure 7.11. The frequency dependent cross coupling is further considered in the *Feed Forward* section later in this chapter.

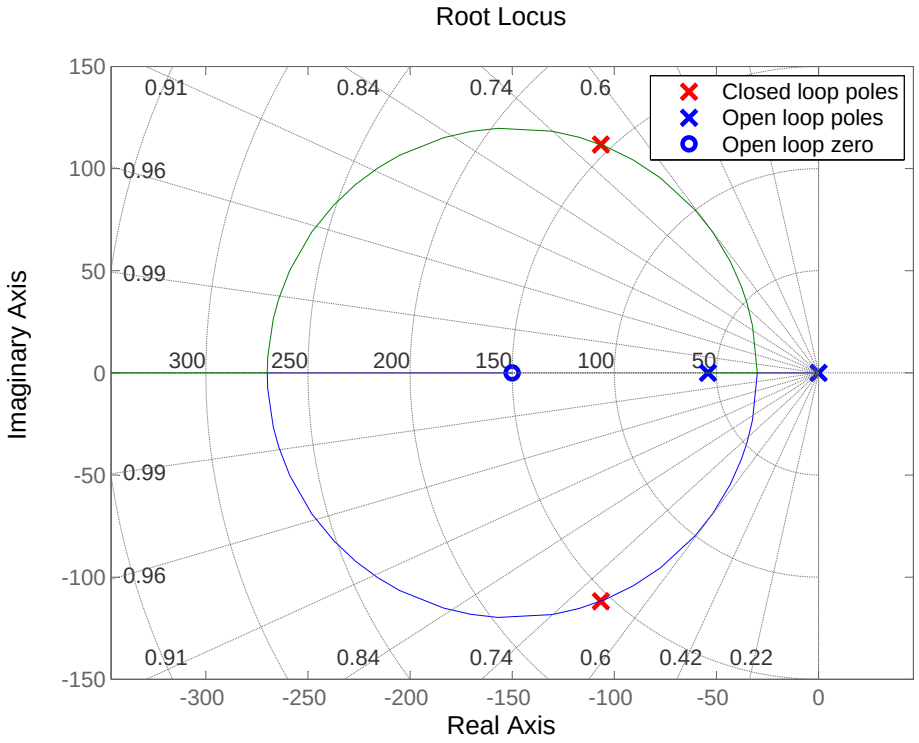

Figure 7.7: *Root locus for $G_q \cdot G_c$. The closed loop poles for the system are also shown in the figure.*

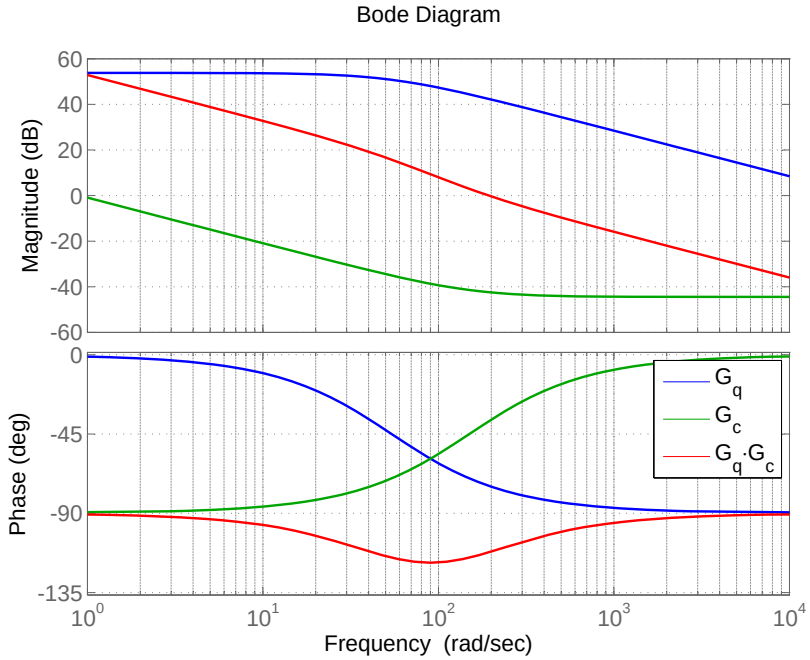

Figure 7.8: *Bode plot for the first order system (G_q), the controller (G_c) and the open loop system $G_q \cdot G_c$.*

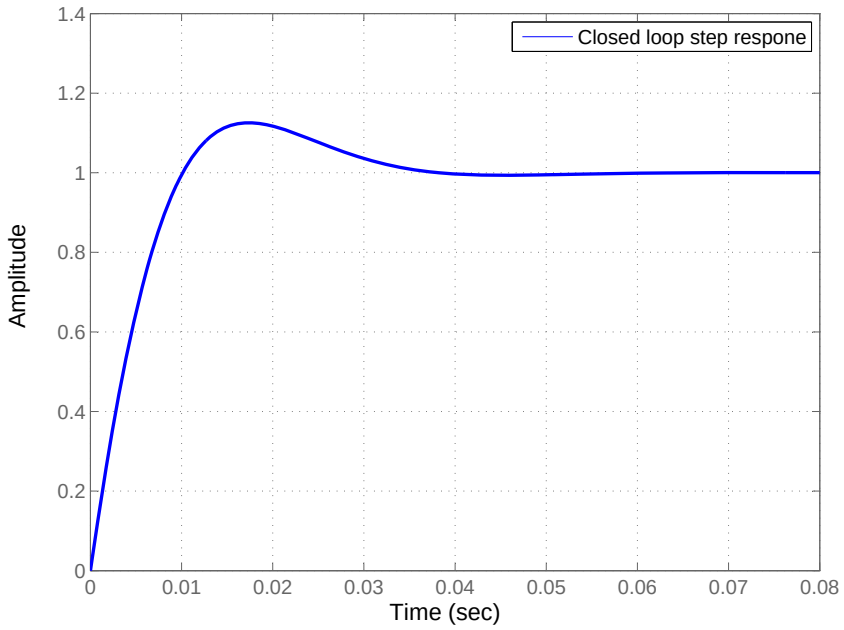

Figure 7.9: *Step response of closed loop system without any cross couplings.*

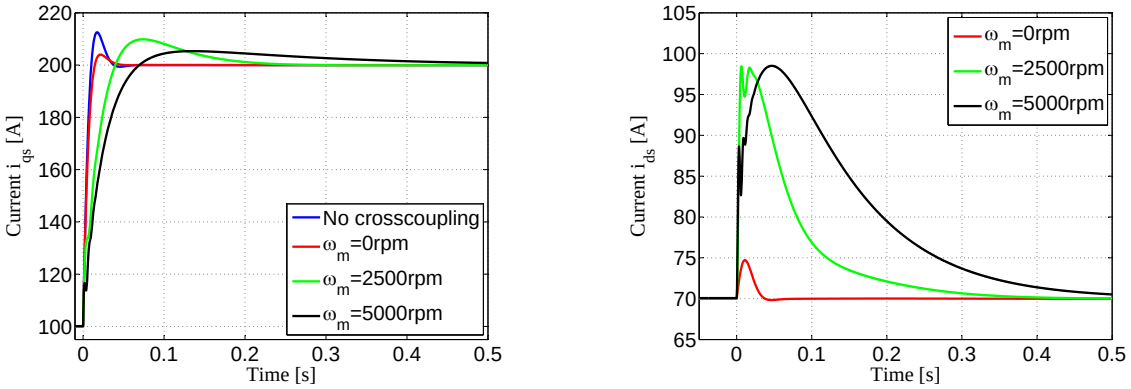

(a) *i_{qs} step response at various velocities.*

(b) *i_{ds} response, when stepping on i_{qs}, at various velocities.*

Figure 7.10: *Current step response at various velocities when stepping on i_{qs} from 100 A to 200 A. i_{ds} is set to 70 A.*

When implementing the controllers in the test setup discretization effects must be considered. The sampling frequency of the DSP is 5000 Hz. When evaluating the discretization effects the first order system is first transformed to the discrete domain by utilizing zero order hold (ZOH). The controller is transformed utilizing a bilinear transformation (Tustin). When in the discrete plane a delay of one sampling period is added to the system. This delay accounts for

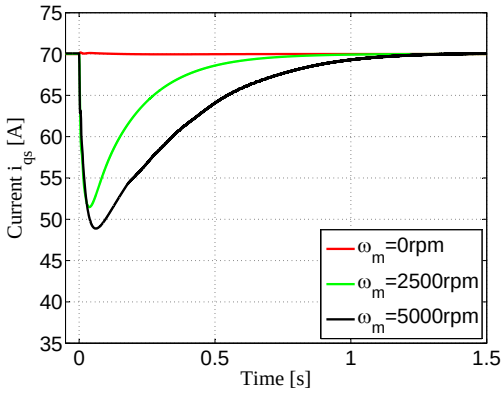

(a) *i_{qs} response, when stepping on i_{ds}, at various velocities.*

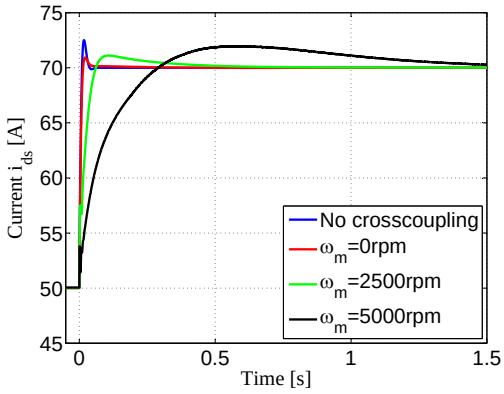

(b) *i_{ds} step response at various velocities.*

Figure 7.11: *Current step response at various velocities when stepping on i_{ds} from 50 A to 70 A. i_{qs} is set to 70 A.*

measurement delays.

The discrete system consisting of the first order system, the controller and the delay is then transformed to the continuous *w*-plane. The *w*-plane allows the same development rules as the *s*-plane.

When transforming the system to the *w*-plane the root locus for the system changes from the original root locus in the *s*-plane, figure 7.7. The open loop system now has two zeros in 10000 (two times the sampling frequency) and one pole in -10000 and of course the original zeros and poles seen in figure 7.7. The root locus for the system in the *w*-plane is seen in figure 7.12. The system also contains another closed loop pole placed in -9370.

The poles and zeros added due to discretization are much faster than the poles and zeros in the original system and has therefore negligible influence on the system performance. The bode plot for the system in the *w*-plane is seen in figure 7.13. The maximum frequency of the induction machine, which according to the datasheet is 169 Hz, is also marked in the bode plot.

As the relative stability margins for the system have not changed significantly at frequencies below the maximum frequency and the added poles and zeros due to discretization are much faster than the original poles and zeros the discretization effects are considered as negligible.

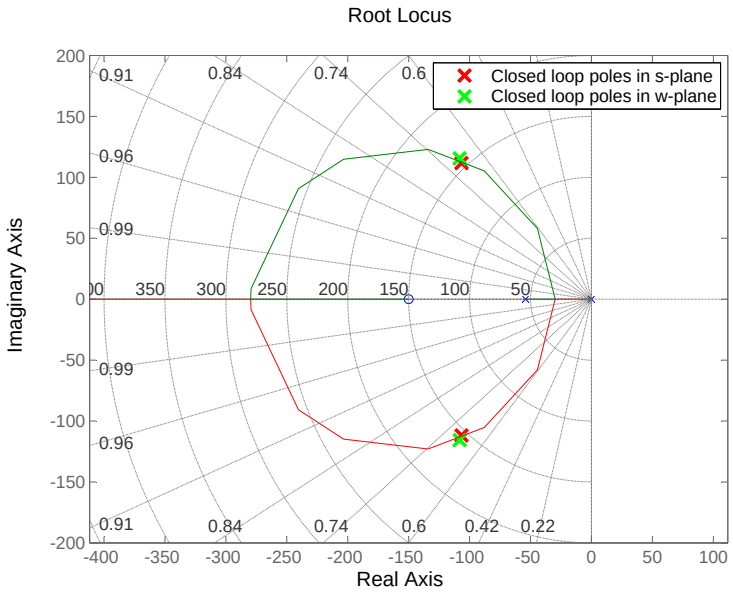

Figure 7.12: *Root locus of the system in the w-plane.*

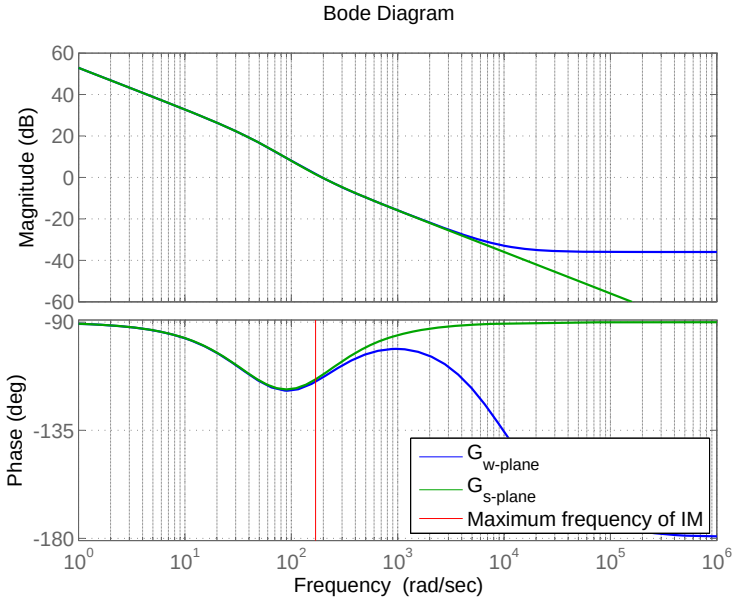

Figure 7.13: *Bode plot of the system in the w-plane compared to the original s-plane.*

Verification of Current Controllers

In order to verify the current controllers the controllers are implemented in the test setup. The flux estimator used is a standard indirect estimator without any improvements as described in section 7.2.1. Various current steps are applied in the test setup and the results are presented in the following. The procedure for the experiments are described in appendix F.8.

In figure 7.14 the q- and d-axis current responses are seen when stepping on the q-axis current from 100 A to 200 A. The d-axis current is set to 70 A throughout this step. The velocity of the rotor is 1000 rpm. In figure 7.15 a similar current step is applied at a velocity of 2500 rpm.
In figure 7.16 the q- and d-axis current responses are seen when stepping on the d-axis current from 50 A to 70 A. The q-axis current is set to 70 A throughout this step. The velocity of the rotor is 1000 rpm. In figure 7.15 a similar current step is applied at a velocity of 2500 rpm. Voltage saturation does not occur during any of the verification experiments.

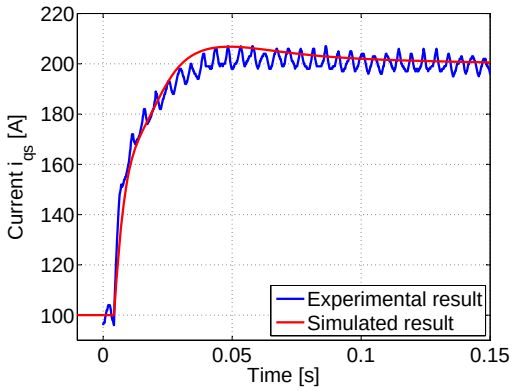

(a) *i_{qs} current response at i_{qs} current step. The rotor velocity is 1000 rpm.*

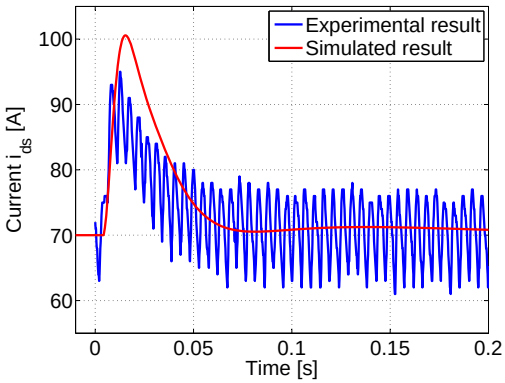

(b) *i_{ds} current response at i_{qs} current step. The rotor velocity is 1000 rpm.*

Figure 7.14: *Current step response at a step on i_{qs} current from 100 A to 200 A. i_{ds} is set to 70 A and the rotor velocity is 1000 rpm.*

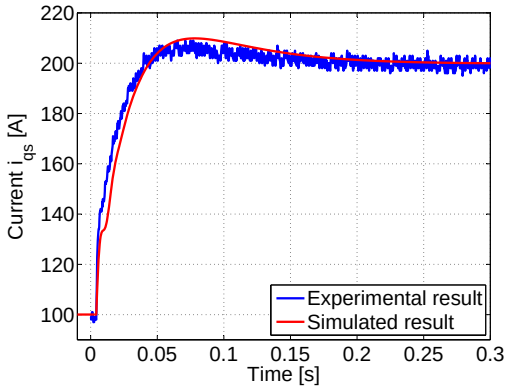

(a) *i_{qs} current response at i_{qs} current step. The rotor velocity is 2500 rpm.*

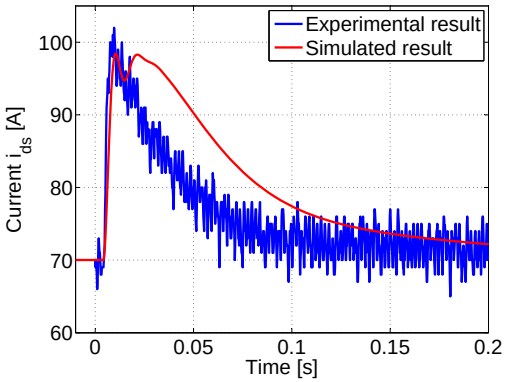

(b) *i_{ds} current response at i_{qs} current step. The rotor velocity is 2500 rpm.*

Figure 7.15: *Current step response at a step on i_{qs} current from 100 A to 200 A. i_{ds} is set to 70 A and the rotor velocity is 2500 rpm.*

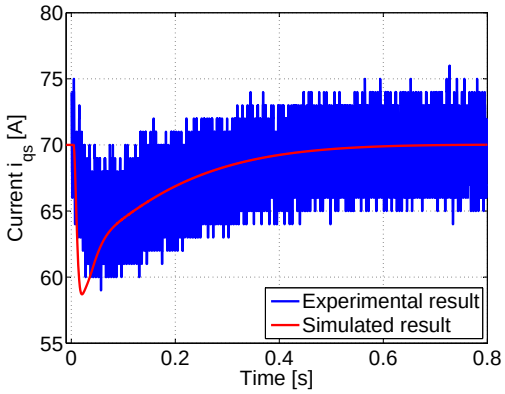

(a) *i_{qs} current response at i_{ds} current step. The rotor velocity is 1000 rpm.*

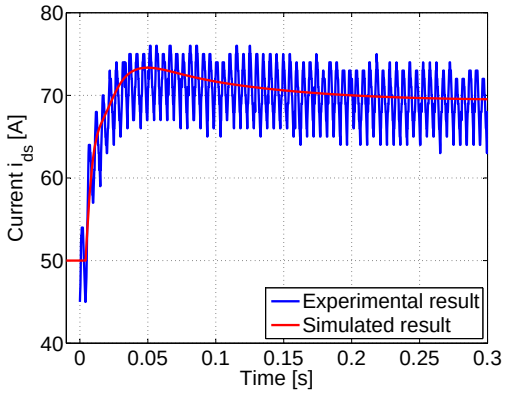

(b) *i_{ds} current response at i_{ds} current step. The rotor velocity is 1000 rpm..*

Figure 7.16: *Current step response at a step on i_{ds} current from 50A to 70A. i_{qs} is set to 70A and the rotor velocity is 1000rpm.*

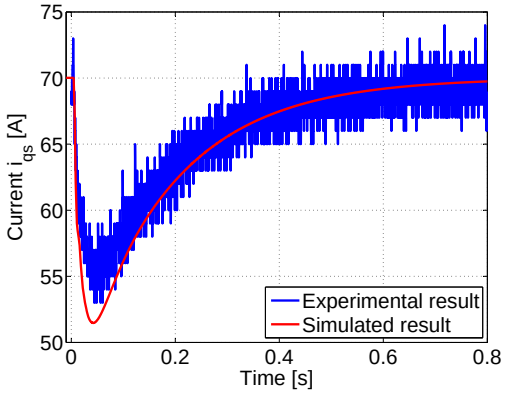

(a) *i_{qs} current response at i_{ds} current step. The rotor velocity is 2500 rpm.*

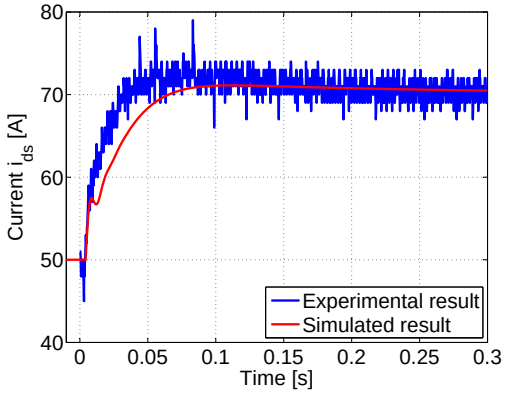

(b) *i_{ds} current response at i_{ds} current step. The rotor velocity is 2500 rpm.*

Figure 7.17: *Current step response at a step on i_{ds} current from 50 A to 70 A. i_{qs} is set to 70 A and the rotor velocity is 2500 rpm.*

The experimental results in all the current steps seem to contain a current ripple. The ripple is most likely caused by dead zones in the inverter. Dead zones are the most significant non linearity of the inverter [Sepe and Lang, 1994]. The dead zone occurs when any of the phase currents crosses zero. The dead zones cause a ripple in the q- and d axis currents with a frequency of six times the fundamental frequency. There can be implemented compensations in the control which reduces the effect of the dead zones. In order to evaluate the consequence of the current ripple the resulting torque ripple is estimated. This is done utilizing equation (7.21) for the torque. The rotor flux, λ_{dr}, is calculated from equation (7.37) and the d-axis current from the experimental result. The rotor flux is then inserted in the torque equation along with

the q-axis current from the experimental result. The rotor flux λ_{dr} is much slower to build up than the i_{ds} current. Because of this the i_{ds} current ripple will not affect the torque in the same manner as the i_{qs} current ripple. But as it is seen that it is the i_{ds} current that has the biggest ripples a worst case example is used. The torque ripple may now be estimated. The largest torque ripple for all the experiments is in the d-axis current step at 1000 rpm, figure 7.16. The torque ripple in this experiment is estimated to $\pm 0.3Nm$. The ripple seems to increase when the velocity decreases. The torque ripple may have an effect on the lifetime of the mechanical elements in the powertrain and also on the driving comfort of the electrical vehicle. The current ripple may also cause the efficiency of the electric vehicle to decrease compared to what may be estimated in the simulation model during driving cycles in chapter 12.

Despite the current ripple the general characteristics of the simulation seems to be reasonable compared to the experimental results. The simulated q-axis currents seems to follow the experimental results better than the d-axis currents, especially at 2500 rpm.
The cross coupling effect is more distinct at high velocity in the experimental results as expected.
Due to general similarity between the experiments and the simulations, the simulation results are considered as valid estimations of the actual system.

Parameter Variation

When evaluating the performance and stability of the system it is important to consider parameter variation. The first order system in equation (7.69) is dependent on stator resistance, R_s, magnetizing inductance, L_M, and leakage inductances, L'_{lr} and L_{ls}. When i_{ds} is increased the magnetizing inductance may decrease due to saturation of the flux. This phenomena is further described in section 7.3.3. As described earlier in this section the time constant for the first order system may however be simplified so that it no longer is dependent on the magnetizing inductance. The simplified first order system for the q-axis current is seen in equation (7.73). Since the first order system is not dependent on the magnetizing inductance, changes due to saturation have no impact on the performance nor the stability of the system.

$$G_q = \frac{i_{qs}}{u_{qs}} = \frac{1/R_s}{1 + p \cdot \frac{L'_{lr}+L_{ls}}{R_s}} \tag{7.73}$$

The leakage inductances are assumed not to saturate since the leakage flux path mostly consist of air [de Mello and Walsh, 1961]. The leakage inductances do therefore not vary during oper-

ation.

The stator resistance may vary due to temperature variations during operation. If the temperature of the induction machine is low the stator resistance decreases and when the temperature of the induction machine increases so does the stator resistance. A high resistance provides a larger pole for the first order system and a low resistance provides a smaller pole. In order to evaluate the variations in performance and stability during operation two operation points are considered.

The first operation condition is a temperature of -10$^{\circ}C$ which can be obtained when starting the electric vehicle on a winter morning. The second operation temperature is 155$^{\circ}C$ which is the maximum continuous temperature allowed according to the datasheet for the induction machine. Utilizing equation (7.104) which describes the relation between stator temperature and stator resistance, the stator resistance can be estimated at each of the conditions.

The bode plot for the system at each of the conditions are seen in figure 7.18. The response at ambient temperature (22$^{\circ}C$) is also seen in the figure. As seen in the bode plot the minimum phase is slightly decreased at low temperature. The stability margin is however still acceptable. As the open loop pole of the first order system varies according to the temperature so does the closed loop poles. This is seen in figure 7.19. In this figure the root locus for the system at ambient temperature is seen. The closed loop poles for the system at the various operation conditions are also depicted. As seen in the figure the open loop pole for the first order system at 155$^{\circ}C$ is higher than at ambient temperature. This results in a slight change in the complex closed loop poles which results in a change in performance as seen later in this section. The system of course has a pole in zero at all temperatures due to the integrator in the PI controller.

In order to evaluate the effect of parameter variation in system performance the step response at the two operation conditions are investigated. The step responses are depicted in figure 7.20. As seen in the figure the overshoot at high temperature is slightly decreased and the settling time is slightly increased.

Since the parameter variation has insignificant effect on the stability margins and the performance of the controllers, the controllers are considered as being robust against parameter variations.

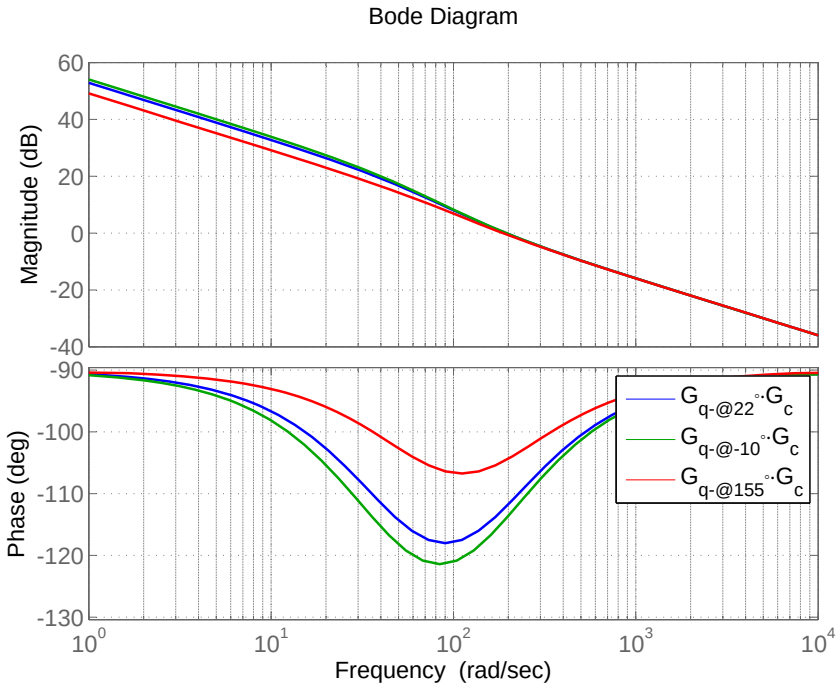

Figure 7.18: *Bode plot for open loop system at various operation conditions.*

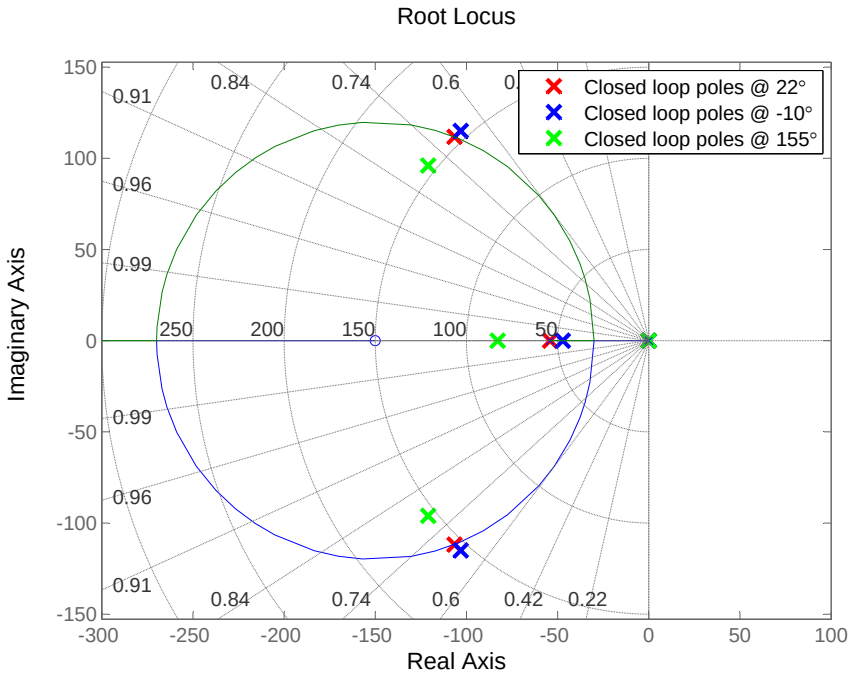

Figure 7.19: *Root locus for system at ambient temperature (22°C). The closed loop poles at temperatures -10°C and 155°C are also seen.*

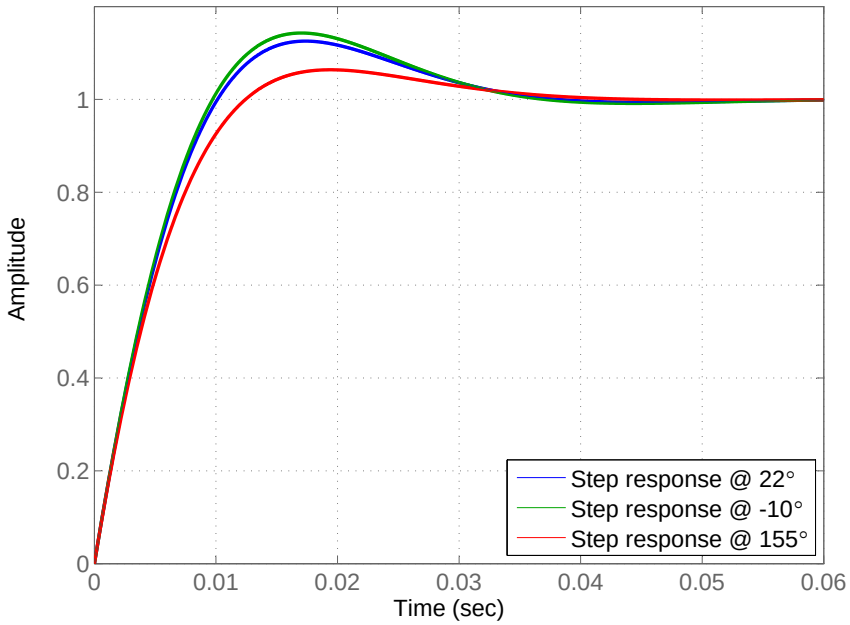

Figure 7.20: *Step response at various operation conditions.*

As seen in the step responses in figure 7.14, 7.15, 7.16 and 7.17 the cross couplings seem to have significant influence on the step response at high velocities as expected when developing the controllers. In order to obtain a better transient current response it is desirable to develop a feed forward compensation for the current control. The feed forward compensation is presented in the following.

Feed Forward Compensation

As described in the preceding the transient current response may be improved by implementing a feed forward compensation. The feed forward compensation is supposed to decrease the cross coupling effect between the q- and d-axis currents. The cross coupling is seen in equation (7.68) and (7.67). For convenience these equations are repeated in equation (7.74) and (7.75).

$$u_{qs} = \left(R_s + p \cdot \left(L_s - \frac{L_M^2}{L_r'}\right)\right) \cdot i_{qs} + \omega_{rf} \cdot \left(L_s - \frac{L_M^2}{L_r'}\right) \cdot i_{ds} \tag{7.74}$$

$$u_{ds} = \left(R_s + p \cdot \left(L_s - \frac{L_M^2}{L_r'}\right)\right) \cdot i_{ds} - \omega_{rf} \cdot \left(L_s - \frac{L_M^2}{L_r'}\right) \cdot i_{qs} \tag{7.75}$$

From the equations the ideal feed forward compensation for the cross coupling between the currents are illustrated as in figure 7.21.

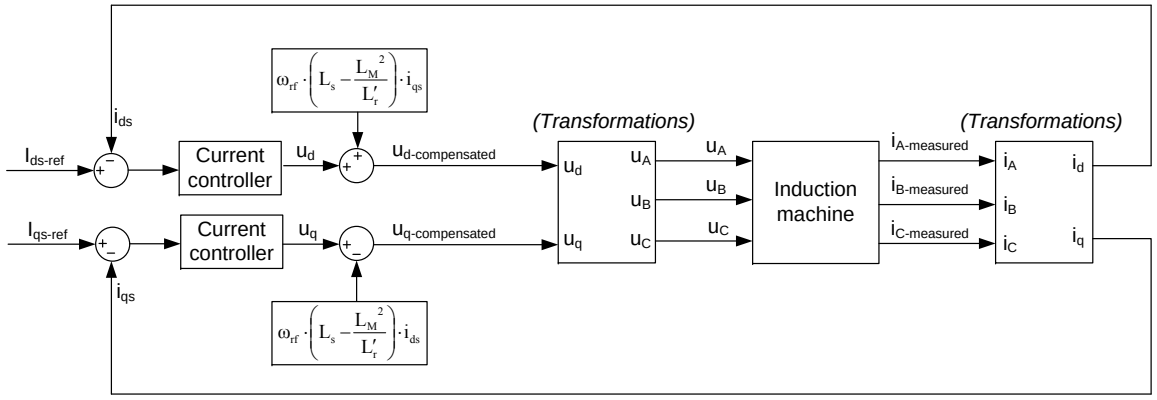

Figure 7.21: *Ideal feed forward compensation for the current control.*

The frequency of the rotor flux, ω_{rf}, may be estimated using the indirect or the direct flux estimator. The current inputs for the compensators may be calculated from the current references. This feed forward compensation strategy is illustrated in figure 7.22. The compensation strategy is only illustrated for the *q*-axis current control but is of course also to be implemented in the *d*-axis current control.

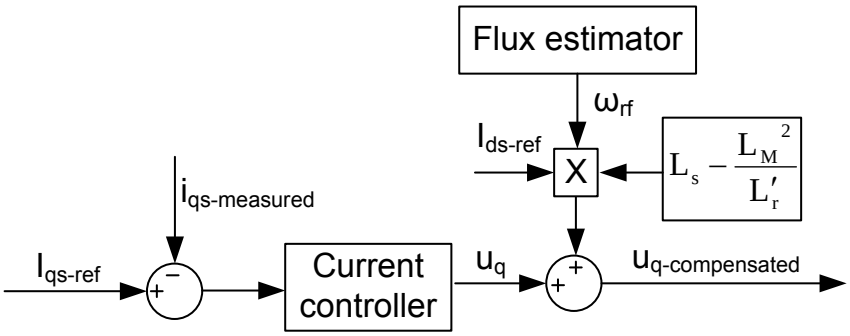

Figure 7.22: *Feed forward compensation strategy for q-axis current using reference current as input to compensator.*

Using reference currents as inputs to the compensators causes the compensation voltage to change instantaneously when applying steps in the current references. This causes the currents to contain unwanted overshoots. This is seen in figure 7.23. In this figure the step response for the system with and without compensation is illustrated. The step is performed on i_{qs} from 100 A to 200 A. i_{ds} is set to 70 A. The rotor velocity is 5000rpm.

As seen in figure 7.23 the currents contain large overshoots when utilizing the compensation strategy illustrated in figure 7.22. It is therefore desirable to improve the compensation strategy in order to decrease the overshoots. This is done by filtering the current references. The filtering is intended to estimate the transient current better when changing the current references. The filter should have the same characteristics as the actual current when performing changes in the

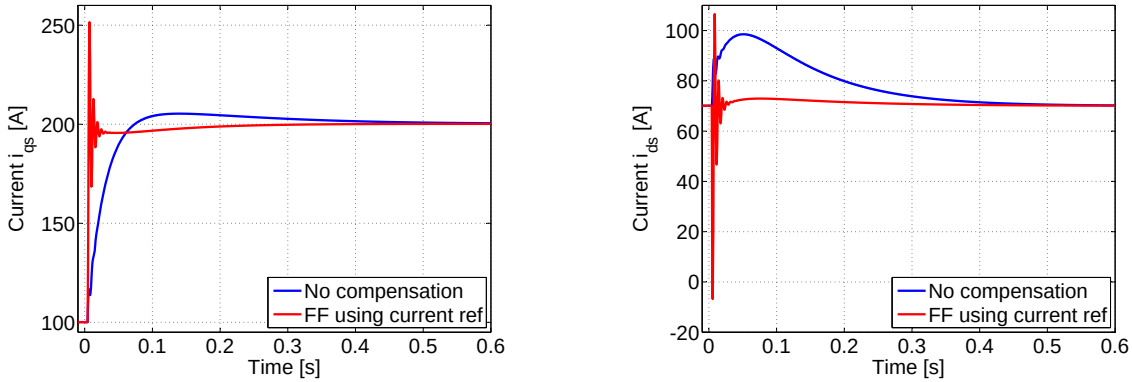

(a) *i_{qs} current response.* ***(b)*** *i_{ds} current response.*

Figure 7.23: *Current step response at a step on i_{qs} current from 100 A to 200 A when using no compensation and when using the feed forward compensation (FF) strategy illustrated in figure 7.22. i_{ds} is set to 70 A and the rotor velocity is 5000rpm.*

current references. A suggestion for the filter is a first order system with the same time constant as the current $\left(\tau = \left(L_s - \frac{L_M^2}{L_r'}\right) \cdot \frac{1}{R_s}\right)$. This feed forward strategy is illustrated in figure 7.24.

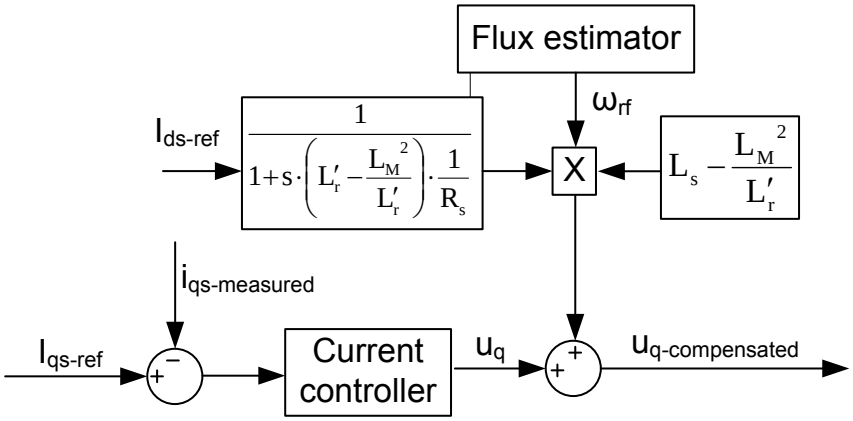

Figure 7.24: *Feed forward compensation strategy for q-axis current using filtered reference current as input to compensator.*

When implementing the improved feed forward compensation the overshoot in the step response is greatly reduced as seen in figure 7.25. As seen when comparing to the system response at 0 rpm the cross couplings are not completely removed. The performance of the compensated system is however better than the non-compensated system as the settling time is greatly reduced. When stepping on the d-axis current the performance is not enhanced when using feed forward. This is seen in figure 7.26. This may be due to the third part of the complete d-axis voltage equation (see equation (7.63)). This part was neglected in order to simplify the voltage equations however when stepping on the d-axis current the change in rotor flux may cause the third part

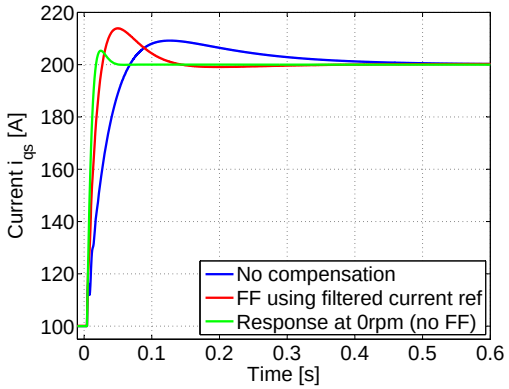

(a) *i_{qs} current response at i_{qs} current step from 100 A to 200 A. The rotor velocity is 5000 rpm and i_{ds} is set to 70 A. The system response at 0 rpm is also plotted.*

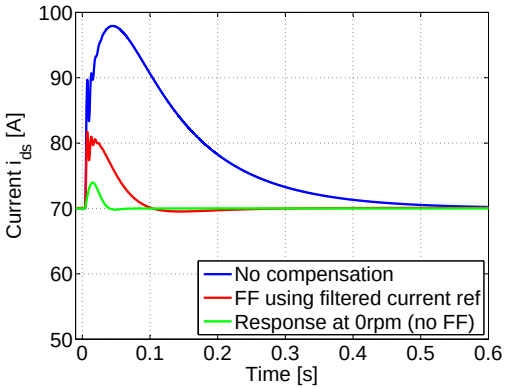

(b) *i_{ds} current response at i_{qs} current step from 100 A to 200 A. The rotor velocity is 5000 rpm and i_{ds} is set to 70 A. The system response at 0 rpm is also plotted.*

Figure 7.25: *Current step response at a step on i_{qs} current from 100 A to 200 A when using no compensation and when using the feed forward compensation (FF) strategy illustrated in figure 7.24. i_{ds} is set to 70 A and the rotor velocity is 5000 rpm.*

of the voltage equation to be significant for the system response.

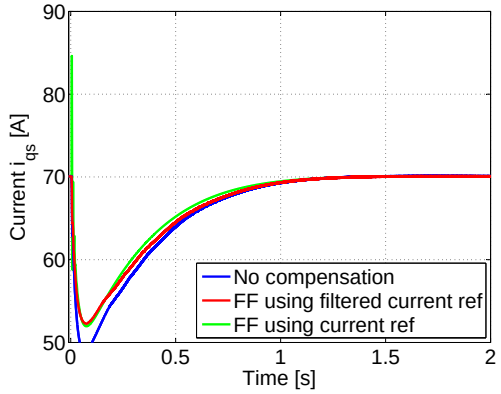

(a) *i_{qs} current response.*

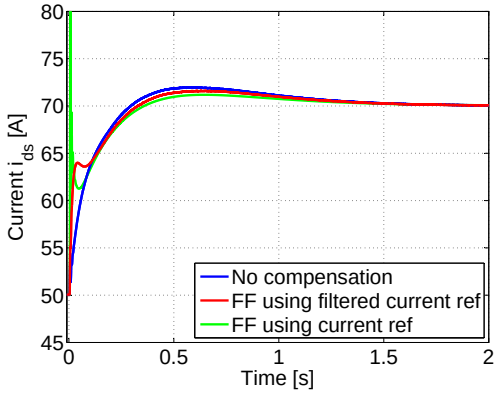

(b) *i_{ds} current response.*

Figure 7.26: *Current step response at a step on i_{ds} current from 50 A to 70 A when using no compensation and when using the compensation strategies illustrated in figure 7.22 and 7.24. i_{qs} is set to 70 A and the rotor velocity is 5000 rpm.*

The feed forward compensation might be expanded in order obtain better response when stepping on the *d*-axis current but this is not investigated.

Since the transient response when stepping on the *q*-axis current is enhanced when using the feed forward compensation illustrated in figure 7.24 the compensation is considered as a profitable addition to the current control for the electric vehicle. The compensation is not imple-

mented in the test setup however it is implemented in the simulation model when testing energy efficient control strategies in chapter 12.

Anti Wind-up

The outputs of the current controllers are voltages that are to be modeled by PWM in the inverter. If the output of the current controllers exceed the available DC-bus voltage the inverter saturates and the controller output will no longer correspond to the inverter output. In this case it is important that the integrator part of the controller does not "'wind-up"' the controller output. The input to the integrator part of the controller must therefore be set to zero. An illustration of the anti wind-up strategy implemented in the control is seen in figure 7.27. As seen in the figure the amplitude of the complex voltage vector from the current controllers is calculated and compared to saturation values. If the voltage is saturated the variable *sat* is set 1 and the input to the integrators is set to 0. Wind-up of the integrators is hereby prevented.

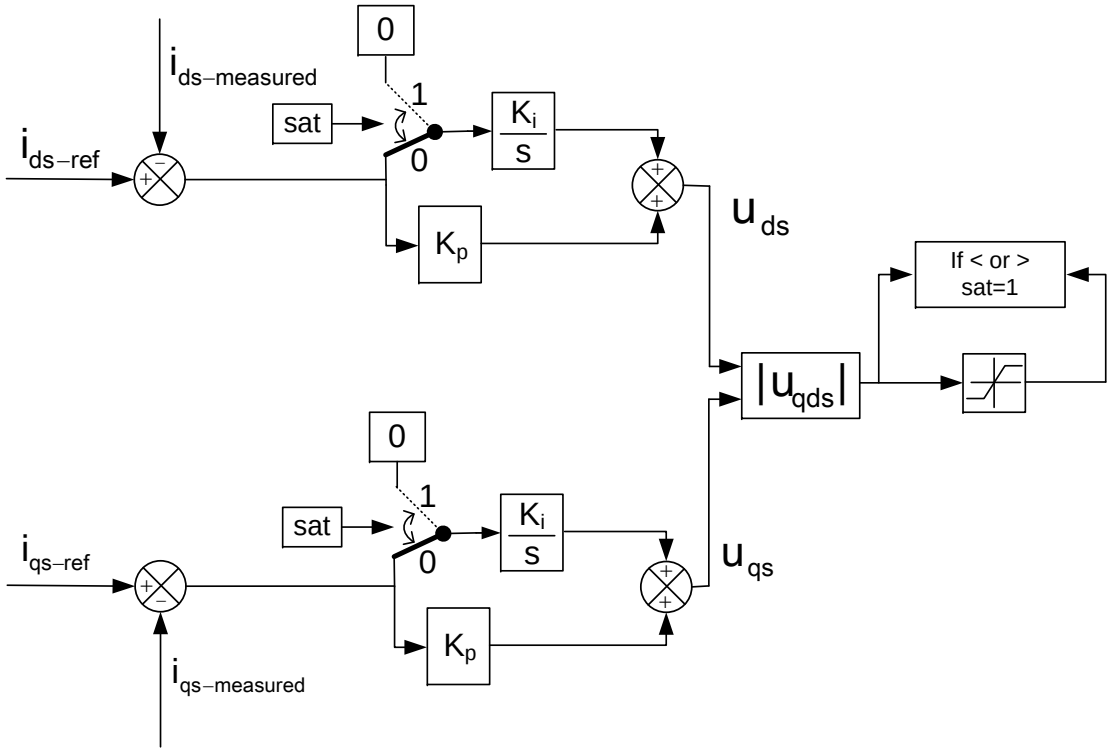

Figure 7.27: *Anti wind-up strategy.*

7.3.2 Development and Implementation of Direct Flux Estimator

In this section controllers for the direct flux estimator presented in section 7.2.2 is developed with regard to implementation considerations.

One of the problems encountered during the implementation of the direct flux estimator is that the current measurements contain bias due to noise and tolerances of the signal electronics and LEM current sensors. An experiment revealed a mean bias current of 0.57 A, but to add a safety margin this current is doubled in the simulations used to determine its effect.

The bias component of the current measurement i^s_{qds} enters both the current and voltage model. The bias current causes a sinusoidal angle error in the current model flux output. For a d-axis stator current of 90 A and a q-axis stator current of 305 A, the flux angle error of the current model has an initial amplitude 0.5 ° at a shaft velocity of 0 rpm. It decreases as the velocity is increased due to the first order system $\frac{L_M}{1+\tau_r \cdot s}$ filtering out the bias current.

The bias current entering the voltage model multiplied with the stator resistance enters the integrator causing the output to drift in the direction of the bias. The result is a flux angle error increasing with time. To avoid this the integrator is replaced with a first order system.

Equation (7.79) describes the output of an integrator. From this equation it is seen that if the frequency ω_{int} is small the integrator can be approximated by a first order system. The first order system is rewritten to its standard form and implemented into the flux estimator sub-component as seen in figure 7.28.

$$output = input \cdot \frac{1}{s} \tag{7.76}$$

$$\Downarrow$$

$$\frac{s}{s+\omega_{int}} \cdot output = input \cdot \frac{1}{s} \cdot \frac{s}{s+\omega_{int}} \tag{7.77}$$

$$\Downarrow$$

$$output - \frac{\omega_{int}}{s+\omega_{int}} \cdot output = input \cdot \frac{1}{s+\omega_{int}} \tag{7.78}$$

$$\Downarrow$$

$$output = input \cdot \frac{1}{s+\omega_{int}} + \frac{\omega_{int}}{s+\omega_{int}} \cdot output \tag{7.79}$$

where: ω_{int} Corner frequency of first order system $[rad/s]$

Choosing a proper size for the time constant is a matter of compromise. As mentioned earlier a small corner frequency is preferable in order to approximate a pure integration. This is especially the case for low frequency inputs. On the other hand to reduce the effect of the bias current it is preferable to have a low DC-gain τ_{int} making the corner frequency large.

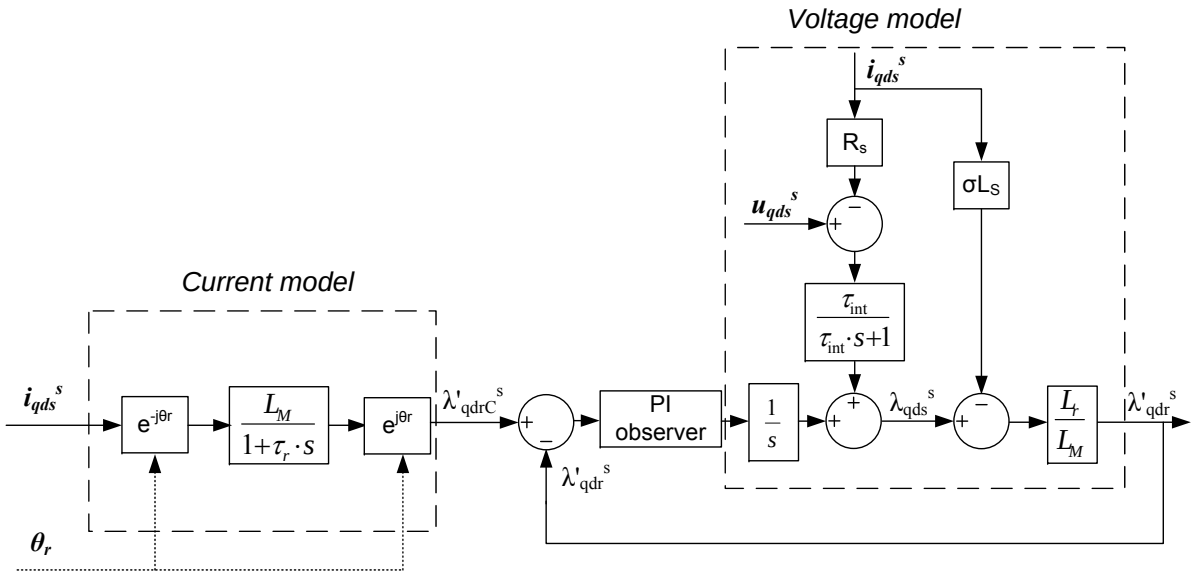

Figure 7.28: *Flux estimator sub-component with integrator replaced by first order system.*

To determine an appropriate characteristic for the first order system and the PI observer the parameter -and signal uncertainties must be taken into account. Due to technical difficulties the direct flux estimator is not implemented into the final solution. It was possible to use current model solely yielding results similar to the indirect flux estimator. Furthermore the voltage model provides reasonable results, but when combining the models something went wrong at low velocities. Figure 7.29 shows steady state IM torque levels at various shaft velocities. The q-axis stator current reference is set to 150 A and the d-axis stator current reference is set to 80 A corresponding to a torque reference of 10.9 Nm.

Some considerations regarding selecting appropriate constants for the PI observer and and low pass filter is done using ideal conditions. The closed loop transfer function for the flux estimator is derived using figure 7.28 and the voltage model flux gain (equation (7.81)). The result is seen in equation (7.84). From simulations it is seen that it is mainly the proportional part, $k_{p.obs}$, of the observer PI that inflicts the characteristic of the transition between the current -and voltage model. To simplify the analysis the integrator gain $k_{i.obs}$ is set to zero. Using this configuration the current gain $G_{current}$ is rewritten to form a first order system (equation (7.87)) and the voltage gain $G_{voltage}$ is rewritten to form the same first order system multiplied by $\frac{L_m}{L_r' \cdot K_{p.obs}} \cdot s$ (equation (7.89)).

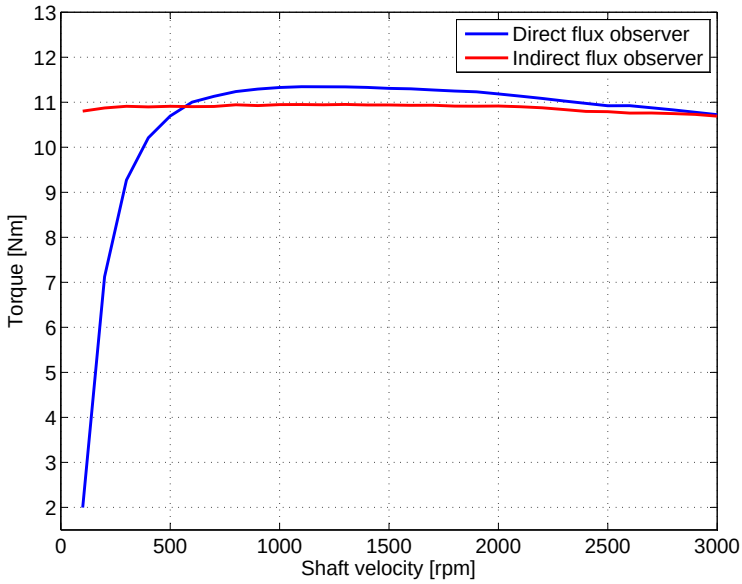

Figure 7.29: *Comparison of torque levels obtained using direct and indirect flux estimator.*

$$\lambda'^{s}_{qdr} = \frac{L'_r}{L_m} \cdot \left(-i^s_{qds} \cdot \sigma L_s + \frac{\tau_{int}}{\tau_{int} \cdot s + 1} \cdot \left(u^s_{qds} - R_s \cdot i^s_{qds} \right) \right) + \frac{L'_r}{L_m} \cdot \frac{1}{s} \cdot G_{obs}(s) \cdot \left(\lambda'^{s}_{qdrC} - \lambda'^{s}_{qdr} \right) \tag{7.80}$$

$$\lambda'^{s}_{VM} = \frac{L'_r}{L_m} \left(-i^s_{qds} \cdot \sigma L_s + \frac{\tau_{int}}{\tau_{int} \cdot s + 1} \cdot \left(u^s_{qds} - R_s \cdot i^s_{qds} \right) \right) \tag{7.81}$$

$$\Downarrow$$

$$\lambda'^{s}_{qdr} = \lambda'^{s}_{VM} + \frac{L'_r}{L_m} \cdot \frac{1}{s} \cdot G_{obs}(s) \cdot \left(\lambda'^{s}_{qdrC} - \lambda'^{s}_{qdr} \right) \tag{7.82}$$

$$= \lambda'^{s}_{VM} + \frac{L'_r}{L_m} \cdot \frac{1}{s} \cdot G_{obs}(s) \cdot \lambda'^{s}_{qdrC} - \frac{L'_r}{L_m} \cdot \frac{1}{s} \cdot G_{obs}(s) \cdot \lambda'^{s}_{qdr} \tag{7.83}$$

$$\Downarrow$$

$$\lambda'^{s}_{qdr} = \frac{1}{1 + \frac{L'_r}{L_m} \cdot \frac{1}{s} \cdot G_{obs}(s)} \cdot \lambda'^{s}_{VM} + \frac{\frac{L'_r}{L_m} \cdot \frac{1}{s} \cdot G_{obs}(s)}{1 + \frac{L'_r}{L_m} \cdot \frac{1}{s} \cdot G_{obs}(s)} \cdot \lambda'^{s}_{qdrC} \tag{7.84}$$

$$= G_{voltage} \cdot \lambda'^{s}_{qdrV} + G_{current} \cdot \lambda'^{s}_{qdrC} \tag{7.85}$$

where:

λ'^{s}_{qdr}	Flux estimated by flux observer $[Wb]$
λ'^{s}_{qdrV}	Flux estimated by voltage model $[Wb]$
λ'^{s}_{qdrC}	Flux estimated by current model $[Wb]$
$G_{voltage}$	Gain for voltage model $[-]$
$G_{current}$	Gain for current model $[-]$

G_{obs} Gain of the PI observer $[-]$

$$G_{current} = \frac{\frac{L'_r}{L_m} \cdot \frac{1}{s} \cdot K_{p.obs}}{1 + \frac{L'_r}{L_m} \cdot \frac{1}{s} \cdot K_{p.obs}} \tag{7.86}$$

$$= \frac{1}{\frac{L_m}{L'_r \cdot K_{p.obs}} \cdot s + 1} \tag{7.87}$$

$$G_{voltage} = \frac{1}{1 + \frac{L'_r}{L_m} \cdot \frac{1}{s} \cdot K_{p.obs}} \tag{7.88}$$

$$= \frac{1}{\frac{L_m}{L'_r \cdot K_{p.obs}} \cdot s + 1} \cdot \frac{L_m}{L'_r \cdot K_{p.obs}} \cdot s \tag{7.89}$$

Bode plots of the current -and voltage gain (for $k_{p.obs} = 100$) is seen in figure 7.30. A bode plot for equation (7.85) is seen in figure 7.31 a where the current model flux output λ'^{s}_{qdrC} is set to 0.030 Wb and the voltage model output λ'^{s}_{VM} is set to 0.033 Wb.

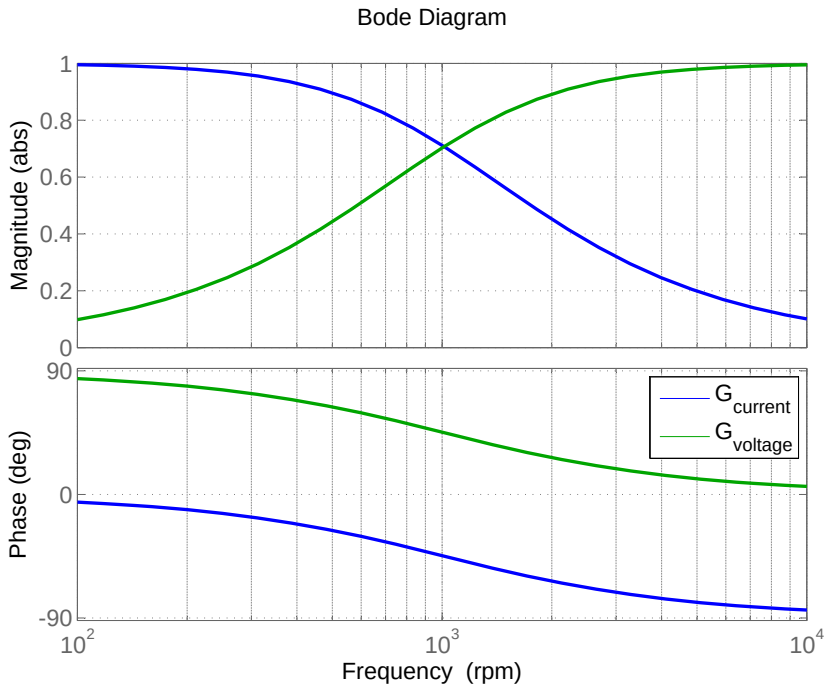

Figure 7.30: *Current -and voltage model gains.*

The bode plots shows that the frequency at which the influence of the current -and voltage model is equal is approximately 1000 rpm corresponding with $\left(k_{p.obs} \cdot L'_r / L_M\right)\ {}^{rad}/_{'s}$ and a shaft velocity of

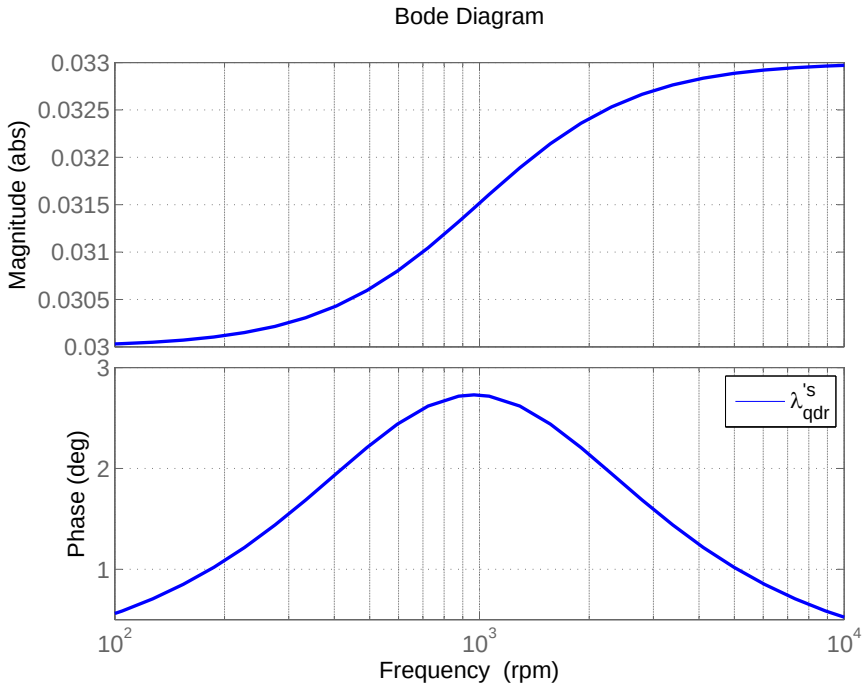

Figure 7.31: *Transition between current -and voltage model. The current model flux output λ'^{s}_{qdrC} is set to 0.030 Wb and the voltage model output λ'^{s}_{VM} is set to 0.033 Wb.*

approximately 500 rpm. The sum of the two complex vectors $G_{voltage}$ and $G_{current}$ (composed by their phase and magnitude at a given frequency) always equals 1 using this configuration.
Using $k_{p.obs} = 100$ the flux angle error for various values of the time constant τ_{int} is seen in figure 7.32. The figure emphasize the fact that a pure integration is best approximated using high values of τ_{int}. On the other hand to limit the amplification of the bias current it is desirable to use low values of τ_{int}. From the plots it is determined that $\tau_{int} = 0.5$ since it in this case induce a maximum angle error of 0.4 °, which is considered acceptable, and provides limited amplification of the bias current.
To determine an appropriate transition between the current -and voltage model the flux angle error is determined for various values of $k_{p.obs}$, using $\tau_{int} = 0.5$. The result is seen in figure 7.33. It is seen that the angle error is reduced using high values of $k_{p.obs}$, but as mentioned earlier it is desirable that the voltage model is dominant in the majority of the velocity spectrum, due to better temperature variation robustness. Therefore a proportional gain $k_{p.obs}$ of 100 corresponding with a transitional shaft velocity of approximately 500 rpm seems reasonable.

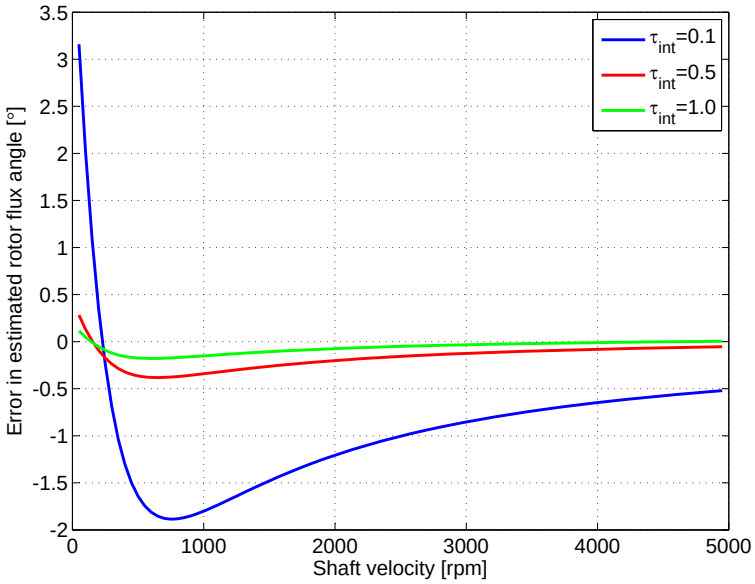

Figure 7.32: *Flux angle error is seen for various values of the time constant τ_{int}. The d-axis stator current is set to 90 A and a q-axis stator current is set to 305 A.*

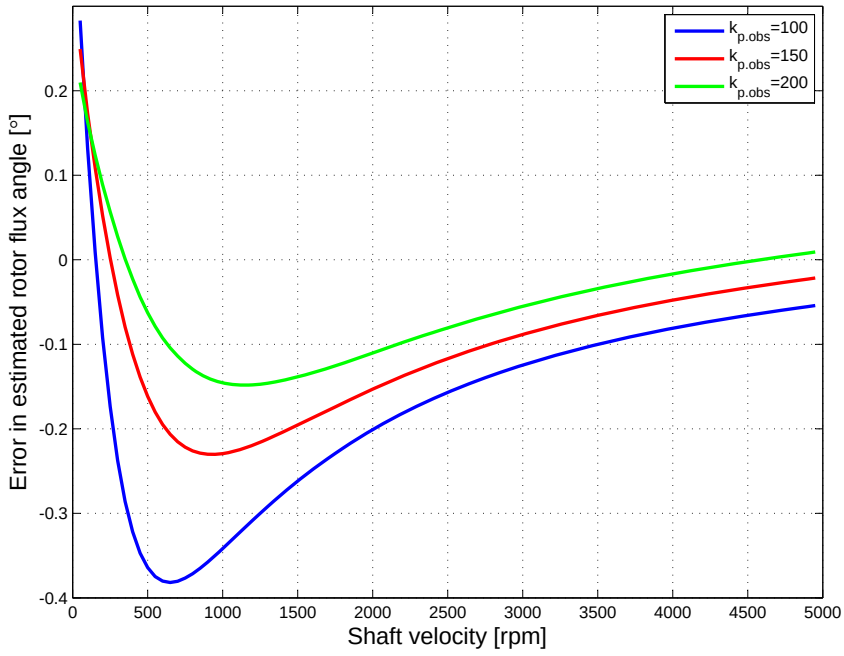

Figure 7.33: *Flux angle errors for various values of $k_{p.obs}$. The d-axis stator current is set to 90 A and a q-axis stator current is set to 305 A.*

As mentioned earlier the direct flux estimator is more robust with respect to variations in rotor temperature. Using the proposed proportional gain ($k_{p.obs} = 100$) simulations showing the angle

error due to temperature variations is seen in figure 7.34. An ideal integrator is used instead of the first order filter to isolate the temperature effect. As seen in the figure the angle error due to temperature decreases as the shaft velocity increases. This is expected since the voltage model which does not contain the rotor resistance parameter becomes more dominant at high velocities c.f. figure 7.30.

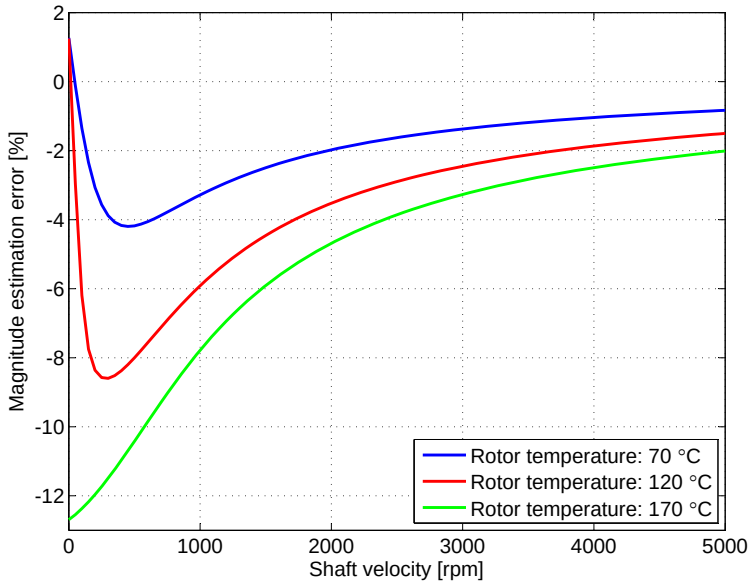

Figure 7.34: *Flux angle error for various rotor temperature levels. The d-axis stator current is set to 90 A and a q-axis stator current is set to 305 A.*

It is examined whether the direct flux estimator is robust with respect to magnetic saturation corresponding with a reduced value of the magnetizing inductance L_M. In figure 7.35 the flux angle -and flux magnitude estimation error is seen for a d-axis stator current of 90 A and a q-axis stator current of 305 A. As seen in the figure the saturation effect induces a relatively large angle error especially at low shaft velocities. The flux magnitude estimation error is significant when using the direct flux estimator, but is still lower than when using the indirect estimation. The indirect flux magnitude estimation error is determined to be $\left({}^{90}/_{(90 \cdot 0.7)}\right) = 43$ % using equation (7.18).

As mentioned earlier the direct flux estimator is not implemented into the final solution due to technical difficulties. Instead it is chosen to further develop the indirect flux estimator i.a. by using temperature and saturation compensation. This is elaborated in the following section.

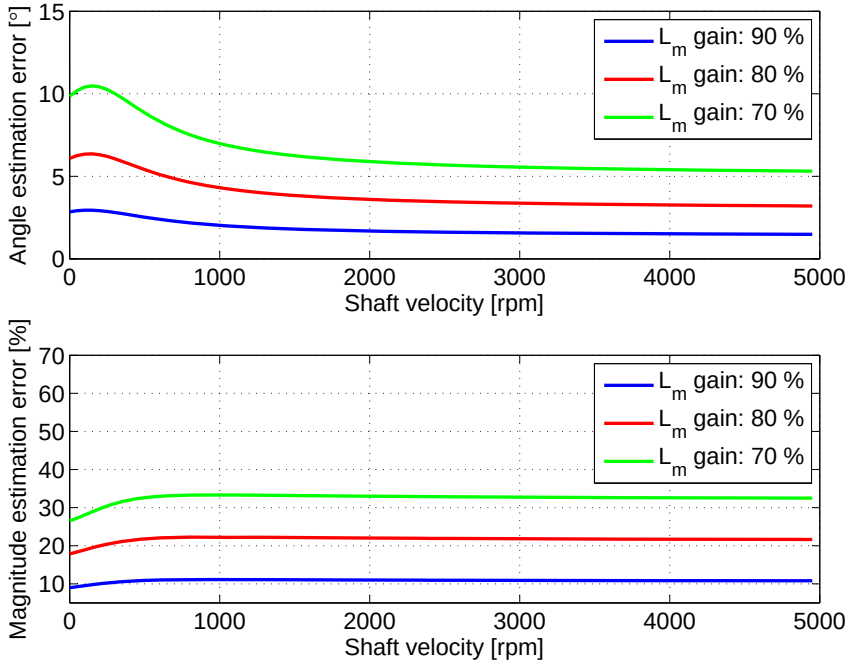

Figure 7.35: *Flux angle -and magnitude error at various magnetic saturation levels. The d-axis stator current is set to 90 A and a q-axis stator current is set to 305 A.*

7.3.3 Indirect Flux Estimator Improvements

In this section improvements to the original indirect flux estimator described in section 7.2.1 is presented. The error in flux angle prevented by implementing the improvements is assessed since it is a good benchmark with regards to obtaining precise d- and q-axis stator currents. In section 7.3.4 it is shown how the improvements are implemented.

Rotor flux Response Improvement

As mentioned earlier this flux estimation is based on steady state considerations. The flux estimator will not properly maintain field orientation during transients which involve changes in the rotor flux magnitude [Novotny and Lipo, 1996, p. 264]. As earlier mentioned the efficiency might be improved by changing the rotor flux magnitude during operation. The estimation can be improved by adding a transient relation between i_{ds} and λ'_{dr}. The relation is derived by isolating i_{dr} in equation (7.12) and inserting the expression in equation (6.5) and utilizing that the rotor voltage and rotor q-axis flux is zero. The relation is seen in equation (7.90).

$$\lambda'_{dr} = \frac{L_M}{1 + p \cdot \tau_r} \cdot i_{ds} \tag{7.90}$$

Inserting equation (7.90) and (7.20) into equation (7.24) yields:

$$\omega_{rf} = \omega_r - R'_r \cdot \frac{i'_{qr}}{\lambda'_{dr}} \tag{7.91}$$

$$= \omega_r - R'_r \cdot \frac{-\frac{L_M}{L_r} \cdot i_{qs}}{\frac{L_M}{1+p\cdot\tau_r} \cdot i_{ds}} \tag{7.92}$$

$$= \omega_r + \frac{\frac{1}{\tau_r} \cdot i_{qs}}{\frac{1}{1+p\cdot\tau_r} \cdot i_{ds}} \tag{7.93}$$

$$= \omega_r + \omega_s \tag{7.94}$$

A comparison of the absolute error in the estimated rotor flux angle with and without flux compensation when utilizing the simulation model is seen in figure 7.36. As seen in the figure the maximum error in the estimated rotor flux angle is reduced by about 25 % for this case. The steady state error at time 0.9 and 1.75 is considered to be the result of Simulink solver tolerance since it varies when altering the relative solver tolerance. The improvement in the flux estimation is beneficial in relation to decreasing the error between actual and reference d -and q-axis currents. In section 7.3.4 it is described how the improved rotor flux estimation is implemented into the control strategy.

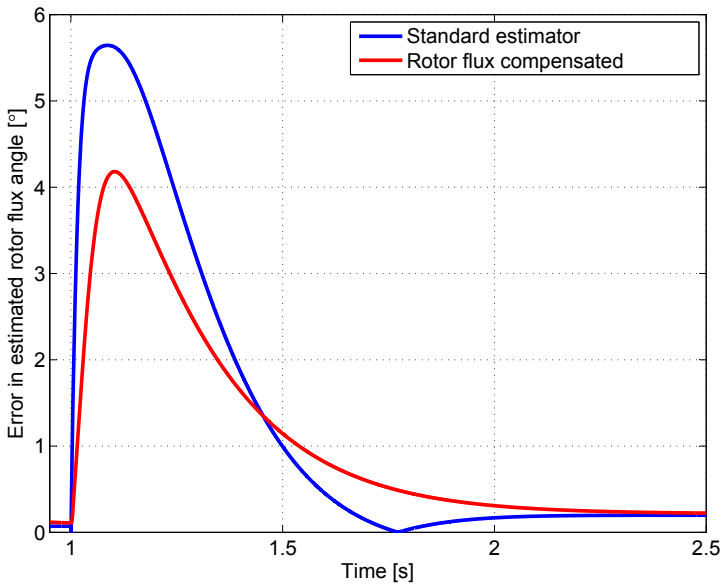

Figure 7.36: *Flux estimator angle error. The shaft velocity is set to 2500 rpm, the q-axis stator current is set to 200 A and the d-axis stator current is set to apply a step from 60 to 120 A.*

One of the main problems encountered when using indirect flux estimation is the dependence of knowing the machine parameters. An error in the rotor time constant τ_r results in steady

state error in the estimated angle. As seen in equation (7.26) τ_r is a function of rotor resistance and rotor inductance. In the following sections compensation strategies for variations in these parameters are considered.

Magnetic Saturation Improvement

When increasing the magnetizing current i_M, the magnetization flux λ_{qdm} will at some point saturate resulting in a change in the magnetizing inductance L_M. In non-saturated condition the magnetizing flux is given by equation (7.95).

$$\begin{aligned} \lambda_{qdm} &= i_m \cdot L_M & (7.95) \\ &= \left(i_{qds} + i'_{qdr}\right) \cdot L_M & (7.96) \end{aligned}$$

where: λ_{qdm} Magnetizing flux $[Wb]$.

i_m Magnetizing current $[A]$.

To determine an expression for the magnetizing inductance as function of the magnetizing current an experiment is performed. At the experiment the IM is operated at no load (zero slip) condition. At this condition zero voltage is induced in the rotor circuit resulting in a steady state circuit only containing a no load resistance, a stator leakage reactance and the magnetizing reactance in which the magnetizing current i_M passes though. By comparing voltage and current amplitudes at the experiment, the impedance of the system is determined at various magnetizing currents. In the steady state model a gain depending on the magnetizing current is applied to the magnetizing inductance ensuring coherence between experiment and steady state model impedance. The gain is seen in figure 7.37 along with a first order approximation of it. The maximum deviation between the processed data from the experiment and the fitted polynomial is 1.42 %-points which is considered acceptable. According to the magnetizing inductance gain of figure 7.37 the gain is approximated by a constant value of 1 at magnetizing currents from 0 to about 90 A. At vurrents above 90 A it decreases at a rate of about 25 % point per 100 A. The expression describing L_M is seen in equation (7.97).

$$L_M = \begin{cases} 320 \cdot 10^{-6} \ [H] & \text{for } i_M \leqq 89.9 \\ \left(-7.95 \cdot 10^{-7} \cdot i_m + 3.92 \cdot 10^{-4}\right) \ [H] & \text{for } i_M > 89.9 \end{cases} \quad (7.97)$$

Nominal magnetizing current is estimated using information from the datasheet and the simulation model presented in chapter 6. From the datasheet the nominal voltage and torque at

2000rpm is seen. In the simulation model the magnetizing current is iteratively varied in order to obtain a voltage amplitude corresponding to the datasheet at nominal torque and velocity. The nominal magnetizing current is determined to i_M=200 A. The nominal magnetizing current is indicated in figure 7.37 showing that the IM is saturated when using nominal magnetization.

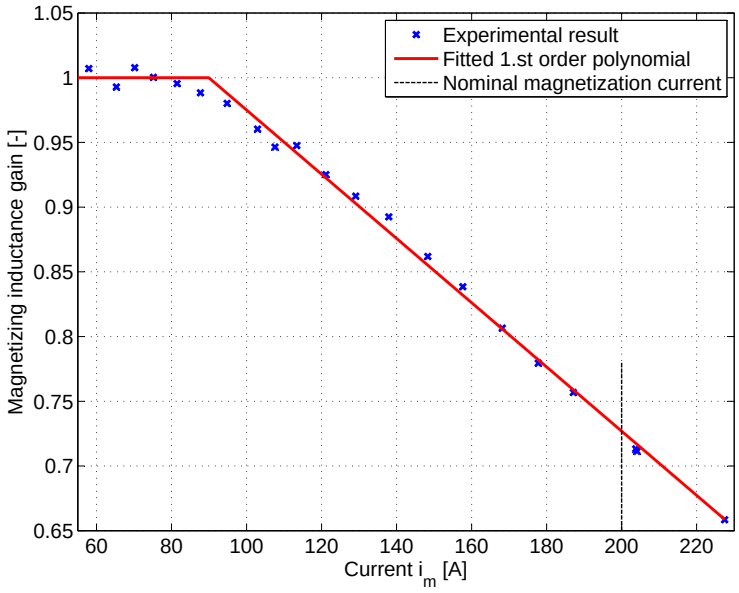

Figure 7.37: *Magnetizing inductance gain as a function of magnetization current.*

In figure 7.38 the result of a simulation illustrating the effect of magnetic saturation is seen. The shaft is set to 1500 rpm, the d-axis stator current is initialized to 85 A and the q-axis stator current is set to deliver a torque of 35 Nm using equation (7.29). After steady state is obtained a soft ramp is applied on the d-axis current. The actual torque obtained at the simulation decreases as i_{ds} increased due to the magnetic saturation.

Figure 7.38 shows that the saturation effect induces a relatively large rotor flux angle error especially when operating the IM at high magnetization levels. Therefore a magnetic saturation compensation of the rotor time constant τ_r which includes the magnetic inductance (equation (7.15)) is implemented into the indirect control algorithm. In section 7.3.4 it is described how the magnetic saturation compensation is implemented into the control strategy.

The magnetic saturation effect is implemented into the indirect control strategy using steady state considerations. In steady state the rotor current only has a q-axis component given by equation (7.20) resulting in an expression for the magnetic flux amplitude seen in equation (7.102). In this the term $\left(1-\frac{L_M}{L_M+L'_{lr}}\right)^2$ equals about $6\cdot 10^{-3}$ for a magnetizing current of 200

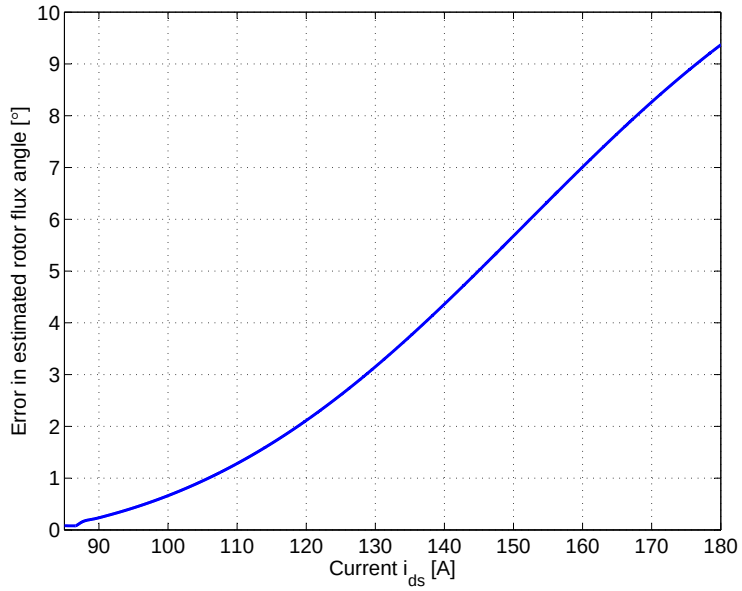

Figure 7.38: *Steady state error in the estimated flux angle due to saturation. The simulation model is set to deliver a torque of 35 Nm at 1500 rpm.*

A. The low influence of the q-axis current on the magnetizing current makes equation (7.103) a reasonable approximation.

$$\lambda_{qdm} = \left(i_{qds} + i'_{qdr}\right) \cdot L_M \tag{7.98}$$

Steady state $\Downarrow$

$$\lambda_{qdm} = \left(i_{qds} + i'_{qr}\right) \cdot L_M \tag{7.99}$$

$$= \left(i_{qds} - \frac{L_M}{L'_r} \cdot i_{qs}\right) \cdot L_M \tag{7.100}$$

$$= \left(i_{ds} + i_{qs} \cdot \left(1 - \frac{L_M}{L_M + L'_{lr}}\right)\right) \cdot L_M \tag{7.101}$$

$\Downarrow$

$$\left|\lambda_{qdm}\right| = \left(i_{ds}^2 + i_{qs}^2 \cdot \left(1 - \frac{L_M}{L_M + L'_{lr}}\right)^2\right)^{1/2} \cdot L_M \tag{7.102}$$

$$\approx i_{ds} \cdot L_M \tag{7.103}$$

Besides improving the flux estimation the torque control may also be improved by calculating the saturated magnetizing inductance L_M. This is due to the fact that L_M is a parameter used for calculation of the q-axis current (equation (7.29)). In section 7.3.4 the implementation of the magnetic saturation compensation is described. In the following section it is examined whether the stator temperature output from the thermal sensor can be used to indicate the temperature of

the rotor circuit making it possible to compensate for changes in rotor resistance affecting the rotor time constant τ_r and thereby the precision of the indirect flux estimator.

Rotor Resistance Improvement

The rotor resistance can be estimated if the rotor temperature is known. In the induction machine used in this project there is no temperature measurements of the rotor however the stator temperature is estimated using a thermal sensor located in the stator windings. If a model describing the relation between rotor and stator temperature is implemented the rotor temperature and hereby the rotor resistance can be estimated.
In order to consider whether a simple model is feasible an experiment is conducted. The experiment is described in appendix F.6. In the experiment the IM is set to operate at various torque levels applied at different stator temperatures. In the experiment the d-axis stator current is at a fixed level of 60 A to ensure a large margin to the point of magnetic saturation (89.9 A). As the temperature increases the error between reference and delivered torque increases.
In the simulation model the rotor resistance in the voltage equations is varied in order to obtain the same torque in the model as in the experiment. From the change in rotor resistance, the rotor temperature can be estimated by using equation (7.104) [Moreno et al., 2001].

$$R'_r = R_0 \cdot (1 + \alpha \cdot (T - T_{Room})) \tag{7.104}$$

where:	R'_r	Actual rotor resistance $[\Omega]$
	R_0	Rotor resistance at room temperature $[\Omega]$
	α	Temperature coefficient $\left[\frac{\Omega}{^\circ C}\right]$
	T	Current temperature $[^\circ C]$
	T_{Room}	Ambient temperature $[^\circ C]$

The temperature coefficient for the rotor is 0.00375 $\frac{\Omega}{^\circ C}$ assuming the rotor squirrel cage is made of aluminum.
The results from the experiment is seen in figure 7.40. From this it is seen that the calculated rotor temperature is consistently higher than the measured stator temperature with a difference between 4 $^\circ C$ and 38 $^\circ C$. The large difference emphasize that the rotor temperature is highly dependent on the load history of the IM and that a complex model dependent of load history hereby is required to estimate the rotor temperature. The experiment however shows that setting the rotor temperature equal to the stator reduces the temperature error compared to assuming it is at room temperature.

In figure 7.39 the result of a simulation describing the effect of rotor resistance variation due to temperature is seen. The shaft is set to a velocity of 2500 rpm, the d-axis stator current is initialized to 60 A and the q-axis stator current is set to deliver a torque of 20 Nm using equation (7.29). The rotor resistance in the voltage equations is sat by using equation (7.104) at a temperature of 105 $^{\circ}C$ meanwhile the rotor resistance in the flux estimation is kept at room temperature. After steady state is obtained a soft ramp is applied on the d-axis current. The actual torque obtained at the simulation was higher than intended due to error in the flux estimation and because magnetic saturation was not taken into effect.
Figure 7.39 shows that the temperature effect on the rotor resistance induces a relatively large error especially when operating the IM at high magnetization levels. Therefore a temperature compensation of the rotor time constant τ_r which includes the rotor resistance is implemented into the indirect control algorithm. To reduce dynamics introduced by noise in the temperature measurement a filter is added in the DSP program. The filter is of first order and has a time constant τ_{Temp} of 0.25 s yielding a rise time of approximately 1 s. Since the time constants of thermal systems in general are large the filter is not considered to affect the reading considerably. In the following section it is described how the temperature compensation is implemented into the control strategy.

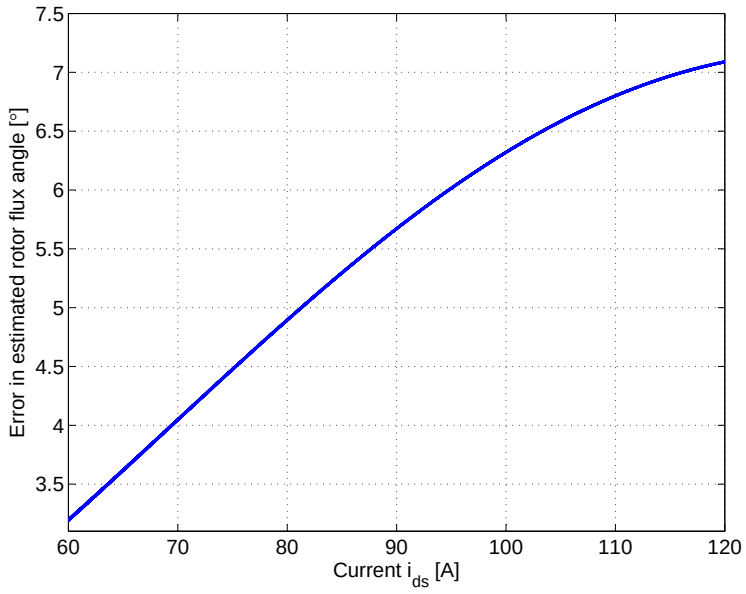

Figure 7.39: *Steady state error in the estimated rotor flux angle for a rotor temperature of 105 °C (85 °C above room temperature). The Simulation model is set to deliver a torque of 20 Nm at 2500 rpm.*

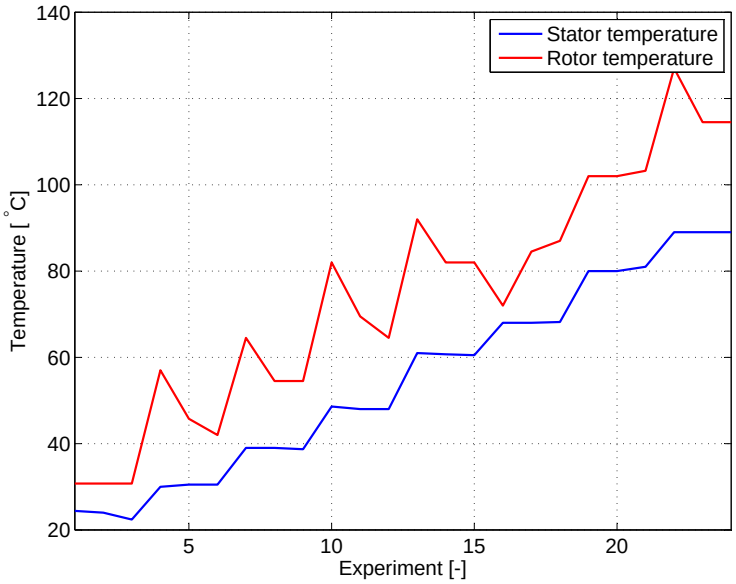

Figure 7.40: *Relation between stator and rotor temperature.*

7.3.4 Implementation of Control Strategy

In this section implementation of the indirect flux estimator is explained. In figure 7.41 a diagram showing the indirect flux estimator implemented in the control algorithm is seen. It is an updated version of the original indirect flux estimation strategy is seen in figure 7.2. As mentioned in the previous sections the improvements include adding a pre-filter to the d-axis stator current reference (equation (7.93)), updating the magnetizing inductance L_M as a function of the d-axis current (equation (7.97)) and updating the rotor resistance R'_r as a function of stator temperature ((7.104)).

Figure 7.42 shows the result of a simulation where the estimated rotor flux angle is compared to the actual rotor flux angle using various configurations. The shaft velocity is set to 2000 rpm the stator q-axis current is set to 330 A and the stator d-axis current is stepped from 90 A to 150 A. Figure 7.42 shows that using rotor flux compensation in general improves the transient response while the compensation of L_M with regard to magnetic saturation improves both steady state -and transient response error. The combination of the flux- and L_M compensation provides a good transient response and zero steady state error. Changes in the rotor temperature would increase the error in the estimated flux angles seen in figure 7.42 but it is not included in this since the actual temperature difference between the stator and the rotor is uncertain.

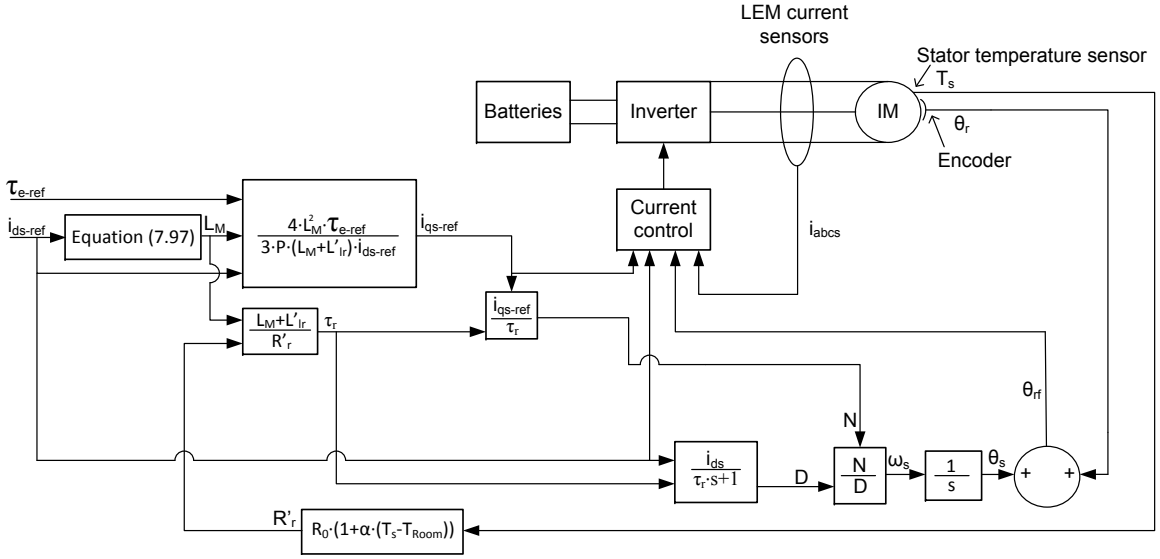

Figure 7.41: *Improved indirect control strategy.*

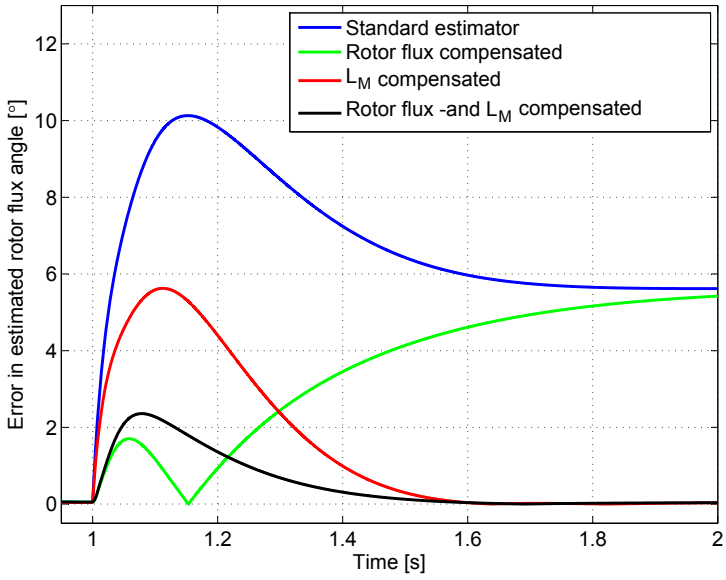

Figure 7.42: *The result of a simulation where the estimated rotor flux angle is compared to the actual using different configurations. The shaft velocity is set to 2000 rpm the stator q-axis current is set to 330 A and the stator d-axis current is stepped from 90 A to 150 A.*

Figure 7.43 shows the result of an experiment where the IM is set to deliver a torque of 25 Nm at 1500 rpm and at various d-axis stator currents i_{ds} using standard indirect control and the improved edition. The figure shows that when applying the improved flux estimator the control maintains better correspondence with the torque reference when i_{ds} exceeds the saturation limit $i_{ds} > 90\,A$. The deviation from the reference for the improved flux estimator at high i_{ds} might

be explained by the fact that the q-axis stator currents effect on the magnetizing current i_M is not taken into account or that the rotor temperature varies from the stator temperature during the experiment.

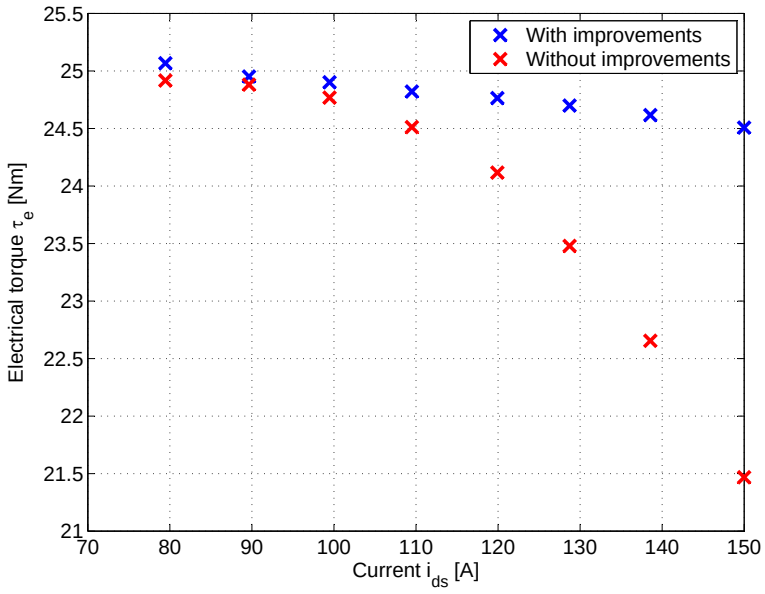

Figure 7.43: *Experiment where the IM is set to deliver a torque of 25 Nm at 1500 rpm and at various d-axis stator currents i_{ds} using standard indirect control and the improved edition.*

The improved indirect control strategy has acceptable transient response with respect to magnetizing flux variation. It has improved robustness with respect to magnetic saturation -and temperature variations compared to the standard indirect control strategy. These factors make the improved indirect control strategy suitable for energy efficient operation of an induction machine propelling an electric vehicle.
The improvements for the indirect flux estimation might also be applicable in the direct flux estimation and a better flux estimation might then be obtained by using direct- instead of indirect control. This however requires a thorough analysis to conclude.

The control strategy for the electric vehicle is now developed. In the following chapter the structure of the DSP program, in which the control strategy is implemented, is described.

CHAPTER 8

DSP PROGRAM

In this chapter the program used on the DSP to control the IM is described. The program is written in C in a program called Code Composer Studio which was enclosed with the DSP.
The general structure of the program is seen in figure 8.1. The program starts with an initialization of variables, tables, structures and dedication of memory to data collection. After the initialization the main function starts. In the main function all peripherals and interrupts are set up and initialized. The interrupts used are PWM, Analogue to Digital Conversion(ADC), and data collect interrupt. The interrupts are prioritized to secure that the most important interrupt always gets executed first. This means that if a lower priority interrupt is on-going when a higher priority interrupt is starting the code pauses the on-going interrupt and jumps to the higher priority interrupt. When the higher priority interrupt is done the code continuous from where it was in the lower priority interrupt. The order from highest to lowest is PWM, ADC and data collect. This chapter contains a description of the three interrupts. The whole program is found on the enclosed CD.

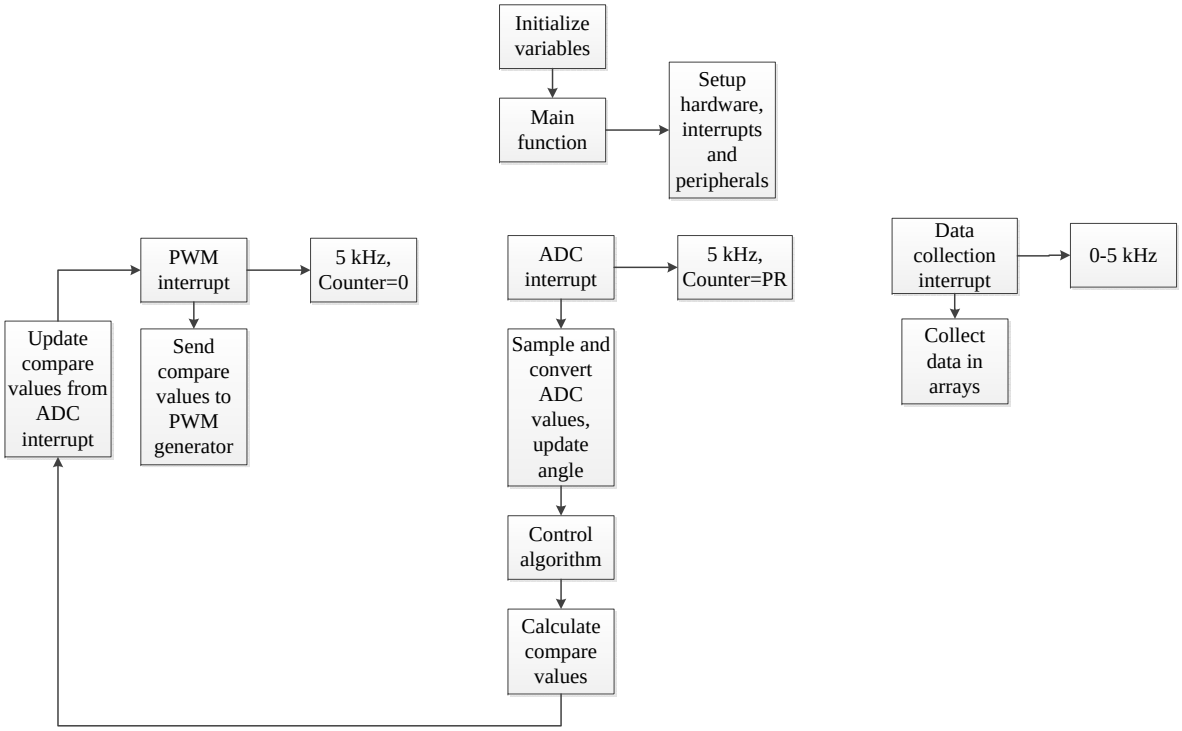

Figure 8.1: *General flow chart of the DSP program for the control of an IM.*

PWM Interrupt

In this section the PWM interrupt is described in more detail. The code executed when the interrupt occurs is fairly simple and does not have many tasks in the program compared to the ADC interrupt.

A counter for the PWM interrupt is initialized to count in triangles, see figure 8.2. By setting the period register (PR) to a certain value the frequency of the interrupt is set. The frequency of the PWM interrupt is the switching frequency for the inverter. The DSP counts with a frequency of 150 MHz and as seen in figure 8.2 the PWM interrupts occurs when the count value reaches 0. Equation (8.2) is used to calculate PR to get a switching frequency of 5 kHz.

$$PR = \frac{1}{f_{sw} \cdot \frac{1}{f_{clock}} \cdot 2} \tag{8.1}$$

$$= \frac{1}{5000Hz \cdot \frac{1}{150 \cdot 10^6 Hz} \cdot 2} = 15000 \tag{8.2}$$

where:

	f_{sw}	Switching frequency $[Hz]$
	f_{clock}	Clock frequency of the DSP $[Hz]$
	PR	Period register value [-]

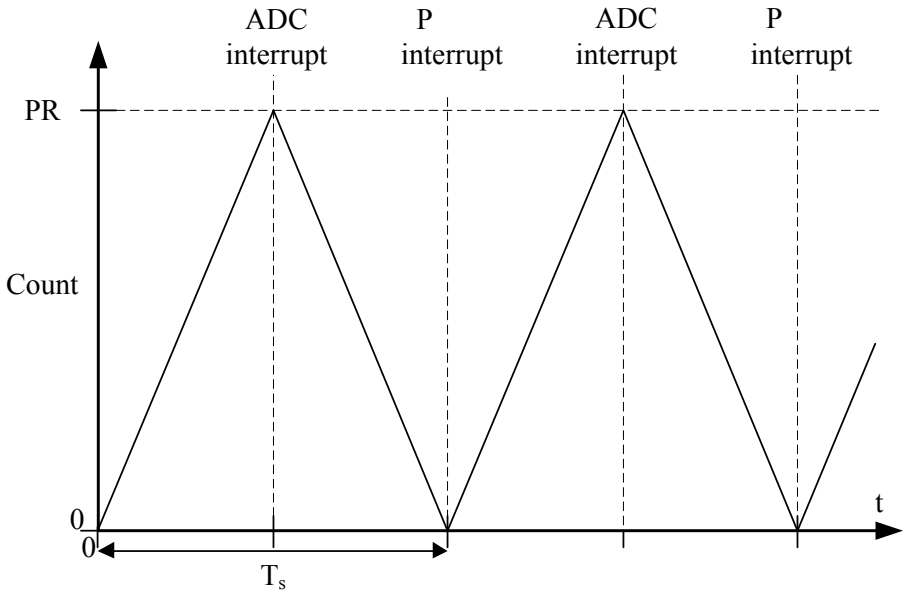

Figure 8.2: *Overview of interrupts execution.*

The PWM interrupt is also set up to send a start of conversion (SOC) signal to the ADC interrupt. This signal tells the ADC channels as the name indicates to start an analog to digital conversion. The PWM interrupt sends this signal when the counter value is equal to PR as seen in figure 8.2. This is smart due to current measurements, this will be explained in the ADC interrupt section.

PWM signals are created by comparing values to the triangular counting signal this is illustrated in figure 8.3. The PWM generator is set up to give high signal when the compare value is above the counter value. The duty cycle of the PWM signals can be set by changing the compare values between zero and PR. The compare values gets updated every PWM interrupt. There are three PWM signals in the program, one for each of the phases A, B and C.

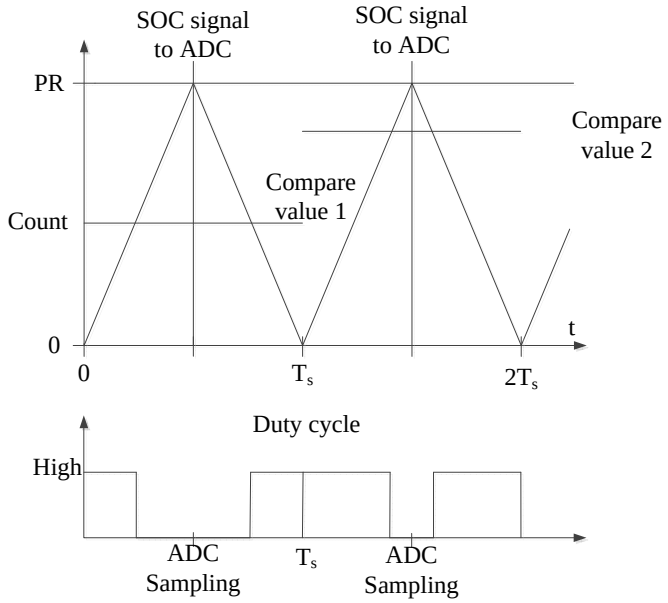

Figure 8.3: *Generating PWM signals.*

ADC Interrupt

In this section the ADC interrupt is described. A flow chart of what occurs in the ADC interrupt is seen in figure 8.4.

It is in the ADC interrupt that the control strategy described in chapter 7 is implemented. The controllers and filters developed in chapter 7 are designed in the continuous s domain. The DSP is digital so the controllers and filters needs to be transformed into the digital domain. All controllers and filters are converted to the digital z domain by the Tustin method, see equation (8.3). The transformation from the digital z domain to DSP code is done from the fact that z^{-1} is old values e.g. $z^{-1} \cdot input$ is the old input. A small example of this is seen in equation (8.4) with a pure integrator.

$$s = \left(\frac{2 \cdot (z-1)}{T_s \cdot (z+1)} \right) \tag{8.3}$$

$$\begin{aligned} \frac{output}{input} &= \frac{1}{s} = \frac{1}{\frac{2 \cdot (z-1)}{T_s \cdot (z+1)}} = \frac{T_s + T_s \cdot z^{-1}}{2 - 2 \cdot z^{-1}} \\ &\Downarrow \\ output &= \frac{T_s \cdot input}{2} + \frac{T_s \cdot input \cdot z^{-1}}{2} + output \cdot z^{-1} \end{aligned} \tag{8.4}$$

The ADC interrupt starts by sampling the ADC channels and converting the measured signals to bit values. These bit values are converted to real values by the transfer functions described

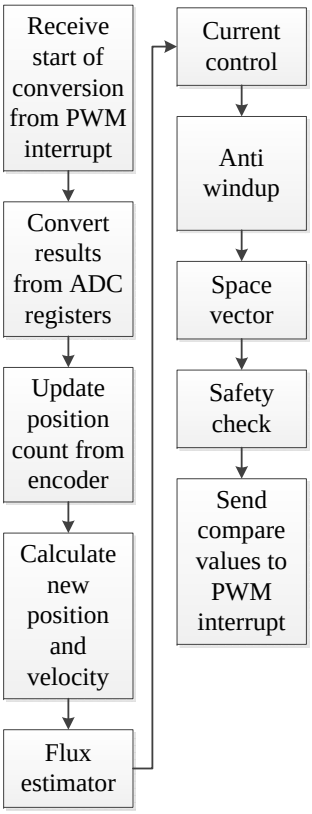

Figure 8.4: *Flow chart of the ADC interrupt*

in section 5.2.7. As mentioned the sampling of the ADC channels is set up to occur when the counter value reaches PR. The timing of the sampling is set due to the current ripple in phase currents. The inductances together with the resistance in the IM functions as a low pass filter and when high frequency PWM signal are used to model a sinusoidal signal, high frequency current ripples are seen in the current signal. To ensure that it is the fundamental current signal that is measured by the DSP the current must be sampled in the middle of the ripple. This is obtained by sampling when the counter reaches PR.
After sampling the ADC channels the program collects the rotor position from the encoder register. The speed is calculated by latching the rotor position into a register at a frequency of 100 Hz and then applying the backward difference method. The speed is only calculated when a new values is latched into the register.

Next the angle of the rotor flux θ_{rf} is calculated from the current references i_{ds-ref} and i_{qs-ref} and the rotor position by using the flux estimator described in section 7.3.3.
The current references i_{ds-ref} and i_{qs-ref} can be set manually through the watch window in Code Composer or through Matlab. In the Electric vehicle they are set by the accelerator and brake pedal. The flux angle θ_{rf} and the measured phase currents are used to calculate the

currents i_{ds} and i_{qs}. The errors between the reference currents and the current currents are calculated and these errors are input to the current controllers developed in section 7.3.1. The current controllers transforms the current errors into the voltages u_d and u_q. These voltages are checked for saturation and anti wind-up is applied if the voltages are saturated. The voltages are then transformed into compare values by space vector modulation.

Before sending signals to the inverter a safety check is performed. The program checks for to high currents, speed, temperature and DC-bus voltage. If any of these thresholds are exceeded the DSP disables the inverter. There is also a check for the balance of the three phase currents see equation (8.5). This should be zero, but if one of the current transducers is defect the control system will not function properly therefore if $i_{balanced}$ is over a given threshold the DSP disables the inverter.

$$i_{balanced} = i_A + i_B + i_C \tag{8.5}$$

After the safety check the compare values for the PWM interrupt are updated.

For the program to function properly it is very important that the ADC interrupt does not last longer than half the PWM interrupt. In figure 8.5 the execution durations for the PWM and ADC interrupt are depicted. It is seen that there is a large margin from the critical point where the ADC interrupt is ongoing when the PWM interrupt starts. This means that there can be added utilities to the ADC interrupt if needed.

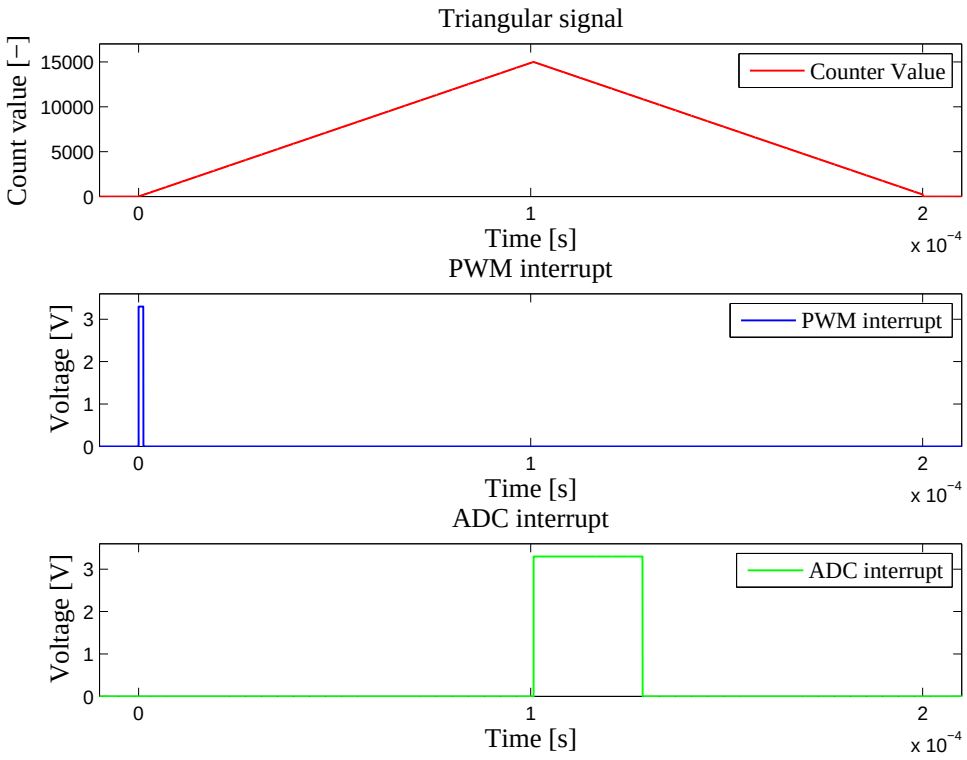

Figure 8.5: *Time of execution for PWM and ADC interrupts.*

Data Collection Interrupt

The data collection interrupt uses a different counter than the other two interrupts and can be set up to collect data in arrays at a desired frequency. The ram in the DSP is dedicated to data collection arrays and the length of these arrays is changed depending on how many arrays are needed. There are about 8000 free 16 bit ram slots available that can be assigned for data collection. Data is always saved in 16 bit format, either as signed short or unsigned short depending on whether the sign is needed. The data is transferred from the DSP to the computer through Matlab.

The program described throughout this chapter is implemented in the test setup and is used in order to perform the mapping described in the proceeding chapter

CHAPTER 9

MAPPING OF INDUCTION MACHINE

In this chapter a mapping of the IM is presented. The mapping is conducted by an automated Matlab algorithm. The mapping is conducted at various speeds, torque and magnetizing currents. The goal of the mapping is to get an overview of the IM's efficiency at various operating points. The goal is also to collect enough data for determination of the unknown parameters in the loss equations presented in section 6.5. The chapter also contains a description of an automated mapping algorithm which is also applicable for other induction machines mounted on the test bench.

9.1 Mapping Algorithm

In this section the automated Matlab mapping algorithm is presented. The Matlab algorithm controls both the Siemens load drive and the IM together with all the measurement signals that are collected. In figure 9.1 a flow chart of the mapping algorithm is seen.
Before the algorithm is started three arrays containing various speeds, torque and magnetizing currents are created. These arrays are called speed, torque and i_{ds} in figure 9.1 and is a part of the initialization of the algorithm. The arrays contain all the operation points for the mapping. To obtain all combinations of the operation points from the arrays three for loops are coded in the algorithm. The three for loops are called inner for loop, middle for loop and outer for loop in figure 9.1. The outer for loop is the speed loop. Here the speed is changed according to the speed array by a command to the Siemens load drive. After each speed change there is a pause of 10 seconds to ensure the machines are in steady state speed. Since the speed loop is the outer

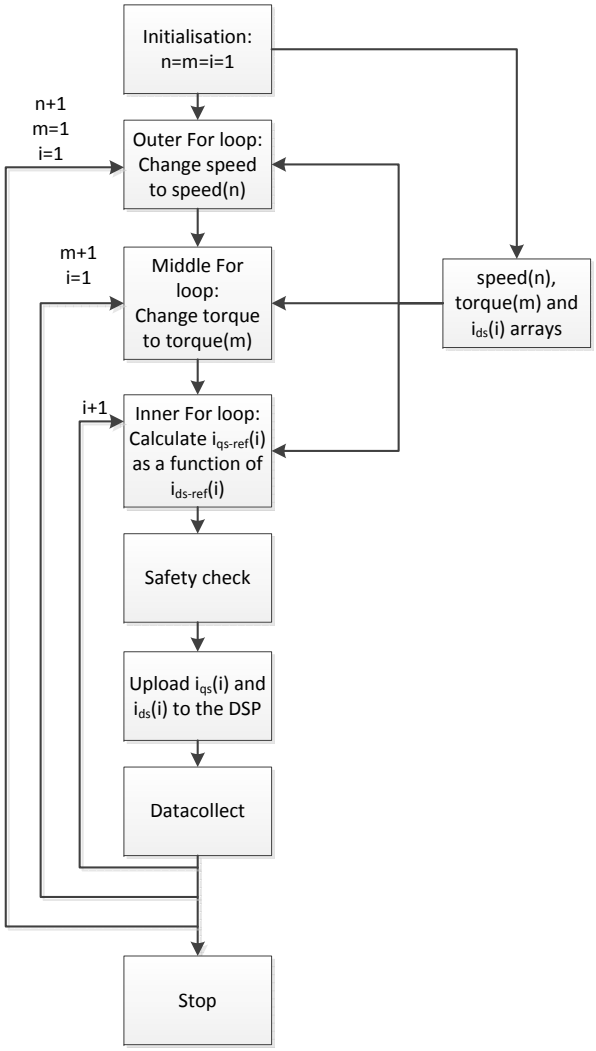

Figure 9.1: *Flowchart for mapping algorithm in Matlab.*

loop the two other loops are completed before a new speed is set, this means that the speed is the parameter which is changed the least. This is smart due to the relatively long time it takes to change the mechanical speed. The middle for loop is where the torque changes according to the torque array. The torque changes after the inner loop is completed. The inner loop is where the magnetizing current i_{ds} is changed and i_{qs} is updated. The inner loop contains most changes in operating points as the magnetizing current i_{ds} is changed in each iteration. First action in the inner loop is the i_{qs} current being calculated from the torque equation, see equation (7.22). As mentioned in section 7.3.3 L_M changes as a function of i_{ds} therefore L_M is calculated before calculating i_{qs} at a given torque and i_{ds}. Because this loop occurs at every iteration there is a safety check in the start of this loop. The safety check checks for errors coming from the DSP. This could be current trip, speed trip etc. If any of these errors occurs the DSP will disable the inverter and hereby stop any output voltage. If the safety check observes any errors it breaks out

of the for loops and goes to stop and gives an error message. There is also a temperature safety in the safety check, if the temperature level exceeds a certain temperature, there is a cooling loop that gets active. This cooling loop is setting a torque reference of zero and waits for the temperature to get below a certain threshold. When the temperature gets below this threshold the mapping is continued from where it was stopped. After the safety check Matlab sends i_{qs} and i_{ds} to the DSP. The DSP set these values as references in the current control. The current operation point is now set. Before data collection there is a pause in the algorithm to assure steady state. The data collection starts by measuring the torque τ_{meas} according to section 5.2.7. The torque measuring is conducted by measuring the torque τ_{meas} over one second with 100 Hz sampling frequency and taking the mean of this array to get one value for the operating point. The speed ω_m is collected at the same time as the torque. After the torque and speed measurements Matlab sends a signal to the DSP to start data collecting the signals measured by the DSP. The DSP is collecting the measured DC current i_{DC}, DC voltage u_{DC}, stator temperature T_{stator}, q-axis stator current i_{qs}, d-axis stator current i_{ds} and α and β voltage amplitudes $u_{\alpha,\beta-amp}$. The DSP collects 200 points of each signal with a sampling frequency of 1000 Hz. Again the mean is taken of each of the signals to store one value per signal per operation point. i_{DC}, u_{DC}, τ_{meas} and ω_m is collected to calculate the input P_{input} -and output power P_{output}. T_{stator} is collected to be able to compensate for alternating temperatures during the mapping if needed, and to see if and when the cooling loop has occurred. i_{qs} and i_{ds} are collected to ensure that the current controller are obtaining the reference currents. They are also collected in order to estimate parameters in the loss equations presented in chapter 10. $u_{\alpha,\beta-amp}$ is also used in the loss equations. Furthermore it is collected to ensure that the voltage amplitude have not saturated. If the voltage amplitude is saturated the i_{qs} and i_{ds} currents most likely does not correspond with the reference currents. If the currents do not correspond with the references the operation point is discarded. When all the for loops are done the algorithm stops the DSP and the Siemens load drive. When calculating the expected mapping time each operating point is expected to take about 15 seconds including changes in references. From results of the mapping the input and output power are calculated for every operating point using equation (9.1) and (9.2). The efficiency is calculated using equation (9.3).

$$P_{input} = i_{DC} \cdot u_{DC} \tag{9.1}$$

$$P_{ouput} = \tau_e \cdot \omega_m \tag{9.2}$$

$$\eta = \frac{P_{output}}{P_{input}} \tag{9.3}$$

9.2 Mapping Results

In this section the results from the mapping are presented and discussed. The mapping is divided in three parts: all around, high torque and high speed. The division in three parts is due to the fact that a wide spread of magnetization currents is desired at all speeds and torque. The variation of magnetization currents are however more limited at high speeds and high torque. At high torque a minimum magnetizing current is limiting the variation since the phase current amplitude becomes too high at low magnetizing currents. At high speeds the back emf becomes too high at high magnetization currents. This causes saturation of the voltage amplitude. The saturation of the voltage amplitude sets a maximum limit of magnetization current at high speeds. Before the mapping is conducted the algorithm is tested for consistency. Two operating points are tested four times in a row to evaluate the variation in results, one at a low power level and one at a high power level. In figure 9.2 the results from the conducted experiments are shown. The largest variation at the low power level is 2.1 % points at $i_{ds} = 80$ A, and the average variation is 1.3 % points. At the high power level the largest variation is 0.7 % points at $i_{ds} = 140$ A, and the average variation is 0.4 % points. It is expected that the variation is larger at lower power levels due to the fact that small inaccuracies in measurements have larger influence at lower power levels than at higher power levels. The variation of results is considered reasonable at power levels from 0.21 kW (500 rpm 4 Nm) and above. However the results are examined for inconsistencies especially at low power levels.

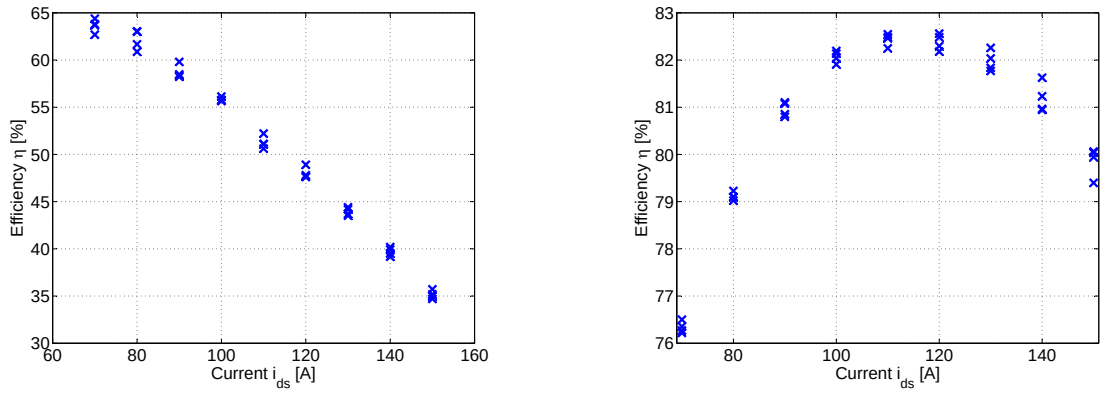

(a) *Efficiency variation at 500 rpm 4 Nm.* ***(b)*** *Efficiency variation at 2500 rpm 20 Nm.*

Figure 9.2: *Efficiency variation at different power levels.*

From the experiment explained above the lowest operating point of the mapping is 500 rpm and 4 Nm torque. The various i_{ds} currents in the all-around mapping are from 65 A to 165 A with a step of 10 A. These i_{ds} currents enables the possibility that i_{ds} is close to equal to i_{qs} at most of

the torque references. These operating points are interesting because when i_{ds} and i_{qs} are equal the stator current i_{qds} is lowest which gives the lowest possible stator conduction loss. The speed operating points for the all-around mapping are from 500 rpm to 2500 rpm with 500 rpm steps. The maximum speed of 2500 rpm is due to the fact that at an i_{ds} current of 165 A results in a high back emf causing the voltage magnitude to saturate if increasing the speed further.The torque array varies from 4 Nm to 20 Nm with 4 Nm steps. At higher torque than 20 Nm the required i_{qs} at i_{ds}=65 A results in a phase current that is too high. The maximum torque of the all-around mapping is therefore set to 20 Nm. The high speed mapping is as mentioned limited by the high back emf. In order to obtain a wide spread of magnetization currents at all high velocities the torque and i_{ds} current array are set individually for each speed level between 3000 rpm and 5000 rpm with 500 rpm steps. The high torque mapping is conducted at 25 Nm. The Siemens drive system nominal torque is 27 Nm. Too ensure a safety margin from the nominal torque of the Siemens drive system a 2 Nm margin is chosen. The safety margin is to ensure that temperature changes etc. does not result in a torque larger than 27 Nm. Due to high phase currents a minimum i_{ds} of 80 A is chosen. The speed array for high torque mapping is similar to the speed array for all around mapping.

The results from the mapping are found on the enclosed CD. In figure 9.3 the efficiencies at a torque of 16 Nm at various speeds and i_{ds} currents are seen. It is seen that the efficiency is increased when raising the speed however the rate it increases is stagnating at high velocities. As seen in figure 9.3 there seems to be an optimum i_{ds} current with regard to efficiency. It is also seen that the optimal i_{ds} current does not seem to change a lot with increasing in speed. This means that at a constant torque the variation of optimal magnetization current according to speed does not result in much change in overall efficiency. At higher speeds however the back emf is so high that i_{ds} has to be changed to avoid voltage saturation. Overall the results in figure 9.3 seems to be credible and consistent, and they can be used to fit loss parameters in chapter 10.
In figure 9.4 efficiencies for various i_{ds} currents at a speed of 3000 rpm and two different torque are seen. Looking at the 8 Nm torque it seems that there is an optimal i_{ds}. The 20 Nm torque does not have an optimum with the operating points used in this mapping at 3000 rpm. i_{ds} could not be set higher because of voltage saturation. In this case is seems the best i_{ds} is the highest possible without going into voltage saturation. Looking at figure 9.4 there seems to be a much bigger potential in changing i_{ds} as a function of the torque to achieve better efficiency. This will be analyzed in chapter 11 where the optimized i_{ds} currents are found. Again the results seems credible and consistent.

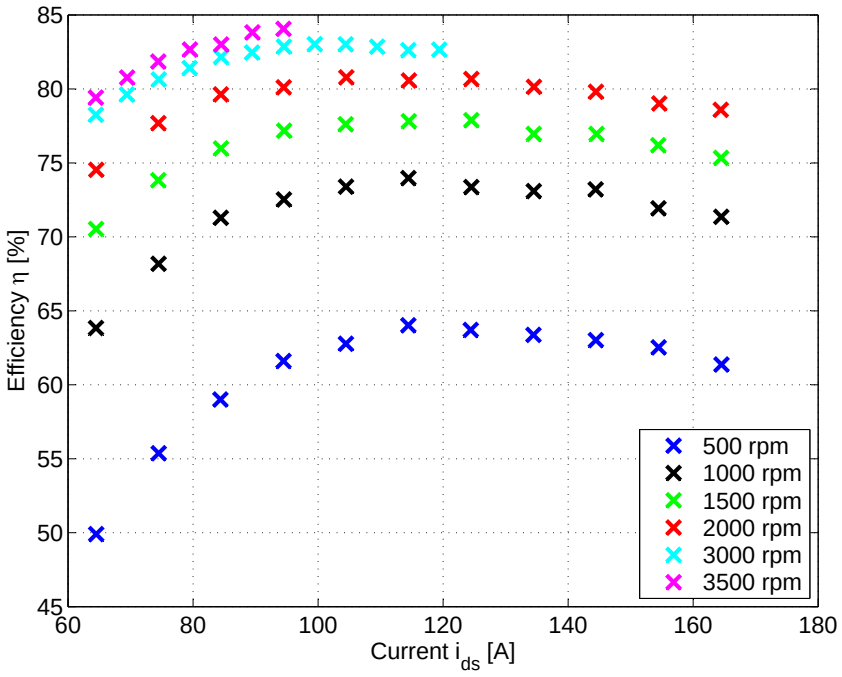

Figure 9.3: *Efficiencies for various i_{ds} currents and speeds at a torque of 16 Nm.*

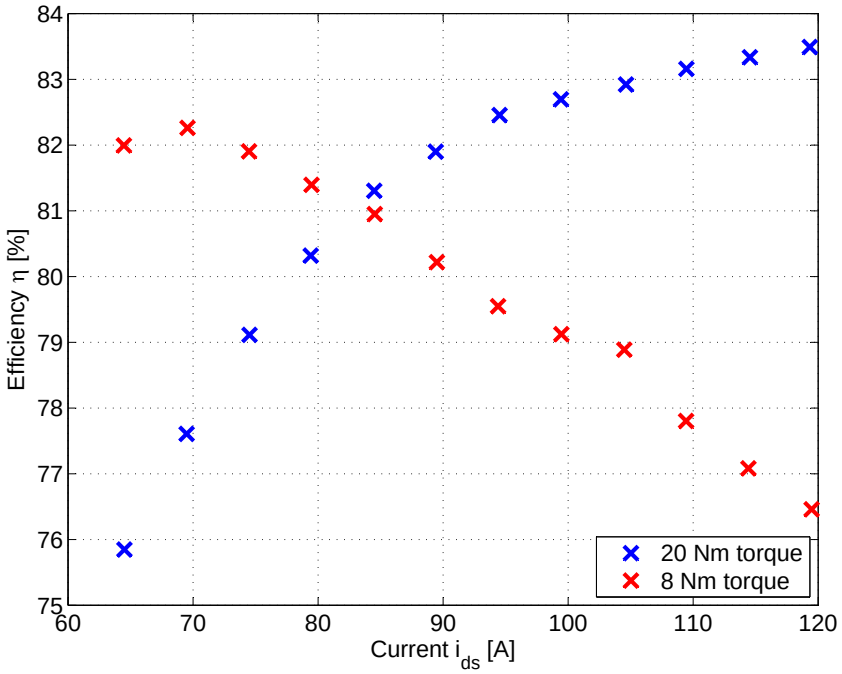

Figure 9.4: *Efficiencies for various i_{ds} currents and torque at a speed of 3000 rpm.*

In figure 9.5 efficiencies at a speed of 500 rpm for various i_{ds} currents and two different torque are seen. At 4 Nm and 500 rpm this is as mentioned earlier in this chapter the lowest power in

the mapping. As seen in figure 9.5 the 4 Nm torque and 25 Nm torque efficiency functions both seem smooth and there seems to be an optimal magnetization current for each torque.

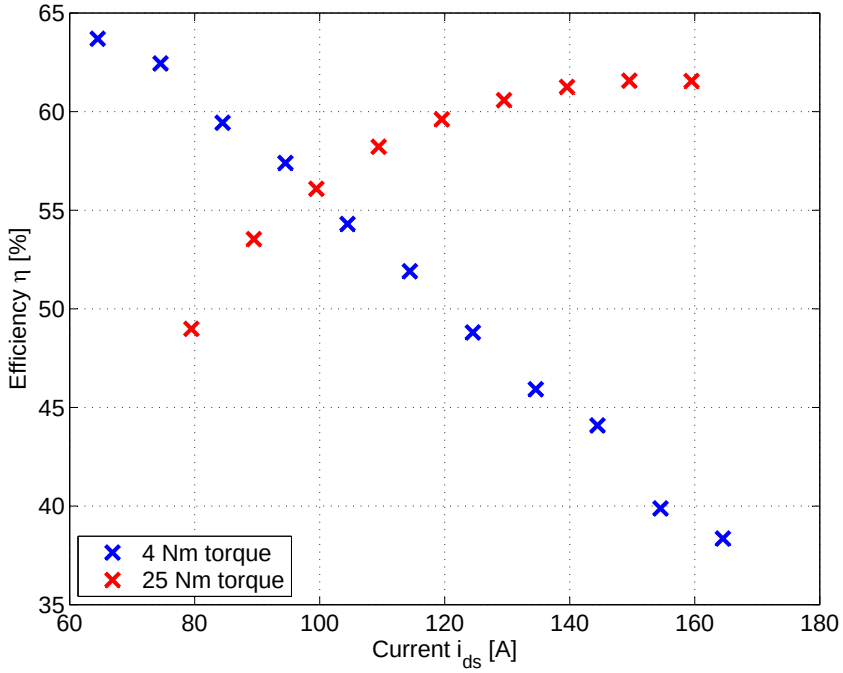

Figure 9.5: *Efficiencies for various i_{ds} currents and torque at a speed of 500 rpm.*

The conclusion of this chapter is that the results from the mapping seems to be credible and consistent and they can be used to finding parameters in the loss equations in chapter 10. Furthermore there seems to be potential for using optimal i_{ds} current to get higher efficiency, especially as a function of the torque, this is done in chapter 11.

Another conclusion of the chapter is that the mapping algorithm together with all the measurement equipment, software and hardware is working properly and could potentially be used for other IM's. The mapping consisting of 475 operating points took around 3-4 hours and one of the major time consumers was cooling down the IM when the stator temperature broke the predefined temperature threshold. The threshold was set at large safety margin from the maximum stator temperature which is 155 °C. If a faster mapping was desired the threshold probably could be increased.

If this mapping should be conducted manually it would take much longer time and the risk of human errors would be significantly larger. The algorithm could still be improved by simple additions such as completely customized operating points enabling individual points of magnetization currents at each speed. This way the mapping could be conducted in one go instead of three. The manual initialization of the mapping would however be more comprehensive. In the

next chapter the mapping results are applied to determine the parameters in the loss equations presented in section 6.5.

CHAPTER 10

ESTIMATION OF LOSS EQUATIONS

In this chapter the unknown parameters in the loss equations presented in section 6.5 is estimated. Using the mapping results from the previous chapter the parameters in the loss equations are determined using a least square optimization algorithm. The optimization algorithm is described and the results are presented and discussed. The optimization algorithm is found on the enclosed CD.

10.1 Optimization Algorithm

In the loss equations presented in section 6.5 there are several parameters that are unknown. The unknown parameters from the inverter equations are resistances and on-voltages of the transistors and diodes and also the switching loss constant K_{sw}. The unknown parameters from the losses in the induction machine are the masses of rotor and stator, the core loss constants $k_{h,s}$ and $k_{r,s}$ and the coefficient for the magnetic material v.

The unknown parameters should ideally be determined separately from experiments however a more time saving method is an optimization using the mapping results to fit the parameters. The idea is to fit the unknown parameters in order to obtain a loss equation that fits the results from the mapping. The general approach of such an optimization is to set start guesses for the unknown parameters. These start guesses are the basis of first iteration of the optimization algorithm. In the starting point the error between the loss equations and the mapping results are evaluated. The gradient and hessian of the error when stepping on each unknown parameter is estimated. From this estimation a proper search direction is calculated. A step is then

taken from the start guesses to new values of the parameters. The step size is dependent on the gradient and hessian. In the new point a new search direction and step size is calculated and a new step is performed. The optimization repeats this procedure until the change in error when performing a step is sufficiently small.
The optimization algorithm used for the estimation of parameters is the *fmincon* function in Matlab. The *fmincon* function handles optimization problems with non-linear constraints.
For the optimization algorithm to work a proper cost function and proper constraints for the design variables (unknown loss parameters) must be determined. The cost function is the function that is to be minimized by the optimization algorithm. In this case the error between the loss equations and the mapping results is to be minimized in all the operating points of the mapping. The cost function is further explained in the preceding section. The constraints for the design variables are determined from what the parameters are expected to be. The constraints are further described later in this section.

10.1.1 Cost Function

The cost function is the function that is to be minimized by the optimization algorithm. In the cost function the following steps are performed:

1. Calculate losses in each operating point using loss equations, $\bar{P}_{loss-eq}$.
2. Calculate losses using input and output power from the mapping at each operating point, $\bar{P}_{loss-actual}$.
3. Calculate $\bar{P}_{error-squared} = \left(\bar{P}_{loss-eq} - \bar{P}_{loss-actual}\right)^2$.
4. Calculate the sum of all elements in error vector $\bar{P}_{error-squared}$.

As seen in the list a least square approach is used in the cost function. The method of least squares involves calculating the square of the error in all operating points and then calculating the sum of all the squared errors as described in the list.

10.1.2 Design Variables

The design variables for the optimization algorithm are the unknown parameters that are to be estimated. The following variables from the loss equations are unknown: $V_{0,t}$, $R_{0,t}$, $V_{0,d}$, $R_{0,d}$, K_{sw}, $\frac{m_r}{m_s}$, ν, $k_{h,s}$ and $k_{e,s}$. The transistors in the inverter are MOSFETs. MOSFETs does not have an on-voltage and functions as a resistance proportional to the gate voltage [Sedra and Smith, 2004, p. 240]. The on-voltage for the transistors, $V_{0,t}$, is therefore set to zero. The diodes in

the inverter are modeled as having an on voltage and no resistance. $R_{0,d}$ is hereby set to zero. The coefficient for the magnetic material is approximately 2 for all modern magnetic materials [Rajput, 2006, p. 242] and is therefore set to 2.

The conduction losses in the motor are dependent on the rotor and stator resistances. The resistances are determined in section 6.3 but may vary from expected values due to temperature uncertainties. The stator temperature is measured during the mapping and the actual stator and rotor resistance is estimated from this temperature. The resistances may however still vary from expected. The stator and rotor resistance are therefore set as design variables to be determined in the optimization.

The design variables for the optimization are therefore:

$$\bar{x} = \begin{Bmatrix} R_{0,t} \\ V_{0,d} \\ K_{sw} \\ \frac{m_r}{m_s} \\ k_{h,s} \\ k_{e,s} \\ R_s \\ R_r \end{Bmatrix} \tag{10.1}$$

10.1.3 Constraints

Since the loss equations are non-linear many local optimum solutions may exist for the optimization problem. It is therefore important to set constraints for the design variables in order to obtain realistic parameters in the loss equations. If the design variables are allowed to obtain any value the loss equations will function as a "black box" where the solution is only valid within the operating points of the mapping. Since the mapping is not performed at torque between 25 Nm to 45 Nm (which is part of the operating area for the IM) it is important that the parameters in the loss equations are realistic so the loss equations can be used to find optimal magnetization currents outside the operating points of the mapping.

The stator resistance is in the loss equations determined from the measured temperature of the stator during the mapping. The stator resistance may however still vary from expected and the constraints for the stator is therefore set to $\pm 5\%$. The rotor resistance in the loss equations is also calculated using the stator temperature. As seen in section 7.3.3 the temperature of the rotor is not similar to the temperature of the stator. The stator temperature is however considered as a better approximation than room temperature. Due to the uncertainty of the rotor temperature

the constraints for the rotor resistance, after being calculated from measured stator temperature, is set to $\pm 20\%$. This corresponds to a temperature uncertainty of 50 $^{\circ}C$.
From figure F.6 on page 68 in appendix the voltage drops across the transistor and diode in the inverter is estimated. The voltage drop across the diode is set to be between 0.2 V and 0.8 V. The voltage drop across the transistor is set to be between 0.2 V and 0.8 V. At a phase current of about 190A this corresponds to a transistor resistance between $1.1m\Omega$ and $4.2m\Omega$.
The core loss constants, $k_{h,s}$ and $k_{e,s}$, are in the optimization set to be positive values. No maximum limit is set. The values of the constants are evaluated after performing the optimization.
The mass relation $\frac{m_r}{m_s}$ is set to be between 0.1 and 2. It is however not expected that the value reaches any of the boundaries. The values are evaluated after the optimization.
The constraints for the switching constant K_{sw} is iteratively set in order to obtain reasonable loss parameters and correspondence with IM efficiencies at operating points described in the datasheet. This correspondence is further described in the results in the preceding section.
The constraints for the design variables are hereby:

x	Min value	Max value	Unit
$R_{0,t}$	0.0011	0.0042	Ω
$V_{0,d}$	0.2	0.8	V
K_{sw}	0	0.0002	V·s
$\frac{m_r}{m_s}$	0.1	2	-
$k_{h,s}$	0	∞	$1/H$
$k_{e,s}$	0	∞	$1/\Omega$
$R_{s,temp}$	-5%	+5%	-
$R_{r,temp}$	-20%	+20%	-

Table 10.1: *Constraints for design variables. The "temp" in the subscripts of resistances denotes that the resistance is calculated from stator temperature before applying the constraints.*

10.2 Results

In order to check the consistency of the optimization several start guesses are tested for each design variable and the same results are obtained for all start guesses. The results for the optimization are as follows:

$$\bar{x} = \begin{Bmatrix} R_{0,t} \\ V_{0,d} \\ K_{sw} \\ \frac{m_r}{m_s} \\ k_{h,s} \\ k_{e,s} \\ R_{s,temp} \\ R_{r,temp} \end{Bmatrix} = \begin{Bmatrix} 0.0042\ \Omega \\ 0.30\ V \\ 0.0002\ V \cdot s \\ 0.71 \\ 33.4\ {}^{1}/_{H} \\ 0.95\ {}^{1}/_{\Omega} \\ +5\ \% \\ +20\ \% \end{Bmatrix} \tag{10.2}$$

The transistor resistance in the inverter and the rotor and stator resistance are set to be the maximum allowable value. This may indicate that the conduction losses in the loss equations are too low and the constraints could have been set higher. As seen later in this section when comparing the loss equations to datasheet efficiencies this might very well be the case.
The mass relation between rotor and stator is set to 0.71. This relation seems reasonable as the stator is expected to be heavier than the rotor.
The core loss constants are evaluated later in this section.
The mean error in power between the mapping results and the loss equations in all operating points of the mapping is 56 W. The mean error in efficiency is 2.4 % points. The largest error in efficiency is 13.7 % points. Since there are three variating factors in the mapping (torque, speed and magnetization current) it is hard to illustrate all efficiency errors in a plot. The largest errors in efficiency however seem to occur at low power. This may be shown by first calculating the mean error of the efficiencies for magnetization currents at each operating point. Since there are positive and negative errors, the mean of the absolute errors are used. The result is seen in figure 10.1. It should be kept in mind that there are several operating points at each data point of the plot due to varying i_{ds} causing a spreading. The spreading in efficiency at each operating point is not seen in the figure. The largest variations in efficiency however are at 4 Nm and 5000 rpm where the efficiency error varies between 4.8% and 12.9%. The lowest variations are at 25 Nm 1500 rpm where the efficiency error varies between -2% and 0.7%.
The electric vehicle is expected to mainly operate at high power levels. Since the errors in the estimated loss equations seems low at high power levels the loss equations are considered usable

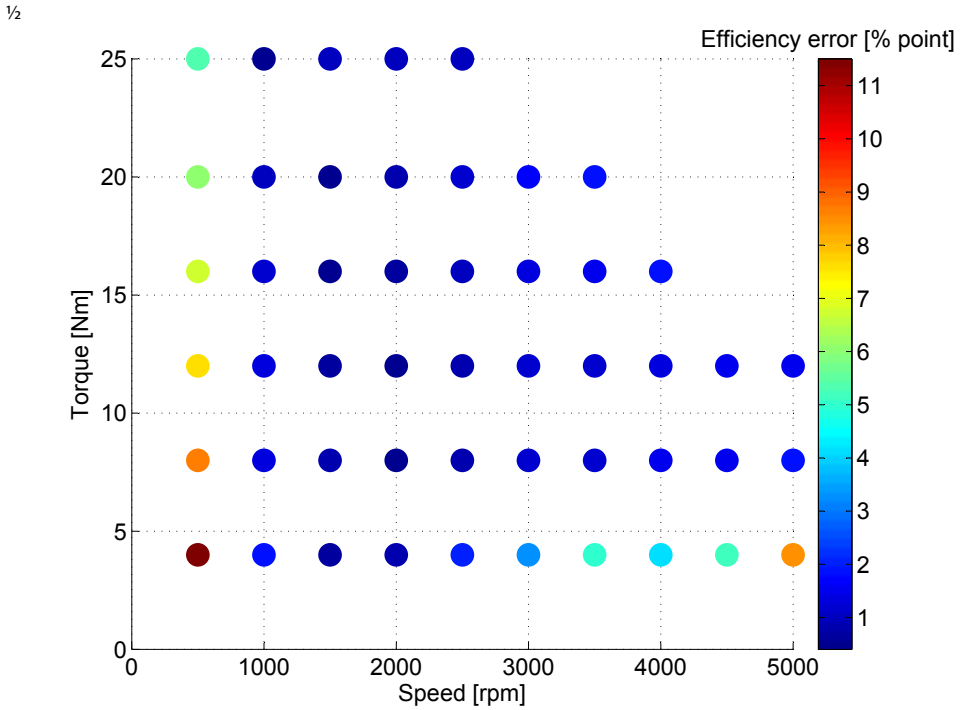

Figure 10.1: *Mean error in efficiency at various operating points.*

for loss simulations of the electric vehicle at least within the operating points in the mapping. When calculating energy optimal magnetization currents using the estimated loss equations it is important that the tendency of the loss equations corresponds with the mapping results. In figure 10.2 the efficiency calculated from the loss equations is compared to the mapping results at various speeds and magnetization currents at a torque of 16 Nm. As seen in the figure the loss equations seem to follow the mapping results best at high speeds (high power). The optimal magnetization current according to the loss equations does not correspond entirely with the optimal magnetization current according to the mapping results at all velocities. The efficiency at the optimal magnetization current according to the mapping is however not much different from the efficiency at the optimal magnetization current according to the loss equations. Using the optimal magnetization current according to the loss equations would therefore provide an efficiency that is close to the actual optimal efficiency.

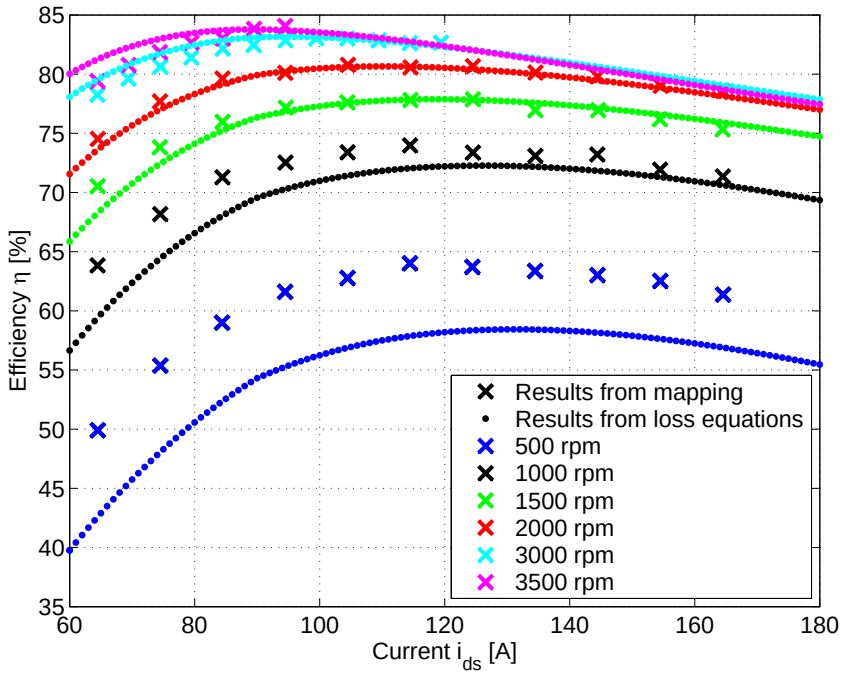

Figure 10.2: *Efficiency calculations from loss equations compared to results from the mapping for various i_{ds} currents and speeds at a torque of 16 Nm. The stator temperature used in the loss equations is 130 °C.*

The loss equations compared to the mapping results at the operating points presented in the previous chapter are seen in figure 10.3. From figure 10.3a and 10.3b it is seen that the error in the loss equations is more distinct at low speed (500 rpm) compared to high speed (3000 rpm) and especially at low power (4 Nm and 500 rpm). The optimal magnetization current according to the loss equations is however considered to correspond satisfactory with the optimal magnetizing current according to the mapping. The loss equations estimated from the optimization are hereby considered as being valid for finding optimal magnetization currents within the operating points of the mapping.

Since it is desirable to determine optimal magnetization currents and general powertrain losses in the entire operating area of the IM the loss equations must be checked in operating points outside the mapping. Since the maximum torque of the Siemens drive system is 27 Nm the loss equations cannot be compared to experimental results for torque above 27 Nm. In the datasheet however three operating points are described. These points are 2000 rpm 45 Nm, 3400 rpm 22.5 Nm and 5000 rpm 13.4 Nm. According to the datasheet the efficiency at 2000 rpm 45 Nm is 80 %, the efficiency at 3400 rpm 22.5 Nm is 87 % and the efficiency at 5000 rpm 13.4 Nm is 90 %. In the datasheet however it is pointed out that the efficiencies are estimates. Using the voltage, torque and rotor velocity at each operating point the magnetizing current, i_{ds}, are

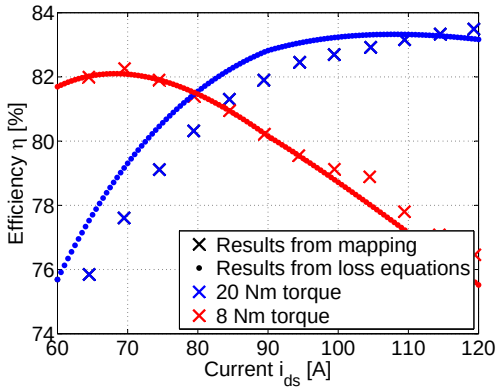

(a) Efficiency calculations from loss equations compared to results from the mapping for various i_{ds} currents at 3000 rpm and at two different torque.

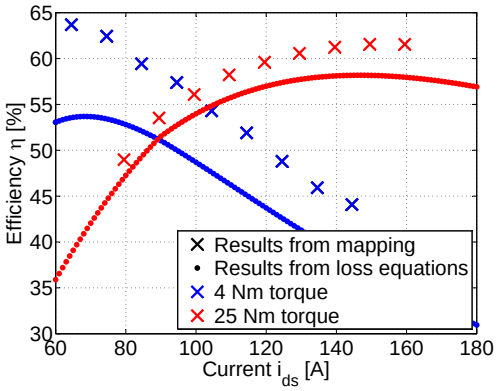

(b) Efficiency calculations from loss equations compared to results from the mapping for various i_{ds} currents at 500 rpm and at two different torque.

Figure 10.3: *Efficiency calculations from loss equations compared to results from the mapping at various torque, velocities and magnetization currents. The stator temperature used in the loss equations is 130 °C.*

determined iteratively in the Simulink model. The magnetizing current is 200 A, 87 A and 59 A at 2000 rpm, 3400 rpm and 5000 rpm respectively. In figure 10.4 the efficiency at the operating points according to the loss equations is depicted.

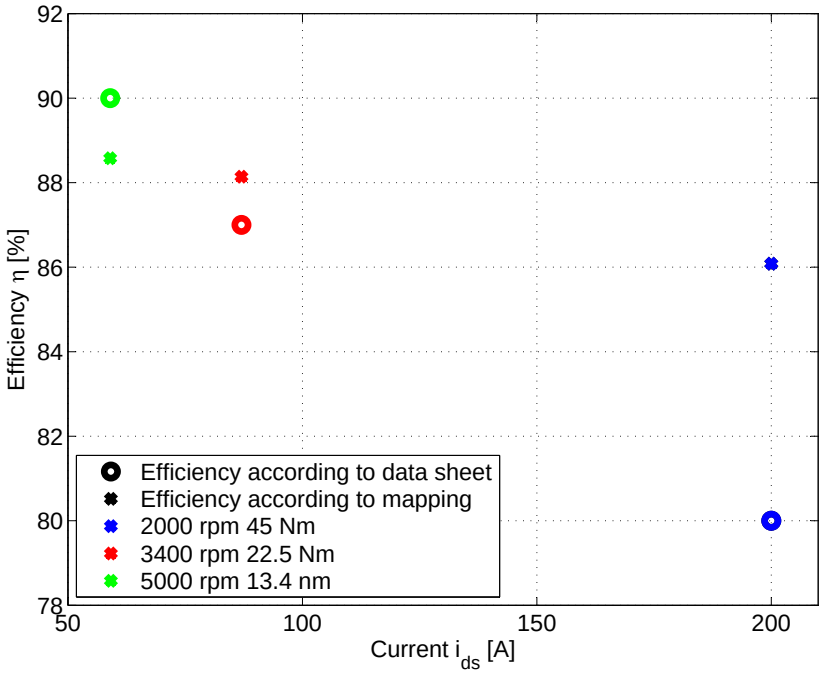

Figure 10.4: *Efficiency calculations from loss equations at operating points described in datasheet. The stator temperature used in the loss equations is 130 °C.*

When comparing the efficiencies from the datasheet with figure 10.4 it is seen that at 2000 rpm 45 Nm the efficiency is about 6 % points too high compared to the datasheet. At 3400 rpm 22.5 Nm it is about 1.1 % point too high and at 5000 rpm 13.4 Nm it is about 1.4% points too low. Since the efficiency is too high at low velocity (especially at high torque levels) and too low at high velocity it seems that the conduction losses are too low in the motor loss equations and the core losses are too high. This corresponds well with the fact that the stator and rotor resistances in the optimization are calculated as the maximum values allowed. Had the constraints been loosened the resistances would have been larger and the core loss constants would have been smaller. The motor losses may then have corresponded better with the efficiencies from the datasheet. The distribution of core- and conduction loss in the induction machine at various operating points is seen in figure 10.5. The core losses increase as function of the speed and the conduction losses increase as function of the torque (and hereby the current) just as expected.

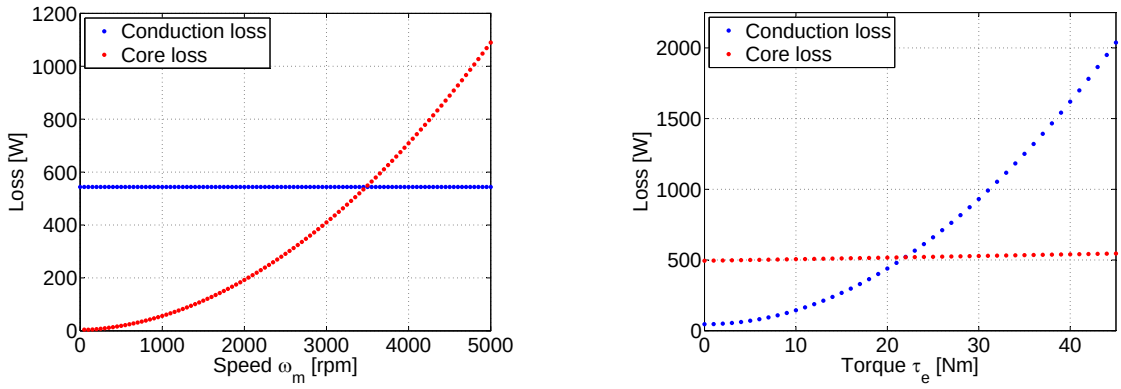

(a) *Conduction and core losses at various velocities. i_{ds} is set to 100 A and the torque is set to 22.5 Nm.*

(b) *Conduction and core losses at various torque. i_{ds} is set to 100 A and the velocity is set to 3400 rpm.*

Figure 10.5: *Core and conduction losses in induction machine at various operating points. The stator temperature used in the loss equations is 130 °C.*

The loss equations could be improved by conducting separate experiments for the components in the inverter in order to set some more realistic constraints. The loss equations are however considered as usable for loss estimation in the powertrain and for determination of optimal magnetization currents in the entire operating area of the induction machine. The optimal magnetizing currents are found in the following chapter.

CHAPTER 11

OPTIMAL MAGNETIZING CURRENT

In the previous chapter it was concluded that the estimated loss equations are suitable for determination of energy optimal magnetizing currents in the entire operating area of the induction machine. In this chapter these energy optimal magnetizing currents are determined. An optimization algorithm is used on the loss equations in order to determine the magnetizing currents that provides the best efficiency in the entire operating area.
As in the previous chapter the applied optimization algorithm is described and the results are presented. The optimization algorithm is found on the enclosed CD.

11.1 Optimization Algorithm

The optimization algorithm is to determine the optimal magnetizing current at all operating points of the induction machine. The optimization algorithm therefore only have one design variable, $i_{ds-optimal}$. At each torque and speed the magnetizing current providing the best efficiency is to be determined. The objective function that is to be minimized at each operating point is therefore the total loss of the inverter and of the IM from the loss equations estimated in the previous chapter.
The constraints for the optimization problem are dependent on the particular operating point and are therefore not linear. The energy optimal magnetization current may conflict with the available DC bus voltage or the maximum phase current allowed. The constraints for the optimization problem is therefore that the modulation index is not allowed to exceed 1.15 (The extra 15 % comes from using space vector modulation) and the length of the i_{qds} current is not

allowed to exceed 430 A. These constraints ensure that required phase voltages do not exceed what is available in the DC bus and that the phase current does not exceed 430 A. The constraint for the design variable i_{ds} is that it has to be positive.
The inputs to the loss equations (modulation index, slip, rotor flux velocity, phase voltages, phase currents, L_M and the phase shift) are calculated using voltage and torque equations described section 6.3, flux equations described in section 7.2.1, the equation for L_M described in section 7.3.3 and the steady state model.

11.2 Results

The start guess for the design variable, i_{ds}, is varied in order to check the consistency of the results. The results are the same at all start guesses. The results are seen in figure 11.1.

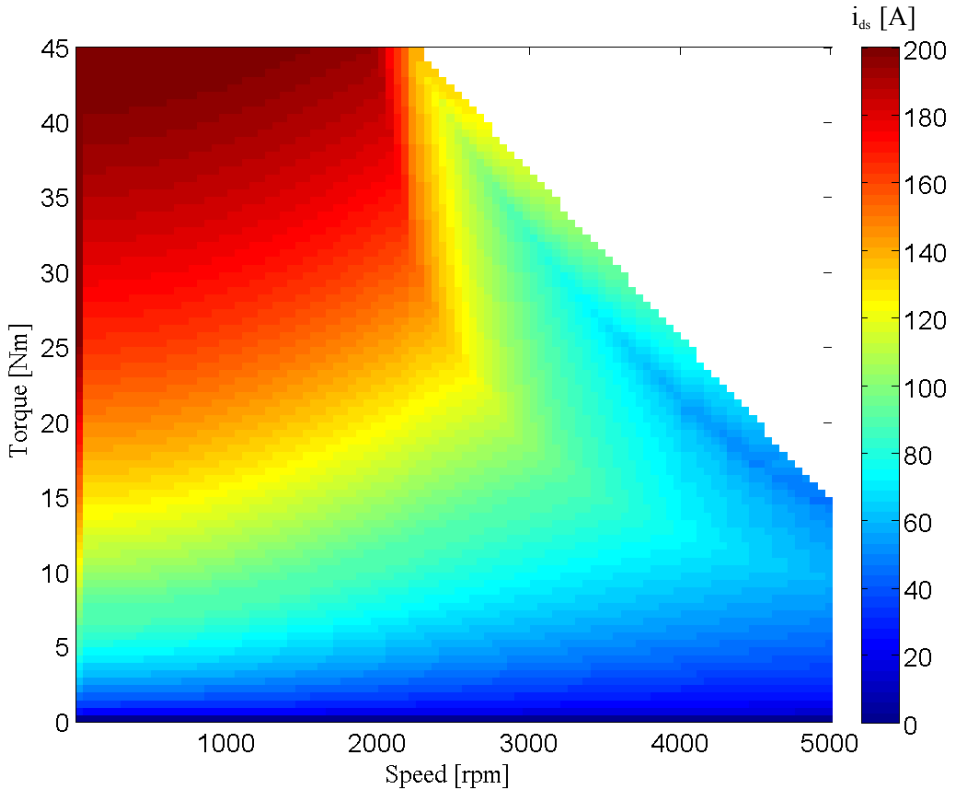

Figure 11.1: *Optimal magnetizing currents in the entire operating area of the induction machine.*

As seen in the figure there are some combinations of torque and speeds that are not obtainable. This is due to the constraints in the optimization algorithm. The optimal magnetizing current is highest at low speeds and high torque. This is expected as the conduction losses and switching losses are dominant at low speeds and the best efficiency hereby is obtained by minimizing the

stator current. When raising the torque the magnetizing current must be increased in order to obtain the lowest stator current. When raising the speed the core losses becomes more significant and the optimal magnetizing current decreases in order to obtain the lowest combination of conduction losses, core losses and switching losses.
In order to verify the validity of the optimization the optimum magnetizing currents are compared to the loss equations at various operating points. This is seen in figure 11.2. As seen in the figure the optimal magnetizing currents correspond well with the loss equations.

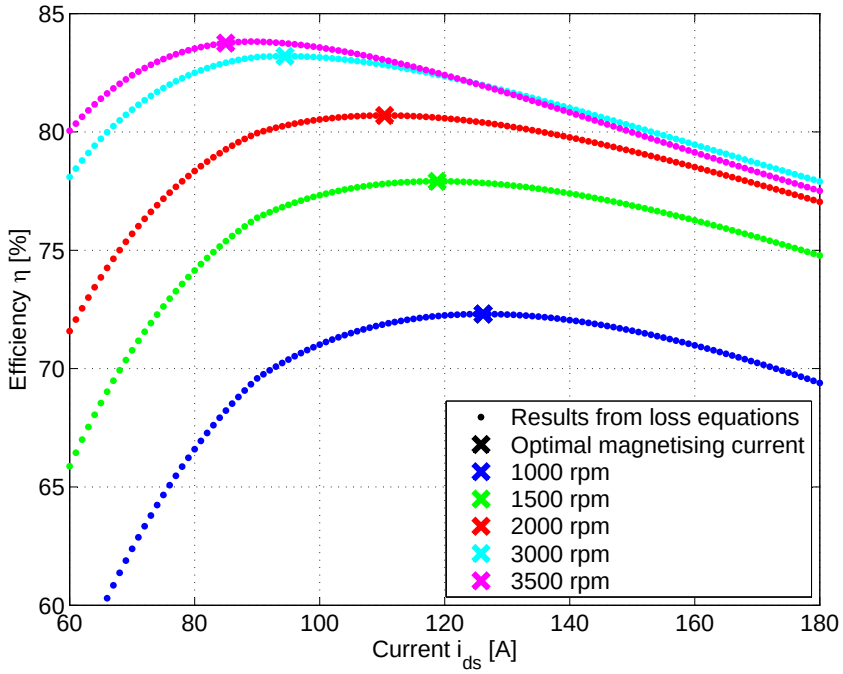

Figure 11.2: *Optimal magnetizing currents compared to loss equations at various speeds.*

In figure 11.3 the optimal currents are compared with the mapping results at various speeds. As expected from the estimation of the loss equations the optimal magnetizing current from the optimization does not correspond entirely with the optimal current according to the mapping. When using the optimal magnetizing current according to the optimization the loss in efficiency, compared to the maximum efficiency attained in the mapping, is however considered acceptable (<1%).
The optimal magnetizing currents determined from the optimization described in this chapter are considered as reasonable compared to the mapping results. The efficiency obtained using the optimal magnetizing currents throughout the entire operating area is seen in figure 11.4.
As seen in figure 11.4 the maximum efficiencies can be obtained at high speed. A better resolution of colors at high efficiencies is seen in figure 11.5.

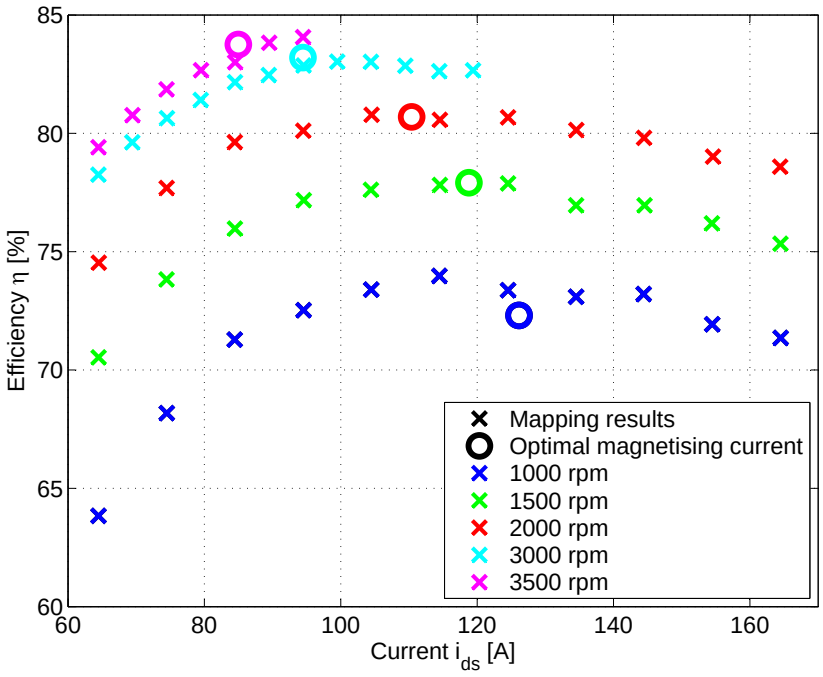

Figure 11.3: *Optimal magnetizing currents compared to mapping results at various speeds.*

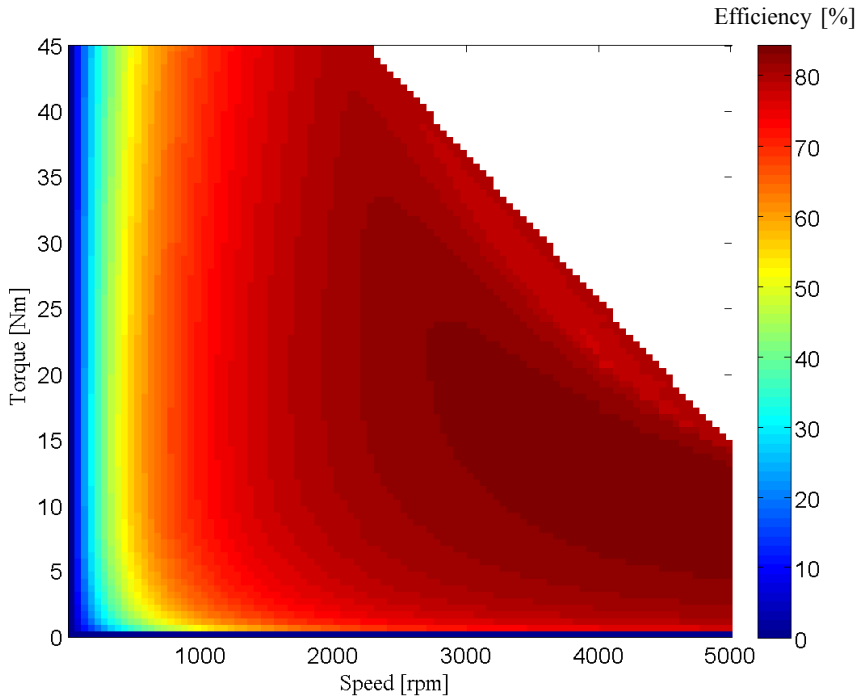

Figure 11.4: *Efficiencies attainable in the operating area using optimal magnetizing currents.*

In the next chapter the implementation of energy optimal control in the electric vehicle is con-

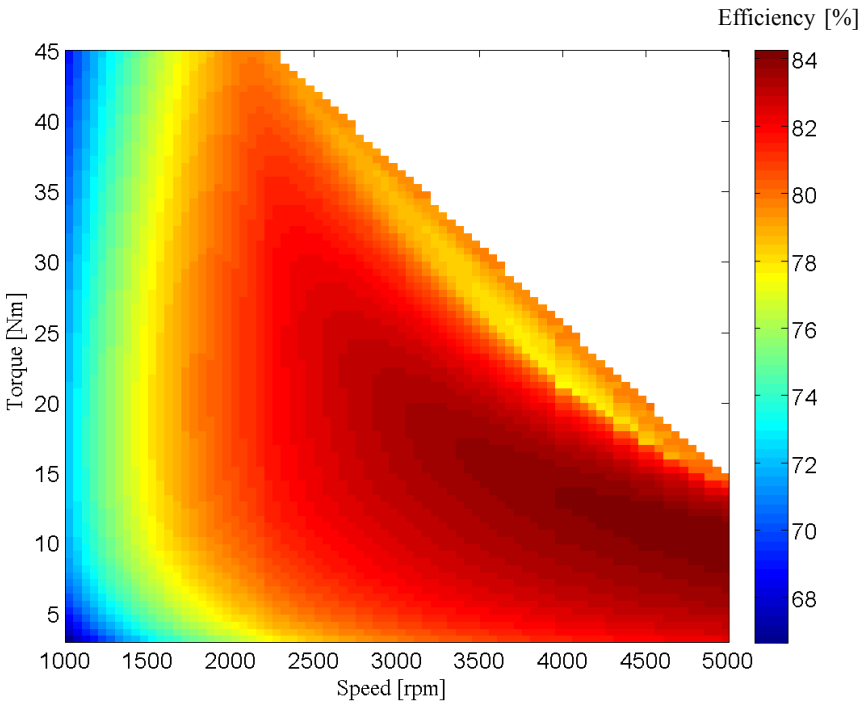

Figure 11.5: *Closer view of figure 11.4.*

sidered. The results from this chapter are utilized in order to obtain an energy efficient field oriented control of the electric vehicle.

CHAPTER 12

IMPLEMENTATION OF ENERGY OPTIMAL CONTROL IN EV

In this chapter an implementation strategy for energy optimal control of the electric vehicle is developed. In the last chapter the most energy efficient magnetizing currents where determined for the entire operating area. An energy optimal control of the electric vehicle is to obtain the best possible efficiency in the entire operating area. A possible implementation strategy for the energy optimal control could therefore be to change the magnetizing current as function of the electrical torque from the induction machine and the rotor speed according to the optimal magnetizing currents determined in the preceding chapter. A problem that must be considered when developing an implementation strategy is the slow response of the magnetizing flux when applying a magnetizing current. Furthermore some of the assumptions in field oriented control (section 7.1) are made on basis of a non-changing rotor flux. These problems may entail that the proposed strategy does not provide an acceptable performance nor a good efficiency.
The dynamics of changing the rotor flux λ'_{dr} is analyzed in this chapter and effects due to parameter variation and cross coupling effects are also examined. Various implementation strategies are developed and tested on a urban driving cycle. The strategies are evaluated by energy efficiency and performance throughout a driving cycle on basis of demands stated in the problem formulation, chapter 3.
The urban drive cycle used is the U.S Environmental Protection Agency's "Urban Dynamometer Driving Schedule" which represents city driving conditions and is used for light duty vehicle testing. Besides evaluating the implementation strategies when simulating the driving cycle the

general performance of the powertrain is also evaluated. The purpose of this evaluation is to determine whether the electric vehicle needs a larger induction machine in order to provide acceptable performance which is expected due to the performance evaluation in section 5.2.3.

12.1 Transient Dynamics of Rotor Flux

In this section the transient dynamics of the d-axis rotor flux λ'_{dr} when changing the magnetizing current is evaluated.
In rotor flux field oriented control the d-axis stator current i_{ds} controls the d-axis rotor flux λ'_{dr}, see equation (7.65), for convenience it is repeated in equation (12.1).

$$\lambda'_{dr} = \frac{L_M}{1 + \frac{L_r}{R'_r} \cdot p} \cdot i_{ds} \tag{12.1}$$

It is seen from equation (12.1) that when changing the d-axis stator current i_{ds} the d-axis rotor flux λ'_{dr} changes exponentially with a time constant of $\tau_r = \frac{L_r}{R'_r}$, see figure 12.1. At no flux saturation and ambient temperature the time constant is calculated as in equation (12.2).

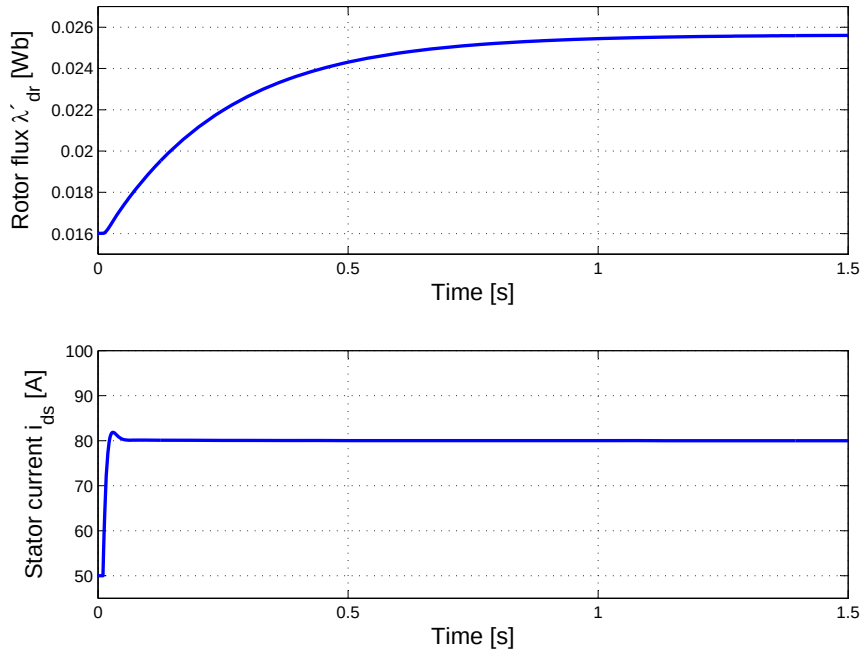

Figure 12.1: *Simulation of the rotor flux response at i_{ds} step in none saturated region, $i_{qs} = 100A$ and speed is 0 rpm.*

$$\tau_r = \frac{L_r}{R'_r} = \frac{3.40 \cdot 10^{-4} H}{0.0014 \Omega} = 0.25 \cdot s \tag{12.2}$$

The time constant τ_r decreases as the flux saturates and it also decreases with increased rotor temperature. The decrease in time constant entails a faster flux dynamic. The highest time constant is hereby obtained at low temperature and no flux saturation. The time it take to reach 98 % of the steady state value is around $4 \cdot \tau_r$ which is 1 s at ambient temperature and no saturation, this is seen in figure 12.1.

The effect of an increased rotor temperature from 22 to 100 °C is seen in figure 12.2. The rotor resistance R'_r is calculated from the rotor temperature as in equation (6.29). τ_r is in this operating point 0.18 s which is a decrease of 28 % from the original τ_r.

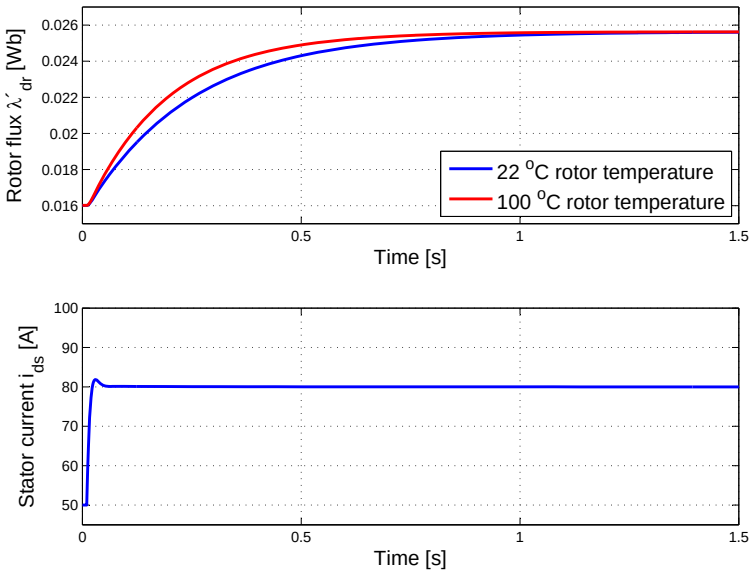

Figure 12.2: *Simulation of the rotor flux response at various temperatures, $i_{qs} = 100A$ and speed is 0 rpm.*

Figure 12.2 is at zero speed operation where there is close to no cross coupling between the q- and d-axis currents. At higher speeds the cross coupling has larger effect on the flux dynamics. In figure 12.3 the flux response from a simulation at 5000 rpm and zero rpm with a step on the d-axis stator current i_{ds} from 50 to 80 A is depicted. It is seen that the cross couplings at 5000 rpm prolongs the time it takes for the flux to reach 98 % of steady state by approximately 0.5 s. This means that the flux dynamics are slower at higher speeds and which should be noted when developing the implementation strategies.

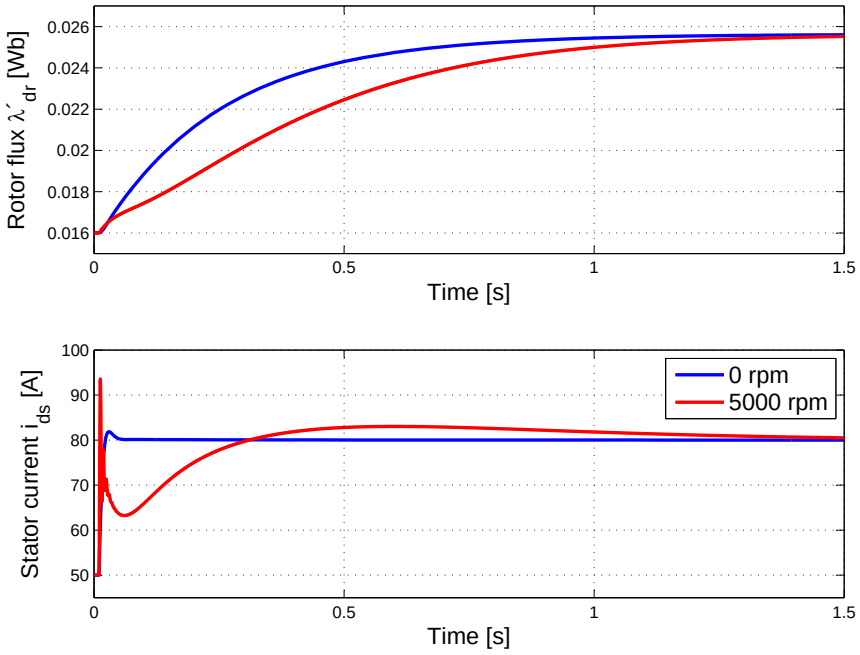

Figure 12.3: *Simulation of the rotor flux response at i_{ds} step in none saturated region, $i_{qs} = 100A$.*

The torque response for changing i_{ds} is similar to the flux response. This is seen from equation (12.3). The torque is proportional with the d-axis rotor flux λ'_{dr} and therefore if the flux is changing slowly so is the torque.

$$\tau_e = \frac{3}{2} \cdot \frac{P}{2} \cdot \frac{L_M}{L_r} \cdot \lambda'_{dr} \cdot i_{qs} \tag{12.3}$$

12.2 Implementation Strategies

This section contains suggestions for implementation strategies of energy optimal control in the electric vehicle. Three strategies are considered.

Strategy 1

The first suggestion for an implementation strategy is varying the magnetizing current as function of the torque reference and the rotor velocity according to the optimal magnetizing currents in the preceding chapter. The strategy is illustrated in figure 12.4. The * on the parameters involving L_M denotes that L_M is to be compensated according to the magnetization current as described in section 7.3.3. The determination of the optimal magnetizing current is done on

basis of the optimal currents according to figure 11.1. The calculated current references are send to the current controllers described in chapter 7.
When using this implementation strategy in the simulated driving cycle it is expected that the desired magnetizing flux is attained in the entire cycle. As the magnetizing current changes severely as function of the torque, a fast changing torque reference may cause the magnetizing flux to never reach steady state. This may compromise the performance and the efficiency.

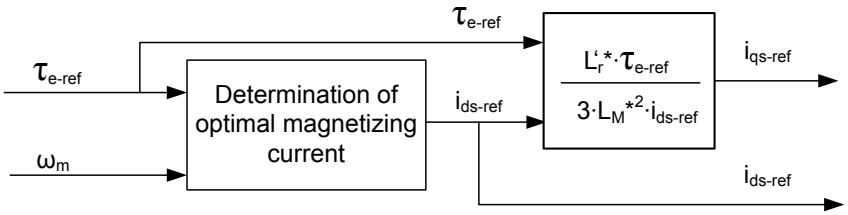

Figure 12.4: *Strategy 1 for implementation of energy optimal control.*

Strategy 2

The second suggestion for an implementation strategy is to apply the nominal magnetizing current according to the datasheet of the induction machine. As mentioned in section 7.3.3 the nominal magnetizing current is determined to 200A using the simulation model and the datasheet. The nominal magnetizing current is applied at speeds from 0 to 2000 rpm. At speeds above 2000 rpm the magnetizing current is limited by voltage saturation. The magnetizing current is hereby a function of rotor velocity. The magnetizing current as function of rotor velocity is depicted in figure 12.5. The strategy is depicted as in figure 12.6.
When using this implementation strategy in the simulated driving cycle it is expected that the desired magnetizing flux corresponds better to the actual magnetizing flux compared to when using strategy 1. This is due to the fact that strategy 2 only uses the velocity to determine the magnetizing current and the variations in desired rotor flux hereby are decreased. As the nominal magnetizing flux is not energy optimal in a large part of the operating area it is expected that the efficiency is worse using strategy 2 compared to strategy 1. The performance however is expected to be improved by using strategy 2.

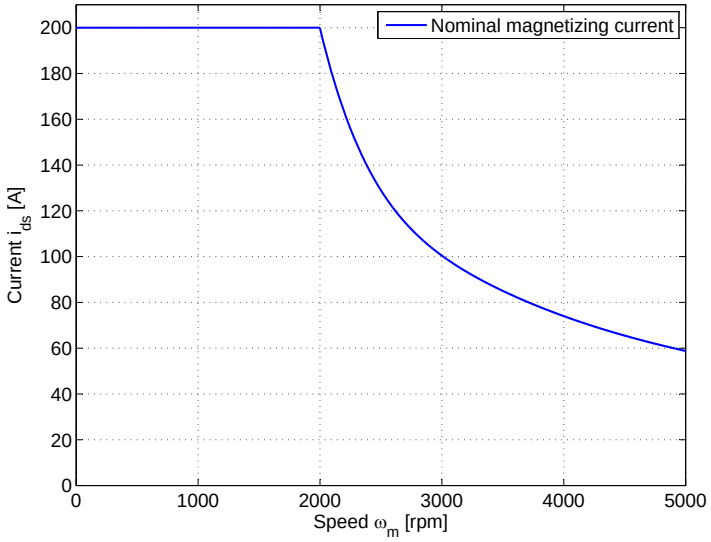

Figure 12.5: *Magnetizing current as function of velocity using strategy 2.*

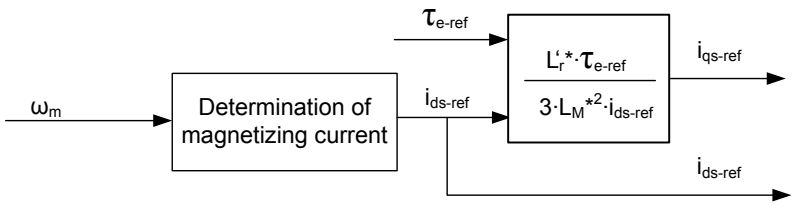

Figure 12.6: *Strategy 2 for implementation of energy optimal control.*

Strategy 3

The third suggestion for an implementation strategy is an extension of strategy 1. The difference from strategy 1 is that the torque reference for determination of magnetizing current is to be filtered. The strategy is illustrated in figure 12.7.

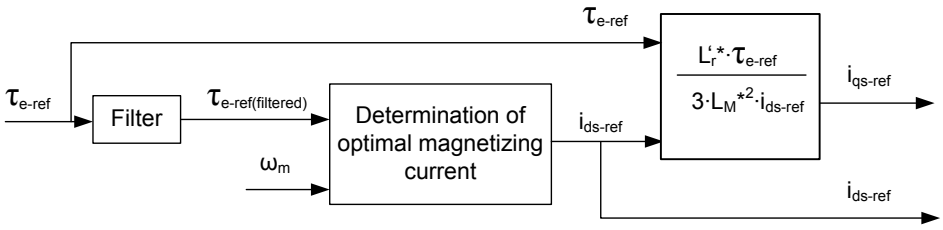

Figure 12.7: *Strategy 3 for implementation of energy optimal control.*

The filter is a first order filter which corresponds to the first order system of the flux, equation (12.1).

Strategy 3 is a compromise between strategy 1 and strategy 2. Strategy 2 is expected to provide

better correspondence between torque reference and actual torque compared to strategy 1 due to the fact that the magnetizing current does not change as function of the torque. In strategy 1 the magnetizing current changes as function of the torque reference and it is therefore expected that fast changes in torque reference will provide bad correspondence between torque reference and actual torque as the time constant for the flux is slow. As the torque reference is filtered in strategy 3 the fast changes in torque will not provide as fast changes in flux reference and a better correspondence between reference and actual torque is therefore expected. Due to the bad correspondence between flux reference and actual flux in strategy 1 when changing the torque reference fast the efficiency obtainable using strategy 3 may actually be better than when using strategy 1.

12.3 Simulation of drive cycle

The driving cycle used for evaluation of implementation strategies is the U.S Environmental Protection Agency's "Urban Dynamometer Driving Schedule" which represents city driving conditions and is used for light duty vehicle testing. The drive cycle is depicted in figure 12.8. The length of the drive cycle is 1369 s and stretches over about 12 km.

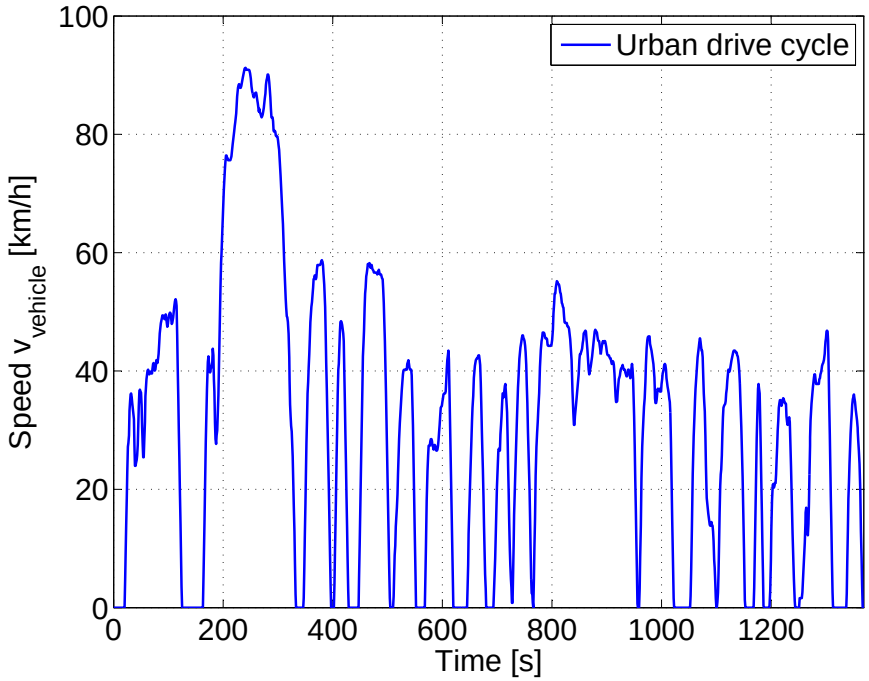

Figure 12.8: *Urban drive cycle.*

When simulating the drive cycle a speed controller is needed in order to obtain desired speeds.

The speed controller used is a PI controller. The simulation of the drive cycle is illustrated as in figure 12.9.

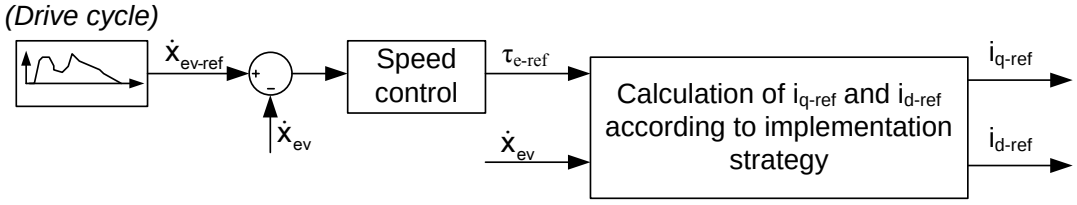

Figure 12.9: *General structure of simulation of drive cycle.*

When a negative torque reference is calculated from the speed control the induction machine is to apply regenerative breaking of the electric vehicle. Besides regenerative braking a mechanical braking is also to be applied. In this report regenerative braking is not considered and therefore only mechanical braking is applied in the simulation. As regenerative breaking is not included the efficiency during the simulation is going to be less than the actual attainable efficiency in the electric vehicle. The mechanical braking is implemented as in figure 12.10. If the output of the speed control is negative the mechanical braking is activated. The brake controller is similar to the speed controller. The output of the brake control is added to the torque equation. When the output of the speed controller becomes positive the brake controller receives zero as input and the integrator in the brake control is reset. Anti wind-up for the speed controller is implemented in the simulation however it is not illustrated in the figure.

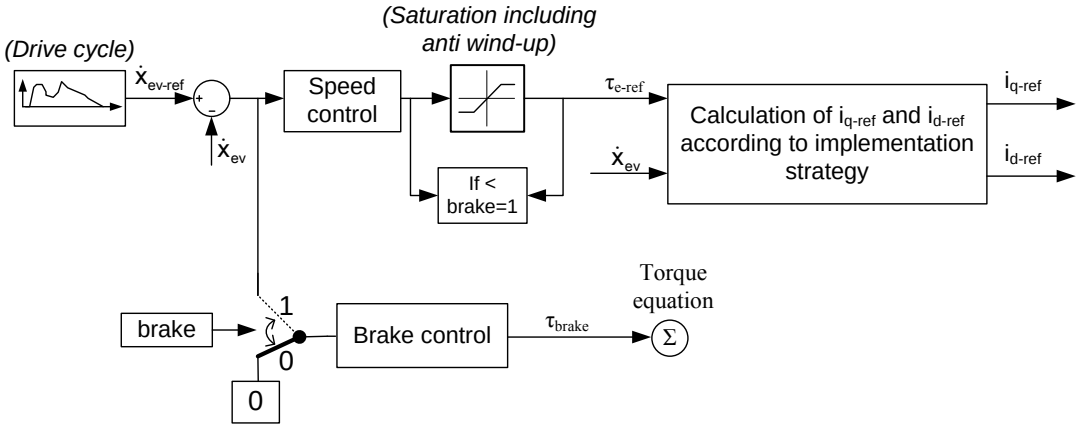

Figure 12.10: *Mechanical braking in simulation.*

As seen in figure 12.8 the maximum speed of the electric vehicle during the drive cycle is 91 $^{km}/_{h}$. As seen in section 5.2.3 the maximum speed of the electric vehicle with the IM implemented is about 69 $^{km}/_{h}$. In figure 12.11 the drive cycle is simulated with strategy 1 implemented.

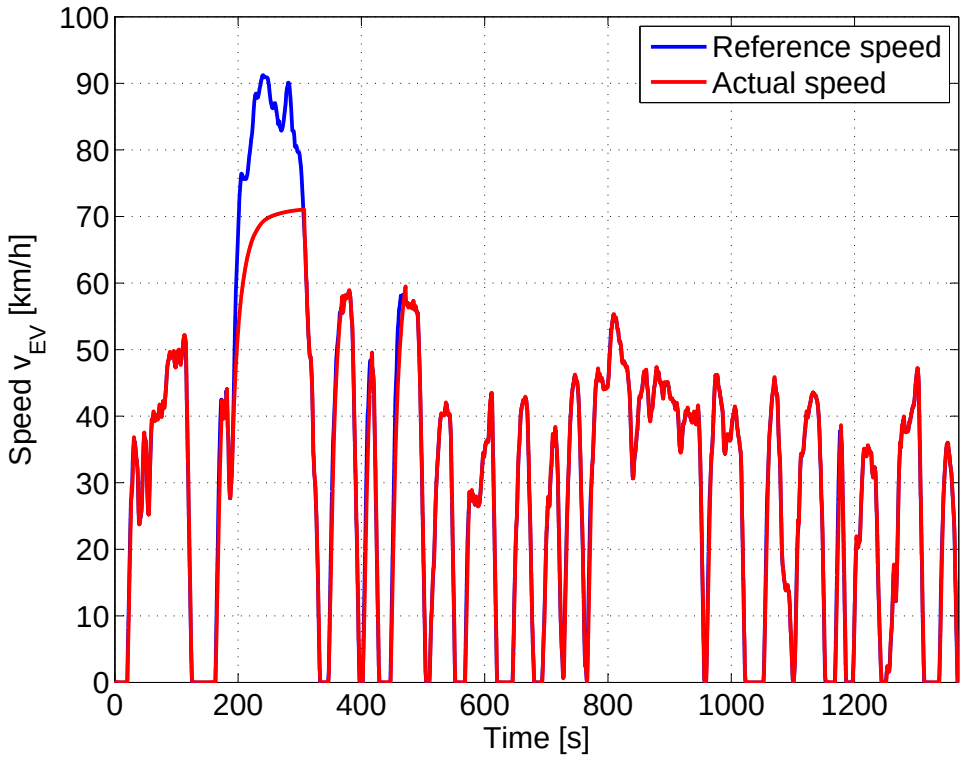

Figure 12.11: *Simulation results using strategy 1 with original IM implemented.*

As expected the maximum velocity of the electric vehicle is about 69 $^{km}/_{h}$. As stated in the demand specification the maximum velocity of the electric vehicle should be at least 80 $^{km}/_{h}$. In order to test the control strategies on an EV that fulfills the demands in the demand specification a larger induction machine is implemented when simulating the drive cycle. This is done by multiplying the electrical torque produced by the induction machine by 2. This simulates an induction machine able to deliver twice the amount of torque as the original induction machine. The maximum velocity of the electric vehicle (and hereby induction machine) is now increased and the optimal magnetizing currents determined in chapter 11 is expanded to contain velocities above 5000 rpm and so is the magnetizing current graph for strategy 2. The maximum speed of the electric vehicle at zero wind speed and zero gradient of the road is about 84 $^{km}/_{h}$. This is seen in figure 12.12.

The efficiency of the induction machine and inverter throughout the drive cycle is evaluated using equation (12.4).

$$\eta_{Drive-cycle} = \frac{E_{input} - E_{loss}}{E_{input}} \tag{12.4}$$

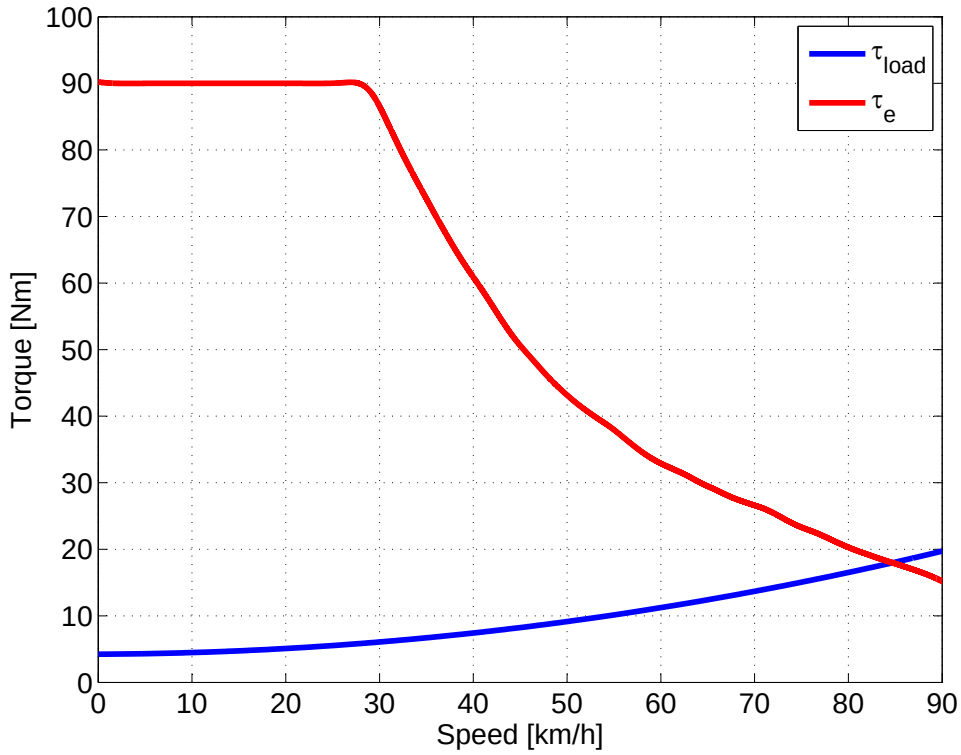

Figure 12.12: *Torque from IM providing twice the torque than the original IM compared to τ_{load}. τ_{load} is the load torque counteracting the electric torque τ_e. These torque are described in section 6.4.*

where:	$\eta_{Drive-cycle}$	Energy efficiency in simulated drive cycle $[-]$
	E_{input}	Total input energy throughout the drive cycle $[J]$
	E_{loss}	Total losses throughout the drive cycle $[J]$

Besides overall efficiency the strategies are also evaluated from the range per battery charge. The battery pack in the Kewet EV consists of 20 cells each containing a nominal energy of 0.512 kWh. 20 Cells hereby yields an energy of 10.24 kWh. The range of the EV per charge is evaluated from equation (12.5). Since the velocity of the electric vehicle does not correspond with the drive cycle at velocities above 84 $^{km}/_{h}$ the length of the drive cycle should be less than 12 km. This is however neglected.

$$L_{EV} = \frac{E_{battery-pack}}{E_{input}} \cdot L_{drive-cycle} \tag{12.5}$$

where:	L_{EV}	Range per charge of EV $[m]$
	$E_{battery-pack}$	Energy in battery pack $[J]$

E_{input}	Total input energy throughout the drive cycle $[J]$
$L_{drive-cycle}$	Length of drive cycle $[m]$

12.4 Evaluation of Implementation Strategies

The implementation strategies are now evaluated from simulations of the drive cycle where the powerful induction machine is implemented.

Implementation of strategy 1

The speed throughout the drive cycle with strategy 1 implemented is depicted in figure 12.13. As seen in the figure the speed reference seems to be reached throughout the drive cycle except at speeds above 84 $^{km}/_{h}$. The maximum error in velocity (when looking aside the velocities above 84 $^{km}/_{h}$) is less than 5 $^{km}/_{h}$. The efficiency throughout the drive cycle is depicted in figure 12.14. The overall efficiency is calculated to 69% using equation (12.4). The total input energy E_{input} for this strategy is 1.53 kWh. From equation (12.5) the length per charge is evaluated to 79.6 km.

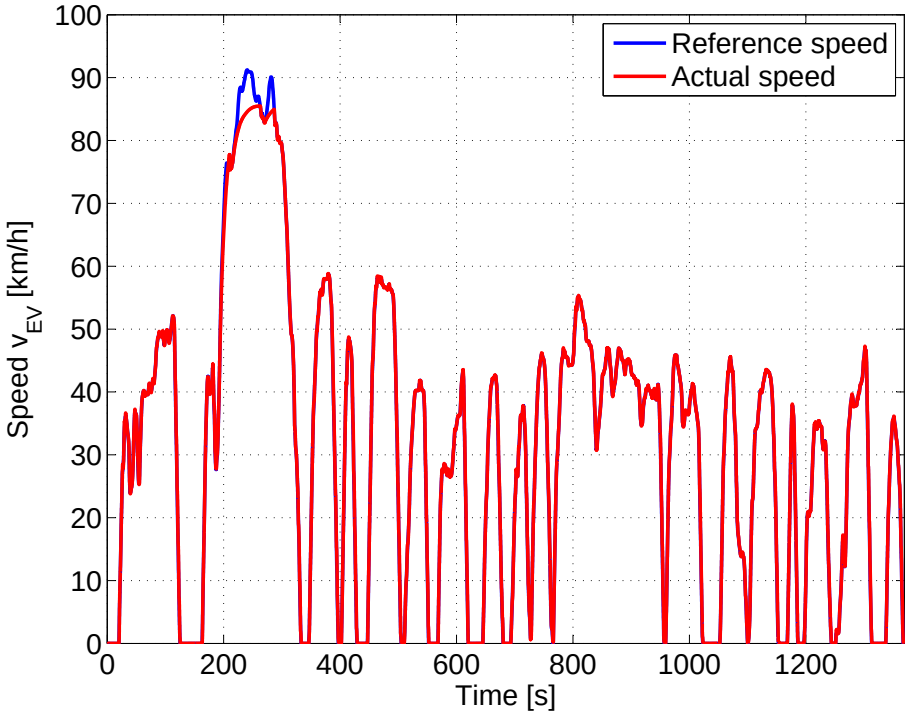

Figure 12.13: *Speed throughout the drive cycle with strategy 1 implemented.*

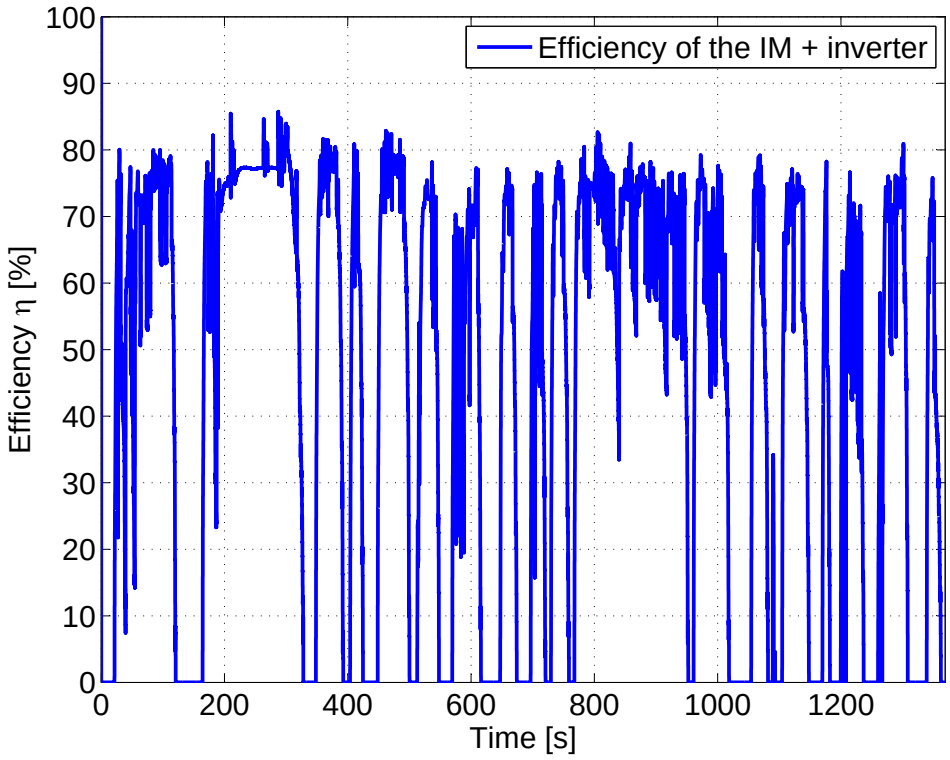

Figure 12.14: *Efficiency throughout the drive cycle with strategy 1 implemented.*

A close up on the speed, torque, rotor flux amplitude, error in rotor flux angle and efficiency is depicted in figure 12.15, 12.16, 12.17, 12.18 and 12.19 respectively. The reference rotor flux amplitude is calculated from the reference current i_{ds-ref} and the saturation compensated magnetizing inductance L_M* as in equation (12.6).

$$\lambda_{dr-ref} = i_{ds-ref} \cdot L*_M \tag{12.6}$$

As seen in figure 12.17 the magnitude of the rotor flux changes according to the torque reference and speed. The amplitude reference is not reached when varying the torque to fast as expected in the presentation of the strategy. This has an effect on the torque as the desired torque references are not reached when varying the reference too fast as seen in figure 12.16.

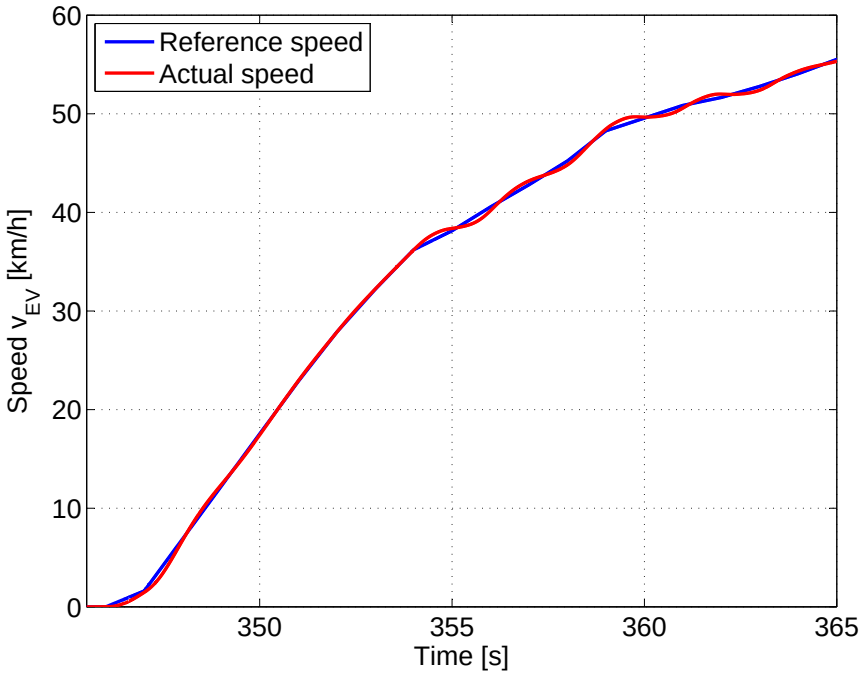

Figure 12.15: *Close up on speed with strategy 1 implemented.*

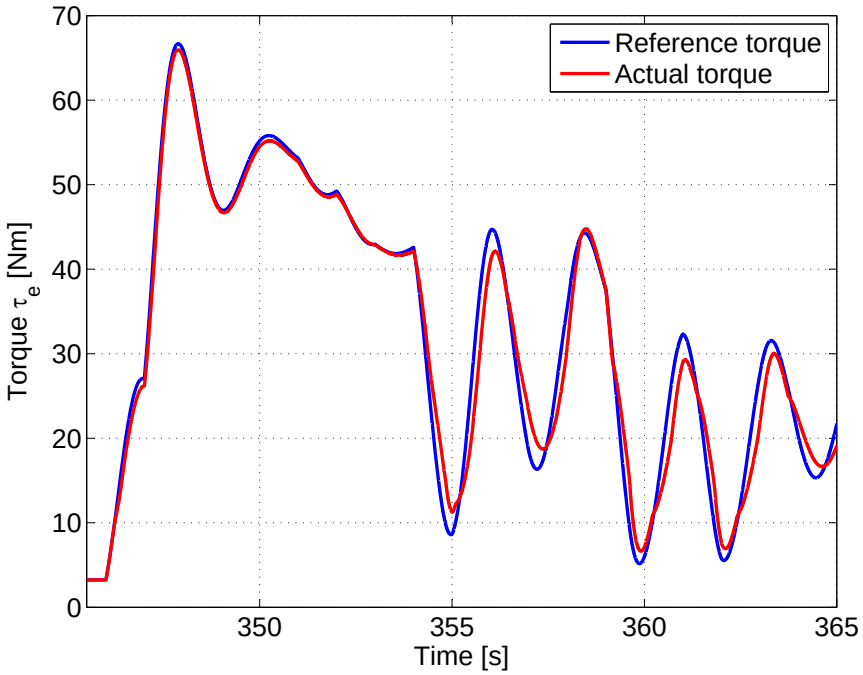

Figure 12.16: *Close up on torque with strategy 1 implemented.*

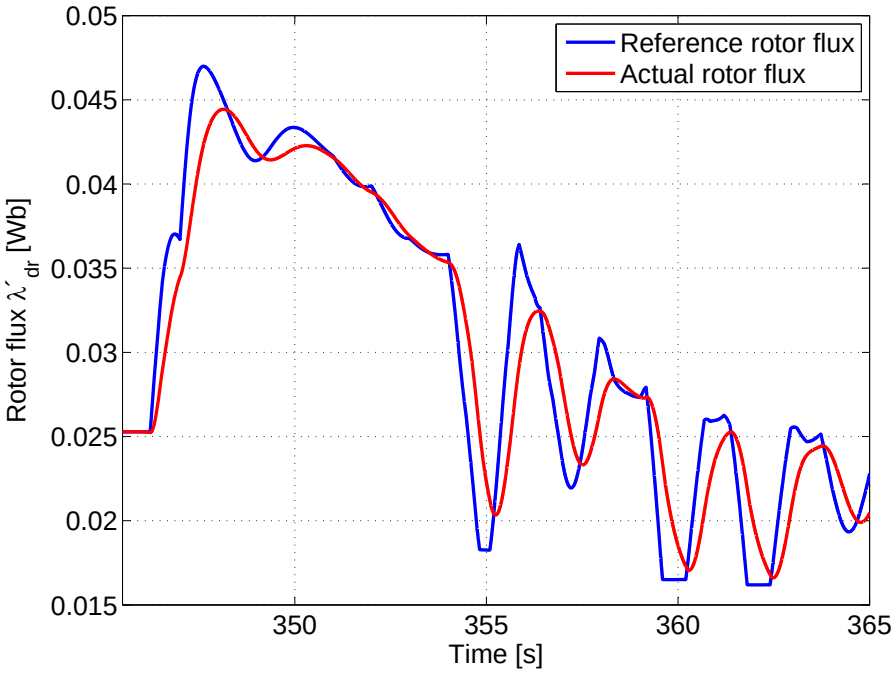

Figure 12.17: *Close up on rotor flux amplitude with strategy 1 implemented.*

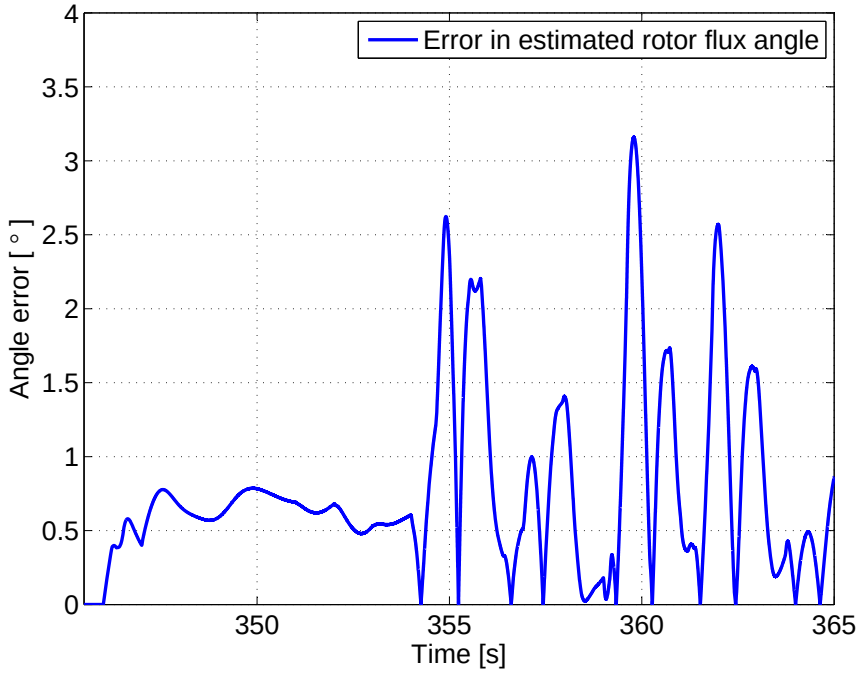

Figure 12.18: *Close up on error in rotor flux angle with strategy 1 implemented.*

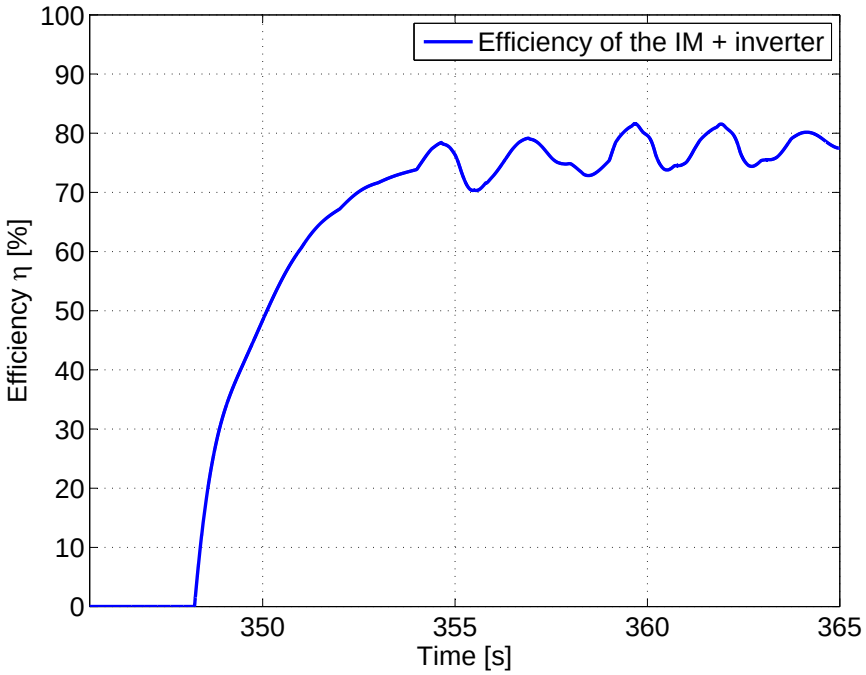

Figure 12.19: *Close up on efficiency with strategy 1 implemented.*

Implementation of strategy 2

The speed throughout the drive cycle with strategy 2 implemented is depicted in figure 12.20. As seen in the figure the speed reference seems to be reached throughout the drive cycle except at speeds above 84 $^{km}/_{h}$. The maximum error in velocity (when looking aside the velocities above 84 $^{km}/_{h}$) is less than 5 $^{km}/_{h}$. The efficiency throughout the drive cycle is depicted in figure 12.21. The overall efficiency is calculated to 65% using equation (12.4). The total input energy E_{input} for this strategy is 1.63 kWh. From equation (12.5) the length per charge is evaluated to 75.1 km.

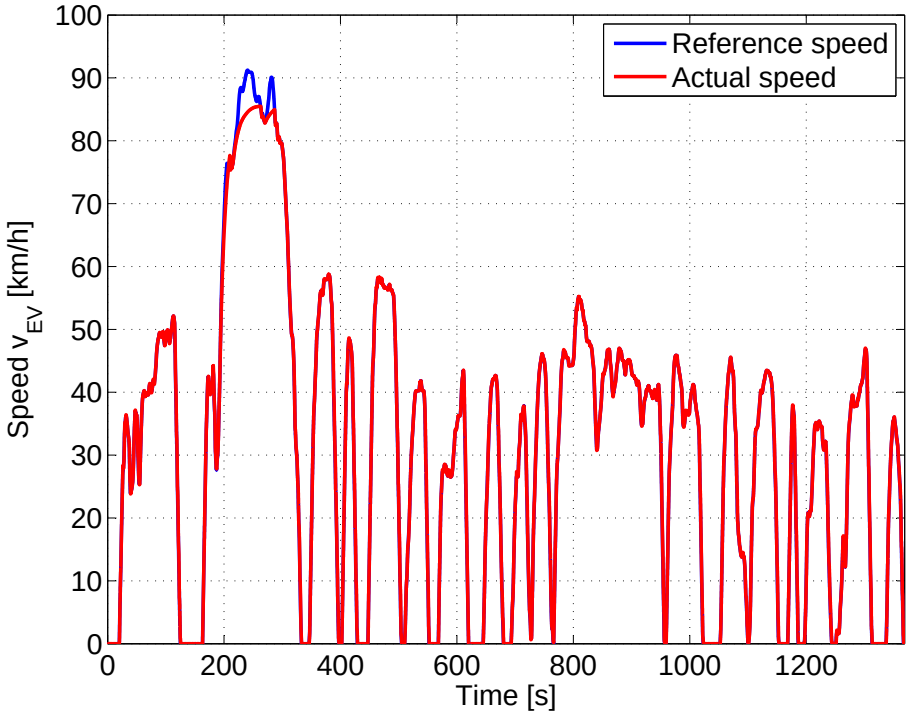

Figure 12.20: *Speed throughout the drive cycle with strategy 2 implemented.*

A close up on the speed, torque, rotor flux amplitude, error in rotor flux angle and efficiency is depicted in figure 12.22, 12.23, 12.24, 12.25 and 12.26 respectively.
As expected the rotor flux magnitude corresponds much better to the desired magnitude compared to strategy 1. This results in a better correspondence between desired torque and actual torque. The effect is also seen in the flux angle error which is less than in strategy 1 and in the speed which corresponds better to the reference than in strategy 1. When comparing the efficiencies in figure 12.21 and 12.14 it seems like the general efficiency is larger using strategy 1. This is also seen in the overall efficiency as strategy 1 provides 69% efficiency and strategy 2 provides 65 % efficiency. When comparing the close up on efficiencies in figure 12.26

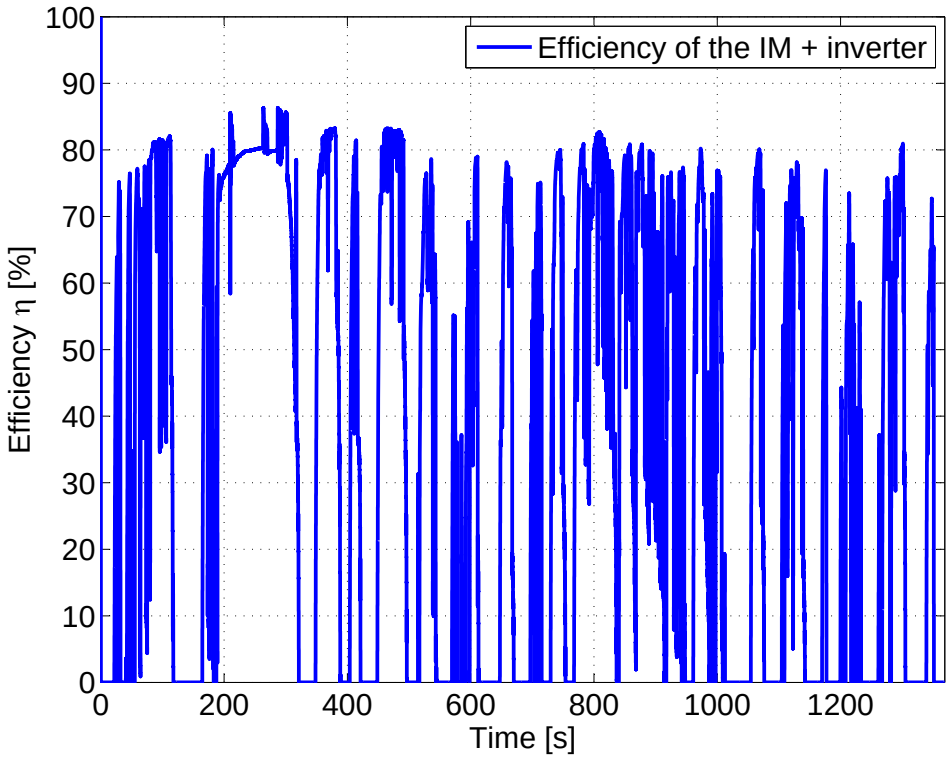

Figure 12.21: *Efficiency throughout the drive cycle with strategy 2 implemented.*

and 12.19 however it seems like the efficiency is higher using strategy 2 when fast changes are applied to the torque reference.

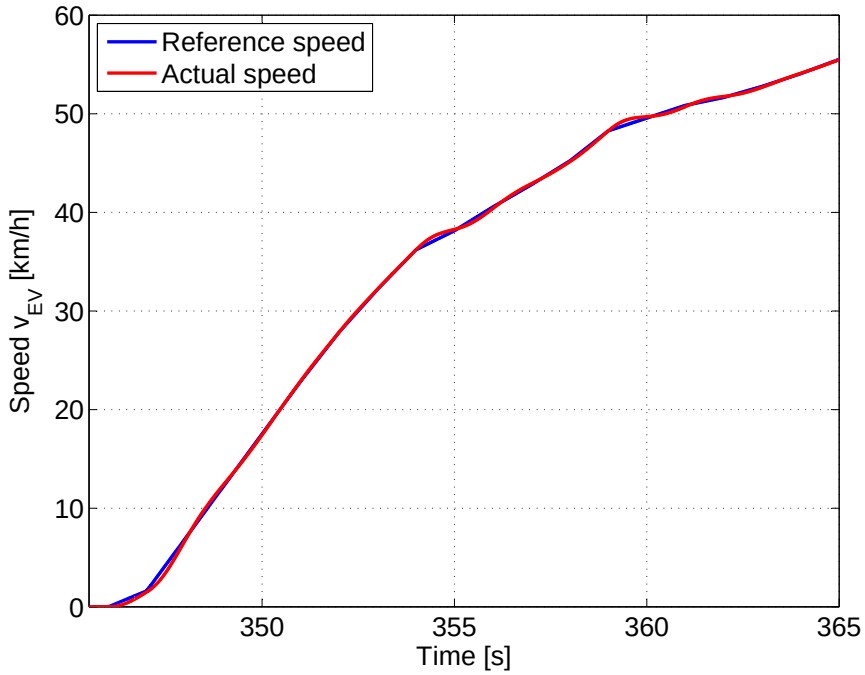

Figure 12.22: *Close up on speed with strategy 2 implemented.*

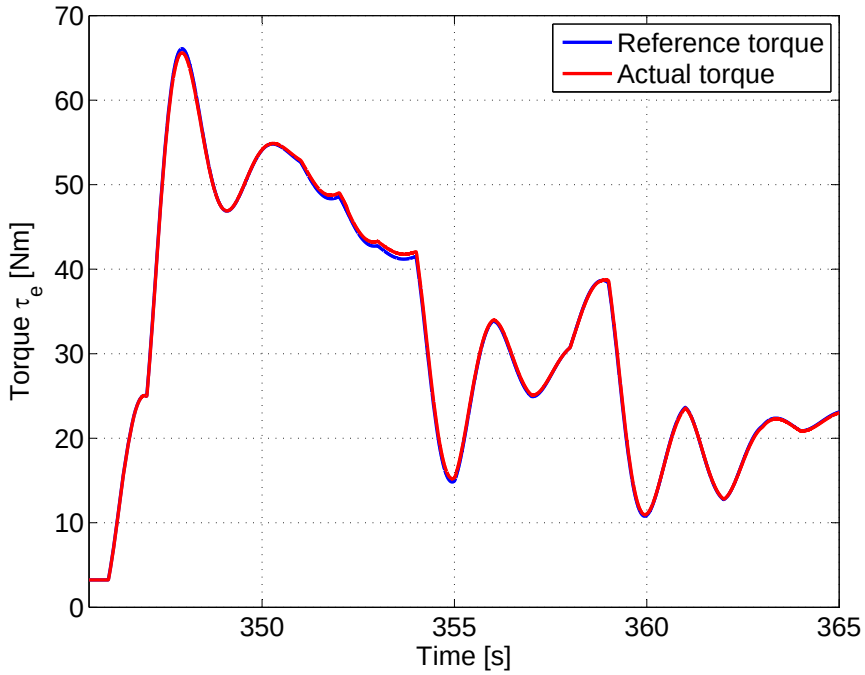

Figure 12.23: *Close up on torque with strategy 2 implemented.*

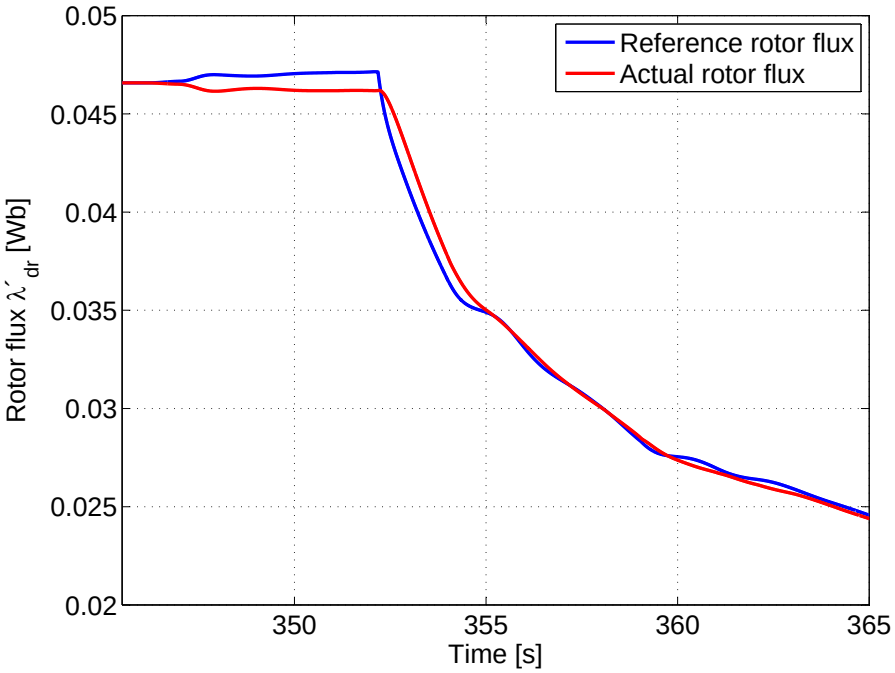

Figure 12.24: *Close up on rotor flux amplitude with strategy 2 implemented.*

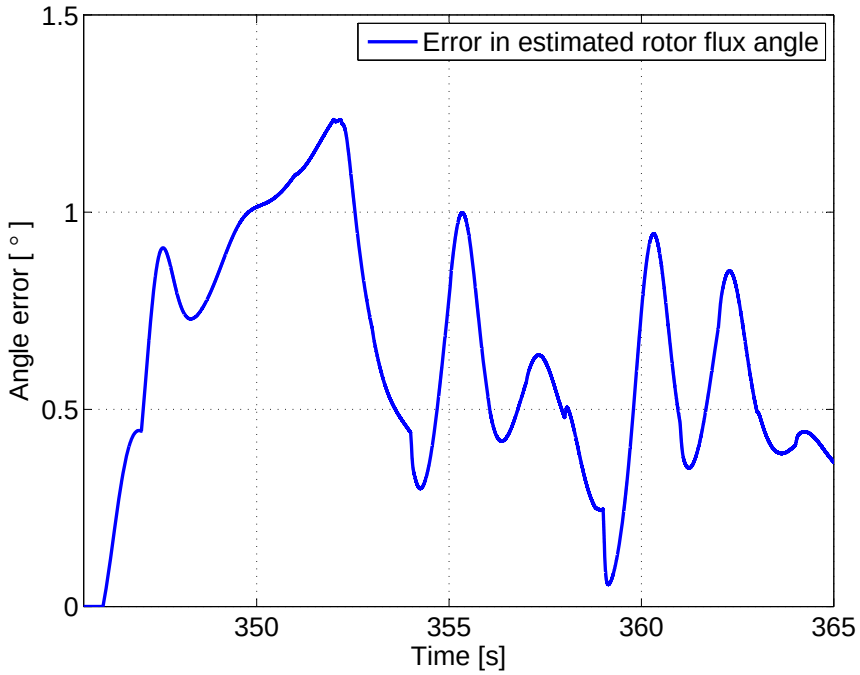

Figure 12.25: *Close up on error in rotor flux angle with strategy 2 implemented.*

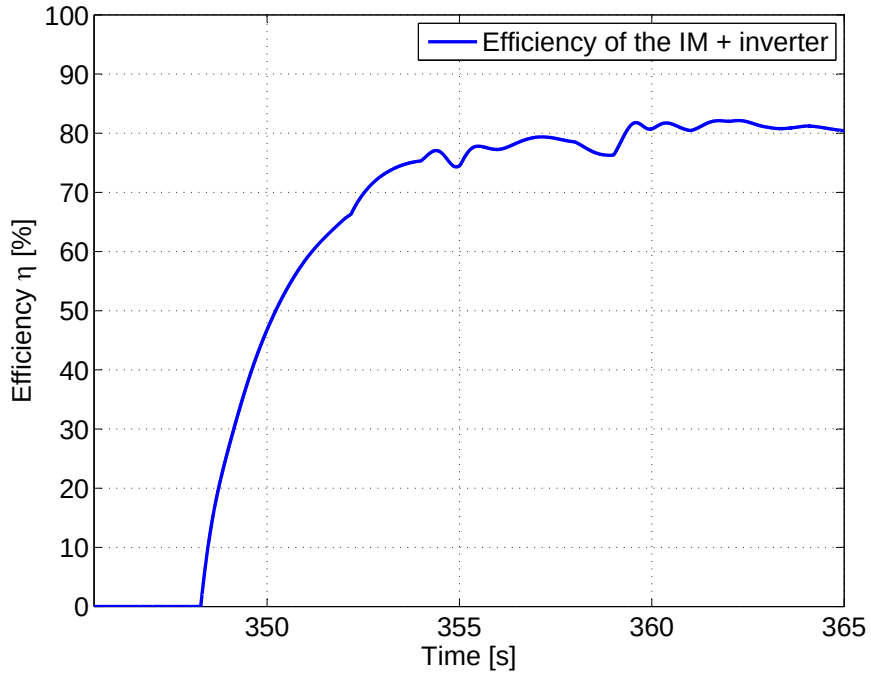

Figure 12.26: *Close up on efficiency with strategy 2 implemented.*

Implementation of strategy 3

The speed throughout the drive cycle with strategy 3 implemented is depicted in figure 12.27. As seen in the figure the speed reference seems to be reached throughout the drive cycle except at speeds above 84 $^{km}/_{h}$. The maximum error in velocity (when looking aside the velocities above 84 $^{km}/_{h}$) is less than 5 $^{km}/_{h}$. The efficiency throughout the drive cycle is depicted in figure 12.28. The overall efficiency is calculated to 69% using equation (12.4). The total input energy E_{input} for this strategy is 1.53 kWh. From equation (12.5) the length per charge is evaluated to 79.6 km.

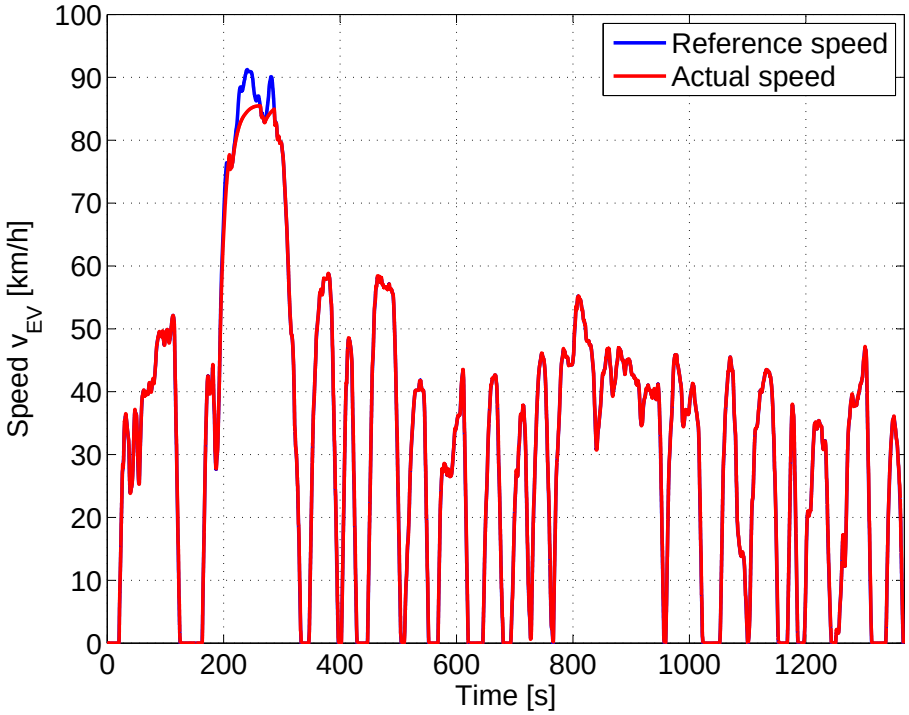

Figure 12.27: *Speed throughout the drive cycle with strategy 3 implemented.*

A close up on the speed, torque, rotor flux amplitude, error in rotor flux angle and efficiency is depicted in figure 12.29, 12.30, 12.31, 12.32 and 12.33 respectively.
The efficiency throughout the drive cycle seems to be similar to strategy 1. This corresponds well with the overall efficiency which is the same as in strategy 1. The correspondence between flux amplitude and reference seems to be slightly better when using strategy 3 compared to when using strategy 1. This is also seen in the flux angle error which is better in strategy 3 than in strategy 1.

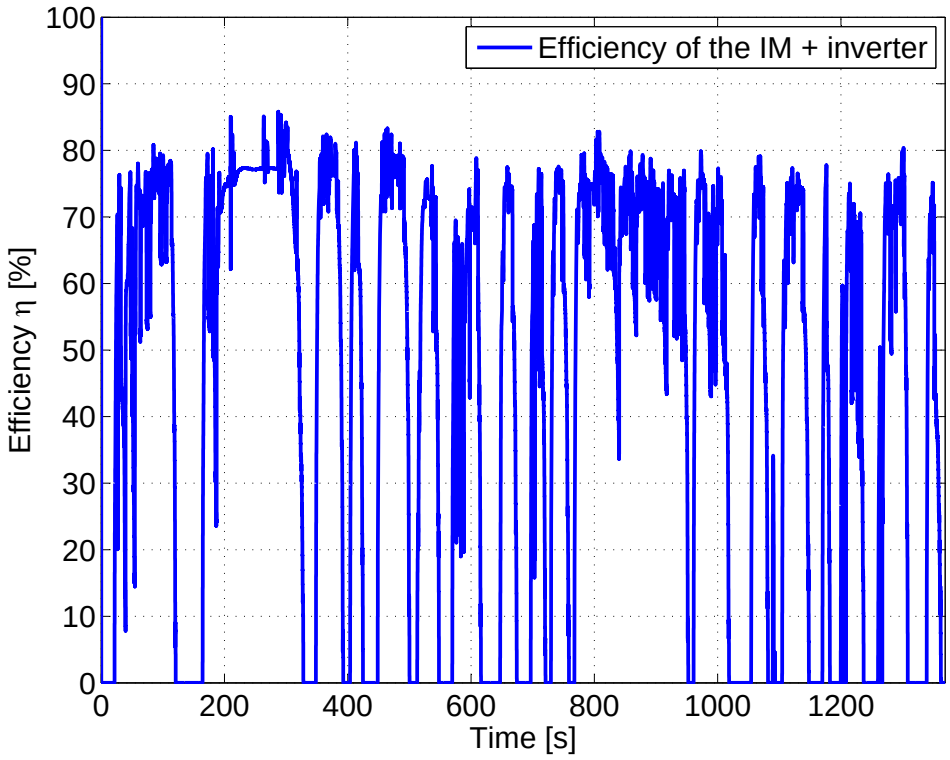

Figure 12.28: *Efficiency throughout the drive cycle with strategy 3 implemented.*

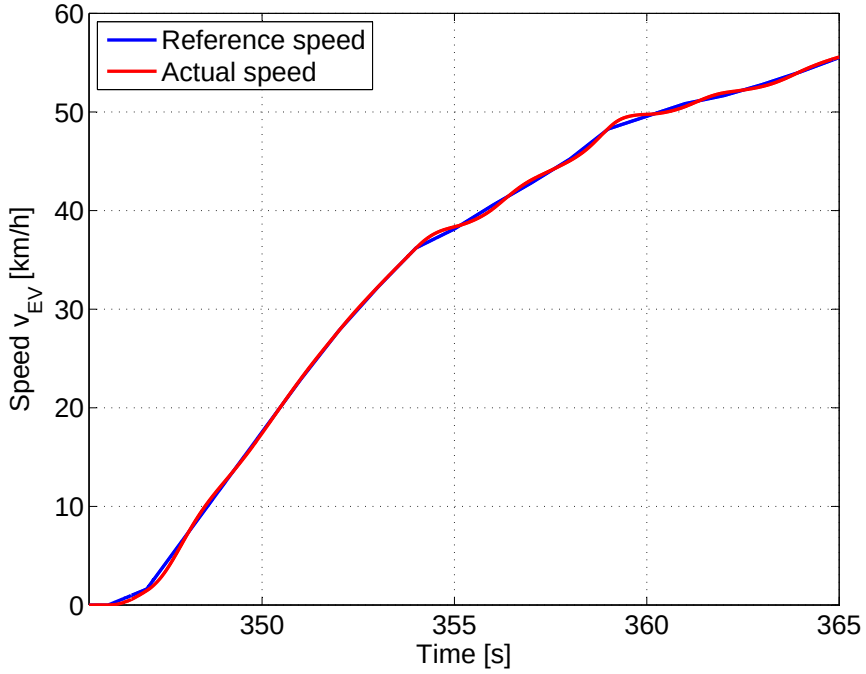

Figure 12.29: *Close up on speed with strategy 3 implemented.*

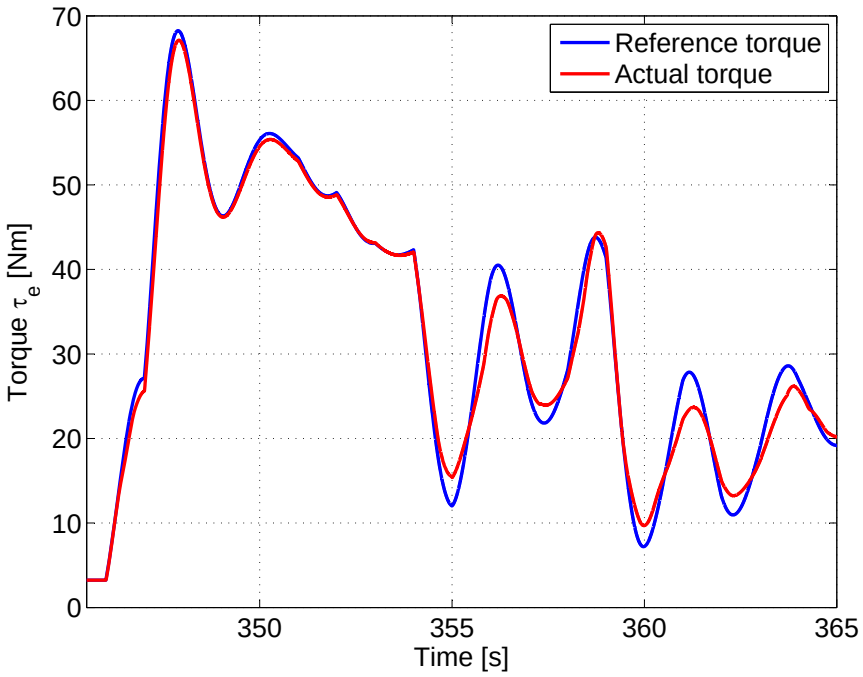

Figure 12.30: *Close up on torque with strategy 3 implemented.*

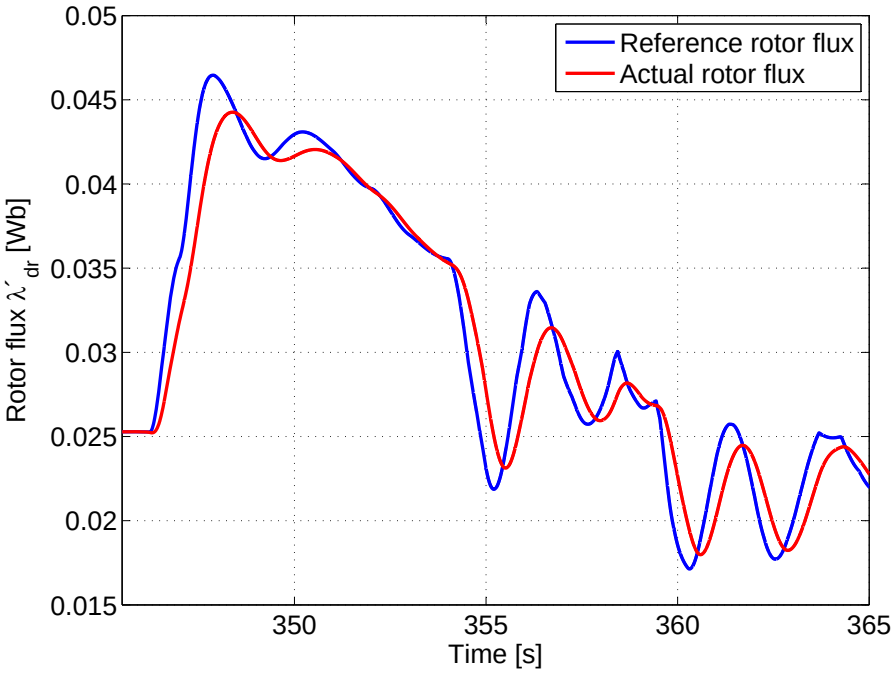

Figure 12.31: *Close up on rotor flux amplitude with strategy 3 implemented.*

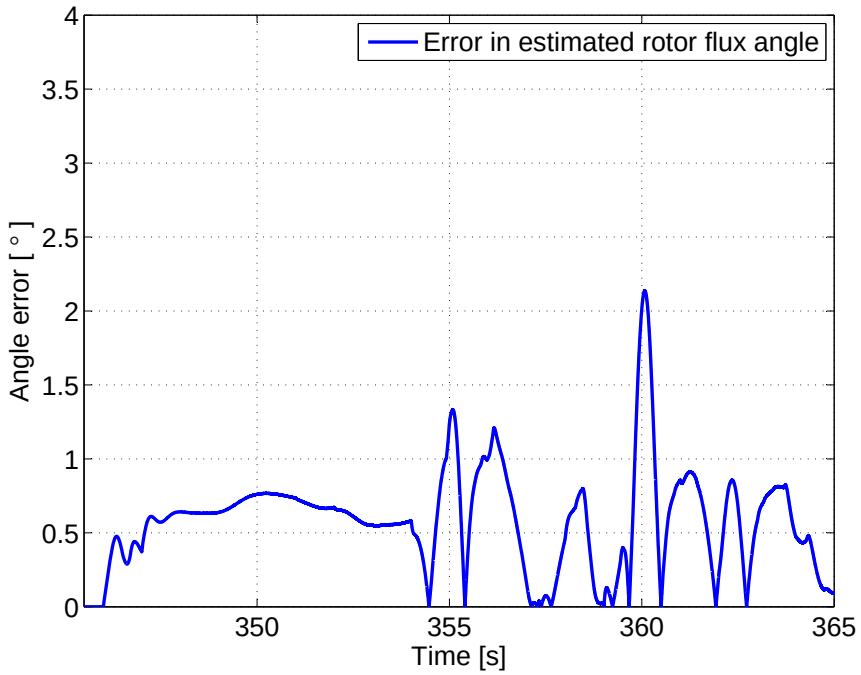

Figure 12.32: *Close up on error in rotor flux angle with strategy 3 implemented.*

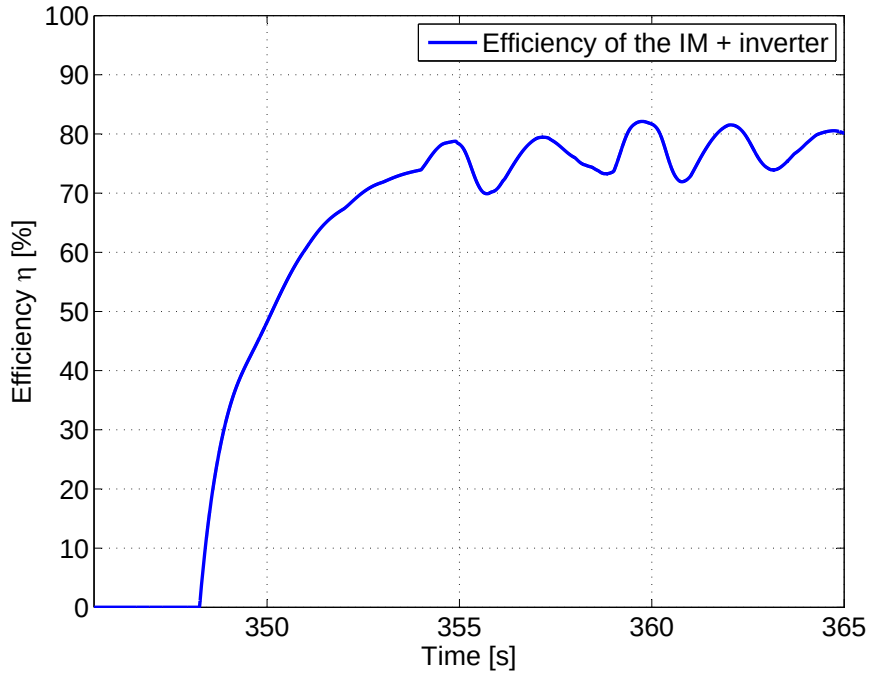

Figure 12.33: *Close up on efficiency with strategy 3 implemented.*

12.5 Impact of Driver Characteristics

The dynamics of the speed controller applied in the simulation model is to correspond to the dynamics of the driver in the EV. The dynamics of the speed controller have significant influence on the performance and efficiency of the strategies throughout the drive cycle.
From figure 12.15, 12.22 and 12.29 it is seen that the speed of the EV in all three strategies overshoots the speed reference several times during the time interval in the figure. This indicates that the speed controller may have too fast dynamics compared to what is expected from a driver. A simulation of strategy 1 is conducted with a much slower speed controller implemented. The velocity throughout the simulation is depicted in figure 12.34. As seen in the figure the correspondence between speed reference and actual speed seems to be slightly worsened using a slower speed control which is expected. The maximum error in velocity (when looking aside the velocities above 84 $^{km}/_{h}$) is still less than 5 $^{km}/_{h}$. The efficiency throughout the drive cycle is depicted in figure 12.35. The overall efficiency is now calculated to 72%. The length per charge is evaluated to 82 km.

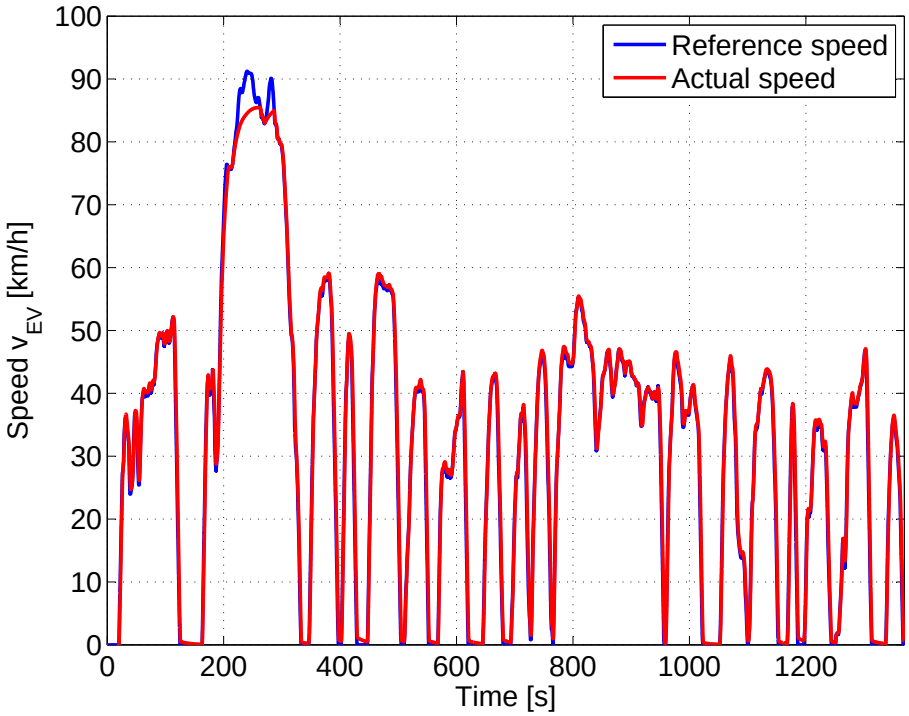

Figure 12.34: *Speed throughout the drive cycle with a slow speed controller and strategy 1 implemented.*

A close up on the speed, torque, rotor flux amplitude, error in rotor flux angle and efficiency is depicted in figure 12.36, 12.37, 12.38, 12.39 and 12.40 respectively. As seen in figure 12.36 the number of overshoots of velocity reference is decreased. The correspondence between rotor

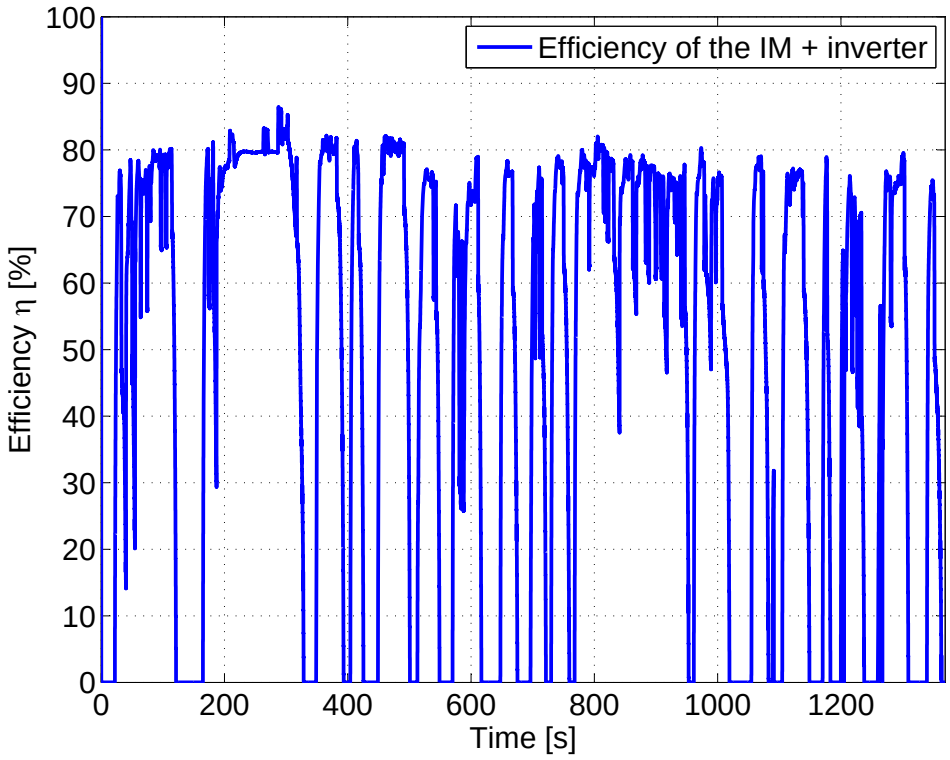

Figure 12.35: *Efficiency throughout the drive cycle with a slow speed controller and strategy 1 implemented.*

flux reference and actual rotor flux is much better which is also seen in the torque. The error in flux angle is decreased and the efficiency is increased.

It is hereby seen that the driver dynamics have great influence on both the performance and energy efficiency.

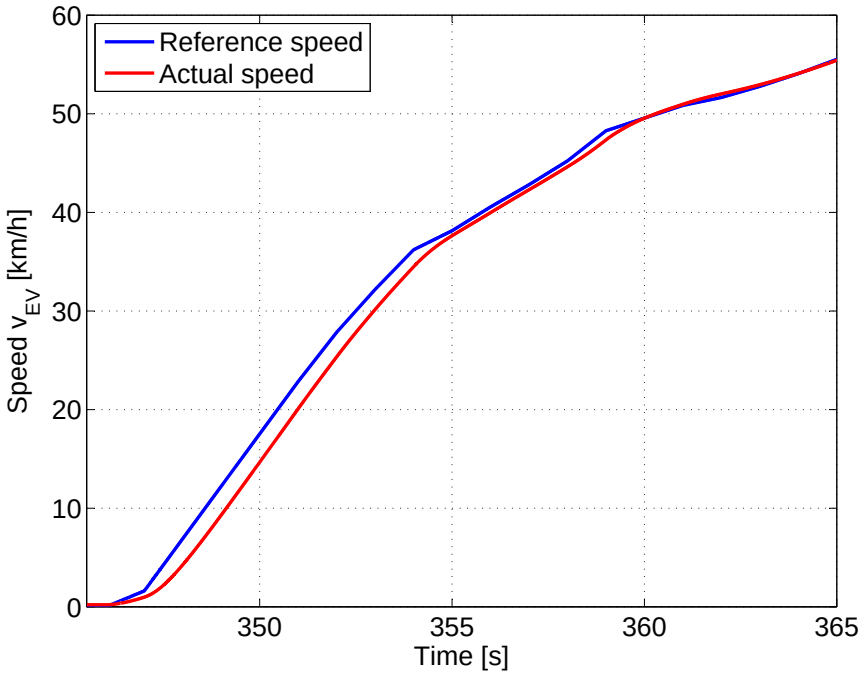

Figure 12.36: *Close up on speed with with a slow speed controller and strategy 1 implemented.*

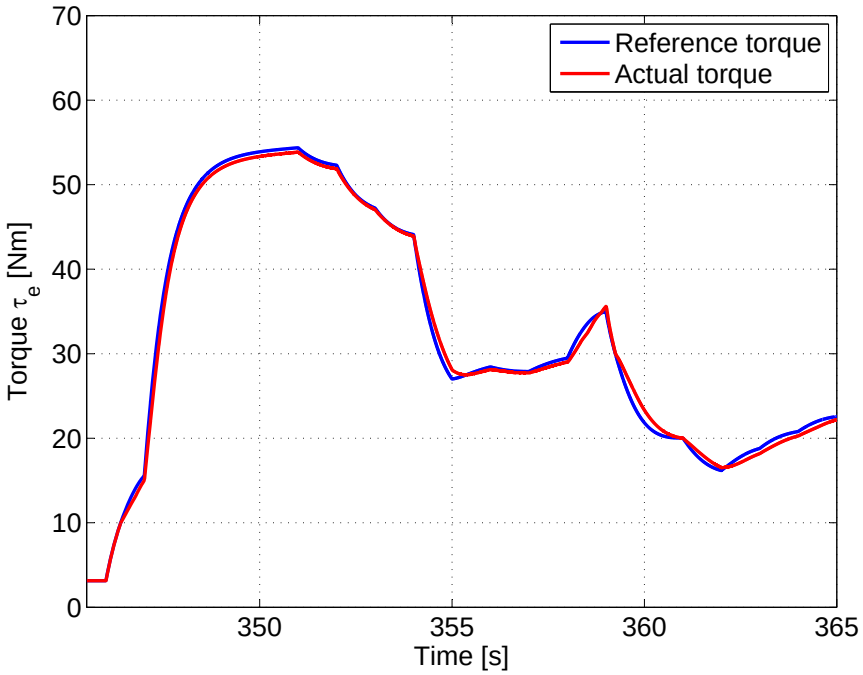

Figure 12.37: *Close up on torque with with a slow speed controller and strategy 1 implemented.*

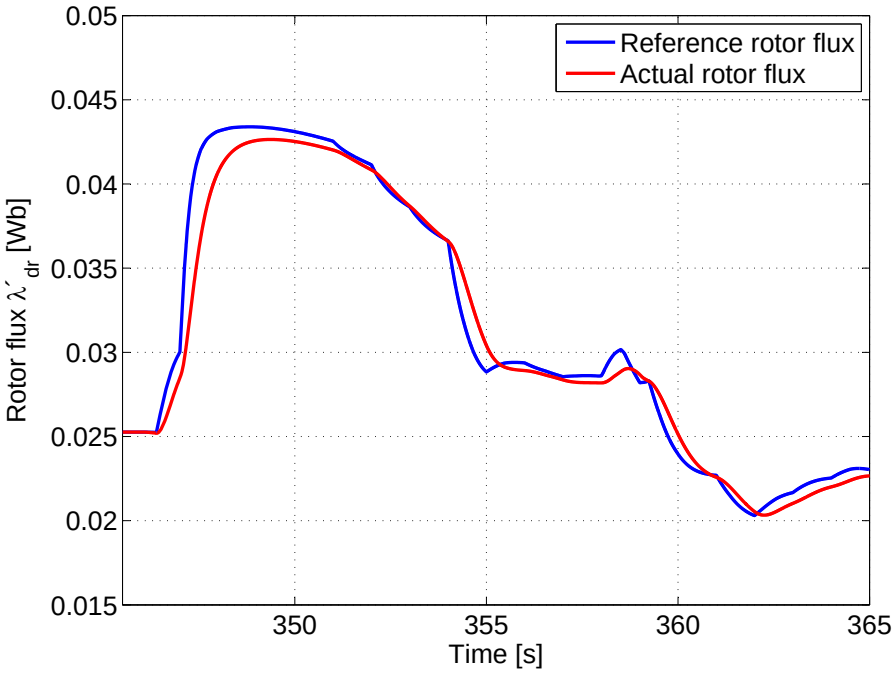

Figure 12.38: *Close up on rotor flux amplitude with a slow speed controller and strategy 1 implemented.*

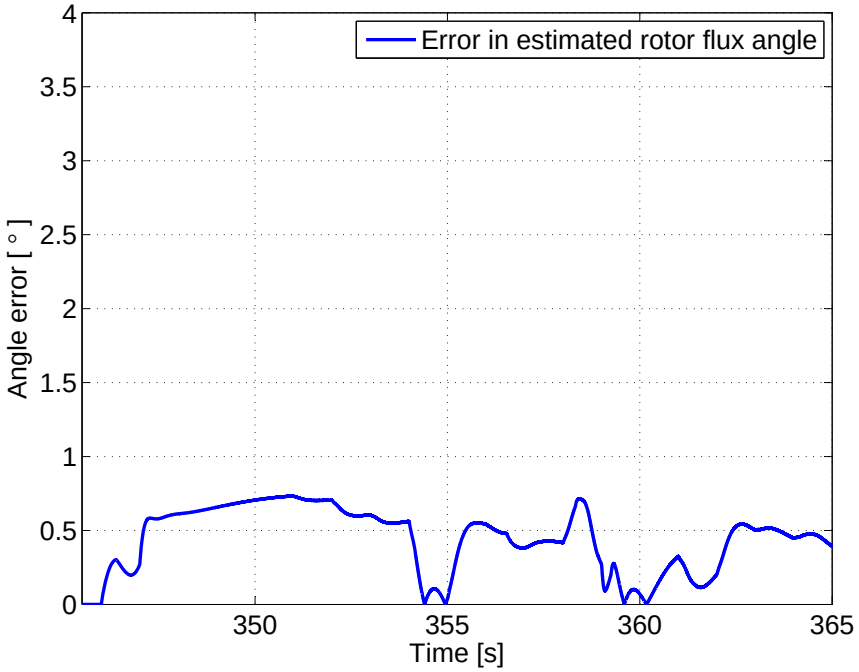

Figure 12.39: *Close up on error in rotor flux angle with a slow speed controller and strategy 1 implemented.*

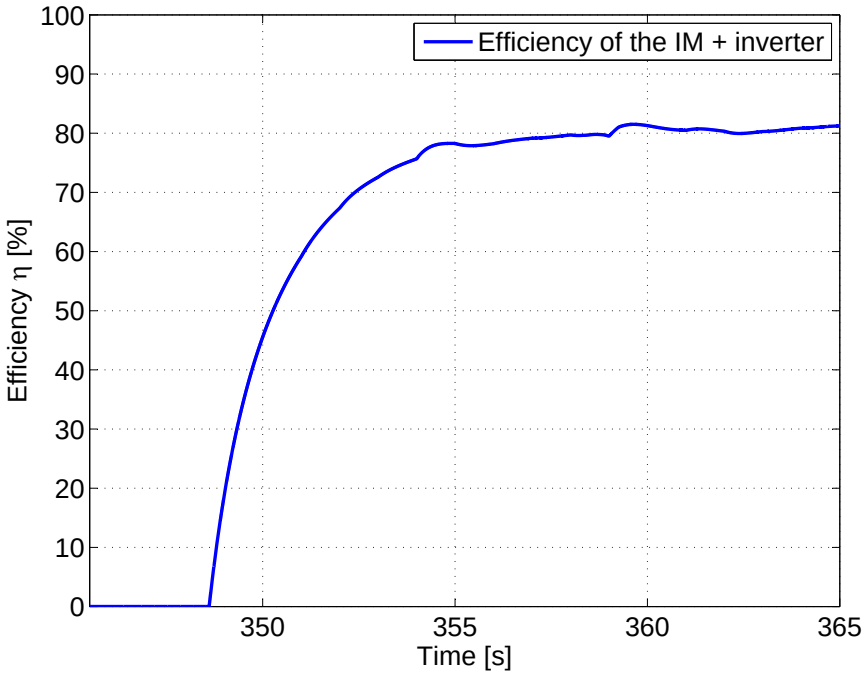

Figure 12.40: *Close up on efficiency with a slow speed controller and strategy 1 implemented.*

12.6 Conclusion for Implementation Strategy

From the simulations of the urban drive cycle it can be concluded that a larger efficiency is attainable when using optimal magnetizing currents (strategy 1 and 3) compared to when using nominal magnetizing current (strategy 2). In order to determine exactly what efficiency is attainable a more detailed analysis on driver dynamics must be performed.

The conclusion of the chapter is that varying the magnetizing current as function of torque and speed has good potential in terms of improving efficiency. The efficiency when utilizing optimal magnetizing currents is 4 %-point better than when applying nominal magnetizing current. The increase in range per charge when utilizing optimal magnetizing currents instead of nominal magnetizing current is 4.4 km which corresponds to an increase in range of 5,8 %. Strategy 1 and 3 are hereby considered as better than strategy 2 as these two provide the best efficiency. As the performance of strategy 3 is slightly better than strategy 1 strategy 3 is considered as the best implementation strategy. The implementation strategies should however be reconsidered and tested when an analysis on driver dynamics is performed.

In the original Kewet the energy per range is 0.144 $^{kWh}/_{km}$. Strategy 3 provides 0.129 $^{kWh}/_{km}$ (calculated from energy in battery pack and range per charge) which is a decrease of 10.6 % in energy consumption from the original Kewet. The implementation of the induction machine, inverter and batteries are therefore considered as profitable additions to the Kewet EV. In order to maximize the efficiency of the induction machine optimal magnetizing currents should be utilized instead of using nominal magnetizing current.

CHAPTER 13

CONCLUSION

As oil prices are rising due to depletion of oil resources the electric vehicle (EV) is becoming a more viable alternative to the internal combustion engine vehicle. Two of the main disadvantages of the EV are the range per charge and the charge time. In this report it is desired to maximize the efficiency of an EV in order to improve the range per charge for an electric vehicle. As a case study an electric vehicle called *Kewet model 5* is at the project groups disposal. The problem formulation is as follows:

How can the efficiency of an induction machine and an inverter for an electric vehicle be maximized by implementing energy efficient control without compromising the performance of the electric vehicle?

In order to test developed control strategies a test setup is constructed. The structure of the test setup is seen in figure 13.1.
For developing control strategies a simulation model of the powertrain is constructed. From the model an indirect field oriented control is developed. The indirect control is expanded from its original form to accommodate flux saturation, rotor temperature changes and transient flux response. The improved indirect control provides a significant improvement to the estimation of rotor flux angle as seen in figure 13.2.

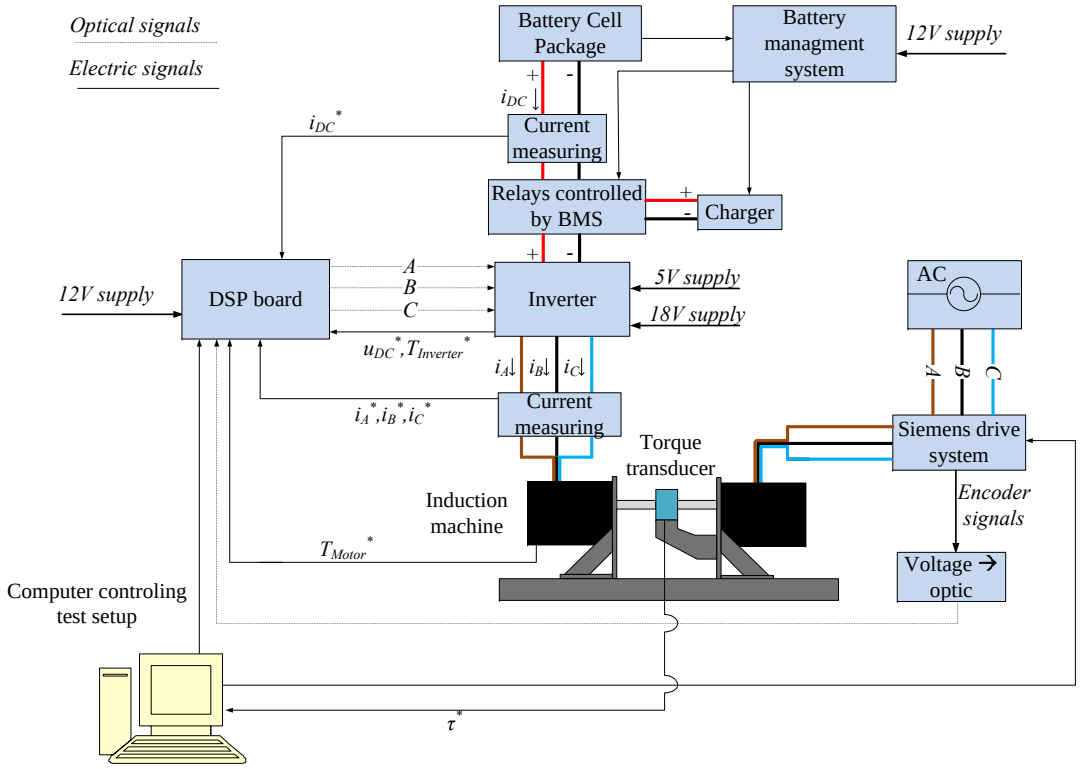

Figure 13.1: *Schematic of test setup.*

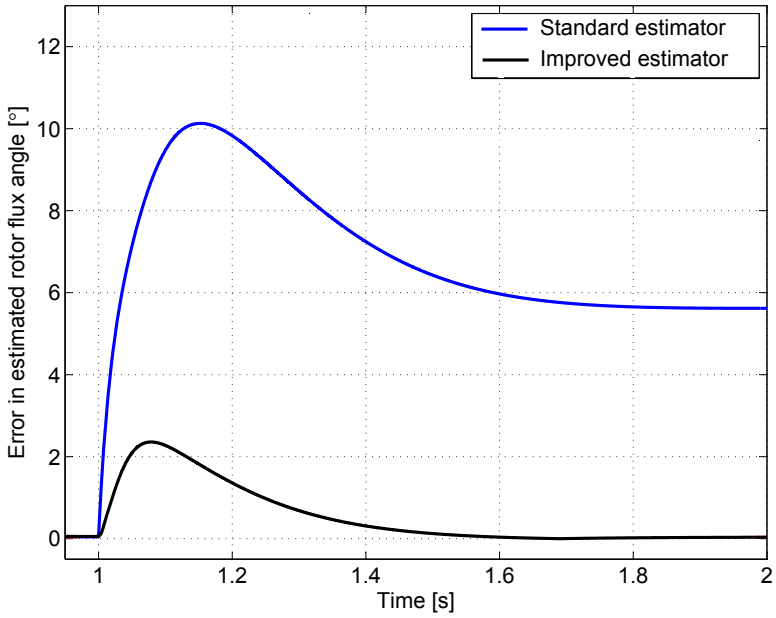

Figure 13.2: *Error in estimated rotor flux angle. The shaft velocity and the q-axis stator current are both constant and the d-axis stator current is set to step from non-saturated region to saturated region.*

In order to obtain energy efficient control of the induction machine it is desirable to determine the magnetizing currents which provides the best efficiencies at all operating points of the induction machine. This is done by first mapping the motor at varying torque, velocity and magnetizing current throughout the operating area of the induction machine. The results are applied in an optimization algorithm to determined loss equations describing the losses in the induction machine. These loss equations are then utilized for determining the energy optimal magnetizing currents. The obtainable efficiencies using the optimal magnetizing currents throughout the operating area of the induction machine is seen in figure 13.3. The Matlab scripts developed for mapping, determination of loss equations and determination of optimal magnetizing currents are also applicable for other induction machines.

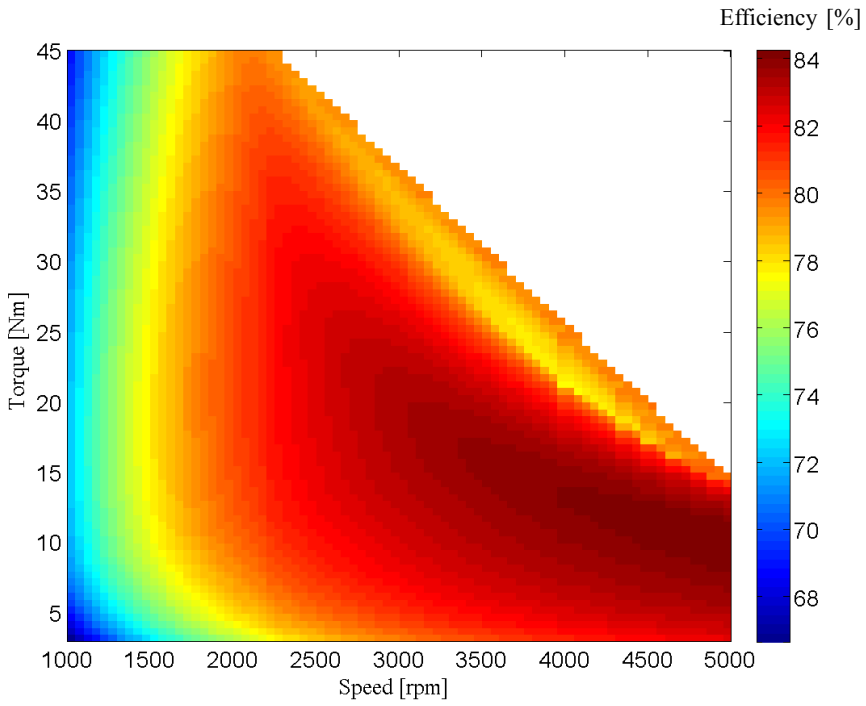

Figure 13.3: *Efficiencies attainable in the operating area using optimal magnetizing currents.*

The implementation of energy efficient control in the EV may compromise the performance of the EV. Therefore three implementation strategies are developed each containing different compromises between performance and efficiency. The strategies are tested by simulating a standard urban drive cycle for light weight vehicles.

By utilizing optimal magnetizing currents an efficiency of 72 % and an acceptable performance is obtained. When utilizing optimal magnetizing currents the increase in range per charge is

increased by 5.8 % compared to when using nominal magnetizing current. In the original Kewet the energy per range was 0.144 $^{kWh}/_{km}$. The most promising strategy provides 0.129 $^{kWh}/_{km}$ which is a decrease of 10.6 % in energy consumption compared to the original Kewet. The implementation of induction machine, inverter and batteries are considered as profitable additions to the Kewet EV. In order to maximize the efficiency of the induction machine optimal magnetizing currents should be utilized instead of using nominal magnetizing current.

CHAPTER 14

FURTHER WORKS

This chapter contains proposals for further works within the topic of the project.

Implementation in EV

Instead of testing the implementation strategies in the simulated drive cycle the powertrain and control system could be implemented in the Kewet EV and the strategies could be tested in the EV instead. The driver experience could be another perspective on the evaluation of the implementation strategies.

Driver Analysis

As stated in the conclusion of chapter 12 a thorough driver analysis is necessary in order to determine attainable efficiency of the EV. The driver analysis could entail another conclusion of which implementation strategy is the best.

Direct Current Control

As stated in the report the direct flux estimation was discarded due to technical difficulties. A proper development of a direct flux estimation may entail a better flux estimation than the improved indirect flux estimation described in the report leading to a better efficiency and/or performance.

Automated Determination of Optimal Magnetizing Current

The algorithms for the mapping of the induction machine, determination of loss equations and determination of optimal magnetizing current are described in the report. For the mapping to work the initializations of speed, torque and magnetizing current arrays must be conducted manually. An algorithm for determination of suitable arrays for an induction machine could be developed. The algorithm could determine suitable arrays using a simulation model of the induction machine.
In order to make the algorithm even more automated an automatic determination of motor parameters can be considered.
Instead of mapping the motor and then determining optimal magnetizing current the optimal magnetizing current could instead be determined online by using an online optimization algorithm determining the magnetizing current that provides the best efficiency at each operating point.

Test Setup for Various Induction Machines

The test setup could be rebuilt in order to be applicable for induction machines with various power, torque and fixture characteristics in order to determine optimal magnetizing current for various induction machines.

BIBLIOGRAPHY

ABM. *Drehstrom-Asynchronmotor bei veränderlicher Frequenz*. Datasheet is located in appendix on figure I.2.

Flemming Abrahamsen. *Energy Optimal Control of Induction Motor Drives*. Aalborg University, 2000. URL: http://vbn.aau.dk/files/44428487/flemming_abrahamsen.pdf.

Søren Juhl Andreasen. *Design and Control of High Temperature PEM Fuel Cell System*. Aalborg University, 2009. URL: http://vbn.aau.dk/files/19025156/Thesis.

Better place. *Renault Fluence Z.E. - Specifications*. URL: http://www.betterplace.com.au/electric-cars/renault-fluence-ze.html.

Bil.guide.dk. *Test af Renault Fluence Z.E.* URL: http://bil.guide.dk/Elbil/Renault/%C3%98konomi/Milj%C3%B8/Motor/Test_af_Renault_Fluence_ZE_2675646.

Bosch. *Automotive Handbook*. Robert Bosch GmbH, 7 edition, 2007. ISBN: 978-0-470-51936-3.

C. C. Chan and K. T. Chau. *Modern Electric Vehicle Technology*. Oxford University Press Inc., 1 edition, 2001. ISBN: 0-19-850416-0.

Citroën. *Citroen C-Zero*. URL: http://www.c-zero.citroen.com/#/dk/leder.

Danskebjerge.dk. *Stejleste bakker i Danmark*. URL: http://www.danskebjerge.dk/stejlest.htm.

F. P de Mello and G.W. Walsh. *Reclosing Transients in Induction Motors with Terminal Capacitors*. IEEE, 1961. URL: http://ieeexplore.ieee.org/stamp/stamp.jsp?tp=&arnumber=4500941.

Mehrdad Ehsani, Yimin Gao, and Ali Emadi. *Modern Electric, Hybrid Electric and Fuel Cell Vehicles Fundamentals, Theory, and Design*. CRC Press: Taylor & Francis Group, 2 edition, 2010. ISBN: 9781420053982.

FDM. *Ejerafgift 2012*. URL: http://www.fdm.dk/biloekonomi/ejerafgift.

Gene F. Franklin, J. David Powell, and Michael Worksman. *Digital Control Dynamic Systems*. Addison-Wesley, 3 edition, 1998. ISBN: 0-201-82054-4.

Honda. *Honda Fit EV*. URL: http://automobiles.honda.com/fit-ev/.

P.L Jansen, R.D. Lorenz, and D.W. Novotny. *Observer-based direct field orientation: analysis and comparison of alternative methods*. IEEE, 1994. URL: http://ieeexplore.ieee.org/stamp/stamp.jsp?tp=&arnumber=297911.

JP.dk. *Fransk elbil til Danmark - 20 øre pr. kilometer*. URL: http://fpn.dk/motor/bil/article1354117.ece.

Kewetmuseum. *Kewet model 5*. URL: http://www.kewetmuseum.mono.net/8808/Modeller.

Paul C. Krause, Oleg Wasynczuk, and Scott D. Sudhoff. *Analysis of electric machinery and drive systems*. John Wiley & Sons, Inc., 2 edition, 2002. ISBN: 047114326x.

J.F. Moreno, F.P. Hidalgo, and M.D. Martinez. *Realisation of tests to determine the parameters of the thermal model of an induction machine*. IEEE, 2001. URL: http://ieeexplore.ieee.org/stamp/stamp.jsp?tp=&arnumber=955372.

Nissan. *Nissan Leaf*. URL: http://www.nissan-global.com/EN/NEWS/2009/_STORY/090802-02-e.html.

D. W. Novotny and T. A. Lipo. *Vector Control And Dynamics of AC Drives*. Oxford Science Publications, 1996. ISBN: 978-0-19-856439-3.

OECD. *OECD Economic Outlook No. 76*. OECD, 2004. URL: http://www.oecd.org/dataoecd/19/6/34080955.pdf.

Oil-price.net. *Crude Oil and Commodity Prices*. URL: http://www.oil-price.net.

Oriental motor. *Basics of Motion Control*. URL: http://www.orientalmotor.com/technology/articles/AC-brushless-brushed-motors.html.

Ali Pearlman. *Car Differential*. URL: http://web.mit.edu/2.972/www/reports/differential/differential.html.

Peugeot. *Peugeot iOn*. URL: http://www.peugeot.com/en/news/2009/9/7/the-new-peugeot-electric-car-ion-zero-emissions.aspx.

Philips. *KTY84 series Silicon temperature sensors*. URL: http://www.datasheetcatalog.org/datasheet/philips/KTY84_SERIES_5.pdf.

Puremobility.com. *Buddy EV*. URL: http://www.puremobility.com/no/buddy/teknisk-info.

R. K. Rajput. *Electrical Engineering Materials*. Laxmi Publications, 1 edition, 2006.

Peter O. Rasmussen. *Slides from the course AC Motor Drives: Converters and Control*. AAU, 2010.

Renault. *Renault Fluence Z.E charging*. a. URL: http://www.renault.com/en/vehicules/renault/pages/fluence-ze.aspx.

Renault. *Fluence - Tekniske egenskaber*. b. URL: http://www.renault.dk/elbiler/fluence-ze/fluence-ze/fluence-ze/motorer-og-specifikationer.

Renault. *RENAULT MEGANE COLLECTION 2012: ENERGY POWER*. c. URL: http://www.google.dk/url?sa=t&rct=j&q=&esrc=s&source=web&cd=1&ved=0CDAQFjAA&url=http%3A%2F%2Fmedia.renault.com%2Fdownload%2Fmedia%2Fspecialfile%2F31641_1_5.aspx&ei=FvpyT9v_IMXc4QTr6tyfDw&usg=AFQjCNGWM5rNTdYhqsPvldvMedwCdngNMQ.

Renault. *Megane - Tekniske egenskaber*. d. URL:
http://www.renault.dk/personbiler/megane/megane/megane/motorer-og-specifikationer.

Roymech. *Gear Efficiency*. URL:
http://www.roymech.co.uk/Useful_Tables/Drive/Gear_Efficiency.html.

Ronnie Belmans Saiful Islam, Achim Woyte and Johan Nijs. *Undersizing inverters for grid connection-what is the optimum?* URL: http://www.esat.kuleuven.be/electa/publications/fulltexts/pub_1057.pdf.

Adel S. Sedra and Kenneth C. Smith. *Microelectronic Curcuits*. Oxford University Press, 5 edition, 2004. ISBN: 019-514252-7.

Paresh C. Sen. *Principles of Electric Machines and Power Electronics*. John Wiley & Sons, 2 edition, 1997. ISBN: 978-0-471-02295-4.

Raymond B. Sepe and Jeffrey H. Lang. *Inverter Nonlinearities and Discrete-Time Vector current Control*. IEEE TRANSACTIONS ON INDUSTRY APPLICATIONS, 1994. URL:
http://ieeexplore.ieee.org/stamp/stamp.jsp?tp=&arnumber=273622&tag=1.

Skatteministeriet. *Afsnit 10: Moms, lønsumsafgift og miljøafgifter*. a. URL:
http://www.skm.dk/publikationer/udgivelser/skattenidanmark2008/6513.

Skatteministeriet. *Registreringsafgift - beregningseksempel*. b. URL:
http://www.skm.dk/tal_statistik/afgiftsberegning/2287.html?rel.

ThunderSky. *Thunder Sky battery cell*. URL:
http://www.everspring.net/product-battery-LFP160AHA.htm.

Western Lithium. *Hybrid/Electric Vehicles*. URL:
http://www.westernlithium.com/hybrid-electric-vehicles/why-electric-vehicles.

Worldometers. *How many cars are produced in the world every year?* URL:
http://www.worldometers.info/cars.

Master Thesis 2011-2012 EMSD

Appendix

By:

Thomas Christensen
Bjørn Bøge
Niels Balzer Sørensen

Aalborg University

CONTENTS

APPENDIX A

BATTERY MODEL

In this section a model of a single battery cell is derived. The purpose of the model is to calculate the terminal voltage of the battery as a function of SOC (State Of Charge) and battery current i_b. Circuit diagrams used to model the battery is seen in figure A.1. The diagram to the left is used to derive an expression for the energy left in the battery. The diagram to the right is used to derive an expression for the voltage response of the battery given a battery current i_b. The model is based on a simplification of [Chen and Rincon-Mora, 2006]. The original battery response circuit[Chen and Rincon-Mora, 2006] was composed of a resistor in series with two R-C connections. The model used in this project consists of a resistor in series with only one R-C connection. It will become evident during the presentation of the results that the simplified system widely represents the battery with sufficient accuracy. In section A.5 the model is expanded to represent the entire battery package consisting of twenty cells. The experiment to determine the parameters for the model is described in appendix A.6.

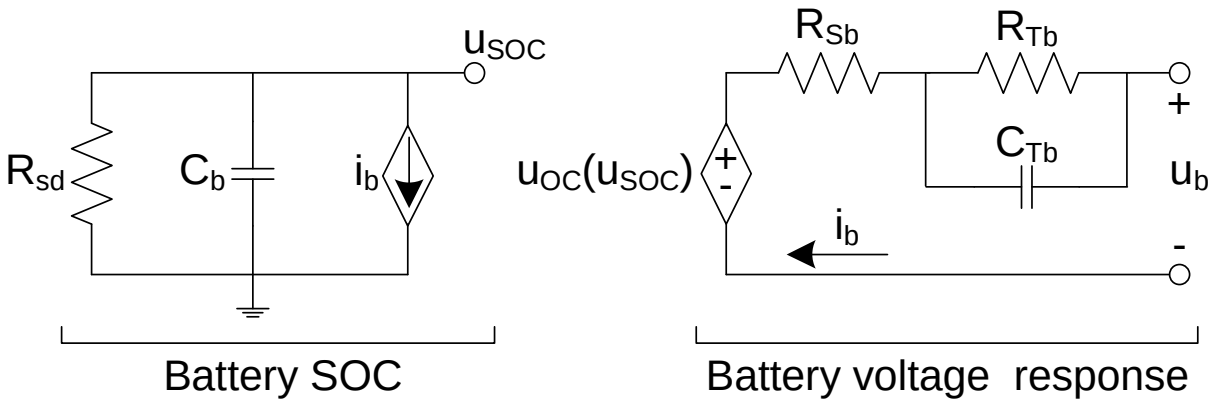

Figure A.1: *Circuit diagrams used to model the battery.*

A.1 Battery State of Charge

The circuit model representing the battery SOC is seen in figure A.1 to the left. It consists of a self-discharge resistor R_{sd} representing the slow discharging of the battery occurring at no load condition and a capacitor C_b representing the capacity of the battery. The self-discharge rate of the battery is less than 3 % monthly see table 5.1 in section 5.2.1.

The self-discharge resistance R_{sd} is disregarded in the model since the batteries are frequently charged and discharged in the test setup and in the electric vehicle causing the self-discharge resistor to have minor impact. The state of charge is determined by the energy left in the capacitor C_b and is directly reflected on the voltage u_{SOC}. The size of the capacitor C_b is determined using equation (A.1). To determine the size of the capacitor C_b at full capacity (SOC= 1), a constant current discharge experiment was conducted. The battery is discharged from full capacity (terminal voltage of 4.25 V) to zero capacity (terminal voltage of 2.5 V) with a current of 75 A which is roughly 0.5 C $(1CA = 160A)$. This experiment took Δt= 7371 s. Using data from this experiment C_b is calculated as in equation (A.2). u_{SOC} will hereby vary between 0 and 1 and will express the state of charge for the battery. The discharge time of the battery is depending on the discharge current limiting the validity of the calculated capacity to discharge currents of approximately 75 A. An increase in discharge current result in a decrease in the capacity of the batteries due to increased losses see figure A.2.

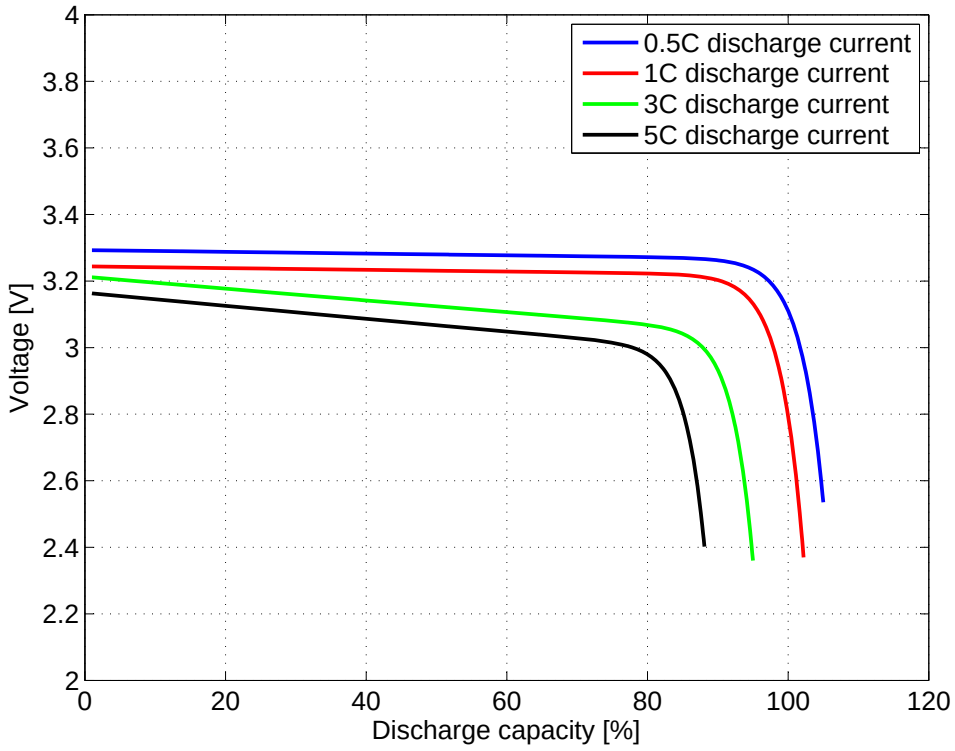

Figure A.2: *Battery discharge capacity at different discharge currents [ThunderSky].*

$$\begin{aligned} i_b &= C_b \cdot \frac{du_{SOC}}{dt} \\ &\Downarrow \\ C_b &= \frac{i_b}{\frac{du_{SOC}}{dt}} \end{aligned} \tag{A.1}$$

where:

	i_b	Battery current flow $[A]$.
	C_b	Battery capacity capacitor $[F]$.
	u_{SOC}	State of charge voltage $[V]$.

$$\begin{aligned} C_b &= \frac{i_{b.experiment}}{\frac{\Delta u_{SOC}}{\Delta t}} \\ &= \frac{75\ A}{\frac{1\ V}{7371\ s}} \\ &= 552.8\ kF \end{aligned} \tag{A.2}$$

where:	C_b	Equivalent battery capacity $[F]$.
	i_b	Battery current flow during experiment $[A]$.
	Δu_{SOC}	State of charge voltage increment during experiment $[V]$.
	Δt	Time increment during experiment $[s]$.

A.2 Battery Voltage Response

The circuit representing the transient response of the battery is seen in figure A.1 to the right. It consists of a resistor in series with a R-C circuit and a voltage source depending on the state of charge voltage u_{SOC}. To determine the parameters of the model, the circuit components are replaced by an impedance Z_{Tot} illustrated in figure A.3. An expression for the total impedance Z_{Tot} is seen in equation (A.3). From this it is seen that resistor R_{Sb} causes instant response while the R-C circuit causes first order response.

To determine the parameters for the model, the size of the three parameters is varied in an iterative manner while the response of the system is compared to experimental results (taken at SOC $\approx$ 50 %) untill coherence exist between model and experiment. The experiment is described in appendix A.6. The parameteers are seen in table A.1. The final result is seen in figure A.4.

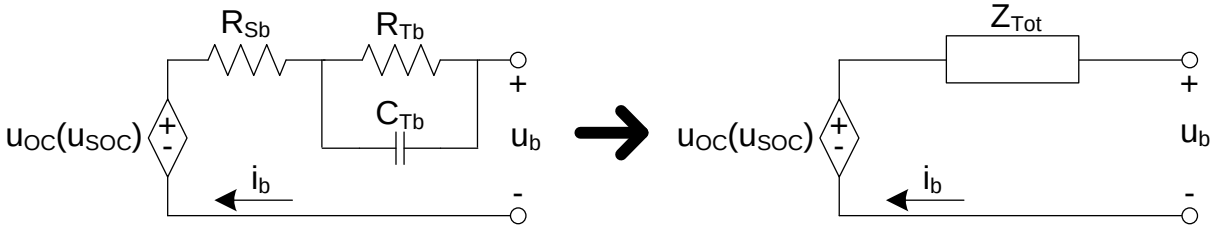

Figure A.3: *Battery response circuit components replaced by one impedance.*

Parameters for battery response model	
C_{Tb}	$2.5 \cdot 10^5$ $[F]$
R_{Tb}	$5.0 \cdot 10^{-4}$ $[\Omega]$
R_{Sb}	$2.09 \cdot 10^{-3}$ $[\Omega]$

Table A.1: *Parametres for battery response model*

$$Z_{Tot} = R_{Sb} + \frac{R_{Tb}}{R_{Tb} \cdot C_{Tb} \cdot s + 1}$$

where:

Z_{Tot}	Impedance of battery response circuit $[\Omega]$.
C_{Tb}	Capacitor in battery response circuit according to figure A.1 $[F]$.
R_{Sb}	Resistor in battery response circuit according to figure A.1 $[\Omega]$.
R_{Tb}	Resistor in battery response circuit according to figure A.1 $[\Omega]$.

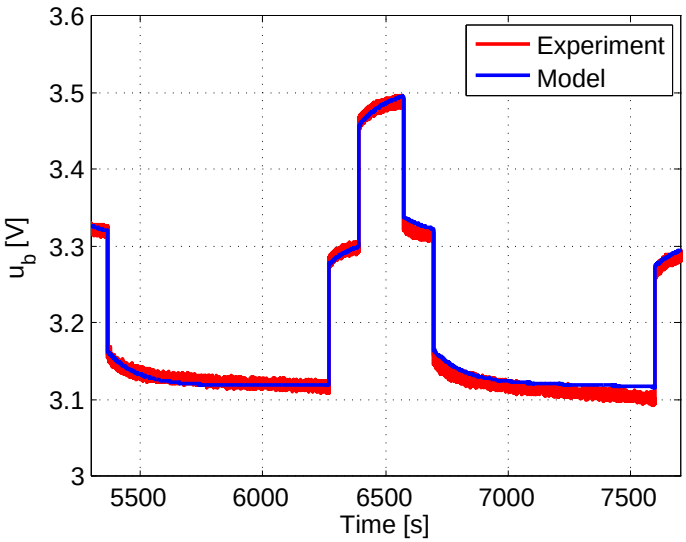

Figure A.4: *Comparison of battery response model and experiment taken at SOC $\approx$ 50 %.*

A.3 Relation between State of Charge and Open Circuit Voltage

In appendix A.6 a relationship between the open circuit voltage u_{OC} and state of charge voltage u_{SOC} is determined through an experiment where open circuit voltage of the battery is taken at various values of SOC. The result compared to a fitted third order polynomial is seen in figure A.5. The polynomial is seen in equation (A.3).

$$u_{OC}(u_{SOC}) = 1.618 \cdot 10^{-6} \cdot u_{SOC}^3 - 2.738 \cdot 10^{-4} \cdot u_{SOC}^2 + 0.0151 \cdot u_{SOC} + 3.0407 \quad \text{(A.3)}$$

A.4 Overall Model for Single Battery Cell

An overall comparison between the model and an experiment is seen in figure A.6. It is seen that coherence exist between model and experiment in the vast majority of SOC range. The deviation between the model and the experiment at low and high SOC values can be explained by the fact that the model is only valid at SOCs between 10 and 90 %. The temperature of the battery can inflict the parameters in the model. The impact of temperature is however neglected. Furthermore the battery capacity C_b is calculated at a discharge current of 75 A. The capacity can deviate at other discharge currents as seen in figure A.2. The model is concidered to describe the dynamics and SOC of the battery satisfactory.

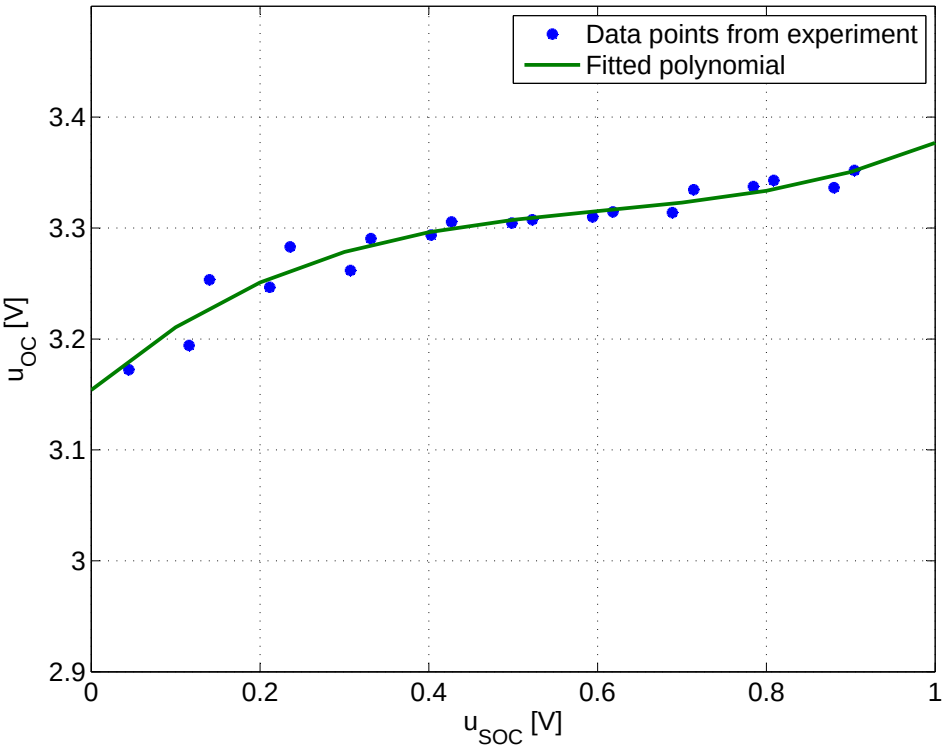

Figure A.5: *Open circuit voltage u_{OC} as a function of state of charge u_{SOC}.*

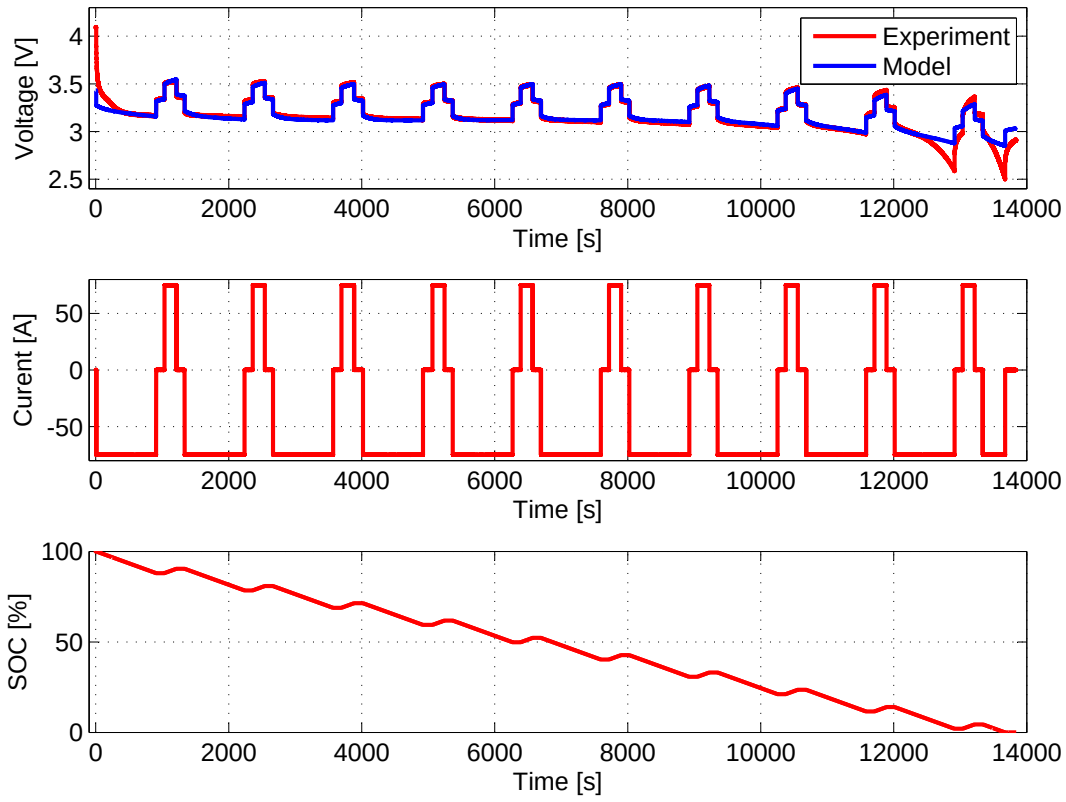

Figure A.6: *Comparrison between model and experiment.*

A.5 Battery Package Model

In this section the battery model is expanded to represent the entire battery package consisting of twenty cells. As mentioned in section 5.2.1 the battery pack is coupled in two parallel series each consisting of ten cells see figure 5.4b. The electrical circuit model of the battery package is seen in figure A.7. Each of the 20 cells are considered identical and the parameters for each cell are therefore identical. The parameters are seen in table A.1.
The relation between the open circuit voltage u_{OC} and the SOC voltage u_{SOC} is also expanded to the whole battery package. This is done by doubling the capacity C_b because there are two parallel branches of batteries, and by multiplying equation (A.3) by ten because of the ten series connected branches.

The battery package model is implemented into an extension to Simulink called Plecs. Plecs features among other components resistors and capacitors. The battery package illustrated figure A.7 is implemented into Plecs along with a resistor in series taking the resistance of the

relays and cable of the test setup into account. A current source is placed between the terminals passing current from an experiment through the package $i_{b.package}$. In figure A.8a the current from the experiment is seen. In figure A.8b the voltage from the experiment is seen along with output voltage from the Plecs model.

As seen in the figure the tendency of the two outputs resembles, but the amplitude of the oscillation deviates a lot. Furthermore the model output contains high frequency noise originating from the input cf. figure A.8a. The high frequency noise is primarily due to the 8 bit discretization of the oscilloscope used to collect data causing a current bit tolerance of 1 A. The lack of coherence between model and experiment can be explained by the fact that the battery pack contains old batteries that might have varying state of charges and has varying parameters in general. The test conditions for the battery stack experiment is also quite different from test conditions for the single cell model since the dynamic examined in this case was very slow while the periodic current signal of figure A.8a has a frequency of 5 kHz.

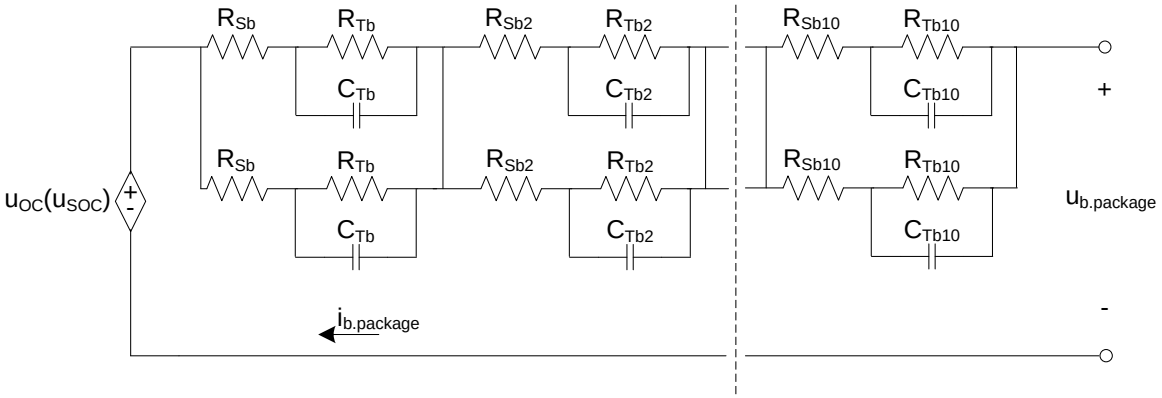

Figure A.7: *Electrical circuit for the battery response for the battery package.*

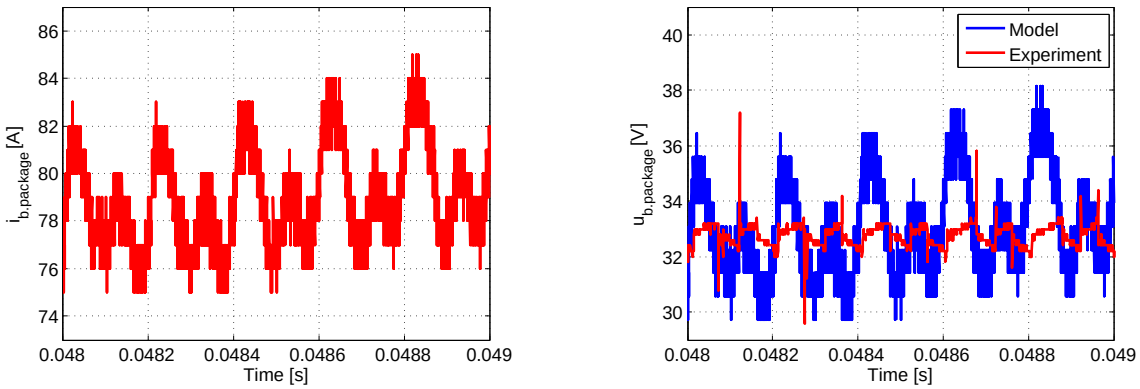

(a) *DC-bus current during experiment.*

(b) *DC-bus voltage during experiment and simulation.*

Figure A.8: *DC-bus voltage and current.*

A.6 Battery Parameters and Capacity

The objective of this experiment is to determine the parameters for the battery model presented in this chapter. Furthermore the capacity of the batteries is determined.

A.6.1 Equipment

- Thundersky 160 Ah battery cell.
- Kepco BOP 1 kW bipolar power supply.
- Temperature controlled box.
- Labview program and transducers monitoring cell voltage, current flow and temperature.

A.6.2 Test Setup

The test setup is depicted in figure A.9.

A.6.3 Execution

The following list contains a description of the execution of the experiment. Figure A.9 is used to support the description.

- Connect battery cell to test-setup.
- Turn on power supply and Labview program.

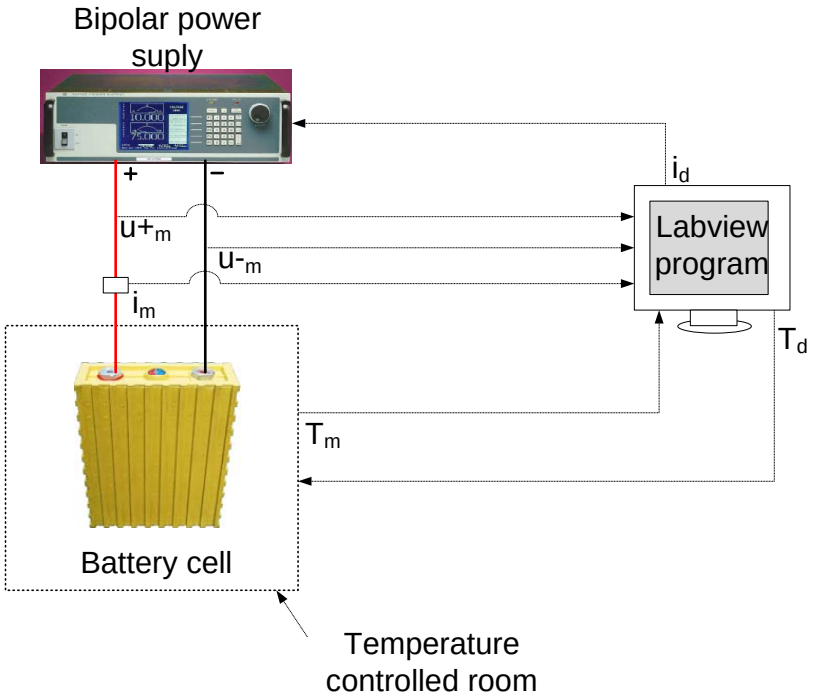

Figure A.9: *Test-setup for battery experiments. The values indexed "d" are the desired values and the values indexed "m" are the meassured values.*

- Charge the battery with a current of 75 A until it is fully charged. This corresponds to a terminal voltage of 4.25 V.
- Discharge the battery with a current of 75 A for approximately 15 minutes.
- Let the battery be idle for approximately 5 minutes.
- Perform current charge step of 75 A for approximately 5 minutes.
- Let the battery be idle for approximately 5 minutes.
- Repeat the last four points until the battery is fully discharged (Terminal voltage of 2.5 V).

A.6.4 Results

In figure A.10 the terminal voltage, current flow and SOC of the battery are displayed. The SOC value is calculated in Simulink using equation (A.4).

$$SOC = \frac{C_{b.ini} - 3600^{-1} \int i_b \, dt}{C_b} \cdot 100 \tag{A.4}$$

where:	SOC	State of charge $[\%]$.
	i_b	Currentflow to the battery $[A]$.
	C_b	Battery capacity $[Ah]$.
	$C_{b.ini}$	Initial battery capacity $[Ah]$.

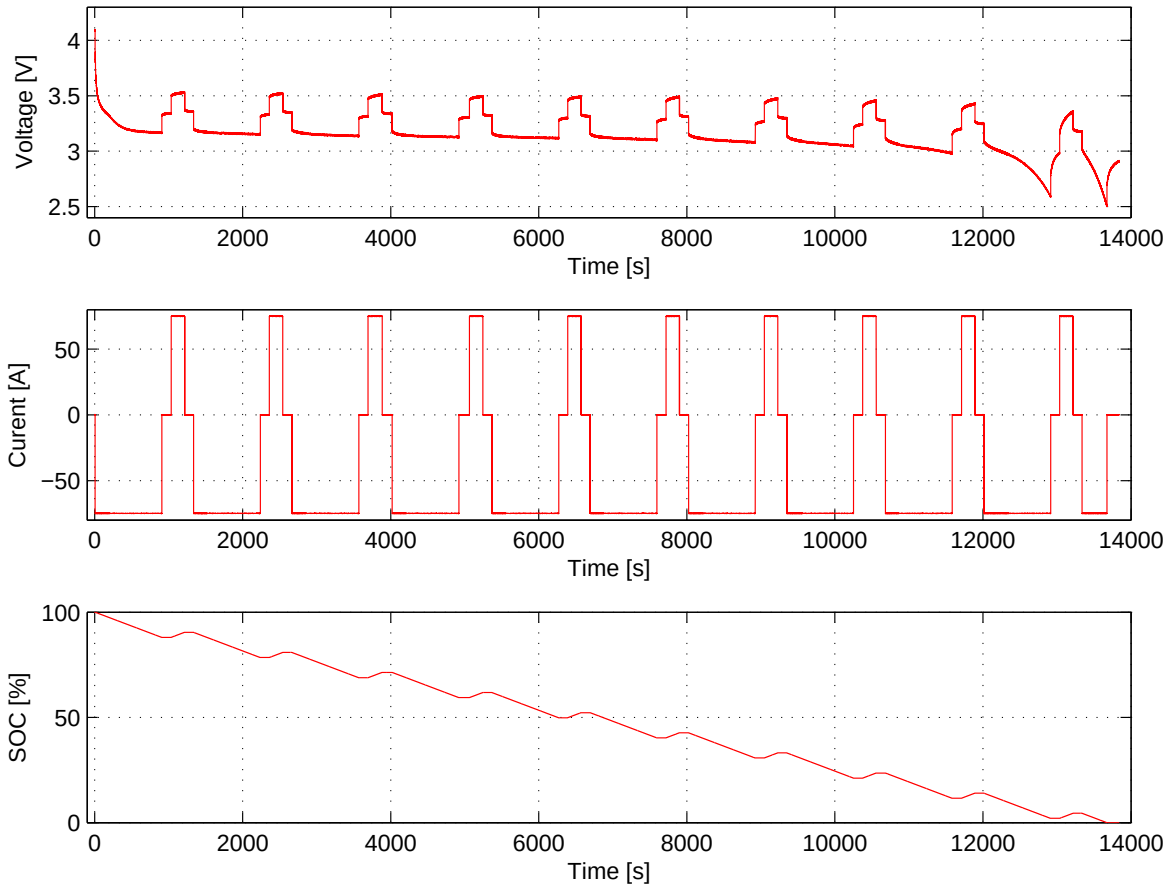

Figure A.10: *Terminal voltage, current flow and State of charge of the battery during the experiment.*

A.6.5 Sources of Error

- Due to losses in the battery the temperature inside the battery is not constant during the experiment. The temperature outside the cover of the battery increased from 27 to 31.5 during the experiment.

A.7 Data Processing

In this section the results from the experiment presented in section A.6.4 is analysed. The aim of the analysis is to determine the parameters for the battery model described in this chapter. Furthermore the capacity of the battery is determined.

A.7.1 Battery capacity

The battery capacity is determined by integrating the current of the experiment. This results in a capacity of 156.4 Ah. This value might be a bit higher in reality since the efficiency of the battery is not taken into account during the charging steps of the experiment. An experiment where the battery was discharged with a constant current of 75 A resulted in a capacity of 153.4 Ah which confirms the capacity within 2 %. The calculated capacity corresponds well with the capacity listed in the datasheet (160 Ah), with a deviation of only 2.3 %.

A.7.2 Relationship between open circuit voltage and state of charge

In this section a relationship between the open circuit voltage and state of charge of the batteries is determined.
Data points for the SOC taken at the end at each idle period and the corresponding battery terminal voltage is plotted in figure A.11. A third order polynomial is generated using the data points from the experiment except the ones taken at a SOC lower than 10 %. According to [Chen and Rincon-Mora, 2006] the model exhibits a large voltage error at a SOC lower than 10 %. The fitted curve only has small acceptable deviations from the data points.

A.7.3 Parameters for battery response

To determine the parameters for the model the step response from the experiment is compared to the equivalent response from the model. The point of comparison is chosen to be at a SOC of approximately 50 %. The model is build up in Simulink and parameters are varied until there is coherence between model and experiment. A detailed view of the comparison is seen in figure A.12 and an overall view of the comparison is shown figure A.13.

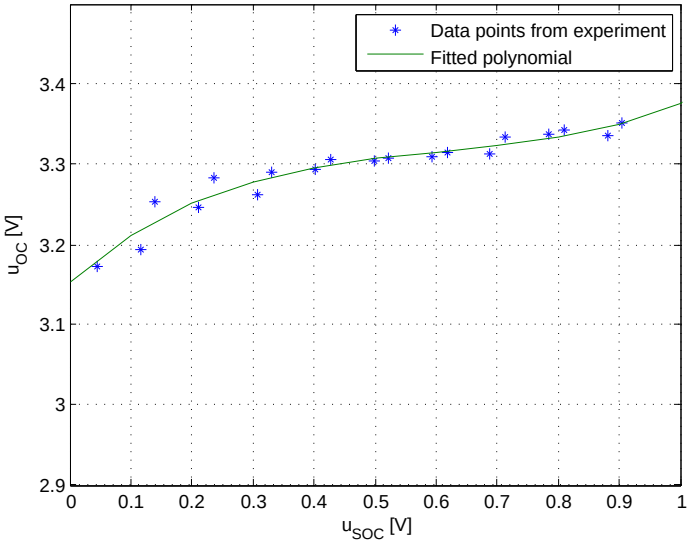

Figure A.11: *OCV as a function of SOC.*

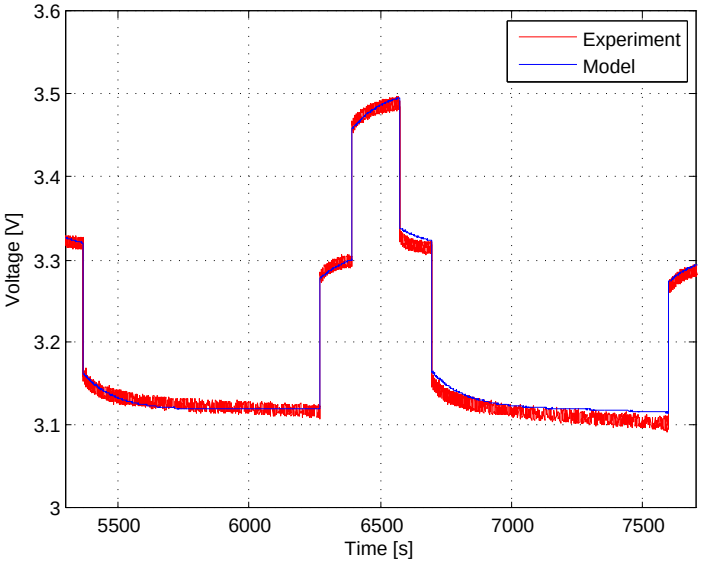

Figure A.12: *Detailed view of the comparison between the experiment and the model taken at a SOC of approximately 50 %.*

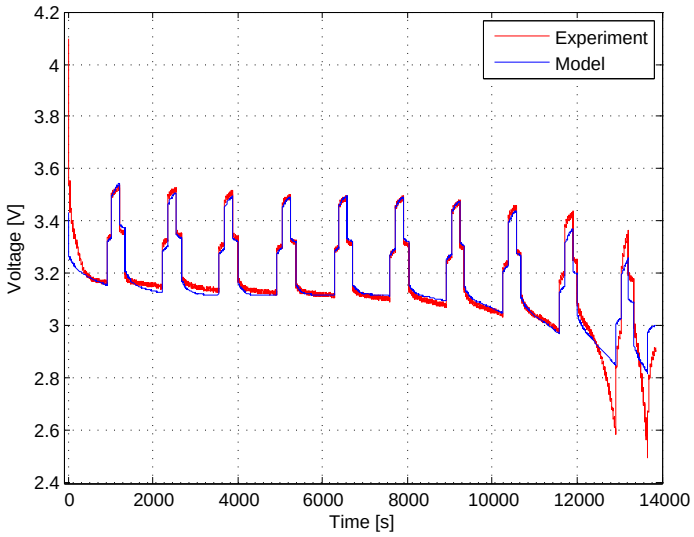

Figure A.13: *Overall view of the comparison between the experiment and the model.*

APPENDIX B

INVERTER

This chapter contains a description of non-linearities and non-ideal phenomenas in the inverter that is not modeled in the simulation model described in the report. Modulations strategies are also considered in this chapter.
The inverter is as mentioned in the report a three phase Sauer Danfoss battery powered inverter. The inverter converts the DC voltage from the battery pack into pulse width modulated (PWM) signals. The inverter consists of six MOSFET transistors and six diodes. The diodes inhibit the current from flowing reverse biased through the transistors and thereby preventing damaging the transistors. A scheme of the electrical circuit is depicted in figure B.1.

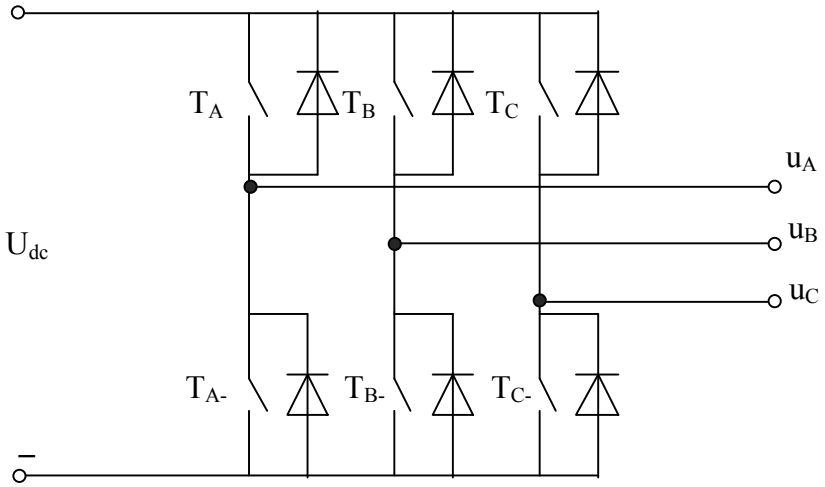

Figure B.1: *Electrical circuit of the three phase inverter.*

Voltage in each phase can be controlled by controlling the transistors in each branch. In order to

avoid shoot through in the branches of the inverter the upper and lower transistor of each branch must not be conducting at the same time. To avoid this a fixed time interval called a dead time applied between the conduction stages of one phase branch ensuring that shoot through does not happen.

Modulation Strategy

The PWM signals can be applied using various strategies which have various advantages. The most basic strategy is sinusoidal PWM (SPWM). Another strategy is space vector PWM (SVPWM). The advantage of SVPWM is the fact that a larger line-line voltage can be obtained compared to SPWM. This is advantageous in the electric vehicle powertrain as the battery voltage varies and a larger line-line voltage therefore can be crucial in order to obtain an acceptable performance for the electric vehicle. In this section the SPWM and SVPWM are both described. In figure B.2 the basic concept of sinusoidal PWM is illustrated. The sine waves in sinusoidal PWM are called the fundamentals, with the fundamental frequency and the fundamental amplitude. A triangular control signal (u_{tri}) along with three sinusoidal compare signals are generated by the DSP. Each compare signal is compared to the control signal generating the switching signals q_A, q_B and q_C. The switching signals contain the necessary information to operate both transistors in each branch. This is expressed mathematically as in equation (B.1).

$$q_A = \begin{cases} 1 & \text{for } u_{tri} \leq u_{A,compare} \Rightarrow T_{A+} = 1 \wedge T_{A-} = 0 \\ 0 & \text{for } u_{tri} > u_{A,compare} \Rightarrow T_{A+} = 0 \wedge T_{A-} = 1 \end{cases} \tag{B.1}$$

where:

	q_A	Switching signal for phase A [-]
	u_{tri}	Amplitude of control signal [V]
	$u_{A,compare}$	Amplitude of compare signal for phase A [V]
	T	Transistor [-]

The concept of sinusoidal PWM is illustrated in figure B.2.
The carrier based PWM used in SPWM can be replaced with Space Vector Pulse Width Modulation (SVPWM) and 15% larger output voltages (line to line) can be achieved. The larger output makes better use of the potential of both inverter and machine and reduces the risk of voltage saturation. SVPWM is explained in the following
To support the explanation of SVPWM figure B.3 is included.
As stated earlier both switches in each branch must not be ON at the same time because this short circuits the DC-bus. If both switches are OFF then the circuit is open. This fact renders eight possible inverter states for a three phase inverter. Each state corresponds to a specific

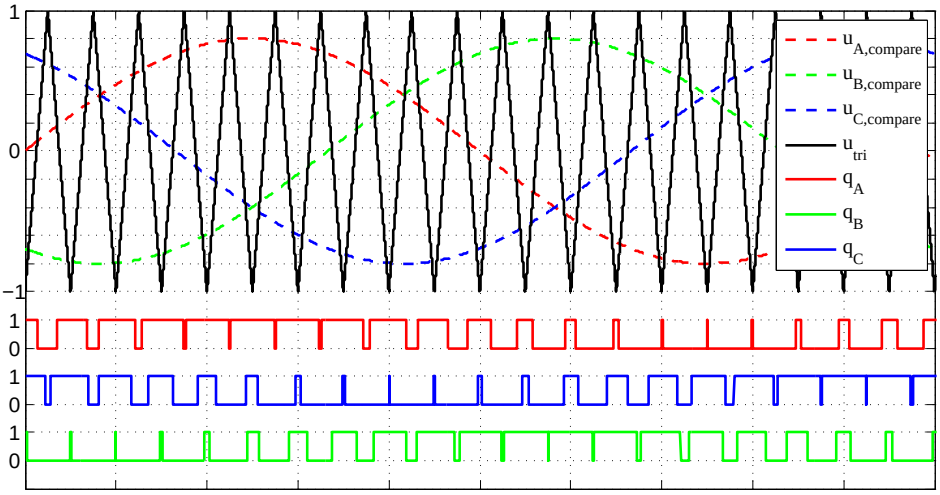

Figure B.2: *Normalized scheme for SPWM generation.*

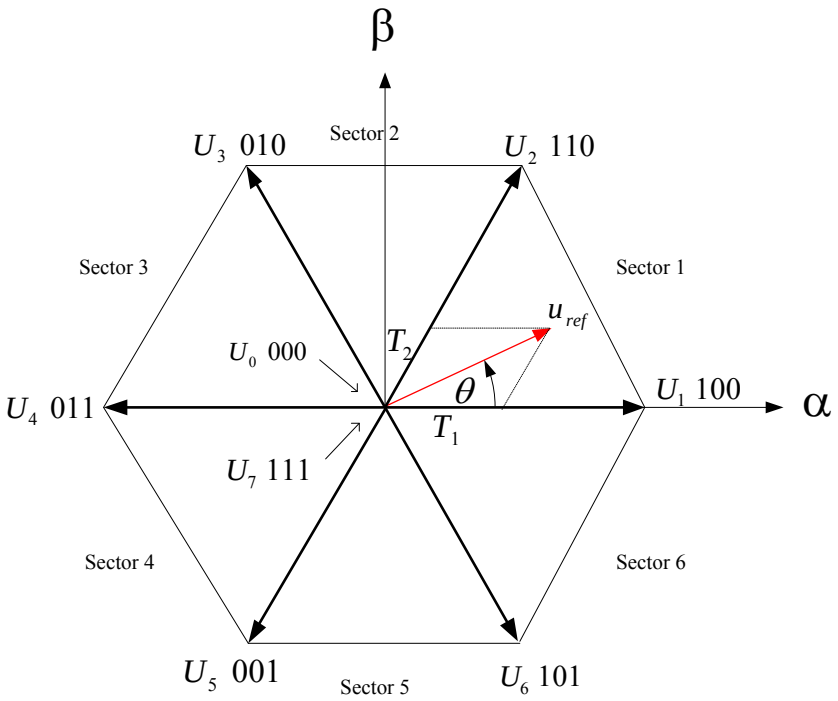

Figure B.3: *Arrangement of active and zero space vectors.*

combination of switches. The states are denoted in binary format. The value 0 indicates that the upper switch is OFF and the lower switch is ON. Three binary values describe all eight possible inverter states. Each of the eight states of the inverter is mapped into the αβ-reference frame as switching state vectors, see figure B.3. Six out of these eight possible inverter states are known as non-zero switching states and the remaining two produce zero output voltage (line to line) and are known as zero switching states. The zero switching states are denoted (000) and (111).

The reference voltage vector (u_{ref}) rotates in the αβ-plane at the same frequency as the desired output voltage. The components of the voltage reference vector are drawn to the adjacent voltage vector states. In figure B.3 the reference voltage vector u_{ref} is located in sector 1. The adjacent voltage vector states are (100) and (110). The components T_1 and T_2 denote the time at which the two states is active. One of the zero switching states must be active in the remaining time of the duty cycle. This is given by equation:

$$P_D = T_0 + T_1 + T_2 \tag{B.2}$$

where:	P_D	Period of a whole duty cycle [s]
	T	The time at which the state is active [s]

A simple way to synthesize the output voltage vector is to use the centered sequence. The switching sequence is depicted in figure B.4.

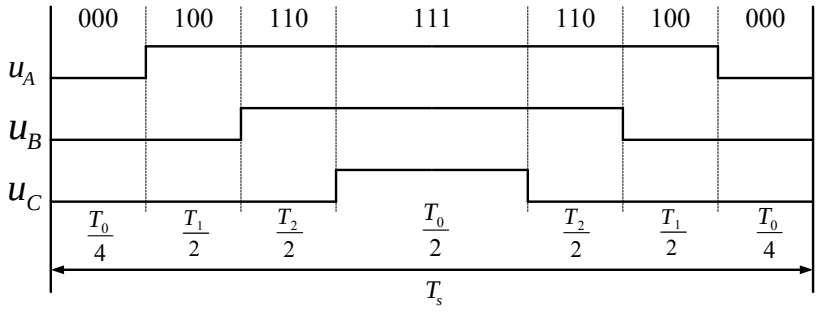

Figure B.4: *Centered sequence.*

The magnitude of each switching state vector is $\frac{2}{3} \cdot u_{dc}$.
The potential of space vector is seen when comparing phase and line-line voltages for SVPWM to SPWM. This is done in the following. In figure B.5a the normalized phase voltages for phase *A* and *B* using SPWM is illustrated. As seen in the figure the amplitude of the signals are 1. In figure B.5b the normalized phase voltages for phase *A* and *B* using SVPWM are illustrated. As seen in the figure the maximum normalized voltage output of the inverter is 1 as when using SPVM. The line-line voltage for each of modulation strategies is depicted in figure B.6. As seen in figure B.6 the line-line voltage amplitude obtained using SVPWM is 15% larger than when using SPWM. Due to this advantage SVPWM is used as modulation strategy in the control for the electric vehicle.

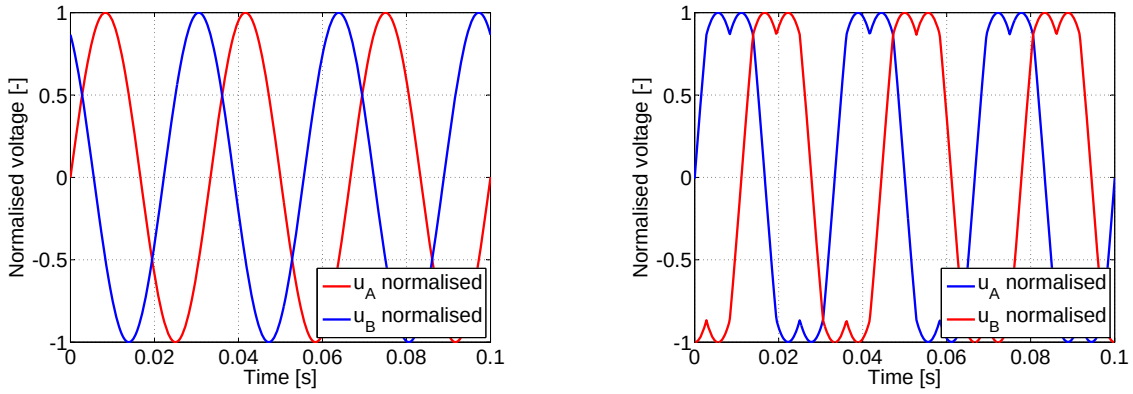

(a) *Normalised phase voltages when using SPWM.* ***(b)*** *Normalised phase voltages when using SVPWM.*

Figure B.5: *Normalised phase voltages for SPWM and SVPWM.*

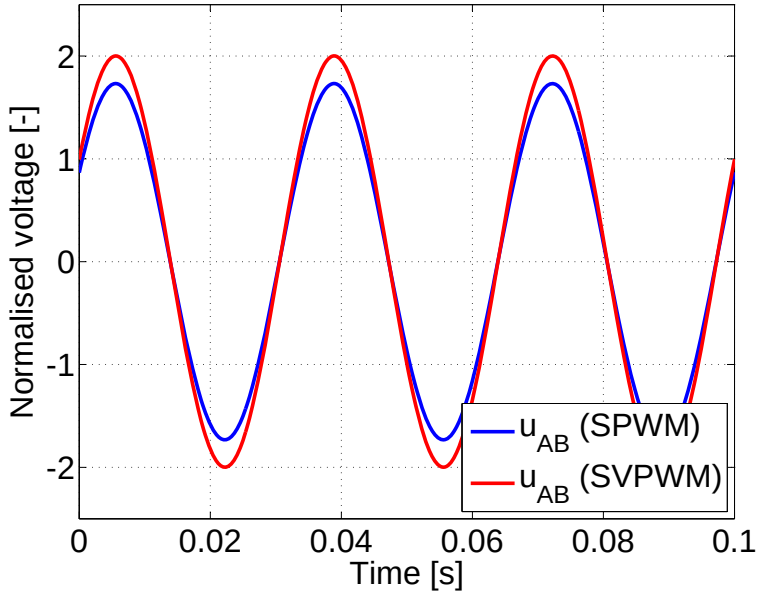

Figure B.6: *Line-line voltages for normalised phase voltages illustrated in figure B.5.*

Modulation ratios

In order to achieve proper Pulse Width Modulation of the compare signals the ratio between the switching signal frequency and the fundamental frequency must have a certain value. The relation between the two frequencies is denoted m_f.

$$m_f = \frac{f_s}{f_1} \tag{B.3}$$

where:	m_f	Frequency modulation ratio [-]
	f_s	Switching frequency [Hz]
	f_1	Fundamental frequency [Hz]

High values of m_f is preferable in order to achieve good modulation of the compare signal consequently high switching frequency (f_s) is preferable. However the disadvantage of a high f_s is that factors as switching losses and dead time become more significant.
Harmonics with higher frequencies than the fundamental frequency appears in the output voltage as a consequence of PWM. These harmonics results in a current ripple in the fundamental current. The size of the current ripple is dependent on the size of the inductance in the phases. A high m_f will result in a relatively small current ripple compared to the fundamental current. The switching frequency of the inverter is set to 5000 Hz. The maximum speed of the induction machine is 5000 rpm corresponding to a fundamental frequency of 167Hz. A fundamental frequency of 167Hz results in an m_f of 30.

Another important ratio is the amplitude modulation ratio (m_a) which is defined as the relation between the peak value of u_{tri} and peak value of $u_{k,compare}$.

$$m_a = \frac{\hat{u}_{k,compare}}{\hat{u}_{tri}}, (k = A,B,C) \tag{B.4}$$

where:	m_a	Amplitude modulation ratio [-]

When modulating a sine signal using SPWM as in figure B.2 m_a must be less than one to avoid over modulation. When using SVPWM the modulation index can be up to 1.15 [Broeck et al., 1988].

Non-ideal Inverter

When the inverter is connected to the induction machine and PWM is used to control the voltage in the three phases non-ideal phenomenas must be considered. Equation (B.1) is an idealized expression because the dynamics of the transistors are neglected. The transistors in the inverter cannot switch on or off momentarily, and therefore the voltage in the phases cannot be changed momentarily. Dead time will induce another deviation from the ideal expression in equation (B.1), since it introduces a delay between opening one transistor in a branch and closing the other.

When current flows through the transistors and diodes in the inverter voltage drops are induced. These voltage drops will result in phase voltages that differs from the DC bus in the inverter, depending on the amplitude of the current flowing through the transistors/diodes.

The DC bus in the inverter is connected to the battery pack. As described in the previous section the terminal voltage of the battery pack is dependent on the current flowing through the battery pack. Since there is a current ripple in the fundamental current in the phases, there will also be a current ripple in the current flowing through the battery pack resulting in a ripple in DC bus voltage. The DC bus voltage can be measured when calculating duty cycles in the DSP but the DC bus voltage will still vary within one duty cycle caused by the voltage ripple.

The effect of dead time and dynamics of transistors is illustrated in figure B.7. The figure shows the normalized PWM signal from the DSP compared to the normalized output voltage from the inverter. The dead time is set to 2 μs on the BPI interface board. The three phases are not connected to the inverter in this experiment, so the variation in DC bus voltage and the voltage drops in transistors and diodes are not present. As seen in the figure the PWM signals are inverted so when the DSP signal is high the inverter output is low. The experiment is further explained in section F.1 in appendix. The figure clearly shows that there is a delay between DSP PWM signal and the inverter output. The transient dynamics of the transistors is present as the voltage does not change momentarily. The transient dynamics of the entire system when switching the transistors is also seen as an overshoot is present in the phase voltage.

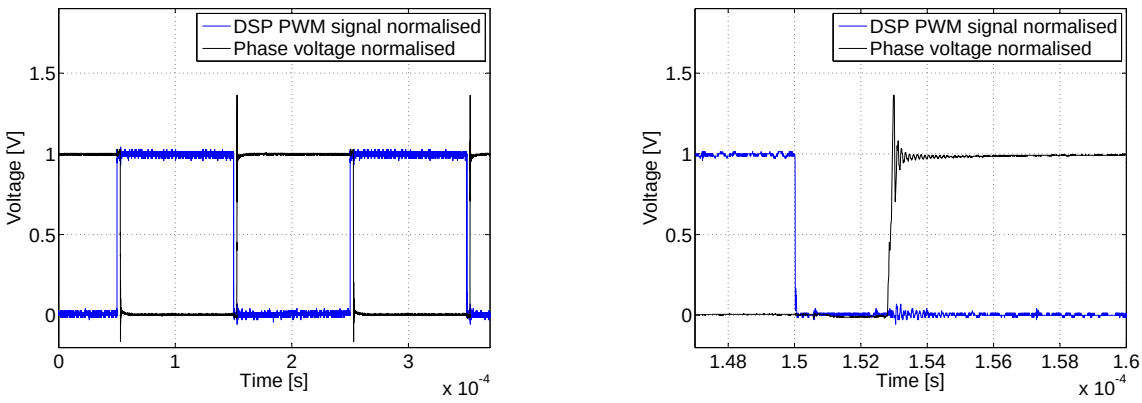

(a) *DSP PWM signal and phase voltage.* ***(b)*** *Close view of DSP PWM signal and phase voltage.*

Figure B.7: *DSP PWM signal and phase voltage.*

The effect of variation in the DC bus is illustrated in figure B.8. In this experiment sinusoidal voltages modulated by PWM are applied on the three phases of the induction machine and the Siemens drive system is set to a constant velocity. The fundamental frequency of the sinusoidal voltage is 60 Hz, the slip is 3% and the amplitude of the voltage is set to 10.15 V. The experiment is further explained in section F.2 in appendix.
The DC-bus voltage is depicted in figure B.8 along with the sampling points of the DSP and a filtered voltage of the DC-bus. As seen in figure B.8 the DC bus voltage is varying within one duty cycle and the sampling of the DSP sometimes intercept the voltage spikes at i.e. 39.12 ms in figure B.8. To avoid this a first order filter is designed having a time constant of 0.16 s. This yields a maximum filtered voltage variation of 0.32 V during the experiment. The rise time of the filter is 0.64 s which along with the voltage variation is considered to be acceptable. The filtered voltage is seen in figure B.8.

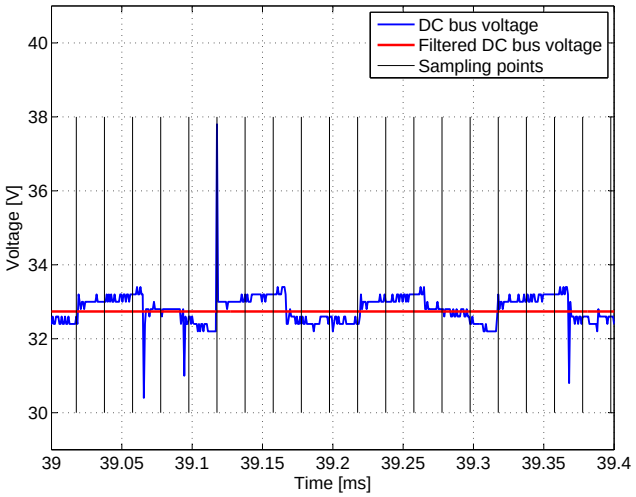

Figure B.8: *Variating DC bus voltage.*

The effect of voltage drops is depicted in figure B.9. The voltage and current measurements from figure B.9 are from the same experiment as figure B.8, described in section F.2 in appendix. In the figure it is seen how the upper and lower bound of the PWM voltage varies when current flows through the phase. To emphasize the variation tendency lines for the upper and lower bounds are added to the figure.
The non-ideal phenomenas described in this section induces errors in phase voltages. The error varies from whether the machine is functioning as a generator or a motor. This is seen from FFT analysis of the voltage signals. When the induction machine is functioning as a generator the FFT analysis shows that the voltage amplitude is higher than intended. When functioning as a motor the FFT analysis shows that the amplitude is lower than intended. This corresponds well

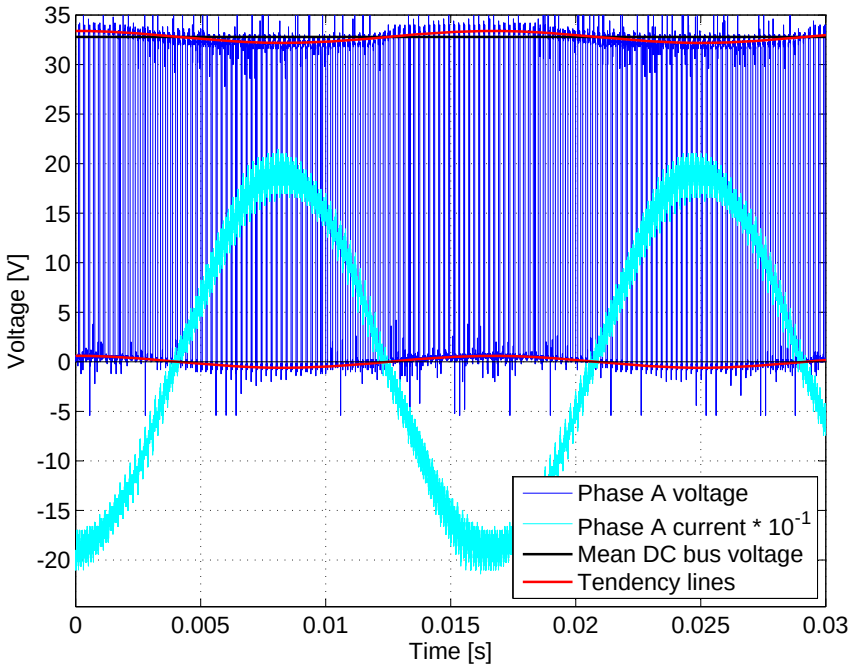

Figure B.9: *Current and voltage in phase A for sinusoidal voltage inputs. The fundamental frequency is 60 Hz, the slip is 3% and the amplitude of the voltage is set to 10.15 V.*

with the fact that the power factor is negative when functioning as a generator. The negative power factor means that the phase current is more than 90° shifted from the phase voltage. In figure B.9 it is seen that when the current is peaking positive the upper and lower bounds of the PWM signal are peaking negatively. The amplitude of the sinusoidal voltage in the phase is therefore lower than intended when the current peaks positive. When the current peaks negatively the bounds peak positively. A positive power factor (a phase shift less than 90°) hereby results in a lower amplitude than intended and a negative power factor (a phase shift above 90°) results in a higher amplitude than intended.

Compensations to reduce the errors caused by the non-ideal phenomenas can be applied in the control strategy. From measurements of the phase currents the phase voltages can be adjusted to compensate for the errors in voltage amplitudes. When using current control this compensation is not crucial as the voltage is adjusted to obtain a desired current. The compensation can however be necessary when estimating the rotor flux.

APPENDIX C

VOLTAGE- AND TORQUE EQUATIONS FOR INDUCTION MACHINE

This section contains a description of the modeling of the induction motor. Voltage equations for the machine are firstly presented and then transformed to an arbitrary reference frame. The torque equation is described and a proper reference frame is chosen for the simulation model.

C.1 Voltage Equations

This section contains a derivation of the voltage equations describing the electric circuit of the induction machine.

The machine used in this project is a 3-phase squirrel cage induction machine.
The stator is delta coupled which means that the electrical circuit in the stator is illustrated as in figure C.1.
It is assumed that the machine is balanced meaning that the three phase impedances ($Z_{s\Delta}$) are equal [Glover et al., 2010, p. 61]. It is also assumed that the voltages applied to the three phases are balanced, which means that the voltages have equal magnitudes and are phase shifted 120°.
The delta coupling is now transformed to an equivalent wye-connected coupling[Glover et al., 2010, p. 63]. This is done by multiplying the impedances by $1/3$, as illustrated in figure C.2.
If the circuit is assumed to be wye-connected when calculating the line impedances from experiments in section 6.3.1, the impedances are already transformed to the equivalent wye-connected

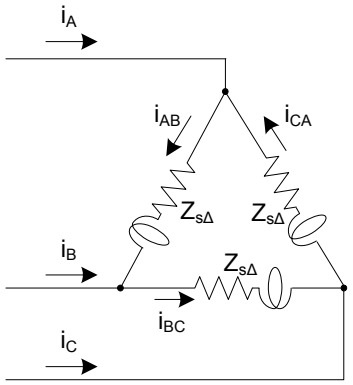

Figure C.1: *Electrical circuit for delta-coupled stator windings.*

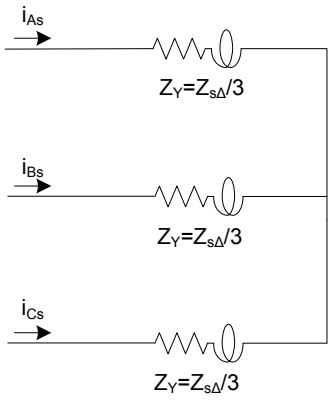

Figure C.2: *Electrical circuit for equivalent wye-coupled stator windings.*

circuit. Since the phase currents in the delta coupled circuit cannot be measured it is desirable to consider the machine as wye-connected as the phase currents in the wye-connected machine can be measured. The circuit is therefore considered as wye-connected throughout the rest of this report.

The windings are assumed to be sinusoidally distributed in the stator. The rotor consists of uniformly distributed aluminum bars that are short circuited at each end of the rotor. It may appear that the uniformly distributed aluminum bars and the sinusoidal distributed windings in the stator will not create a smooth torque characteristic, however in most induction machines the uniformly distributed winding is adequately described by its fundamental sinusoidal component and is represented by an equivalent 3-phase winding [Krause et al., 2002, p. 144]. The rotor is therefore considered as consisting of three 120° shifted, sinusoidally distributed phases.

The derivation of voltage equations is based on [Krause et al., 2002]. An electrical equivalent circuit for the squirrel cage induction motor when considered as wye-connected is illustrated in figure C.3.

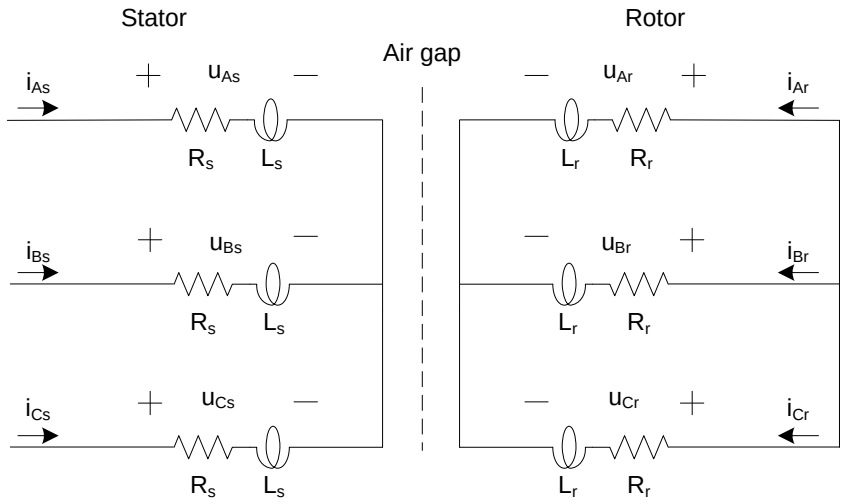

Figure C.3: *Electrical equivalent diagram of the wye connected, squirrel cage induction machine.*

Rotor and stator phase quantities are illustrated in figure C.4. θ_r is the angle between phase A in the stator and phase A in the rotor.
The voltage equations describing the machine are expressed as [Krause et al., 2002, p. 142]:

$$\bar{u}_{ABCs} = \bar{R}_s \cdot \bar{i}_{ABCs} + p \cdot \bar{\lambda}_{ABCs} \tag{C.1}$$

$$\bar{u}_{ABCr} = \bar{R}_r \cdot \bar{i}_{ABCr} + p \cdot \bar{\lambda}_{ABCr} \tag{C.2}$$

where:	$\bar{\lambda}_{ABCs}$	Stator flux linkage $[Wb]$
	$\bar{\lambda}_{ABCr}$	Rotor flux linkage $[Wb]$

and

$$\bar{f}^T_{ABCs} = [f_{As}\ f_{Bs}\ f_{Cs}] \tag{C.3}$$

$$\bar{f}^T_{ABCr} = [f_{Ar}\ f_{Br}\ f_{Cr}] \tag{C.4}$$

The subscripts s and r denotes parameters and variables associated with the stator and rotor

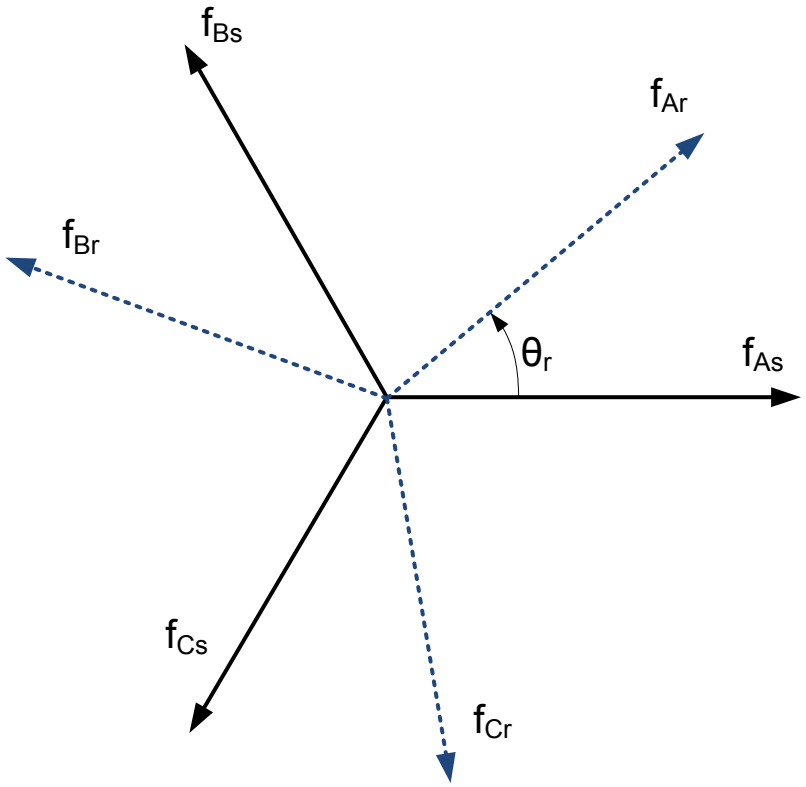

Figure C.4: *Illustration of rotor and stator phase quantities.*

respectively. p is the $^{d}/_{dt}$ operator. $\bar{R}_s$ and $\bar{R}_r$ are expressed as:

$$\bar{R}_s = \begin{bmatrix} R_s & 0 & 0 \\ 0 & R_s & 0 \\ 0 & 0 & R_s \end{bmatrix} \tag{C.5}$$

$$\bar{R}_r = \begin{bmatrix} R_r & 0 & 0 \\ 0 & R_r & 0 \\ 0 & 0 & R_r \end{bmatrix} \tag{C.6}$$

where:	R_s	Stator winding resistance $[\Omega]$
	R_r	Rotor winding resistance $[\Omega]$

The machine is considered as linear which implies that the relation between current and flux in each winding is linear. When the flux reaches a curtain value the relation between current and flux is no longer linear, as the flux will saturate. This is however not considered in the model. The flux linkages are hereby expressed as:

$$\begin{bmatrix} \bar{\lambda}_{ABCs} \\ \bar{\lambda}_{ABCr} \end{bmatrix} = \begin{bmatrix} \bar{L}_s & \bar{L}_{sr} \\ (\bar{L}_{sr})^T & \bar{L}_r \end{bmatrix} \cdot \begin{bmatrix} \bar{i}_{ABCs} \\ \bar{i}_{ABCr} \end{bmatrix} \tag{C.7}$$

The winding inductances are expressed as:

$$\bar{L}_s = \begin{bmatrix} L_{ls}+L_{ms} & -\frac{1}{2}\cdot L_{ms} & -\frac{1}{2}\cdot L_{ms} \\ -\frac{1}{2}\cdot L_{ms} & L_{ls}+L_{ms} & -\frac{1}{2}\cdot L_{ms} \\ -\frac{1}{2}\cdot L_{ms} & -\frac{1}{2}\cdot L_{ms} & L_{ls}+L_{ms} \end{bmatrix} \tag{C.8}$$

$$\bar{L}_r = \begin{bmatrix} L_{lr}+L_{mr} & -\frac{1}{2}\cdot L_{mr} & -\frac{1}{2}\cdot L_{mr} \\ -\frac{1}{2}\cdot L_{mr} & L_{lr}+L_{mr} & -\frac{1}{2}\cdot L_{mr} \\ -\frac{1}{2}\cdot L_{mr} & -\frac{1}{2}\cdot L_{mr} & L_{lr}+L_{mr} \end{bmatrix} \tag{C.9}$$

$$\bar{L}_{sr} = L_{sr} \begin{bmatrix} cos(\theta_r) & cos(\theta_r+\frac{2\pi}{3}) & cos(\theta_r-\frac{2\pi}{3}) \\ cos(\theta_r-\frac{2\pi}{3}) & cos(\theta_r) & cos(\theta_r+\frac{2\pi}{3}) \\ cos(\theta_r+\frac{2\pi}{3}) & cos(\theta_r-\frac{2\pi}{3}) & cos(\theta_r) \end{bmatrix} \tag{C.10}$$

where:

L_{ls}	Stator leakage inductance $[H]$
L_{lr}	Rotor leakage inductance $[H]$
L_{ms}	Stator magnetising inductance $[H]$
L_{mr}	Rotor magnetising inductance $[H]$
L_{sr}	Mutual inductance between rotor and stator windings $[H]$
θ_r	Angle between stator and rotor coordinate systems $[rad]$

The flux linkage for the stator is, as seen in equation (C.7), a function of the stator and rotor currents. Considering the flux linkage for phase A in the stator, i_{As} is multiplied with the leakage inductance and the magnetizing inductance. A current in phase A in the stator will hereby obviously provide a magnetizing flux in phase A and a leakage flux providing no magnetizing effect. A current in the other two stator phases will provide a negative flux in phase A. This is due to the fact that the phases are shifted 120°.

A current in the rotor phases will also provide a flux in phase A in the stator, this flux is however dependent on the angle θ_r between the stator and rotor coordinate systems. The maximum flux linkage from e.g. phase A in the rotor to phase A in the stator is $i_{Ar}\cdot L_{sr}$. This flux linkage is obtained when θ_r=0 as the flux in phase A in the rotor is pointing in the exact same direction as the flux in phase A in the stator. This is seen in figure C.4.

The coupling between the stator and rotor is considered as a transformer with a proper turns ratio. The ratio is obviously dependent on the number of turns in rotor and stator but also on the structure of the rotor and stator, e.g. skewed rotor windings.
When considering the stator and rotor as a transformer the voltage relation between stator and rotor is dependent on the turns ratio, as will the current relation. Using the ratio the rotor current and voltage is referred to the stator system by the following equations:

$$\bar{i}'_{ABCr} = \frac{N_r}{N_s} \cdot \bar{i}_{ABCr} \tag{C.11}$$

$$\bar{u}'_{ABCr} = \frac{N_s}{N_r} \cdot \bar{u}_{ABCr} \tag{C.12}$$

where: N_s Number of turns in stator $[-]$

N_r Number of turns in rotor $[-]$

The rotor inductance and resistance can also be referred to the stator system. This is done using an energy conservation equation for the transformer. Considering the rotor resistance and inductance as one equivalent impedance, the following equations are expressed as:

$$Z_r = \frac{u_r}{i_r} \tag{C.13}$$

$$Z'_r = \frac{u'_r}{i'_r} = \frac{u_r \cdot \frac{N_s}{N_r}}{i_r \cdot \frac{N_r}{N_s}} = \frac{u_r}{i_r} \cdot \left(\frac{N_s}{N_r}\right)^2 = Z_r \cdot \left(\frac{N_s}{N_r}\right)^2 \tag{C.14}$$

The rotor impedance referred to the stator is hereby the turns ratio squared. The referred rotor resistance and inductance is therefore expressed as:

$$\bar{R}'_r = \bar{R}_r \cdot \left(\frac{N_s}{N_r}\right)^2 \tag{C.15}$$

$$\bar{L}'_r = \bar{L}_r \cdot \left(\frac{N_s}{N_r}\right)^2 \tag{C.16}$$

The mutual inductance is expressed as:

$$\bar{L}'_{sr} = \bar{L}_{sr} \cdot \left(\frac{N_s}{N_r}\right) \tag{C.17}$$

The three inductances L_{ms}, L_{mr} and L_{sr} is expressed by the following equations [Krause et al., 2002, p. 55]:

$$L_{ms} = \left(\frac{N_s}{2}\right)^2 \cdot \frac{\pi\mu_0 rl}{l_g} \tag{C.18}$$

$$L_{mr} = \left(\frac{N_r}{2}\right)^2 \cdot \frac{\pi\mu_0 rl}{l_g} \tag{C.19}$$

$$L_{sr} = \left(\frac{N_s}{2}\right) \cdot \left(\frac{N_r}{2}\right) \cdot \frac{\pi\mu_0 rl}{l_g} \tag{C.20}$$

where:		
	μ_0	Permeability constant $\left[\frac{H}{m}\right]$
	r	Radius of airgap $[m]$
	l	Depth of airgap $[m]$
	l_g	Length of airgap $[m]$

The relation between the inductances is expressed as:

$$L_{ms} = \left(\frac{N_s}{N_r}\right)^2 \cdot L_{mr} \tag{C.21}$$

$$L_{ms} = \left(\frac{N_s}{N_r}\right) \cdot L_{sr} \tag{C.22}$$

The referred inductances, $\bar{L_r}'$ and $\bar{L_{sr}}'$, is expressed using equation (C.9), (C.10), (C.16), (C.17), (C.21) and (C.22):

$$\begin{aligned} \bar{L}'_r &= \left(\frac{N_s}{N_r}\right)^2 \cdot \begin{bmatrix} L_{lr}+L_{mr} & -\frac{1}{2}\cdot L_{mr} & -\frac{1}{2}\cdot L_{mr} \\ -\frac{1}{2}\cdot L_{mr} & L_{lr}+L_{mr} & -\frac{1}{2}\cdot L_{mr} \\ -\frac{1}{2}\cdot L_{mr} & -\frac{1}{2}\cdot L_{mr} & L_{lr}+L_{mr} \end{bmatrix} \\ &= \begin{bmatrix} L'_{lr}+L_{ms} & -\frac{1}{2}\cdot L_{ms} & -\frac{1}{2}\cdot L_{ms} \\ -\frac{1}{2}\cdot L_{ms} & L'_{lr}+L_{ms} & -\frac{1}{2}\cdot L_{ms} \\ -\frac{1}{2}\cdot L_{ms} & -\frac{1}{2}\cdot L_{ms} & L'_{lr}+L_{ms} \end{bmatrix} \end{aligned} \tag{C.23}$$

$$\begin{aligned} \bar{L}'_{sr} &= \left(\frac{N_s}{N_r}\right) \cdot L_{sr} \cdot \begin{bmatrix} cos(\theta_r) & cos(\theta_r+\frac{2\pi}{3}) & cos(\theta_r-\frac{2\pi}{3}) \\ cos(\theta_r-\frac{2\pi}{3}) & cos(\theta_r) & cos(\theta_r+\frac{2\pi}{3}) \\ cos(\theta_r+\frac{2\pi}{3}) & cos(\theta_r-\frac{2\pi}{3}) & cos(\theta_r) \end{bmatrix} \\ &= L_{ms} \cdot \begin{bmatrix} cos(\theta_r) & cos(\theta_r+\frac{2\pi}{3}) & cos(\theta_r-\frac{2\pi}{3}) \\ cos(\theta_r-\frac{2\pi}{3}) & cos(\theta_r) & cos(\theta_r+\frac{2\pi}{3}) \\ cos(\theta_r+\frac{2\pi}{3}) & cos(\theta_r-\frac{2\pi}{3}) & cos(\theta_r) \end{bmatrix} \end{aligned} \tag{C.24}$$

The voltage equations are rewritten:

$$\begin{bmatrix} \bar{u}_{ABCs} \\ \bar{u}'_{ABCr} \end{bmatrix} = \begin{bmatrix} \bar{R}_s + p \cdot \bar{L}_s & p \cdot \bar{L}'_{sr} \\ p \cdot (\bar{L}'_{sr})^T & \bar{R}'_r + p \cdot \bar{L}'_r \end{bmatrix} \cdot \begin{bmatrix} \bar{i}_{ABCs} \\ \bar{i}'_{ABCr} \end{bmatrix} \tag{C.25}$$

The voltage equations are stated in the *ABC* reference-frame. In order to simplify the voltage equations and to express a simple torque equation another reference frame can be chosen. The next section contains a transformation of the voltage equations to an arbitrary reference-frame.

C.2 Transformation of Voltage Equations to an Arbitrary Reference-frame

In order to simplify the voltage equations derived in the previous section a transformation of the equations is conducted in this section. The equations are first transformed to an arbitrary reference-frame. A proper reference-frame is chosen in section C.4.

A general transformation of the 3-phase variables of the rotor circuit to an arbitrary rotating $qd0$ reference-frame is expressed as[Krause et al., 2002, p. 147]:

$$\bar{f}'_{qd0r} = \bar{K}_r \cdot \bar{f}'_{ABCr} \tag{C.26}$$

Where $\bar{K}_r$ and $\bar{f}'_{qd0r}$ is expressed as:

$$\bar{K}_r = \frac{2}{3} \cdot \begin{bmatrix} cos\beta & cos(\beta - \frac{2\pi}{3}) & cos(\beta + \frac{2\pi}{3}) \\ sin\beta & sin(\beta - \frac{2\pi}{3}) & sin(\beta + \frac{2\pi}{3}) \\ \frac{1}{2} & \frac{1}{2} & \frac{1}{2} \end{bmatrix} \tag{C.27}$$

$$\beta = \theta_{rf} - \theta_r \tag{C.28}$$

$$\bar{f}'^T_{qd0r} = \begin{bmatrix} f'_{qr} & f'_{dr} & f'_{0r} \end{bmatrix} \tag{C.29}$$

The angle θ_{rf} is illustrated in figure C.5. As seen in the figure θ_{rf} is the angle between phase A in the stator and the q axis in the rotating $qd0$ reference-frame. The 0 axis in the $qd0$ reference-frame is normal to the d, q plane.

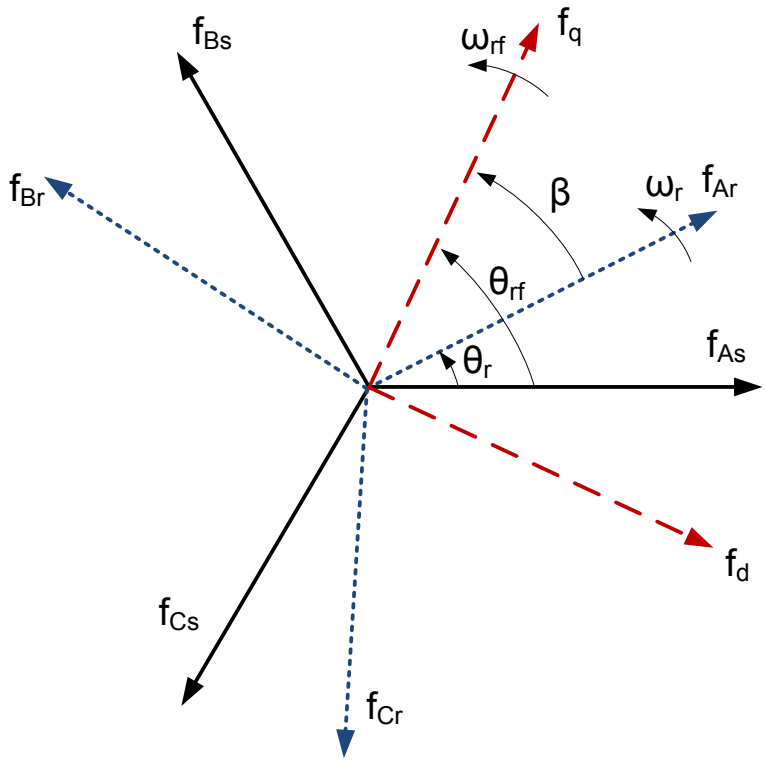

Figure C.5: *Relation between 3-phase ABC reference-frame and arbitrary rotating qd0 reference-frame*

The velocities ω_{rf} and ω_r are the velocity of the arbitrary reference-frame and the electric velocity of the rotor shaft respectively.

The transformation matrix in equation (C.27) is used to transform variables from the 3-phase rotor reference frame to the $qd0$ reference-frame. The coefficient $2/3$ is chosen to maintain the same length of the current and voltage vectors for sinusoidal steady state [Novotny and Lipo, 1996, p. 56]. When transforming variables from the 3-phase stator reference frame to the $qd0$ reference-frame the angle β is simply replaced by θ_{rf} in the transformation matrix. The new transformation matrix can hereby be expressed as:

$$\bar{K}_s = \frac{2}{3} \cdot \begin{bmatrix} cos\theta_{rf} & cos(\theta_{rf} - \frac{2\pi}{3}) & cos(\theta_{rf} + \frac{2\pi}{3}) \\ sin\theta_{rf} & sin(\theta_{rf} - \frac{2\pi}{3}) & sin(\theta_{rf} + \frac{2\pi}{3}) \\ \frac{1}{2} & \frac{1}{2} & \frac{1}{2} \end{bmatrix} \tag{C.30}$$

The voltage equations derived in the previous section is transformed to the $qd0$ reference-frame. Equation (C.25) is written as:

$$\bar{u}_{ABCs} = \bar{R}_s \cdot \bar{i}_{ABCs} + p \cdot \bar{\lambda}_{ABCs} \tag{C.31}$$

$$\bar{u}'_{ABCr} = \bar{R}'_r \cdot \bar{i}'_{ABCr} + p \cdot \bar{\lambda}'_{ABCr} \tag{C.32}$$

Using equation (C.26) the voltage equations is transformed[Krause et al., 2002, p. 115]:

$$\bar{u}_{qd0s} = \bar{K}_s \cdot \bar{R}_s \cdot \bar{K}_s^{-1} \cdot \bar{i}_{qd0s} + \bar{K}_s \cdot p \cdot \left[\bar{K}_s^{-1} \cdot \bar{\lambda}_{qd0s}\right] \tag{C.33}$$

$$\bar{u}'_{qd0r} = \bar{K}_r \cdot \bar{R}'_r \cdot \bar{K}_r^{-1} \cdot \bar{i}'_{qd0r} + \bar{K}_r \cdot p \cdot \left[\bar{K}_r^{-1} \cdot \bar{\lambda}'_{qd0r}\right] \tag{C.34}$$

The following equations are expressed as:

$$\bar{K}_s \cdot \bar{R}_s \cdot \bar{K}_s^{-1} = \bar{R}_s \tag{C.35}$$

$$\bar{K}_r \cdot \bar{R}'_r \cdot \bar{K}_r^{-1} = \bar{R}_r \tag{C.36}$$

The last term in equation (C.33) is rewritten as:

$$\bar{K}_s \cdot p \cdot \left[\bar{K}_s^{-1} \cdot \bar{\lambda}_{qd0s}\right] = \bar{K}_s \cdot p \cdot \left[\bar{K}_s^{-1}\right] \cdot \bar{\lambda}_{qd0s} + \bar{K}_s \cdot \bar{K}_s^{-1} \cdot p \cdot \bar{\lambda}_{qd0s} \tag{C.37}$$

$$p \cdot \left[\bar{K}_s^{-1}\right] = \omega_{rf} \cdot \begin{bmatrix} -sin\theta_{rf} & cos\theta_{rf} & 0 \\ -sin(\theta_{rf} - \frac{2\pi}{3}) & cos(\theta_{rf} - \frac{2\pi}{3}) & 0 \\ -sin(\theta_{rf} + \frac{2\pi}{3}) & cos(\theta_{rf} + \frac{2\pi}{3}) & 0 \end{bmatrix} \tag{C.38}$$

$$\bar{K}_s \cdot p \cdot \left[\bar{K}_s^{-1}\right] = \omega_{rf} \cdot \begin{bmatrix} 0 & 1 & 0 \\ -1 & 0 & 0 \\ 0 & 0 & 0 \end{bmatrix} \tag{C.39}$$

The last term in equation (C.34) is rewritten in the same manor.
The voltage equations are now expressed as [Krause et al., 2002, p. 149]:

$$\bar{u}_{qd0s} = \bar{R}_s \cdot \bar{i}_{qd0s} + \omega_{rf} \cdot \bar{\lambda}_{dqs} + p \cdot \bar{\lambda}_{qd0s} \tag{C.40}$$

$$\bar{u}'_{qd0r} = \bar{R}'_r \cdot \bar{i}'_{qd0r} + (\omega_{rf} - \omega_r) \cdot \bar{\lambda}'_{dqr} + p \cdot \bar{\lambda}'_{qd0r} \tag{C.41}$$

Where:

$$\left(\bar{\lambda}_{dqs}\right)^T = \begin{bmatrix} \lambda_{ds} & -\lambda_{qs} & 0 \end{bmatrix} \tag{C.42}$$

$$\left(\bar{\lambda}'_{dqr}\right)^T = \begin{bmatrix} \lambda'_{dr} & -\lambda'_{qr} & 0 \end{bmatrix} \tag{C.43}$$

Using the transformation equation (C.26) the flux linkages are expressed as:

$$\begin{bmatrix} \bar{\lambda}_{qd0s} \\ \bar{\lambda}'_{qd0r} \end{bmatrix} = \begin{bmatrix} \bar{K}_s \cdot \bar{L}_s \cdot \bar{K}_s^{-1} & \bar{K}_s \cdot \bar{L}'_{sr} \cdot \bar{K}_r^{-1} \\ \bar{K}_r \cdot (\bar{L}'_{sr})^T \cdot \bar{K}_s^{-1} & \bar{K}_r \cdot \bar{L}'_r \cdot \bar{K}_r^{-1} \end{bmatrix} \cdot \begin{bmatrix} \bar{i}_{qd0s} \\ \bar{i}'_{qd0r} \end{bmatrix} \tag{C.44}$$

From equation (C.8), (C.23) and (C.10) it is expressed that:

$$\bar{K}_s \cdot \bar{L}_s \cdot (\bar{K}_s)^{-1} = \begin{bmatrix} L_{ls}+L_M & 0 & 0 \\ 0 & L_{ls}+L_M & 0 \\ 0 & 0 & L_{ls} \end{bmatrix} \tag{C.45}$$

$$\bar{K}_r \cdot \bar{L}'_r \cdot (\bar{K}_r)^{-1} = \begin{bmatrix} L'_{lr}+L_M & 0 & 0 \\ 0 & L'_{lr}+L_M & 0 \\ 0 & 0 & L'_{lr} \end{bmatrix} \tag{C.46}$$

$$\bar{K}_r \cdot \bar{L}'_{sr} \cdot (\bar{K}_s)^{-1} = \bar{K}_s \cdot \bar{L}'_{sr} \cdot (\bar{K}_r)^{-1} = \begin{bmatrix} L_M & 0 & 0 \\ 0 & L_M & 0 \\ 0 & 0 & 0 \end{bmatrix} \tag{C.47}$$

Where L_M=$\frac{3}{2} \cdot L_{ms}$.
The voltage equations in the $qd0$ reference frame are now expressed as:

$$u_{qs} = R_s \cdot i_{qs} + \omega_{rf} \cdot \lambda_{ds} + p \cdot \lambda_{qs} \tag{C.48}$$

$$u_{ds} = R_s \cdot i_{ds} - \omega_{rf} \cdot \lambda_{qs} + p \cdot \lambda_{ds} \tag{C.49}$$

$$u_{0s} = R_s \cdot i_{0s} + p \cdot \lambda_{0s} \tag{C.50}$$

$$u'_{qr} = R'_r \cdot i'_{qr} + (\omega_{rf} - \omega_r) \cdot \lambda'_{dr} + p \cdot \lambda'_{qr} \tag{C.51}$$

$$u'_{dr} = R'_r \cdot i'_{dr} - (\omega_{rf} - \omega_r) \cdot \lambda'_{qr} + p \cdot \lambda'_{dr} \tag{C.52}$$

$$u'_{0r} = R'_r \cdot i'_{0r} + p \cdot \lambda'_{0r} \tag{C.53}$$

Where the flux linkages is expressed as:

$$\lambda_{qs} = L_{ls} \cdot i_{qs} + L_M \cdot (i_{qs} + i'_{qr}) \tag{C.54}$$

$$\lambda_{ds} = L_{ls} \cdot i_{ds} + L_M \cdot (i_{ds} + i'_{dr}) \tag{C.55}$$

$$\lambda_{0s} = L_{ls} \cdot i_{0s} \tag{C.56}$$

$$\lambda'_{qr} = L'_{lr} \cdot i'_{qr} + L_M \cdot (i_{qs} + i'_{qr}) \tag{C.57}$$

$$\lambda'_{dr} = L'_{lr} \cdot i'_{dr} + L_M \cdot (i_{ds} + i'_{dr}) \tag{C.58}$$

$$\lambda'_{0r} = L'_{lr} \cdot i'_{0r} \tag{C.59}$$

The voltage equations are now transformed to an arbitrary reference-frame. The torque equation for the arbitrary reference-frame is presented in the next section.

C.3 Torque Equation

In this section the torque equation is derived. The power dissipated in the motor is expressed as:

$$P_e = u_{As} \cdot i_{As} + u_{Bs} \cdot i_{Bs} + u_{Cs} \cdot i_{Cs} + u_{Ar} \cdot i_{Ar} + u_{Br} \cdot i_{Br} + u_{Cr} \cdot i_{Cr} \tag{C.60}$$

The idea is now to make an expression involving complex vectors that is proven to express the power dissipated in the machine[Novotny and Lipo, 1996, p. 68]. The following equation is used:

$$u^s_{ABCs} \cdot i^{s*}_{ABCs} = \frac{2}{3} \cdot (u_{As} + \bar{a} u_{Bs} + \bar{a}^2 u_{Cs}) \cdot \frac{2}{3} \cdot (i_{As} + \bar{a}^2 i_{Bs} + \bar{a} i_{Cs}) \tag{C.61}$$

Where * denotes that the vector is complex conjugated, $a = e^{j2\pi/3}$ and ^{s} denotes that the complex vectors are given in a stationary reference frame.
The equation is expressed as:

$$\begin{aligned} u^s_{ABCs} \cdot i^{s*}_{ABCs} &= \frac{4}{9} \cdot [u_{As} \cdot i_{As} + \bar{a}(u_{Bs} \cdot i_{As} + u_{As} \cdot i_{Cs}) + \bar{a}^2 \cdot (u_{As} \cdot i_{Bs} + u_{Cs} \cdot i_{As} + u_{Bs} \cdot i_{Cs}) \\ &\quad + \bar{a}^3 \cdot (u_{Bs} \cdot i_{Bs} + u_{Cs} \cdot i_{Cs}) + \bar{a}^4 \cdot (u_{Cs} \cdot i_{Bs})] \\ &= \frac{4}{9} \cdot [u_{As} \cdot i_{As} + u_{Bs} \cdot i_{Bs} + u_{Cs} \cdot i_{Cs} + \bar{a} \cdot (u_{Bs} \cdot i_{As} + u_{As} \cdot i_{Cs} + u_{Cs} \cdot i_{Bs}) \\ &\quad + \bar{a}^2 \cdot (u_{As} \cdot i_{Bs} + u_{Cs} \cdot i_{As} + u_{Bs} \cdot i_{Cs})] \end{aligned} \tag{C.62}$$

Taking the real part of the expression:

$$\begin{aligned} Re\,(u^s_{ABCs} \cdot i^{s*}_{ABCs}) &= \frac{4}{9} \cdot \{u_{As} \cdot i_{As} + u_{Bs} \cdot i_{Bs} + u_{Cs} \cdot i_{Cs} \\ &\quad - \frac{1}{2} \cdot [u_{As} \cdot (i_{Bs} + i_{Cs}) + u_{Bs} \cdot (i_{As} + i_{Cs}) + u_{Cs} \cdot (i_{As} + i_{Bs})]\} \end{aligned} \tag{C.63}$$

Since the sum of currents is zero the expression becomes:

$$Re\,(u^s_{ABCs} \cdot i^{s*}_{ABCs}) = \frac{2}{3} \cdot \{u_{As} \cdot i_{As} + u_{Bs} \cdot i_{Bs} + u_{Cs} \cdot i_{Cs}\} \tag{C.64}$$

Comparing equation (C.64) to equation (C.60) the power dissipated in the rotor and stator is expressed as:

$$\begin{aligned} P_e &= u_{As} \cdot i_{As} + u_{Bs} \cdot i_{Bs} + u_{Cs} \cdot i_{Cs} + u_{Ar} \cdot i_{Ar} + u_{Br} \cdot i_{Br} + u_{Cr} \cdot i_{Cr} \\ &= \frac{3}{2} \cdot \left\{ Re\,(u^s_{ABCs} \cdot i^{s*}_{ABCs}) + Re\left(u'^s_{ABCr} \cdot i'^{s*}_{ABCr}\right)\right\} \end{aligned} \tag{C.65}$$

The power in the rotor circuit is expressed with stator referred variables however since the rotor voltage/current product is independent of the turns ratio, the power is expressed with normal rotor variables as well.

The complex vectors in the stationary reference-frame can easily be transformed to the $qd0$ reference-frame. This is done by applying the angle θ_{rf} between the stationary reference-frame and the rotating reference-frame as seen in figure C.5 on page 33:

$$\bar{f}_{qd0s} = e^{-j\theta_{rf}} \cdot \bar{f}_{ABCs} \tag{C.66}$$

$$\bar{f}_{ABCs} = e^{j\theta_{rf}} \cdot \bar{f}_{qd0s} \tag{C.67}$$

$$\bar{f}'_{ABCr} = e^{j(\theta_{rf}-\theta_r)} \cdot \bar{f}'_{qd0r} \tag{C.68}$$

Equation (C.65) can now be rewritten:

$$P_e = \frac{3}{2} \cdot Re\left\{ (e^{j\theta_{rf}})\ cdotu_{qds} \cdot (e^{-j\theta_{rf}}) \cdot i^*_{qds} + (e^{j(\theta_{rf}-\theta_r)}) \cdot u'_{qdr} \cdot (e^{-j(\theta_{rf}-\theta_r)}) \cdot i'^*_{qdr} \right\} \tag{C.69}$$

$$= \frac{3}{2} \cdot Re\left\{ u_{qds} \cdot i^*_{qds} + u'_{qdr} \cdot i'^*_{qdr} \right\} \tag{C.70}$$

$$P_e = \frac{3}{2} \cdot Re\left[\bar{u}_{qds} \cdot \bar{i}^*_{qds} + \bar{u}'_{qdr} \cdot \bar{i}'^*_{qdr} \right] \tag{C.71}$$

Where $\bar{f}_{qd} = f_q - j \cdot f_d$ and * denotes that the vector is complex conjugated.
Equation (C.40) and (C.41) can now be inserted into equation (C.60) and the following equation is expressed as [Novotny and Lipo, 1996, p. 73]:

$$\begin{aligned} P_e = {} & \frac{3}{2} \cdot \left[R_s \cdot |\bar{i}_{qds}|^2 + R'_r \cdot |\bar{i}'_{qdr}|^2 \right] + \frac{3}{2} \cdot p \cdot \left[\frac{L_{ls}}{2} \cdot |\bar{i}_{qds}|^2 + \frac{L'_{lr}}{2} \cdot |\bar{i}'_{qdr}|^2 + \frac{L_M}{2} \cdot |\bar{i}_{qds} + \bar{i}'_{qdr}|^2 \right] \\ & + \frac{3}{2} \cdot Re\{ j \cdot \omega_{rf} \cdot \left[(L_{ls} + L_M) \cdot |\bar{i}_{qds}|^2 + L_M \cdot \bar{i}'_{qdr} \cdot \bar{i}^*_{qds} \right] \\ & + j \cdot (\omega_{rf} - \omega_r) \cdot \left[(L'_{lr} + L_M) \cdot |\bar{i}'_{qdr}|^2 + L_M \cdot \bar{i}_{qds} \cdot \bar{i}'^*_{qdr} \right] \} \end{aligned} \tag{C.72}$$

As seen in equation (C.72) the power dissipated in the motor consists of three terms. The first term accounts for power dissipated in stator and rotor resistances. The second term corresponds to the time rate of change of the magnetic energy stored in the inductances. The third term accounts for the energy that is transformed from electrical to mechanical energy. This term is called the electromechanical output power, P_{em}.
Some of the terms in P_{em} only have imaginary parts and P_{em} can therefore be written as:

$$\begin{aligned} P_{em} &= \frac{3}{2} Re\{j \cdot \omega_{rf} \cdot L_M \cdot \bar{i}'_{qdr} \cdot \bar{i}^*_{qds} + j \cdot (\omega_{rf} - \omega_r) \cdot L_M \cdot \bar{i}_{qds} \cdot \bar{i}'^*_{qdr}\} \\ &= \frac{3}{2} \cdot Re\{j \cdot \omega_{rf} \cdot L_M \cdot \left(\bar{i}'_{qdr} \cdot \bar{i}^*_{qds} + \bar{i}_{qds} \cdot \bar{i}'^*_{qdr}\right) - j \cdot \omega_r \cdot L_M \cdot \bar{i}_{qds} \cdot \bar{i}'^*_{qdr}\} \end{aligned} \quad \text{(C.73)}$$

It is shown that for two complex numbers, $\bar{a}$ and $\bar{b}$, the following relation is applied:

$$\bar{a} \cdot \bar{b}^* + \bar{a}^* \cdot \bar{b} = 2(a_r \cdot b_r + a_i \cdot b_i) \quad \text{(C.74)}$$

This relation show that the first part of the electromechanical power has no real part, and the equation is hereby be expressed as:

$$\begin{aligned} P_{em} &= -\frac{3}{2} \cdot Re\left\{j \cdot \omega_r \cdot L_m \bar{i}_{qds} \cdot \bar{i}'^*_{qdr}\right\} \\ &= \frac{3}{2} \cdot Im\left\{\omega_r \cdot L_m \cdot \bar{i}_{qds} \cdot \bar{i}'^*_{qdr}\right\} \\ &= \frac{3}{2} \cdot \omega_r \cdot L_m \cdot \left(i_{qs} \cdot i'_{dr} - i_{ds} \cdot i'_{qr}\right) \end{aligned} \quad \text{(C.75)}$$

Applying the relation between electrical and mechanical velocity:

$$\omega_r = \frac{P}{2} \cdot \omega_m \quad \text{(C.76)}$$

where:	P	Number of poles in motor $[-]$
	ω_m	Mechanical velocity $[rad/s]$

The electromagnetic torque is determined:

$$\begin{aligned} \omega_m \tau_e &= \frac{3}{2} \cdot \frac{P}{2} \cdot \omega_m \cdot L_M \cdot \left(i_{qs} \cdot i'_{dr} - i_{ds} \cdot i'_{qr}\right) \\ &\downarrow \\ \tau_e &= \frac{3}{2} \cdot \frac{P}{2} \cdot L_M \cdot \left(i_{qs} \cdot i'_{dr} - i_{ds} \cdot i'_{qr}\right) \end{aligned} \quad \text{(C.77)}$$

C.4 Choice of Reference-frame for simulation model

The choice of reference frame can provide simplifications to the voltage equations as some of the terms becomes zero.

A stationary reference-frame is chosen as the velocity of the reference-frame, ω_{rf}, is zero. The d-axis is called α and the q-axis is called β. The stationary reference frame is illustrated in figure C.6.

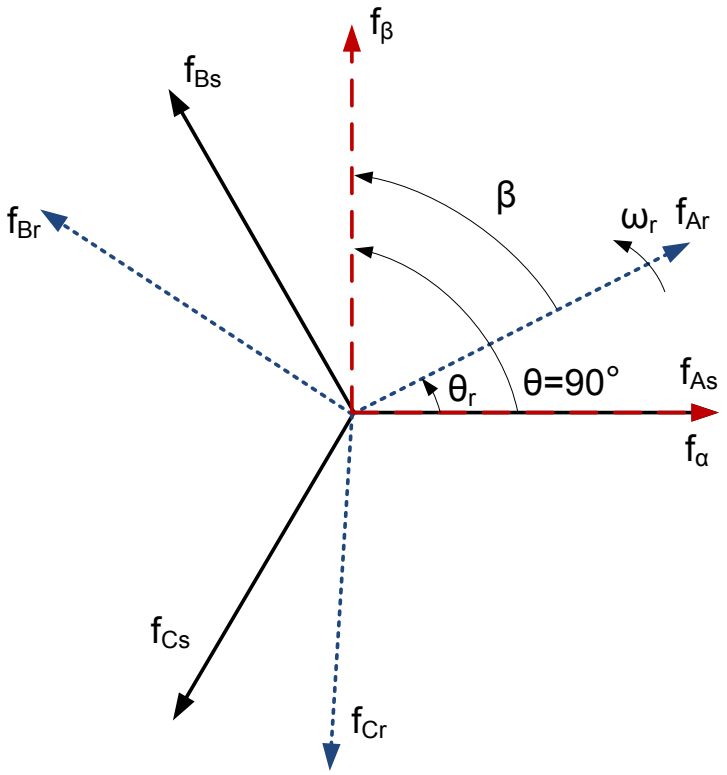

Figure C.6: *Rotor and stator phase quantities in the* αβ *reference-frame.*

From equation (C.26) and (C.27) the following is expressed for phase quantities in the 0-direction [Novotny and Lipo, 1996, p. 57]:

$$\bar{f}_{0s} = \frac{1}{3} \cdot \left[\bar{f}_{as} + \bar{f}_{bs} + \bar{f}_{cs} \right] \tag{C.78}$$

Since the sum of currents in the three phases in the stator is assumed to be zero when considered as wye-connected, all other phase quantities also sums to zero [Novotny and Lipo, 1996, p. 57]. This of course also accounts for the rotor quantities. Therefore the zero-sequence quantities, $\bar{f}_{0s}$ and $\bar{f}_{0r}$, are always zero, and equation (C.50) and (C.53) becomes zero.
The voltage equations are hereby expressed as:

$$u_{\alpha s} = R_s \cdot i_{\alpha s} + p \cdot \lambda_{\alpha s} \tag{C.79}$$

$$u_{\beta s} = R_s \cdot i_{\beta s} + p \cdot \lambda_{\beta s} \tag{C.80}$$

$$u'_{\alpha r} = R'_r \cdot i'_{\alpha r} + \omega_r \cdot \lambda'_{\beta r} + p \cdot \lambda'_{\alpha r} \tag{C.81}$$

$$u'_{\beta r} = R'_r \cdot i'_{\beta r} - \omega_r \cdot \lambda'_{\alpha r} + p \cdot \lambda'_{\beta r} \tag{C.82}$$

Where the flux linkages are expressed as:

$$\lambda_{\alpha s} = L_{ls} \cdot i_{\alpha s} + L_M \cdot (i_{\alpha s} + i'_{\alpha r}) \tag{C.83}$$

$$\lambda_{\beta s} = L_{ls} \cdot i_{\beta s} + L_M \cdot (i_{\beta s} + i'_{\beta r}) \tag{C.84}$$

$$\lambda'_{\alpha r} = L'_{lr} \cdot i'_{\alpha r} + L_M \cdot (i_{\alpha s} + i'_{\alpha r}) \tag{C.85}$$

$$\lambda'_{\beta r} = L'_{lr} \cdot i'_{\beta r} + L_M \cdot (i_{\beta s} + i'_{\beta r}) \tag{C.86}$$

The torque equation in the $\alpha\beta$ reference-frame is expressed as:

$$T_e = \frac{3}{2} \cdot \frac{P}{2} \cdot L_M \cdot \left(i_{\beta s} \cdot i'_{\alpha r} - i_{\alpha s} \cdot i'_{\beta r} \right) \tag{C.87}$$

The voltage and torque equations are now expressed in the stationary $\alpha\beta$ reference-frame and are modeled in Simulink.

APPENDIX D

STEADY STATE MODEL OF THE INDUCTION MACHINE

In this section a steady state model of the induction machine is presented. The model is based on the description in [Sen, 1997]. The basic electrical diagram representing the induction machine presented section 6.3 is repeated in figure D.1 for convenience. If balanced three phase current flows in the stator a rotating magnetic field will be produced in the air gap of the machine rotating at the synchronous velocity ω_e. This induces a voltage in the rotor windings rotating at slip velocity $s \cdot \omega_e$. As a result the electrical per-phase diagram of the induction machine seen in figure D.2 (e) is similar to a transformer. The model describes the operation of a single phase of the induction machine. In the following sections the stator and rotor circuits are elaborated.

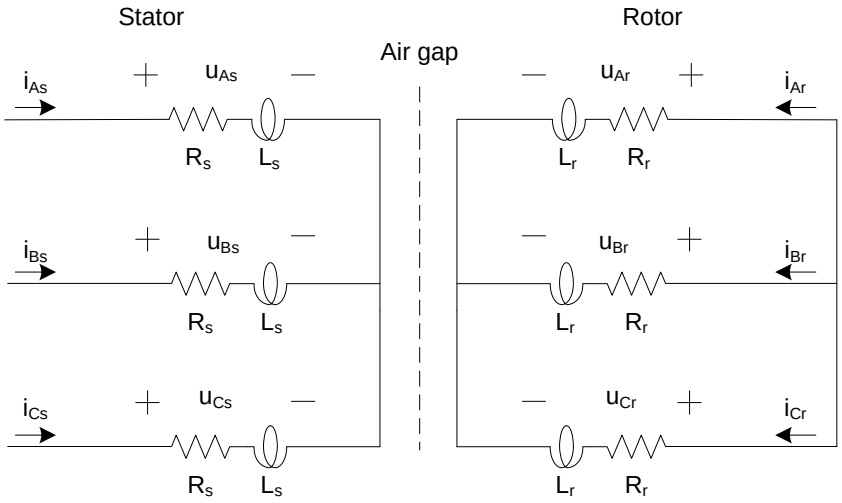

Figure D.1: *Electrical equivalent diagram of the wye-connected, squirrel cage induction machine.*

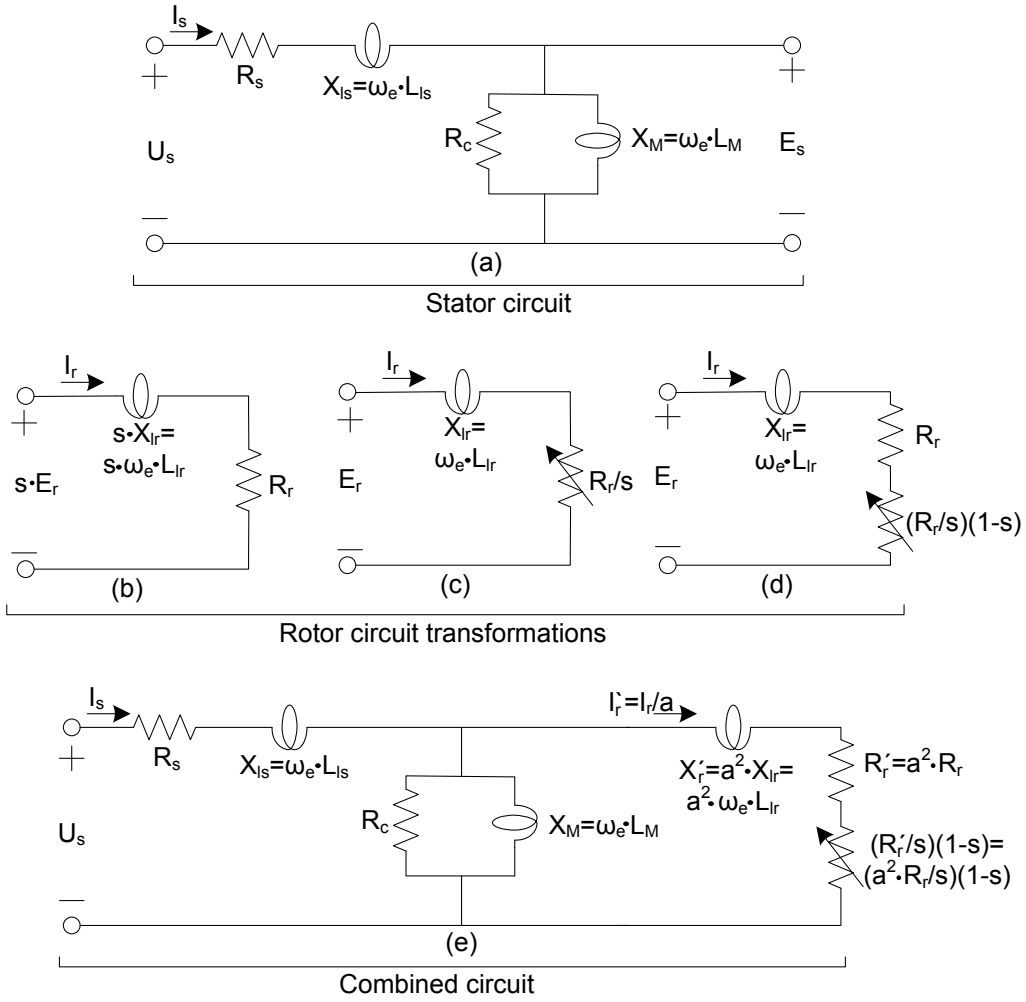

Figure D.2: *Steady state induction machine circuits.*

D.0.1 Stator Circuit

The steady state stator circuit is seen in figure D.2 (a)

where:	U_s	Per phase terminal RMS voltage $[V]$.
	I_s	Per phase stator RMS current $[A]$.
	R_s	Per phase stator resistance $[\Omega]$.
	L_{ls}	Per phase stator leakage inductance $[H]$.
	R_c	Per phase core loss resistance $[\Omega]$.
	L_{ms}	Per phase stator magnetizing inductance for the stator $[H]$.
	E_s	Per phase induced voltage in stator windings $[V]$.
	X_{Index}	Per phase reactance $[\Omega]$.
	ω_e	Supply angular velocity $[^{rad}/_s]$.

When an AC voltage of amplitude U_s (RMS) and frequency ω_e is applied at the terminal of the induction machine a voltage of E_s (RMS) is induced in the stator windings.

D.0.2 Rotor Circuit

The steady state rotor circuit is seen in figure D.2 (b), (c) and (d)

where:	s	Slip of the induction machine $[-]$.
	E_r	Per phase induced voltage in rotor windings at standstill $[V]$.
	I_r	Per phase rotor RMS current $[A]$.
	R_r	Per phase rotor resistance $[\Omega]$.
	L_{lr}	Per phase rotor leakage inductance $[H]$.
	ω_e	Supply angular velocity $[^{rad}/_s]$.

From the circuit it is seen that a large slip s results in a large induced voltage in the rotor circuit and thereby a large current flowing in the rotor windings. The transformation of circuit (b) to (c) and (d) is used to combine the stator and rotor circuit and to derive an expression for the mechanical power of the induction machine.

D.0.3 Combined Circuit

In figure D.2 (e) the stator circuit is combined with the rotor circuit. The link between the two circuits is the turns ratio defined equation (D.1). From the circuit it is seen that the induced voltage in the rotor circuit is given by equation (D.2).

$$a = \frac{N_s}{N_r} \tag{D.1}$$

where: a Turns ratio $[-]$.
N_s Number of turns in the stator windings $[-]$.
N_r Number of turns in the rotor windings $[-]$.

$$E_r = E_s \cdot a \tag{D.2}$$

D.0.4 Power Flow in the Induction Machine at Steady State

The rotor circuit of figure D.2 (d) is transformed to be at stator frequency. Therefore the power flow of this circuit represents the power flow through the air gap [Sen, 1997]. The power flow through this circuit is given by equation (D.3). The first term represents the losses in the conductors of the rotor circuit and the last term represents the mechanical power developed by the induction machine. The mechanical power of the induction machine is thereby given by equation (D.4). From equation (D.4) it is seen that it is desirable to have low values of slip to ensure efficient operation. According to Sen [1997] typical values of slip are 1 to 5 %.

$$P_{ag} = I_r^2 \cdot \left(R_r + \frac{R_r}{s}(1-s) \right) \tag{D.3}$$

where: P_{ag} Power flow through the air gap $[W]$.

$$P_{em} = I_r^2 \cdot \frac{R_r}{s}(1-s) \tag{D.4}$$
$$= (1-s) \cdot P_{ag} \tag{D.5}$$

where: P_{em} Mechanical power flow $[W]$.

D.0.5 Simplified Model

In this section the induction machine model is simplified to ease the analysis of the circuit and to reduce circuit components. The simplified circuit is seen in figure D.3 only differs from the

original model by the lack of the resistance R_c taking the core losses into account. The effect of removing R_c is compensated by adding additional mechanical coulomb and viscous friction [Sen, 1997]. To simplify the analysis, the stator resistance R_s, leakage reactance X_{ls} and the magnetizing reactance is combined in a Thevenin equivalent circuit in the following.

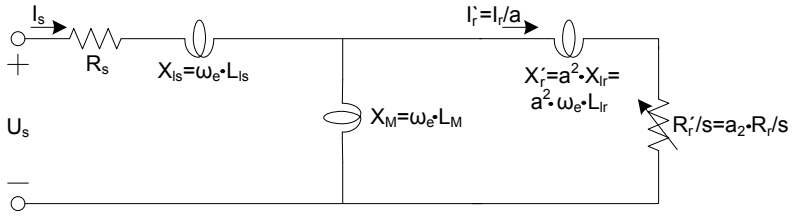

Figure D.3: *Simplified electrical circuit model of the induction machine.*

D.0.6 Thevenin Equivalent Circuit

In this section the simplified model is converted to a Thevenin equivalent circuit to further ease the analysis. The aim is to convert the simplified model is seen in figure D.3 into the Thevenin equivalent circuit is seen in figure D.4. To determine the Thevenin parameters R_{th} and X_{th} the terminals of the voltage source U_{th} is shorted and the impedance of the circuit containing stator resistance R_s, leakage reactance X_{ls} in parallel with the magnetizing reactance X_M is determined. The Thevenin impedance is illustrated in figure D.5 and the value of it is calculated in equation (D.6). The Thevenin voltage U_{th} is the open circuit voltage of the Thevenin circuit seen in figure D.6 and is determined in equation (D.9).

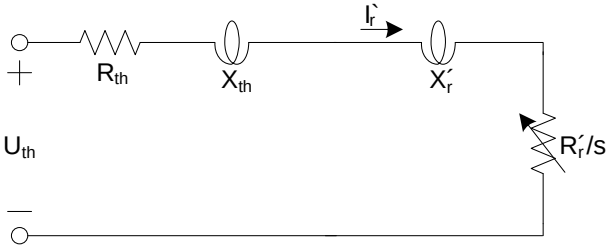

Figure D.4: *Thevenin equivalent circuit.*

$$Z_{th} = \frac{(R_s + jX_{ls}) \cdot jX_M}{R_s + j(X_{ls} + X_M)} \tag{D.6}$$

$$= \frac{R_s \cdot X_M^2}{R_s^2 + (X_{ls} + X_M)^2} + j \cdot \frac{\left(R_s^2 + X_{ls} \cdot (X_{ls} + X_M)\right) \cdot X_M}{R_s^2 + (X_{ls} + X_M)^2} \tag{D.7}$$

$$= R_{th} + j \cdot X_{th} \tag{D.8}$$

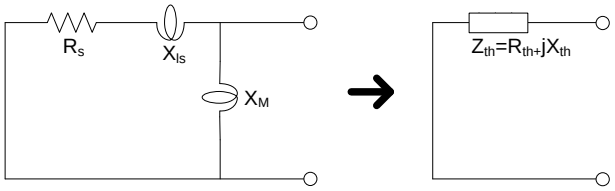

Figure D.5: *Thevenin impedance transformation.*

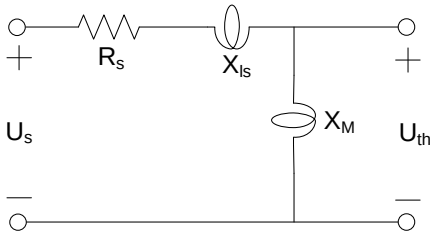

Figure D.6: *The Thevenin voltage.*

$$U_{th} = \frac{|X_M|}{|X_M + X_{ls} + R_s|} \cdot U_s \tag{D.9}$$

$$= \frac{X_M}{\left((X_M + X_{ls})^2 + R_s^2\right)^{1/2}} \cdot U_s \tag{D.10}$$

D.0.7 Torque Characteristics

In this section an expression expressing the developed torque of the induction machine is derived. In section D.0.4 an expression describing the mechanical power flow of the induction machine was determined and is repeated in equation (D.11) for convenience. This equals mechanical power of the shaft which results in equation (D.12). The slip relation between the mechanical angular velocity ω_{rm} and the electrical angular velocity ω_e results in equation (D.13). Finally an expression for the electro mechanical torque T_e as a function of electrical angular velocity ω_e, stator referred rotor current $I_r^{'}$ and slip s is obtained in equation (D.16).
Using the Thevenin equivalent circuit of figure D.4 an expression for the stator referred rotor current $I_r^{'}$ is obtained in equation (D.17). Inserting this expression into the torque in equation (D.16) yields an expression for the torque as a function of electrical angular velocity ω_e, Thevenin voltage U_{th} and slip s is seen in equation (D.20). Multiplying equation (D.20) by three ensures that all phases of the induction machine is taken into account. Equation (D.20) (times three) is implemented into a simulation model to enable analysis of the torque characteristic of the induction machine. Varying the slip while using constant terminal voltage U_s and electrical angular velocity ω_e results in the torque slip characteristic is seen in figure D.7. From this it

is seen that there is an almost linear relationship between slip and torque at low slip values ($|s| < 5\%$). The peak torque at $s \approx \pm 10\%$ could also be calculated analytically by differentiating equation (D.20) with respect to s and setting it equal to zero and solving for values of s. The relationship between slip and torque of figure D.7 indicates that the induction machine operating using scalar control is self regulating at low slip values i. e. if the mechanical load increases the shaft acceleration $\dot{\omega}_{rm}$ causes the mechanical angular velocity ω_{rm} to decrease increasing the slip s until equilibrium is achieved.

$$P_{em} = I_r^2 \cdot \frac{R_r}{s}(1-s) \tag{D.11}$$

$$\omega_{rm} \cdot T_e = I_r^2 \cdot \frac{R_r}{s}(1-s) \tag{D.12}$$

$$\Downarrow$$

$$(1-s) \cdot \omega_e \cdot T_e = I_r^2 \cdot \frac{R_r}{s}(1-s) \tag{D.13}$$

$$\Downarrow$$

$$\omega_e \cdot T_e = I_r^2 \cdot \frac{R_r}{s} \tag{D.14}$$

$$\Downarrow$$

$$T_e = \frac{1}{\omega_e} \cdot I_r^2 \cdot \frac{R_r}{s} \tag{D.15}$$

$$= \frac{1}{\omega_e} \cdot I_r^{'2} \cdot \frac{R_r^{'}}{s} \tag{D.16}$$

$$I_r^{'} = \frac{U_{th}}{\left| R_{th} + \frac{R_r^{'}}{s} + X_{th} + X_r^{'} \right|} \tag{D.17}$$

$$= \frac{U_{th}}{\left(\left(R_{th} + \frac{R_r^{'}}{s} \right)^2 + (X_{th} + X_r^{'})^2 \right)^{1/2}}$$

$$T_e = \frac{1}{\omega_e} \cdot I_r^{'2} \cdot \frac{R_r^{'}}{s} \tag{D.18}$$

$$= \frac{1}{\omega_e} \cdot \left(\frac{U_{th}}{\left(\left(R_{th} + \frac{R_r^{'}}{s} \right)^2 + (X_{th} + X_r^{'})^2 \right)^{1/2}} \right)^2 \cdot \frac{R_r^{'}}{s} \tag{D.19}$$

$$= \frac{1}{\omega_e} \cdot \frac{U_{th}^2}{\left(R_{th} + \frac{R_r^{'}}{s} \right)^2 + (X_{th} + X_r^{'})^2} \cdot \frac{R_r^{'}}{s} \tag{D.20}$$

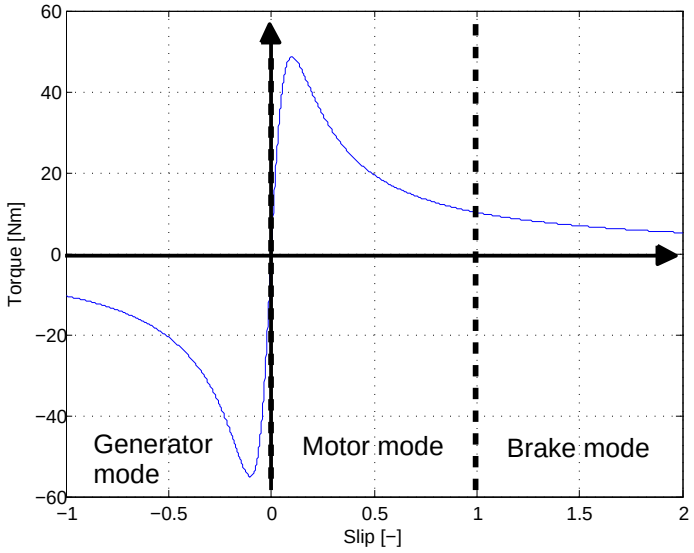

Figure D.7: *Torque - slip characteristic of the induction machine.*

D.1 Machine Parameters obtained using Steady State Model

In this section the steady state model from appendix D is used to derive simplified electrical circuits under specified conditions. The idea is to conduct experiments that replicate the specified conditions and use measurements to calculate the motor parameters. These experiments and data analysis are found in appendix E.

D.1.1 DC Test

To determine the stator resistance a DC voltage is applied between two terminals of the induction machine. At steady state DC voltage input the resultant magnetic field of the stator is constant resulting in no voltage induced in the rotor circuit. The impedance contribution of the inductors at DC is zero whereby the impedance between the two terminals is given by two phase resistances added with resistance of the cables used in the experiment. The results and a description of the experiment is seen in appendix E.1.

D.1.2 No Load Steady State Model

In this section the steady state model is simplified to no load condition. The applied stator voltage U_{NL} is a AC source with given RMS value and frequency. The electrical circuit for the no load test is seen in figure D.8. The rotor branch of the circuit is gone because the slip s is zero causing the term $\frac{R'_r}{s}$ to equal infinity and therefore no current is flowing in the rotor branch of the circuit. In general the resistance R_{NL} contains information about the stator resistance R_s,

the rotational losses which contains friction, windage and iron losses. At the experiment the rotor velocity was kept at synchronous speed using another electric machine. This eliminates the friction and windage contribution to R_{NL} leaving the stator resistance and iron loss part. R_{NL} is calculated from the power consideration that all input power is deposed in the no load resistance R_{NL}:

$$R_{NL} = \frac{P_{NL}}{3 \cdot I_{NL}^2} \tag{D.21}$$

where:	R_{NL}	No load resistance $[\Omega]$.
	P_{NL}	No load input power $[W]$.
	I_{NL}	No load current $[A]$.

As seen in figure D.8 there are still two unknown parameters: X_{ls} and X_M. The sum of these parameters is called X_{NL}:

$$X_{NL} = X_{ls} + X_M \tag{D.22}$$

where:	X_{NL}	No load reactance $[\Omega]$.
	X_{ls}	Stator leakage reactance at no load $[\Omega]$.
	X_M	Magnetizing reactance at no load $[\Omega]$.

X_{NL} is found by calculating the total impedance of the circuit (equation (D.23)) and then calculating X_{NL} by Pythagoras (equation (D.24)). Equation (D.22) is used in section D.1.3 in connection with other steady state circuit equations to determine the machine parameters.

$$Z_{NL} = \frac{U_{NL}}{I_{NL}} \tag{D.23}$$

where:	Z_{NL}	No load impedance $[\Omega]$.
	U_{NL}	No load voltage $[V]$.

$$X_{NL} = \sqrt{Z_{NL}^2 - R_{NL}^2} \tag{D.24}$$

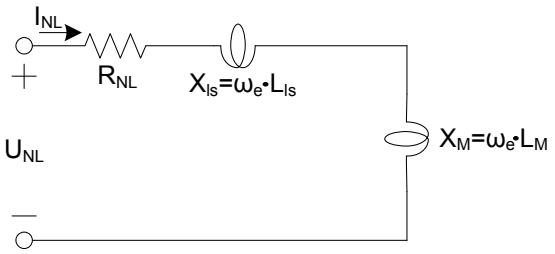

Figure D.8: *Electrical circuit at no load condition.*

D.1.3 Standard Steady State Model

In this section the results from the previous sections is used together with an experiment where the motor is loaded to find the unknown parameters X_{ls}, X'_{lr}, X_M and R'_r. The idea is to set up equations describing relationships between the parameters. The equations are implemented into a Matlab M-file to ease computational effort.
The experiment is conducted with the same voltage amplitude and frequency as in the no load experiment. The electric circuit for the load test condition is seen in figure D.9. An assumption used in this section is that stator leakage reactance X_{ls} and stator referred rotor reactance X_{lr} is equal (equation (D.25)).

$$X_{ls} = X_{lr} \tag{D.25}$$

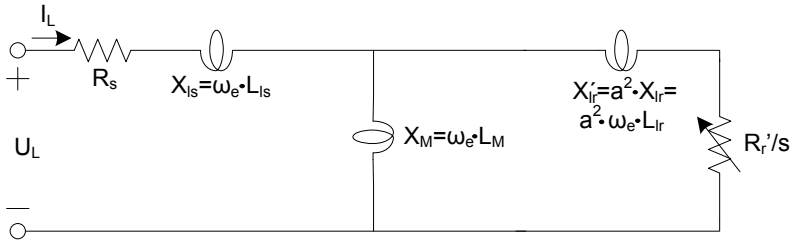

Figure D.9: *Standard steady state electrical circuit.*

An equivalent circuit with an equivalent impedance Z_{eq} consisting of a resistance R_{eq} and reactance X_{eq} is seen in figure D.10. The equivalent impedance is the impedance of the magnetizing inductance branch in parallel with the rotor leakage -and resistance branch. It is given by equation (D.27).
The equivalent resistance R_{eq} is given by equation (D.26). Furthermore it is the real part of the equivalent impedance and is given by equation (D.29).

$$R_{eq} = \frac{P_L}{3 \cdot I_L^2} - R_s \tag{D.26}$$

where: R_{eq} Equivalent resistance $[\Omega]$.

P_L Load test input power $[W]$.

I_L Load test current $[A]$.

$$\begin{aligned} Z_{eq} &= \frac{\left(X_{ls}\cdot j+\frac{R'_r}{s}\right)\cdot X_M\cdot j}{X_{ls}\cdot j+\frac{R'_r}{s}+X_M\cdot j} \\ &= \frac{\frac{R'_r}{s}\cdot X_M^2}{\left(\frac{R'_r}{s}\right)^2+(X_{ls}+X_M)^2}+\frac{\left(\left(\frac{R'_r}{s}\right)^2+X_{ls}\cdot(X_{ls}+X_M)\right)\cdot X_M}{\left(\frac{R'_r}{s}\right)^2+(X_{ls}+X_M)^2}\cdot j \end{aligned} \tag{D.27}$$

$$R_{eq} = Re\left(Z_{eq}\right) \tag{D.28}$$

$$= \frac{\frac{R'_r}{s}\cdot X_M^2}{\left(\frac{R'_r}{s}\right)^2+(X_{ls}+X_M)^2} \tag{D.29}$$

The rotor resistance term is isolated in equation (D.29) resulting in equation (D.30).

$$R'_r = \frac{-\left(\sqrt{X_M^4-4\cdot R_{eq}^2\cdot(X_{ls}+X_M)^2-X_M^2}\right)}{2\cdot R_{eq}}\cdot s \tag{D.30}$$

In equation (D.22) X_{ls} is isolated yielding equation (D.31).

$$X_{ls} = X_{NL}-X_M \tag{D.31}$$

Equation (D.25), (D.30) and (D.31) is three equations with four unknowns given computed test result R_{eq} (equation (D.26)) and X_{NL} (equation (D.24)). This means that given a magnetizing reactance X_M the stator leakage reactance X_{ls}, stator referred rotor reactance X_{lr} and rotor resistance can automatically be updated using Matlab. The impedance for the whole circuit is given by equation (D.27) plus the stator resistance R_s and stator leakage reactance X_{ls}, see figure D.10. Finally using Ohm's law (equation (D.33)) and the total impedance (equation (D.32)), the magnetizing reactance is adjusted (along with corresponding leakage reactances and rotor resistance) until the current calculated in equation (D.33) and the current in the experiment is equal.

$$Z_{SS} = Z_{eq}+R_s+j\cdot X_{ls} \tag{D.32}$$

$$I_L = \frac{U_L}{Z_{SS}} \tag{D.33}$$

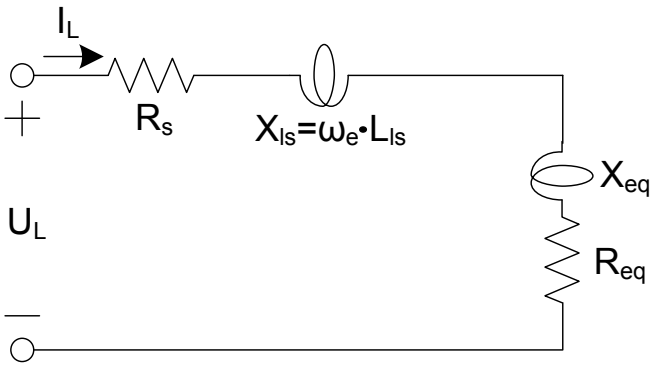

Figure D.10: *Equivalent circuit for standard operation.*

APPENDIX E

MACHINE PARAMETER EXPERIMENTS

This chapter contains descriptions of experiments conducted to determine the machine parameters.

E.1 DC-test

The objective of this experiment is to determine the stator resistance used in the model. This is done by applying DC voltage to the terminals of the induction machine while measuring the current flowing.

E.1.1 Equipment

- General setup described in section 5.2 in the report.
- Lambda DC power supply.
- Current probe.
- Voltage probe.
- Induction machine

E.1.2 Test Setup

The test setup is depicted in figure E.1.

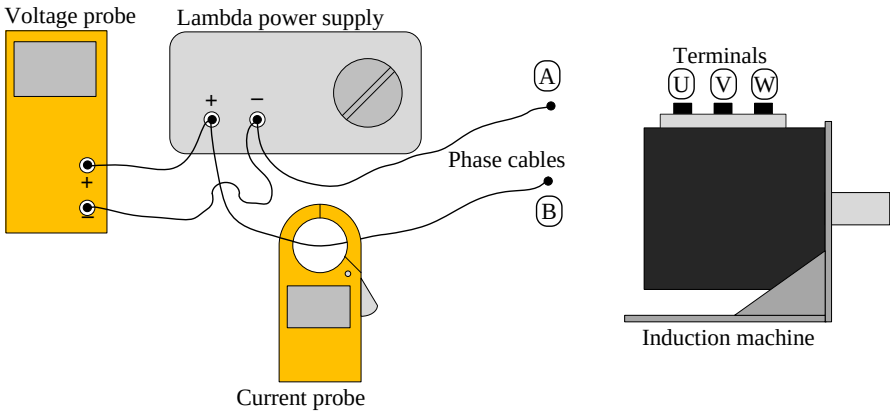

Figure E.1: *Test setup for determining the stator resistance.*

E.1.3 Execution

The following list contains a description of the execution of the experiment. Figure E.1 is used to support the description.

1. Connect the Phase cables (A) and (B) to the terminals (U) and (V) respectively.
2. Turn on the *Lambda* power supply, voltage probe and current probe.
3. Ramp the output voltage of the power supply until a current of approximately 200 A is flowing through the stator windings.
    a) Measure current flow and voltage potential.
4. Turn off *Lambda* power supply.
5. Disconnect phase cable (B) from phase (V) and connect it to phase (W).
6. Repeat item 2 to 4.
7. Disconnect phase cables (A) and (B) from the terminals and short circuit the cables.
8. Turn on the *Lambda* power supply.
9. Ramp the output voltage of the power supply until a current of approximately 200 A is flowing through the phase cables.
    a) Measure current flow and voltage potential.
10. Turn off *Lambda* power supply.

E.1.4 Results

The results are presented in table E.1. The resistance is calculated using Ohm's law. The stator resistance used in the model is half of line-line resistance plus phase cables and is equal to 2.04 $m\Omega$.

Wiring	Voltage $[V]$	Current $[A]$	Resistance $[m\Omega]$
Phase U, V and phase cables	0.824	201.8	4.08
Phase U, W and test cables	0.839	205,5	4.08
Two test cables	0.168	202.5	0.82

Table E.1: *Results from DC experiments.*

E.1.5 Sources of Error

- Power dissipated in the conductors during the experiment is converted to heat. This results in an increased temperature over time which results in an increase in the internal resistance of the conductors.
- Wires placed inconvenient to each other or external electrical equipment can induce noise to the measurements.

E.2 No Load and Load Transformer Experiment for Parameter Identification

In this section the experiments for finding the machine parameters for the IM is described. The theory behind the experiments is found in section D.1. In these experiments two transformers are used to cancel out all the higher order harmonics that occur when using a PWM inverter to feed the drive. The transformers are necessary because the IM is a low voltage machine that will not work on the 400 V supply from the net. One of the transformers is a variable transformer making it possible to adjust the voltage amplitude by the users request.

E.2.1 Equipment

- General setup described in section 5.2 in the report.
- Current probe.
- Voltage probe.
- Oscilloscope.
- Induction machine.
- 3 phase transformer (transformation ratio 1:5).
- 3 phase variable transformer, see figure E.2 for name plate (Schuntermann transformatoren, Typ: 400/25).

E.2.2 Test Setup

The test setup is depicted in figure E.3.

E.2.3 Execution

The following list contains a description of the execution of the experiment. Figure E.3 is used to support the description.

- Make sure the transformers is not connected to supply and turn down the variable transformer to minimum voltage.

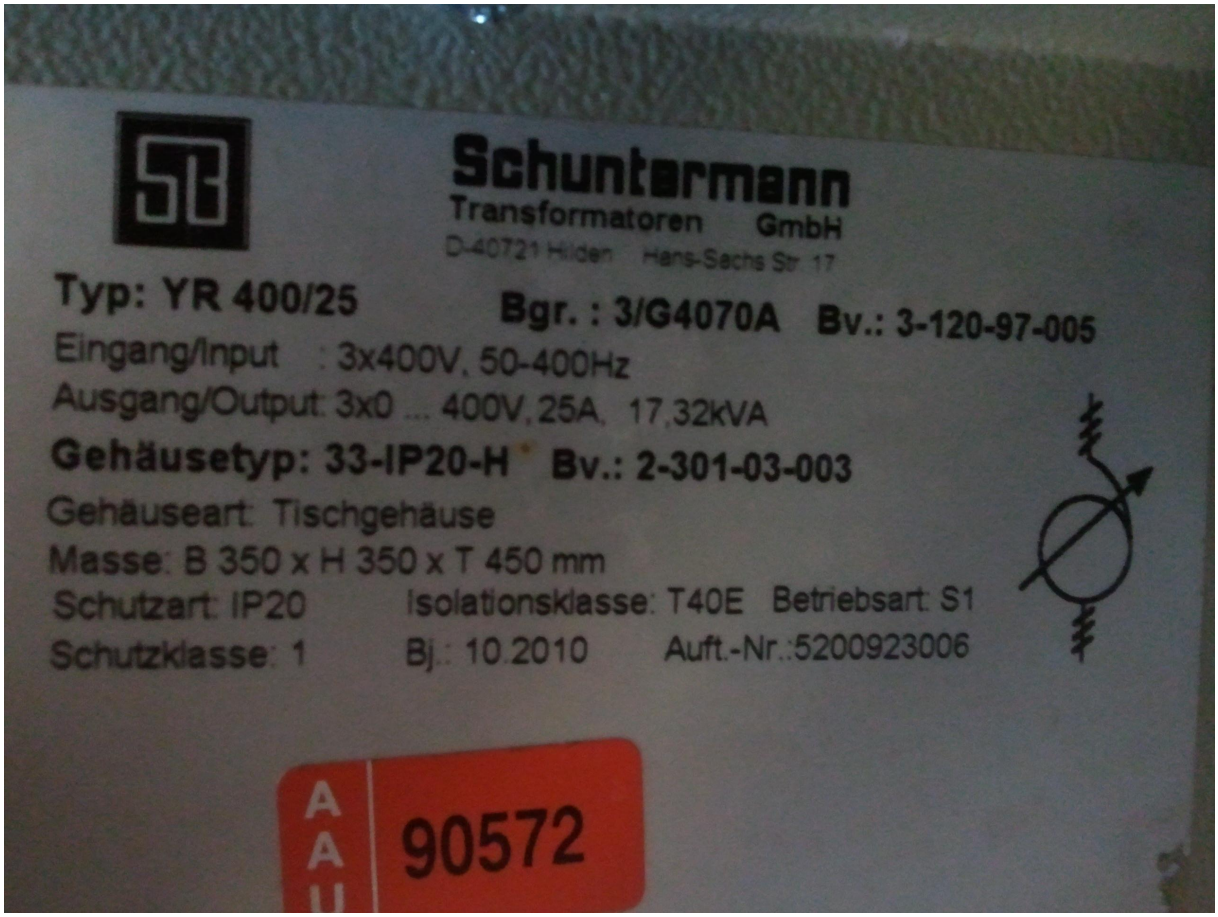

Figure E.2: *Nameplate for variable 3 phase transformer used in the experiment.*

- Set the load drive(Siemens drive system) to rotate at synchronous speed at 50 Hz (1500 rpm). This will induce no load situation.
- Connect the transformers to supply and slowly increase the voltage from the variable transformer while simultaneously ensure that the currents does not exceed the max allowable currents for the variable transformer(25 A), IM and the other transformer. Stop when voltage amplitude reaches the nominal voltage for this condition.
- Collect phase currents and voltages from the oscilloscope, make sure there is steady state. This is the no load results from this experiment.
- Slowly decrease the load drive's speed to force a slip generating a load. Stop decreasing the speed when the max current for the equipment is reached. Make sure to write down the speed.
- Collect phase currents and voltages from the oscilloscope, make sure there is steady state. This is the load results from this experiment.

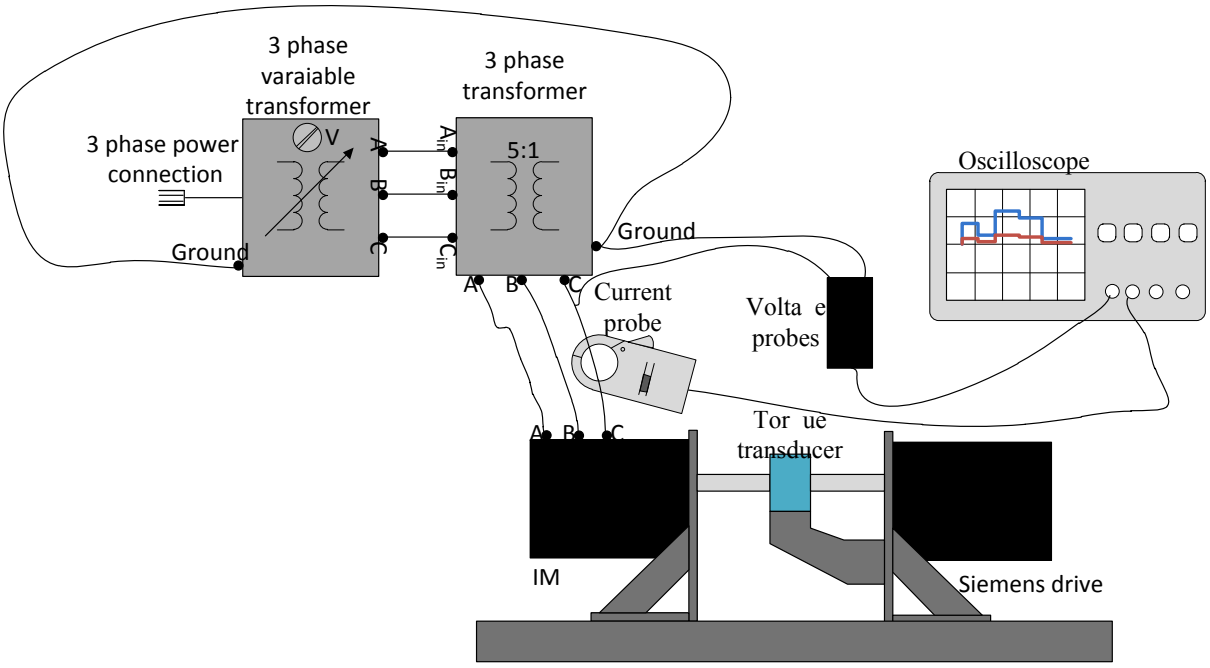

Figure E.3: *Test setup for no load and load experiment for parameter identification.*

E.2.4 Results

In this section the results from the experiment is presented. The results from the no load experiment is seen in figure E.4 and figure E.5. The results from the load experiment is seen in figure E.6 and figure E.7. In table E.2 the results from experiment is seen.

Steady state measurements from experiment		
	No load experiment	Load experiment
Phase voltage amplitude	8.5 V	8.5 V
Phase current amplitude	79.7 A	174 A
Mechanical speed	1500 rpm	1460 rpm
Power factor	0.072	0.79

Table E.2: *Results from the no load and load experiment.*

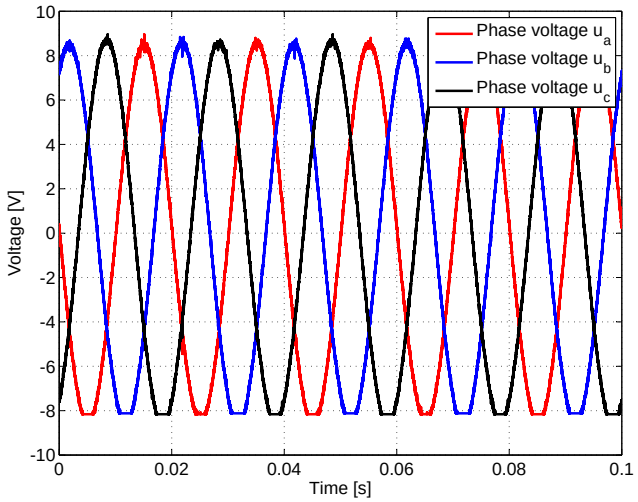

Figure E.4: *Phase voltages for the experiment at no load.*

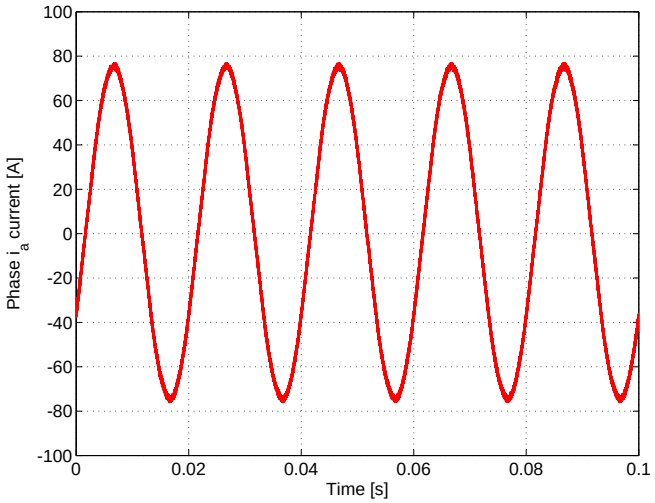

Figure E.5: *Phase current for the experiment at no load.*

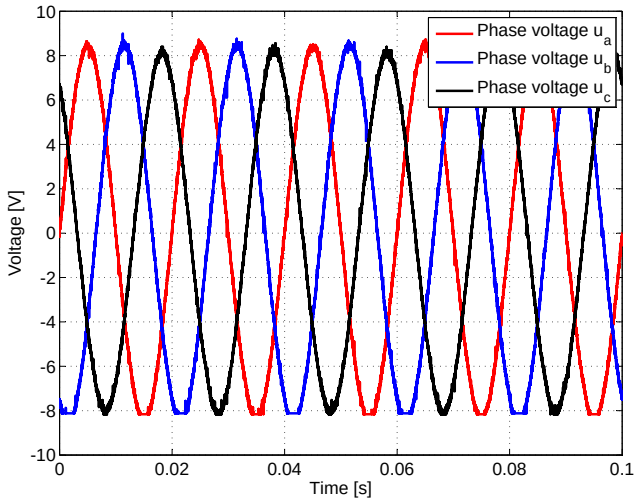

Figure E.6: *Phase voltages for the experiment at load.*

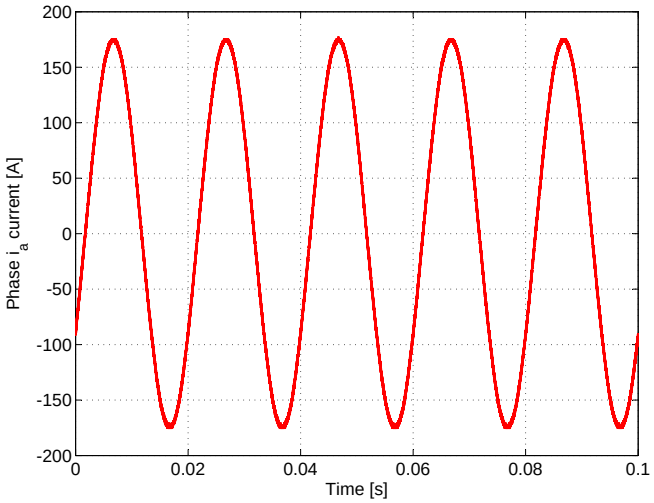

Figure E.7: *Phase current for the experiment at no load.*

E.3 Machine Parameters Fitting

In this section the theory and equations from section D.1 together with the results from chapter E is used to fit the machine parameters to get good accordance between model and experiments. The relations between the machine parameters is set up in MATLAB and the dynamic simulation model in SIMULINK is used with inputs from the experiments.
The first parameter R_s is calculated from the DC-test described in section D.1.1 and E.1. The results from section E.1 is for two phases and with a cable meaning that the resistance from one phase alone is:

$$R_s = \frac{R_{phase-phase} - 2 \cdot R_{cable}}{2} = \frac{4.08m\Omega - 0.82m\Omega}{2} = 1.63m\Omega \tag{E.1}$$

From section D.1.2 the following is calculated from the no load experiment:

$$R_{NL} = \frac{P_{NL}}{3 \cdot I_{NL}^2} = \frac{3 \cdot \frac{8.5V}{\sqrt{2}} \cdot \frac{79.7A}{\sqrt{2}} \cdot 0.072}{3 \cdot \left(\frac{79.7A}{\sqrt{2}}\right)^2} = 7.68m\Omega \tag{E.2}$$

$$Z_{NL} = \frac{U_{NL}}{I_{NL}} = \frac{\frac{8.5V}{\sqrt{2}}}{\frac{79.7A}{\sqrt{2}}} = 0.107\Omega \tag{E.3}$$

$$X_{NL} = \sqrt{Z_{NL}^2 - R_{NL}^2} = 0.107\Omega \tag{E.4}$$

From the load experiment the last calculation is performed before the fitting:

$$R_{eq} = \frac{P_L}{3 \cdot I_L^2} = \frac{3 \cdot \frac{8.5V}{\sqrt{2}} \cdot \frac{174A}{\sqrt{2}} \cdot 0.79}{3 \cdot \left(\frac{174A}{\sqrt{2}}\right)^2} = 0.039\Omega \tag{E.5}$$

Now the relationships from section D.1.3 is used together with results from the load experiment to fit the parameters by only changing one parameter X_M. X_M is changed in a iterative process and a simulation result is compared with experiment results. The end result is $X_M = 0.10065\Omega$, $R'_r = 0.0014\Omega$ and $X_{ls} = X'_{lr} = 0.0061\Omega$. The reactances is transformed to inductances by:

$$L = \frac{X}{\omega_e} \tag{E.6}$$

The equation above gives the following inductances: $L_M = 0.32038mH$ and $L_{ls} = L'_{lr} = 0.01942mH$. The result from the experiment and the simulation with the fitted machine parameters is seen in figure E.8.

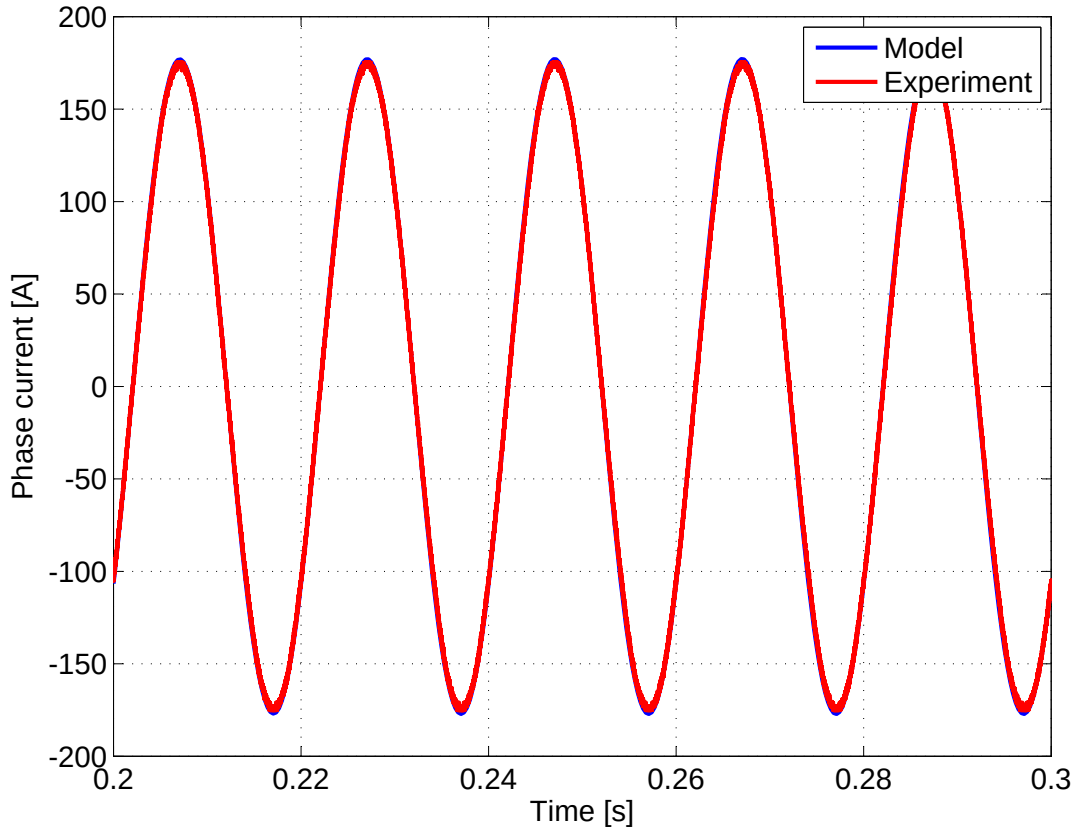

Figure E.8: *Comparison between results from experiment and the simulation model with fitted machine parameters.*

APPENDIX F

EXPERIMENTS ON THE TEST SETUP

This chapter contains descriptions of various experiments conducted on the test setup.

F.1 No load Experiment for Determination of Inverter non-ideal Phenomenas

The objective of this experiment is to determine non-ideal phenomenas in the inverter output.

F.1.1 Equipment

- General setup described in section 5.2 in the report.
- Current probe.
- Voltage probe.
- Oscilloscope.
- Induction machine.
- Inverter.
- DSP connected to a laptop.

F.1.2 Test Setup

The test setup is depicted in figure F.1.

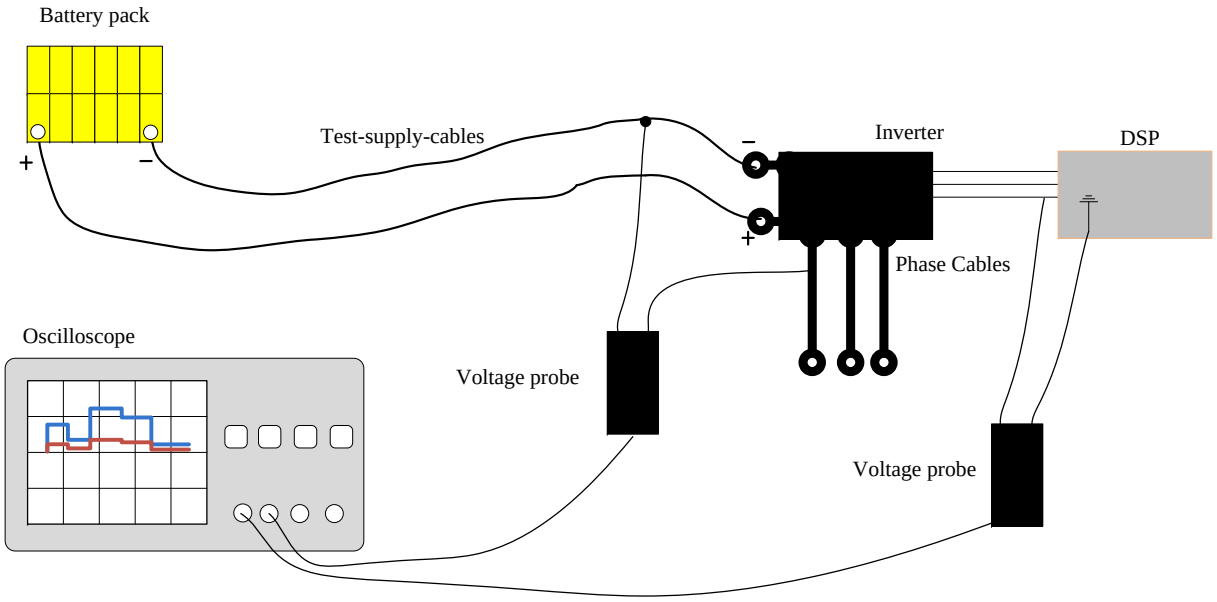

Figure F.1: *Setup for determination of non-ideal phenomenas at no-load.*

F.1.3 Execution

The following list contains a description of the execution of the experiment. Figure F.1 is used to support the description.

- Turn on the oscilloscope, voltage probes, inverter and DSP.
- Set the duty cycle on each phase to 0.5.
- Measure voltage output from DSP and from inverter.

F.1.4 Results

Results from the experiment is seen in figure F.2.

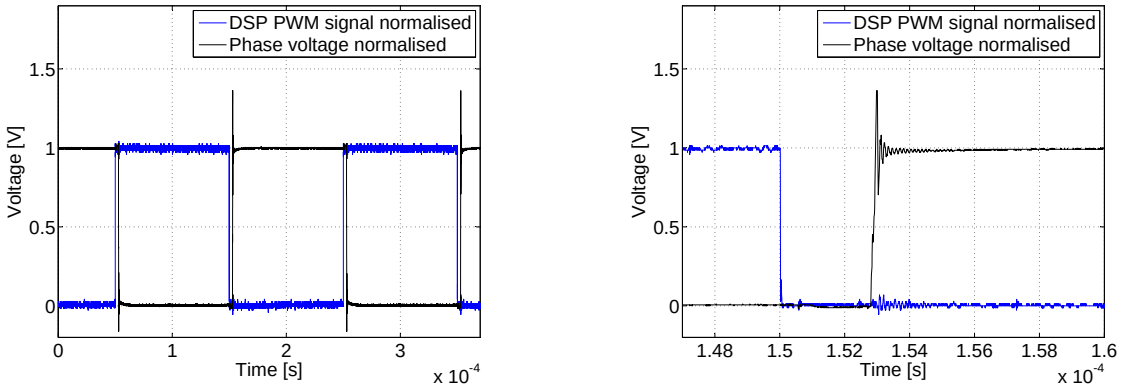

(a) *DSP PWM signal and phase voltage.*

(b) *Close view of DSP PWM signal and phase voltage.*

Figure F.2: *DSP PWM signal and phase voltage.*

F.2 Slip Experiment for Determination of Inverter non-ideal Phenomenas

The objective of this experiment is to determine non-ideal phenomenas in the inverter output.

F.2.1 Equipment

- General setup described in section 5.2 in the report.
- Battery pack
- Current probes.
- Voltage probe.
- Oscilloscope.
- Induction machine.
- Inverter.
- DSP connected to a laptop.
- Siemens drive system.

F.2.2 Test Setup

The test setup is depicted in figure F.3.

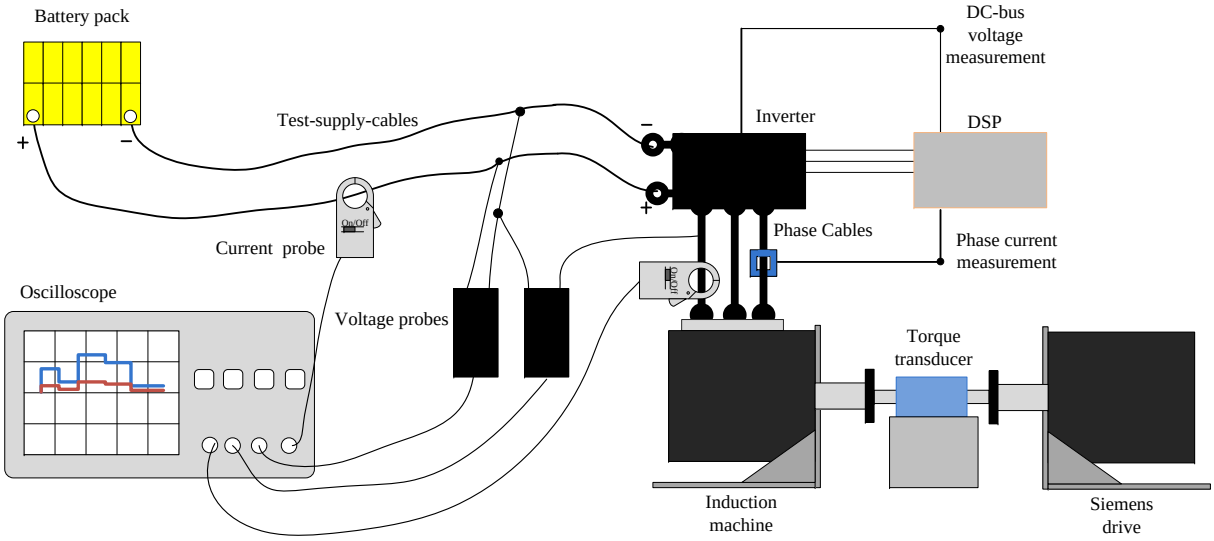

Figure F.3: *Setup for determination of non-ideal phenomenas when loaded.*

F.2.3 Execution

The following list contains a description of the execution of the experiment. Figure F.3 is used to support the description.

- Turn on the oscilloscope, voltage probes and current probes, inverter, DSP and Siemens drive.
- Use the steady state voltage procedure described in appendix F.7. Set the fundamental frequency to 60 Hz and the fundamental amplitude to 10.15 V.
- Set the Siemens drive to a velocity of 1854 rpm.
- Measure voltages and currents using oscilloscope.

F.2.4 Results

Results are seen in figure F.4 and figure F.5. Close-ups on phase and DC voltages when the current is at its maximum is seen in figure F.6.

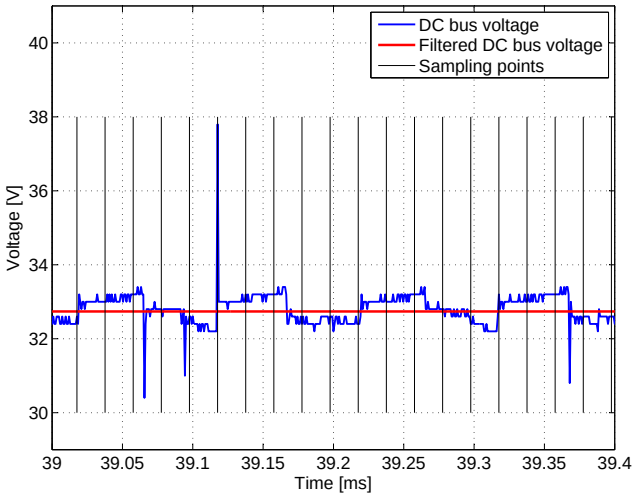

Figure F.4: *Variating DC bus voltage.*

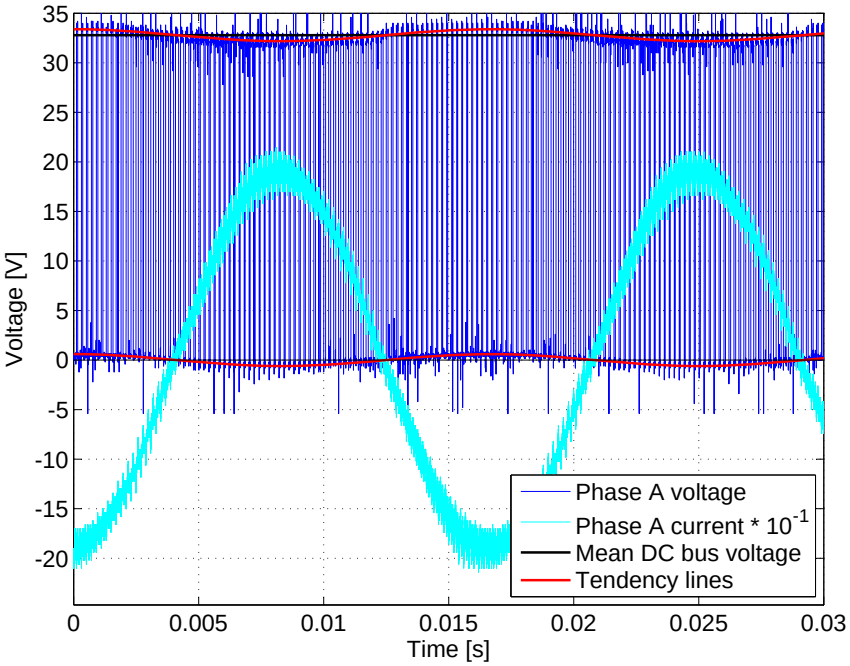

Figure F.5: *Current and voltage in phase A for sinusoidal voltage inputs.*

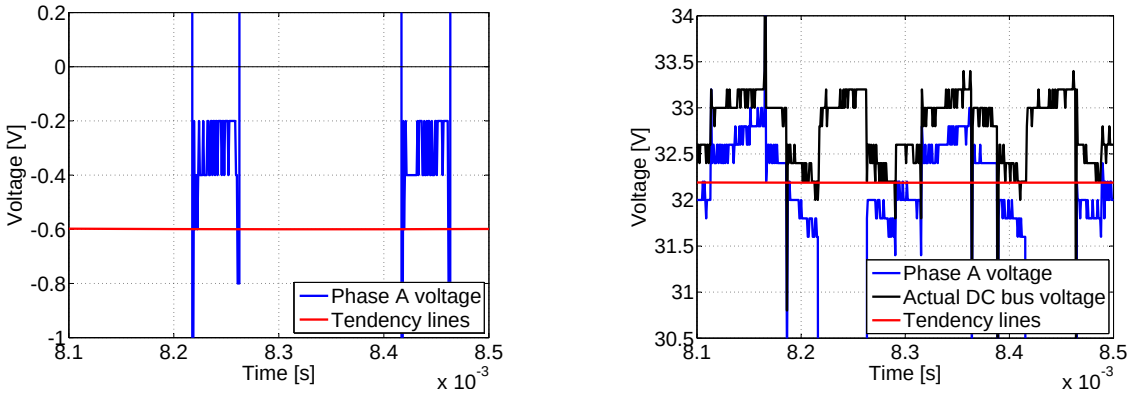

(a) *Voltage drop across diode.*

(b) *Voltage drop across transistor.*

Figure F.6: *Close ups of figure F.5 where the current is at its maximum.*

F.3 Dynamic Verification of Voltage Equations

In this section the experiment conducted to verify the dynamic behavior of the voltage equations for the IM is described. The experiment is conducted by controlling the IM open loop with a V/Hz algorithm at a given frequency and voltage amplitude. When the IM reaches steady state a step in the load torque is performed by the load drive(Siemens drive system). The voltages are measured before and after the torque step to get the steady state amplitudes that are used in the simulation model to be able to verify the voltage equations. The torque is measured before and after the load torque step. The steady state mechanical speed is measured before and after the load step. The voltage amplitude and frequency together with the torque before and after the step is used as inputs for the model. The mechanical speed before and after the load torque step together with the measured current is used for a comparison of the model and experiment.

F.3.1 Equipment

- General setup described in section 5.2 in the report.
- Current probe.
- Voltage probe.
- Oscilloscope.
- Induction machine.
- Inverter.
- DSP connected to a laptop.

F.3.2 Test Setup

The test setup is depicted in figure F.7. The voltage probes is used to measure the PWM voltage signal from the inverter. The current probe is used to measure the phase current i_A.

F.3.3 Execution

The following list contains a description of the execution of the experiment. Figure F.7 is used to support the description.

- Turn on the oscilloscope, voltage probes, inverter and DSP.

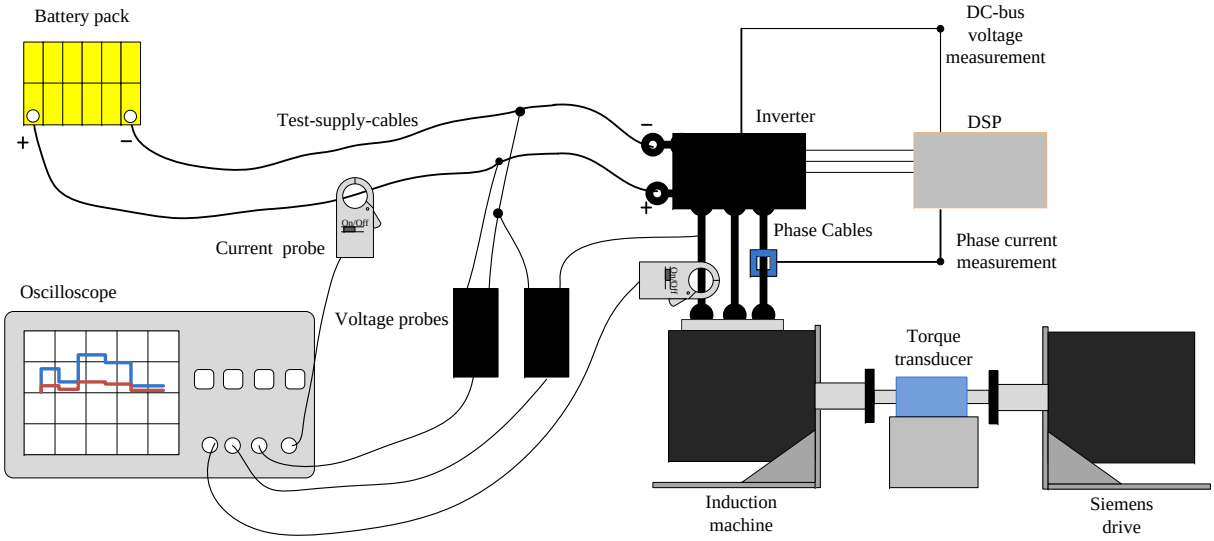

Figure F.7: *Setup for dynamic verification experiment.*

- Set the load drive(Siemens drive system) to deliver 0 Nm torque.
- Start up the IM using the steady state voltage procedure described in appendix F.7. The voltage amplitude is set to 11.0 V and the frequency is set to 60 Hz.
- Wait for the IM the get into steady state
- Measure the torque at no load.
- Measure the mechanical speed.
- Measure the voltage PWM signals.
- Measure the current from a phase(Make sure you measure before, during and after the load step).
- Perform a load torque step on the load drive(14 Nm).
- Measure the torque.
- Measure the mechanical speed.
- Measure the voltage PWM signals.

F.3.4 Data Processing

In this section the data measured from the experiment is used to calculate inputs for the dynamic voltage equations. In the model it is not possible to use PWM voltage signals as input, therefore

a TFT analysis is performed on the PWM signals to get the frequency and amplitude of the fundamental frequency.

F.3.5 Results

In this section the results from experiment is presented. In table F.1 the steady state measurements from the experiment is listed. In figure F.8 the phase current is seen before, during and after the torque step.

Steady state measurements from experiment		
	Before torque step	After torque step
Rotor velocity	1796 rpm	1734 rpm
Phase voltage amplitude	11 V	10.15 V
Phase voltage frequency	60 Hz	60 Hz
Load Torque	0.7 Nm	15.3 Nm
Phase current amplitude	85 A	245 A

Table F.1: *Steady state measurements from experiment before and after the torque step.*

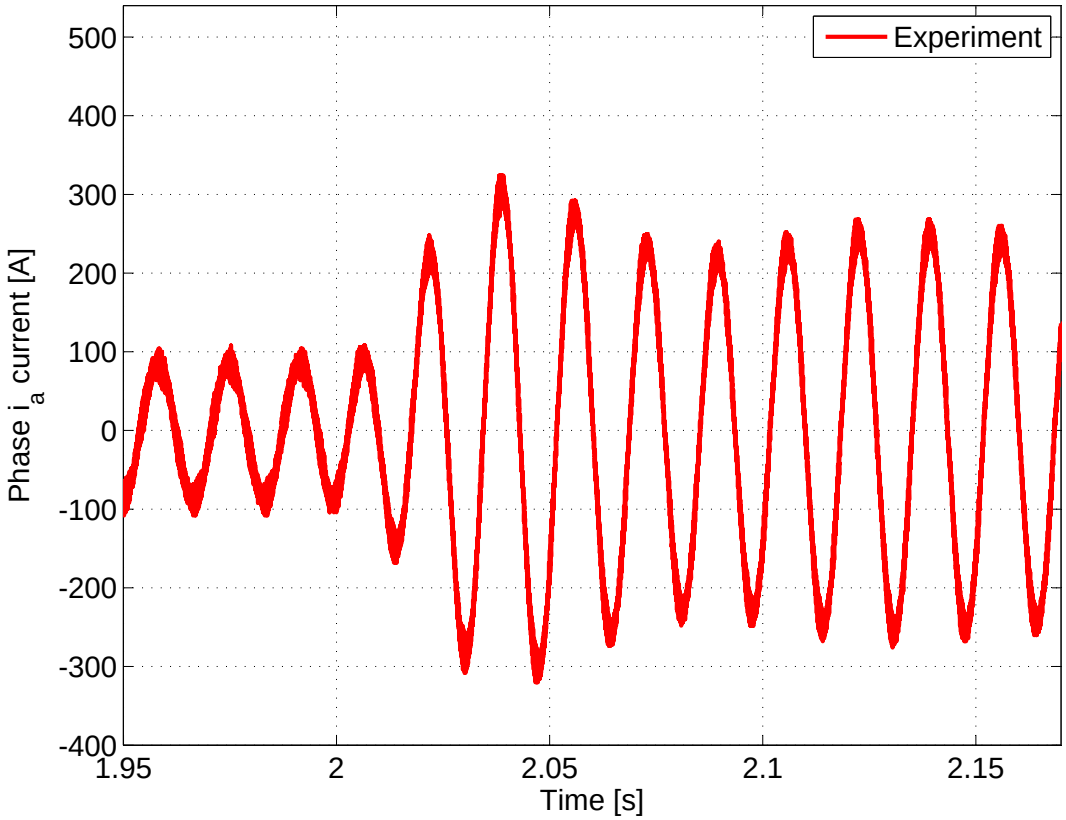

Figure F.8: *Measured Current for phase i_a before, during and after a load torque step*

F.4 Friction in Torque Measurement

The objective of this experiment is to determine the friction in the measured torque from the torque transducer.

F.4.1 Test Setup

General setup described in section 5.2 in the report.

F.4.2 Execution

The following list contains a description of the execution of the experiment.

- Set the Siemens drive system to a constant velocity.
- Collect torque measurements from torque transducer.
- Repeat at various velocities.

F.4.3 Results

Results are seen in figure F.9. The mean of the torque at each velocity is seen in figure F.10.

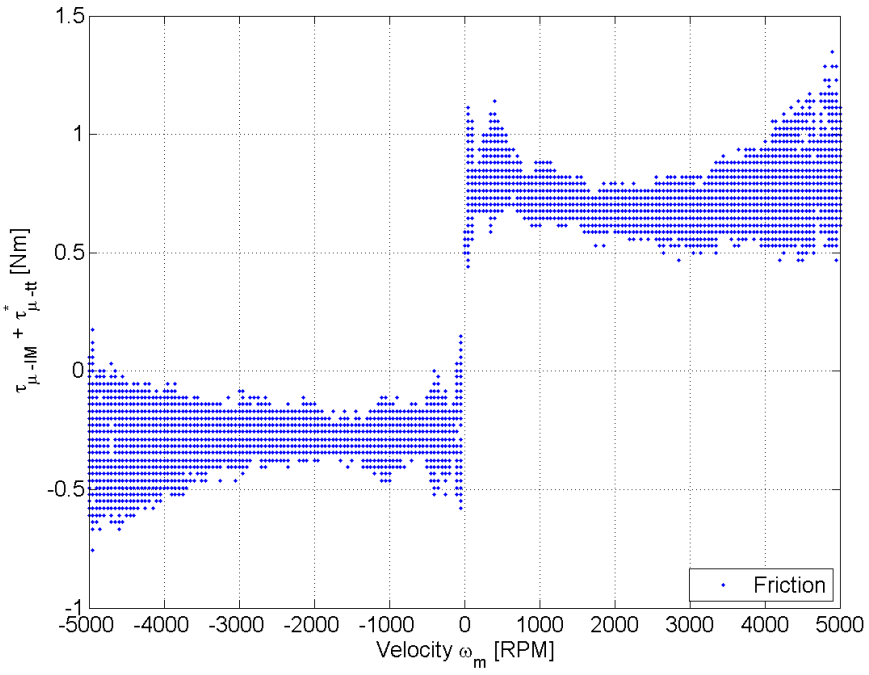

Figure F.9: *Friction measured by torque transducer as function of rotor velocity.*

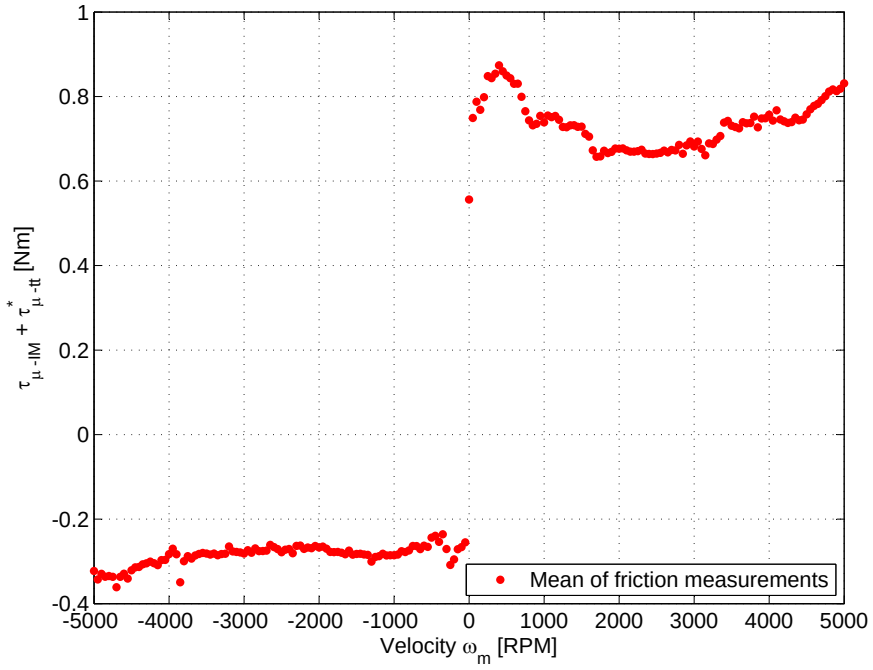

Figure F.10: *Mean of the friction measured by the torque transducer as function of rotor velocity.*

F.5 Moment of Inertia for the Test Setup

The objective of this experiment is to determine the moment of inertia for the test setup.

F.5.1 Theory

The torque equation used in this is experiment is:

$$J_{test-setup} \cdot \dot{\omega}_m = \tau_e - \tau_{Siemens} - \tau_{\mu-IM} - \tau_{\mu-tt} - \tau_{\mu-Siemens} \tag{F.1}$$

where:

$J_{test-setup}$	Moment of inertia for test setup	$[kg \cdot m^2]$
ω_m	Angular velocity of shaft	$[rad/s]$
τ_e	Torque from induction machine	$[Nm]$
$\tau_{Siemens}$	Torque from Siemens drive system	$[Nm]$
$\tau_{\mu-IM}$	Friction from bearings in induction machine	$[Nm]$
$\tau_{\mu-tt}$	Friction from bearings in torque transducer	$[Nm]$
$\tau_{\mu-Siemens}$	Friction from bearings in Siemens machine	$[Nm]$

When applying no torque from the induction machine the moment of inertia is expressed as:

$$\begin{aligned} J_{test-setup} \cdot \alpha_m &= -\tau_{Siemens} - \tau_{\mu-IM} - \tau_{\mu-tt} - \tau_{\mu-Siemens} \\ &\downarrow \\ J_{test-setup} &= \frac{-\tau_{Siemens} - \tau_{\mu-IM} - \tau_{\mu-tt} - \tau_{\mu-Siemens}}{\alpha_m} \end{aligned} \tag{F.2}$$

α_m Angular acceleration of shaft $[rad/s^2]$

When applying a constant acceleration from the Siemens drive system the moment of inertia is calculated by measuring the torque from the Siemens drive system while accelerating. This torque is called τ_{acc}. The velocity at which the torque is measured is then applied and the torque is measured again. The torque measured at constant velocity is the sum of all friction torque in the test setup and is called τ_{fric}. The moment of inertia is now calculated as:

$$J_{test-setup} = \frac{-\tau_{acc} - \tau_{fric}}{\alpha_m} \tag{F.3}$$

F.5.2 Test Setup

General setup described in section 5.2 in the report.

F.5.3 Execution

The following list contains a description of the execution of the experiment.

- Set the Siemens drive system to accelerate at a predefined angular acceleration.
- Collect torque measurements using the torque calculations in the Siemens drive system while accelerating.
- Observe the velocity, ω_τ, at which the torque was measured at.
- Apply a constant velocity of ω_τ.
- The friction torque at ω_τ are now known and the moment of inertia is calculated using equation (F.3)
- Repeat at various accelerations.

$\alpha_m \left[rad/s^2\right]$	$\tau_{acc}\,[Nm]$	$\tau_{fric}\,[Nm]$	$J_{test-setup}\left[kg \cdot m^2\right]$
-209.5	$7.05_{@-136rpm}$	$-0.85_{@-136rpm}$	0.0296
-209.5	$7.07_{@-1124rpm}$	$-0.93_{@-1124rpm}$	0.0293
-209.5	$7.29_{@-2147rpm}$	$-1.06_{@-2147rpm}$	0.0297
-314.2	$10.14_{@-432rpm}$	$-0.79_{@-432rpm}$	0.0298
-314.2	$10.12_{@-1874rpm}$	$-0.96_{@-1874rpm}$	0.0292
-157.1	$5.69_{@-198rpm}$	$-0.85_{@-198rpm}$	0.0308
-157.1	$5.57_{@-957rpm}$	$-0.91_{@-957rpm}$	0.0297
-157.1	$5.54_{@-1681rpm}$	$-0.93_{@-1681rpm}$	0.0294
-157.1	$5.69_{@-2461rpm}$	$-1.04_{@-2461rpm}$	0.0296

Table F.2: *Results from experiment for determination of moment of inertia in test setup. The velocities subscripted at the measured torque and friction torque indicate the velocity at which they are measured.*

F.5.4 Results

Results are seen table F.2. The sign of the torque and accelerations in the table are set according to figure 6.9 in the report.

The moment of inertia is determined by calculating the mean of the results from the experiments. The moment of inertia is set to $0.030 kg \cdot m^2$.

F.6 Estimation of Rotor Temperature

The objective of this experiment is to determine whether a relation between stator and rotor temperature can be established.

F.6.1 Theory

The relation between resistance and temperature is expressed as in equation (F.4) where α=0.00389$\frac{Ohm}{^\circ C}$ for the rotor if the squirrel cage is assumed to be made of aluminum [Moreno et al., 2001]:

$$R = R_0[1+\alpha(T-T_{amb})] \tag{F.4}$$

where:	R	Actual resistance $[Ohm]$
	R_0	Resistance at ambient temperature $[Ohm]$
	α	Temperature coefficient $\left[\frac{Ohm}{^\circ C}\right]$
	T	Current temperature $[^\circ C]$
	T_{amb}	Ambient temperature $[^\circ C]$

F.6.2 Equipment and Test Setup

The test setup is described in section 5.2 in the report. The equipment used for the experiment is:

- General setup described in section 5.2 in the report.
- Simulation model described in section 6.6 in the report.

F.6.3 Execution

The following list contains a description of the execution of the experiment.

- Apply field oriented control in the test setup including indirect flux estimation.
- Set the Siemens drive system to a constant velocity of 1000 rpm.
- Apply various torque on the induction machine and measure the actual torque using the mean of 200 measure points from the torque transducer.

- Open the simulation model and vary the rotor resistance in the voltage equations until the model produces the same torque as the test setup.
- Using the tuned rotor resistance calculate the estimated rotor temperature with equation (F.4)
- Set the torque from the induction machine to 20 Nm.
- Set the velocity of the Siemens drive system to 1500 rpm.
- Wait for the stator temperature to reach a desired level and repeat from point 1.

F.6.4 Results

Results are seen table F.3. The ambient temperature during the experiment was $22°C$. The stator and rotor temperatures are illustrated in figure F.11.

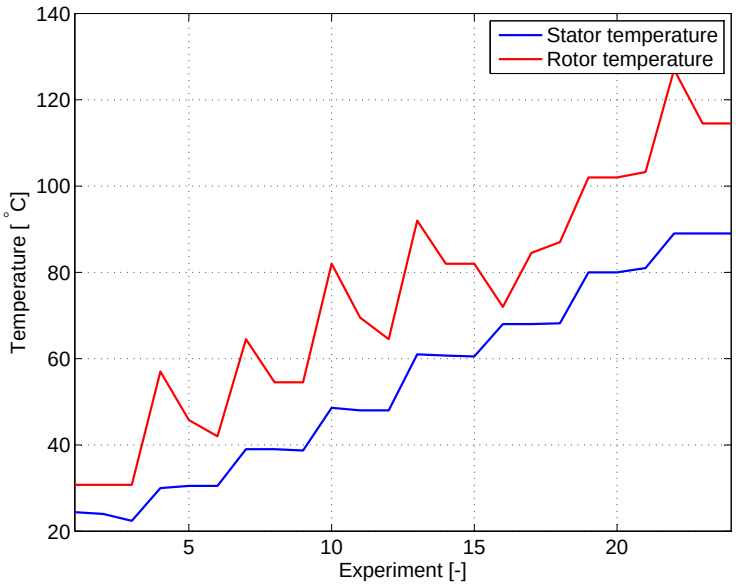

Figure F.11: *Relation between stator and rotor temperature.*

F.6.5 Discussion

The results of the experiment shows that there is no simple relation between stator and rotor temperature. The rotor temperature seems to be above the stator temperature however this cant be proven to be valid in all cases.

$T_s[^\circ C]$	$\tau_{calc}[Nm]$	$i_{ds}[A]$	$i_{qs}[A]$	$\tau_{meas}[Nm]$	$\Delta R_s[\%]$	$T_{r-estimated}[^\circ C]$
24.4	6.6	60	120	6.6	3.5	31
24	10.9	60	200	11.2	3.5	31
22.4	15.2	60	280	15.5	3.5	31
30	6.6	60	120	7	14	57
30.5	10.9	60	200	11.7	10	46
30.5	15.2	60	280	16.3	8	42
39	6.6	60	120	7.1	17	65
39	10.9	60	200	12	13	55
38.7	15.2	60	280	16.9	13	55
48.6	6.6	60	120	7.3	24	82
48	10.9	60	200	12.5	19	70
48	15.2	60	280	17.5	17	65
61	6.6	60	120	7.4	28	92
60.7	10.9	60	200	12.9	24	82
60.5	15.2	60	280	18.4	24	82
68	6.6	60	120	7.2	20	72
68	10.9	60	200	13	25	85
68.2	15.2	60	280	18.7	26	87
80	6.6	60	120	7.5	32	102
80	10.9	60	200	13.5	32	102
81	15.2	60	280	19.5	33	103
89	6.6	60	120	7.7	42	127
89	10.9	60	200	13.9	37	115
89	15.2	60	280	20	37	115

Table F.3: *Results from rotor temperature estimation experiment.*

F.6.6 Sources of Error

The rotor temperature is dependent on how the stator temperature is increased. If the induction machine is set to provide a large torque at a large velocity in order to increase the stator temperature fast the increase in rotor temperature will differ from when the same stator temperature is reached at a lower power.

The estimation of the temperature is based on the simulation model, the error in torque and the stator temperature.
Errors in the stator temperature causes errors in the rotor temperature estimation.
The error in torque can be caused by other factors than varying rotor resistance. An error in magnetising inductance or rotor inductance also results in an error in torque (as seen in equation (7.21) in the report).

F.7 Steady State Voltage Procedure

In this section the procedure for applying sinusoidal voltage to the stator terminals while the shaft is rotating is described.
In general the sinusoidal voltage that is to be modulated by PWM is described by equation (F.5) for phase A.

$$v_A = A \cdot \sin(\omega_e \cdot t + \phi) \tag{F.5}$$

where:	v_A	Voltage applied to phase A $[V]$.
	A	Amplitude of the applied voltage $[V]$.
	ω_e	Angular velocity of the applied voltage $[^{rad}/_{s}]$.
	ϕ	Phase shift $[rad]$.
	t	Time $[s]$.

The procedure is described by the following list.

1. The shaft velocity is set by the Siemens drive to mach the desired synchronous velocity ω_e. In general this means that the mechanical velocity is set to half of the synchronous velocity due to the machines two polepair construction.
2. The amplitude A is set to zero.
3. The synchronous velocity is set to the desired value.
4. The voltage amplitude A is slowly ramped up to the desired value.
5. The shaft velocity is set to mach the desired slip.

F.8 Step in Currents for Verification of Current Controllers

The objective of this experiment is to verify the developed current controllers.

F.8.1 Equipment and test setup

The test setup is described in section 5.2 in the report. The equipment used for the experiment is:

- General setup described in section 5.2 in the report.
- Simulation model described in section 6.6 in the report.

F.8.2 Execution

The following list contains a description of the execution of the experiment.

- Apply field oriented control in the test setup including standard indirect flux estimation without improvements.
- Set the Siemens drive system to a desired constant velocity.
- Apply desired current steps using the field oriented control.
- Measure the currents.
- Open the simulation model and apply the same current steps at the same velocity.
- Repeat at various velocities and current steps.

F.8.3 Results

The results are seen in section 7.3.1 on page 99 in the report.

F.8.4 Discussion

The results of the experiment has acceptable comparison with the expected results from the simulation model as described in the report.

APPENDIX G

CALCULATIONS FOR SPLINE CONNECTION AND INTERFERENCE FIT

The original spline connection between the induction machine and the differential in the electrical vehicle had 6.3 mm engagement. The spline on the IM is an internal spline. An example of an internal spline is seen in figure G.1. Depending on the quality of the connection the maximum stress in the connection varies. Expecting the lowest quality of connection, the maximum stress is 138 MPa (20000 psi)[Institute, 1996]. The maximum stress is calculated using the following equation.

$$\tau_{spline} = \frac{16 \cdot T}{\pi \cdot d_p^2 \cdot l} \tag{G.1}$$

where:	T	Applied torque $[Nm]$
	d_p	Pitch diameter $[m]$
	l	Length of spline engagement $[m]$
	τ_{spline}	Shear stress in the spline $[Pa]$

From equation (G.1) the maximum torque is calculated using the maximum stress. The pitch diameter for the spline is 0.02 m. The maximum torque that can be applied is 69 Nm, which is 153% of the max torque that the motor can deliver. The IM can deliver even higher torque at lower velocities causing the maximum torque of 69 Nm to be unacceptable.
The spline connection has the following specifications:

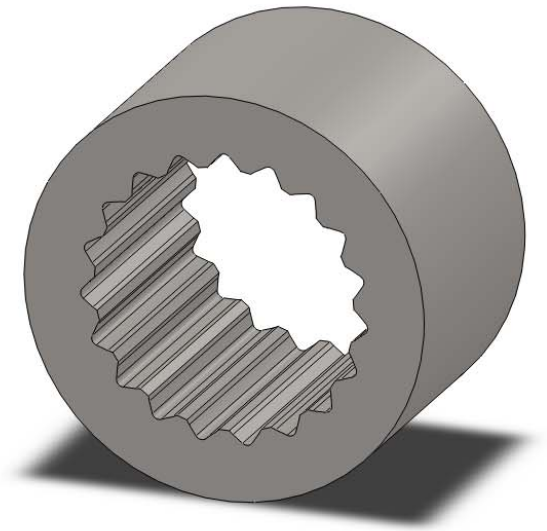

Figure G.1: *Example of internal spline.*

Data for internal spline	
Type	ANSI B92.1 (Flat root side)
Pitch	24/48
Number of teeth	19
Pressure angle	45
Tolerance class	5

Table G.1: *Specifications for internal spline.*

A new internal spline was produced having the same specifications as the original. The new spline provides 18.5mm engagement and the maximum transmittable torque is now 205 Nm, which is 456% of the maximum torque of the induction machine.

Interference Fit

As mentioned in section 5.2.3 in the main rapport the part that was shrinked on the rotor shaft containing the internal spline interface broke. Therefore a new part is made and the interference fit on the new part is designed in this section see figure 5.13 in section 5.2.3 in main rapport. The design is based on a measured shaft diameter and from this measurement the inner hub diameter is designed to form an interference fit. The calculations is based on equations in [Norton, 2006]. An interference fit is seen in figure G.2. To create a tight joint interference the rule of thousandths is used. It simply means that there is a simple relationship between the

shaft diameter and the diamentral interference δ ($\delta = 2 \cdot \Delta r$). The rule says that for a given shaft diameter the diametral inteference δ should be 0.001 to 0.002 times the shaft diameter, where the smaller amount (0.001) should be used for smaller shaft diameters (up to $25.4mm$). In this case the radius of the rotor shaft r_s is measured with a micrometer screw see table G.2 and by the rule of thousandths the diametral interference is:

$$\begin{aligned} \delta &= 0.001 \cdot 2 \cdot r_s && \text{(G.2)} \\ &= 25.03 \cdot 10^{-3} mm && \text{(G.3)} \end{aligned}$$

It is now possible to calculate the obtainable torque to see if it is acceptable for the application see equation (G.5), the values used for the parameters are seen in table G.2

$$\begin{aligned} T &= \frac{\pi \cdot L \cdot r \cdot \mu \cdot \delta}{\frac{1}{E_h} \cdot \left(\frac{r_{oh}^2 + r^2}{r_{oh}^2 - r^2} + \nu_h \right) + \frac{1}{E_s} \cdot \left(\frac{r^2}{r^2} - \nu_i \right)} && \text{(G.4)} \\ &= 353.1 Nm && \text{(G.5)} \end{aligned}$$

where:

	L	Length of interference fit $[m]$
	μ	Friction coefficient between shaft and hub $[-]$
	r	Nominal radius of the interface between the hub and shaft $[m]$, see equation (G.7)
	δ	Diametral interference $[m]$
	E_h	Young's module for the hub material $[Pa]$
	E_s	Young's module for the shaft material $[Pa]$
	r_{oh}	Outer radius of the hub $[m]$
	ν_h	Poisson's ratio for the hub material $[-]$
	ν_s	Poisson's ratio for the shaft material $[-]$

$$\begin{aligned} r &= r_s - \frac{\delta}{2} && \text{(G.6)} \\ &= 12.502 mm && \text{(G.7)} \end{aligned}$$

The torque calculated in equation (G.5) of $353.1Nm$ is acceptable as the maximum motor torque is $45.0Nm$. Now the inner diameter r_h is calculated:

$$r_h = r_s - \frac{\delta}{2} \tag{G.8}$$
$$= 12.502mm \tag{G.9}$$
$$d_h = 25.005mm \tag{G.10}$$

The inner diameter of the hub cannot be made exact therefore a tolerance is specified and the worst case obtainable torque is calculated to insure that the inference fit is acceptable. The specified inner diameter is seen in equation (G.11). With this tolerance the minimum obtainable torque is $212.1Nm$ which is acceptable.

$$d_h = 25.005mm^{+0.01mm}_{-0.0mm} \tag{G.11}$$

Data for interference fit	
r_s	12.515 mm
δ	$25.03 \cdot 10^{-3}$ mm
r	12.502 mm see equation (G.7)
r_{oh}	22.5 mm
E_h	210 MPa
E_s	210 MPa
ν_h	0.28
ν_s	0.28
μ	0.15 [Norton, 2006, p. 535]

Table G.2: *Values for inteference fit.*

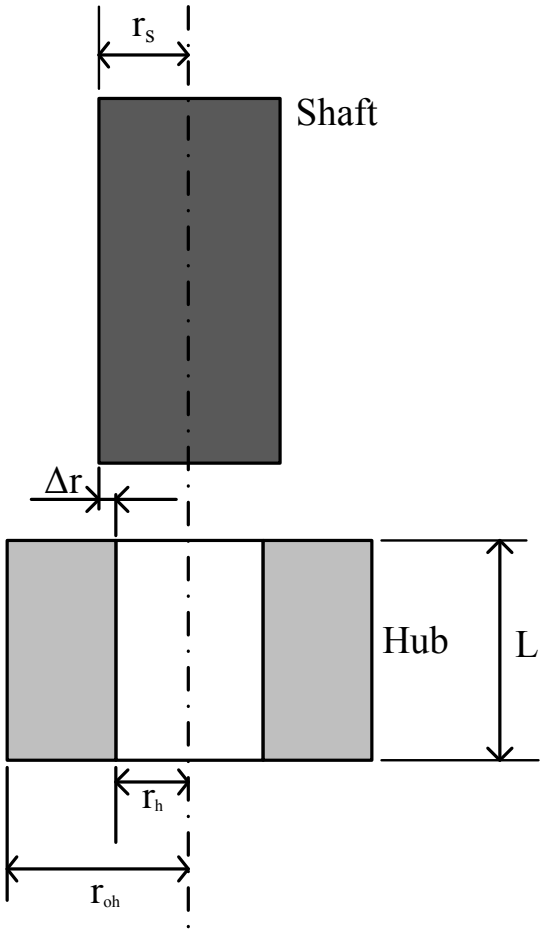

Figure G.2: *Typical interference fit.*

APPENDIX H

DESIGN OF BOARDS FOR SIGNAL ELECTRONICS

This chapter contains descriptions of the boards for signal electronics used in this project.

H.1 BPI Interface Board

The battery powered inverter (BPI) interface board is the board connected to the inverter. The BPI interface board is designed by Torben N. Matzen (Adjunkt AAU) and produced by the project group. Schematics for the board is seen in figure H.1, H.2 and H.3. Figure H.2 and figure H.3 are sub systems that are a part of the main schematic in figure H.1. The sub systems are to be inserted in the green boxes in figure H.1.

A photo of the interface board is seen in figure H.4.The BPI interface board contains eight optical input ports. Six for PWM signals and two for enable and reset. The input ports are connected to a FPGA on the board. Utilizing all six PWM inputs the six transistors in the inverter can be controlled separately. In this project however only three PWM inputs are utilized.
The dead time is set by the user using the dip-switch on the board. The FPGA calculates when to open and close the transistors in the inverter using the PWM inputs, the dead time set by the user and the clock frequency from the crystal.
The BPI interface board is also equipped with two output ports used for fail signals from the inverter and auxiliary. These ports are however not utilized in this project.

The display on the board displays status messages for the inverter.

The signals from the FPGA are send to the transistors through an IDE cable.
The DC bus voltage is measured and a current pump is utilized to convert the voltage into a current signal to be send to the DSP through a RJ45 cable. The schematic for the current pump is seen in figure H.3. The temperature of the inverter is also converted into a current signal and send to the DSP through a RJ45 cable.

The inverter is supplied by a 5V DC supply and a 18V DC supply. The VHDL-code for the microchip written by Torben N. Matzen is seen in section H.3.

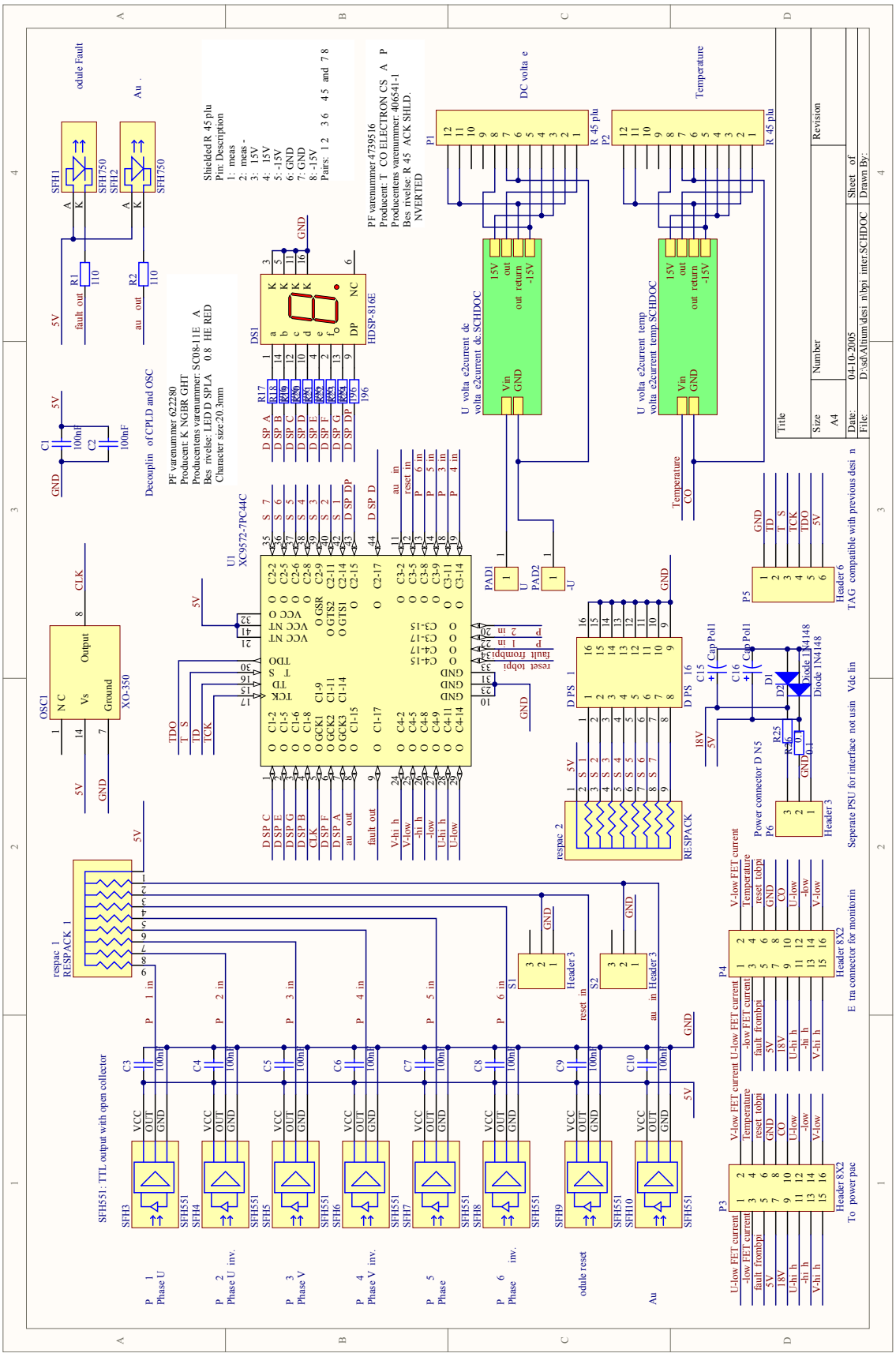

Figure H.1: *Schematic of BPI interface board (1/3)*

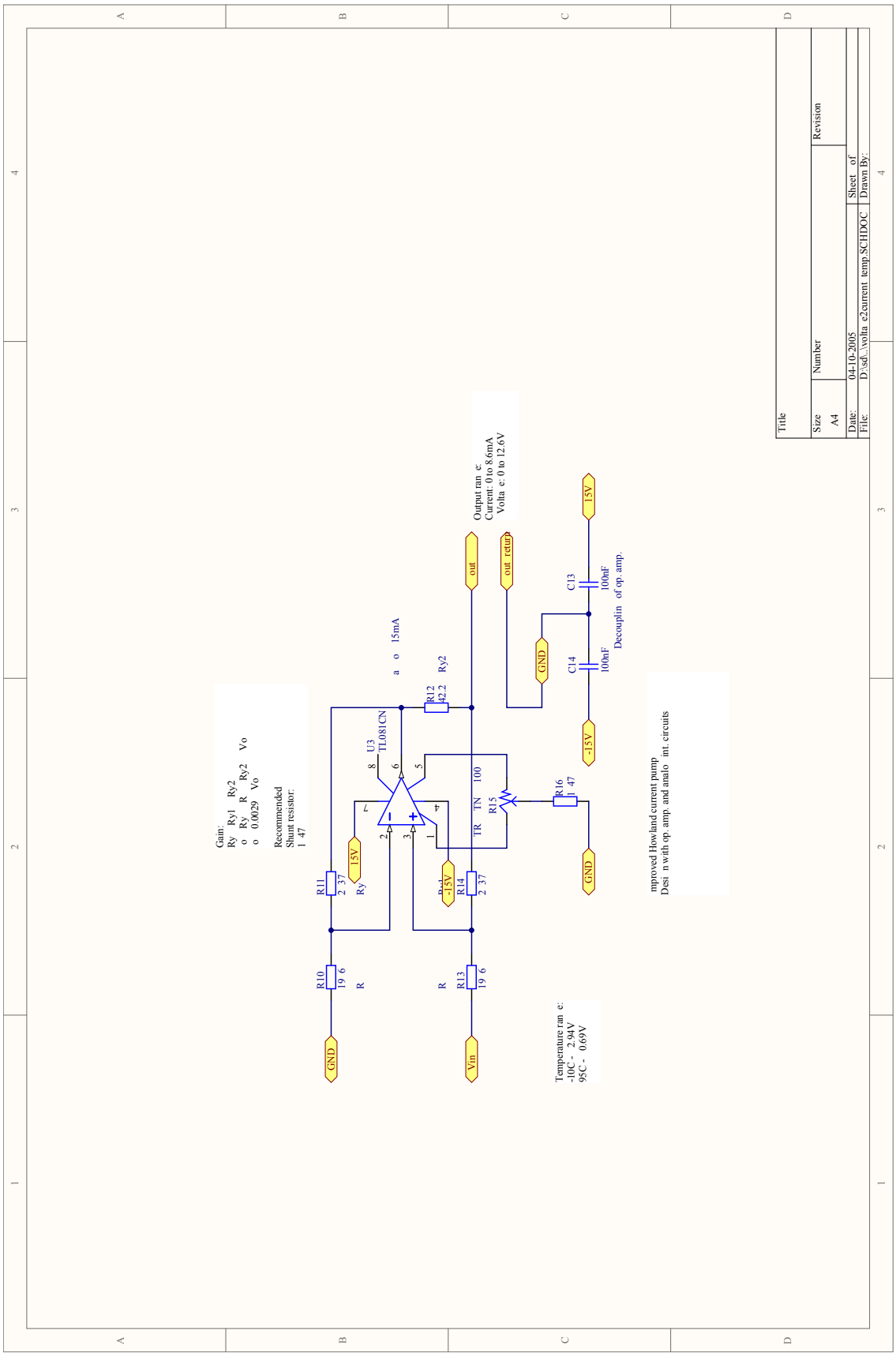

Figure H.2: *Schematic of BPI interface board (2/3)*

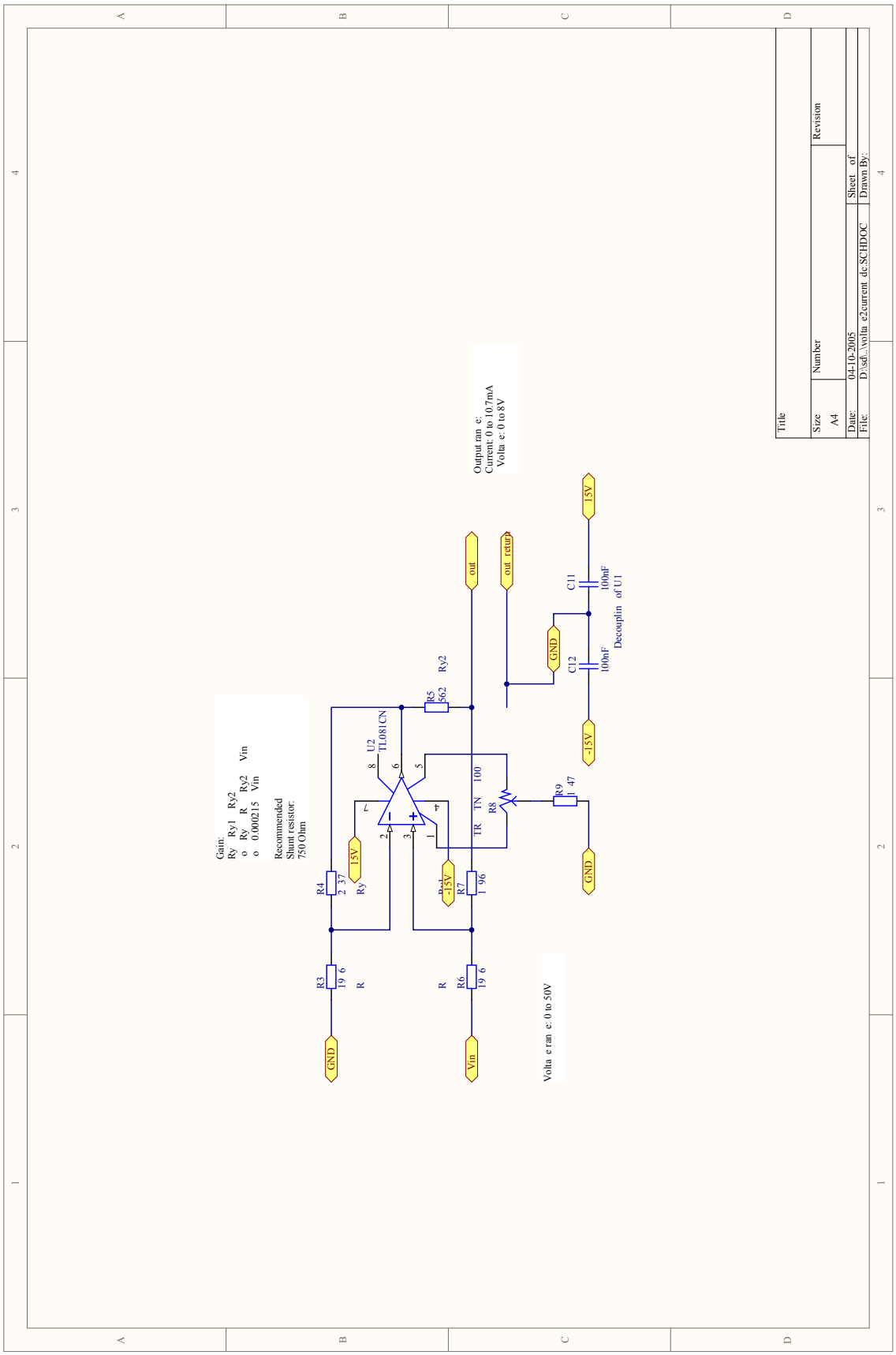

Figure H.3: *Schematic of BPI interface board (3/3)*

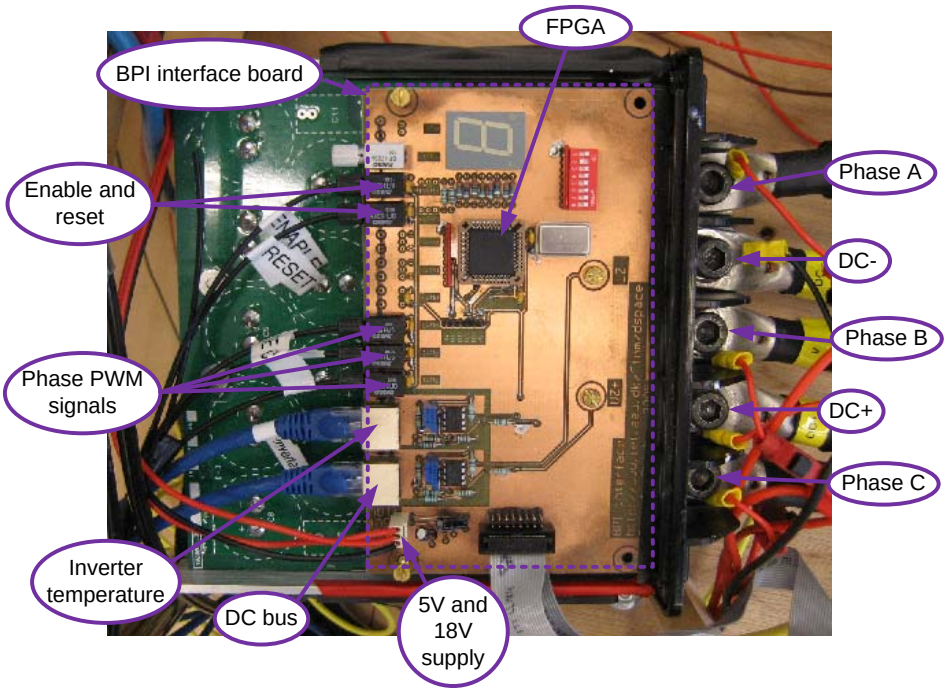

Figure H.4: *Sauer Danfoss inverter.*

H.2 DSP Board

The DSP board consists of three separate boards that are connected, a main DSP board, an optical board and a supply board. The three boards are seen in figure H.5.

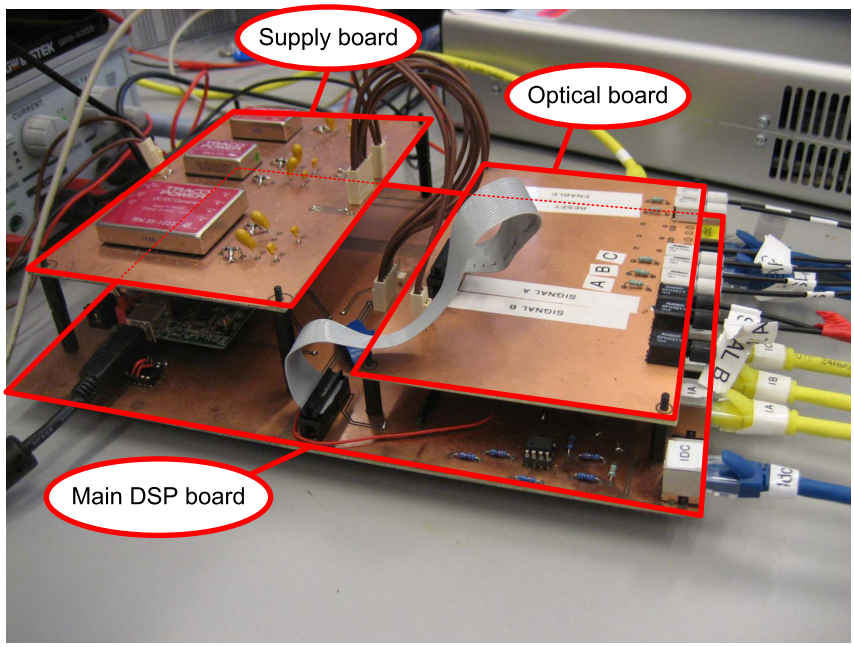

Figure H.5: *DSP board.*

Supply board

The supply board has the function of supplying the entire system including DSP board, inverter and BMS system. The supply board produced in this project does not include all the needed supply voltages, and a new supply board must therefore be produced before an implementation in the electric vehicle. In the test stand however laboratory supplies are used to power the inverter and BMS, and the supply board only powers the DSP board. The supply board is seen in figure H.6 and the schematic is seen in figure H.7.
The supply board uses a 12 V DC laboratory supply corresponding to the 12 V DC battery supply in the electric vehicle. The board outputs 5 V DC for the optical board and various voltages for the main DSP board, as seen in figure H.6.

Main DSP board

The main DSP board is seen in figure H.8. Schematics are seen in figure H.9, figure H.9 and figure H.9.
The main DSP board is connected to the supply board and the optical board as illustrated in

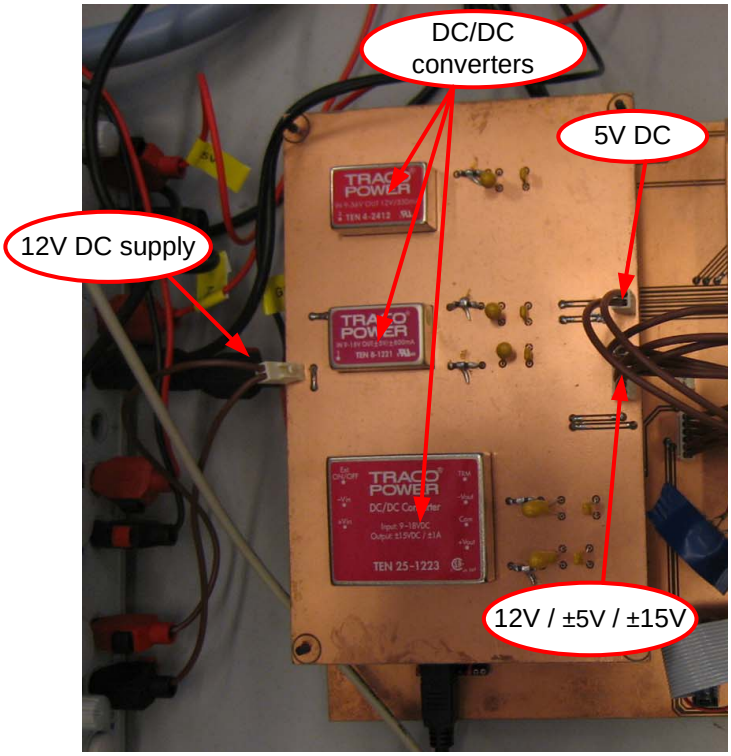

Figure H.6: *Supply board.*

figure H.8. The measured currents from the LEM transducers are send to the DSP board through RJ45 cables. The currents are transferred to voltage signals and send to the DSPs ADC channels. The motor temperature, inverter temperature and DC bus voltage are processed on the DSP board and also send to the DSPs ADC channels.

The accelerator and brake pedal in the electric vehicle is connected to the DSP board. When connected to the DSP board the pedals function as variable electrical resistors dependent on pedal position. The pedal positions is used as torque references for the induction machine.

The BMS is connected to the DSP board in order to supply the BMS and in order to receive information from the BMS e.g. state of charge.

When implementing the system in the electrical vehicle it is desirable for the driver to be able to change drive mode. These drive modes could be e.g. reverse, sport mode, economical mode, normal mode. The switching of mode is done by utilizing the auxiliary port and a manual switch in the dashboard.

Optical board

The optical board contains optical in- and output ports. The optical board is seen in figure H.12. A schematic of the board is seen in figure H.13.

The optical board is connected to the main DSP board as seen in figure H.12. The 5 V DC

supply comes from the supply board and is used to power the input ports.

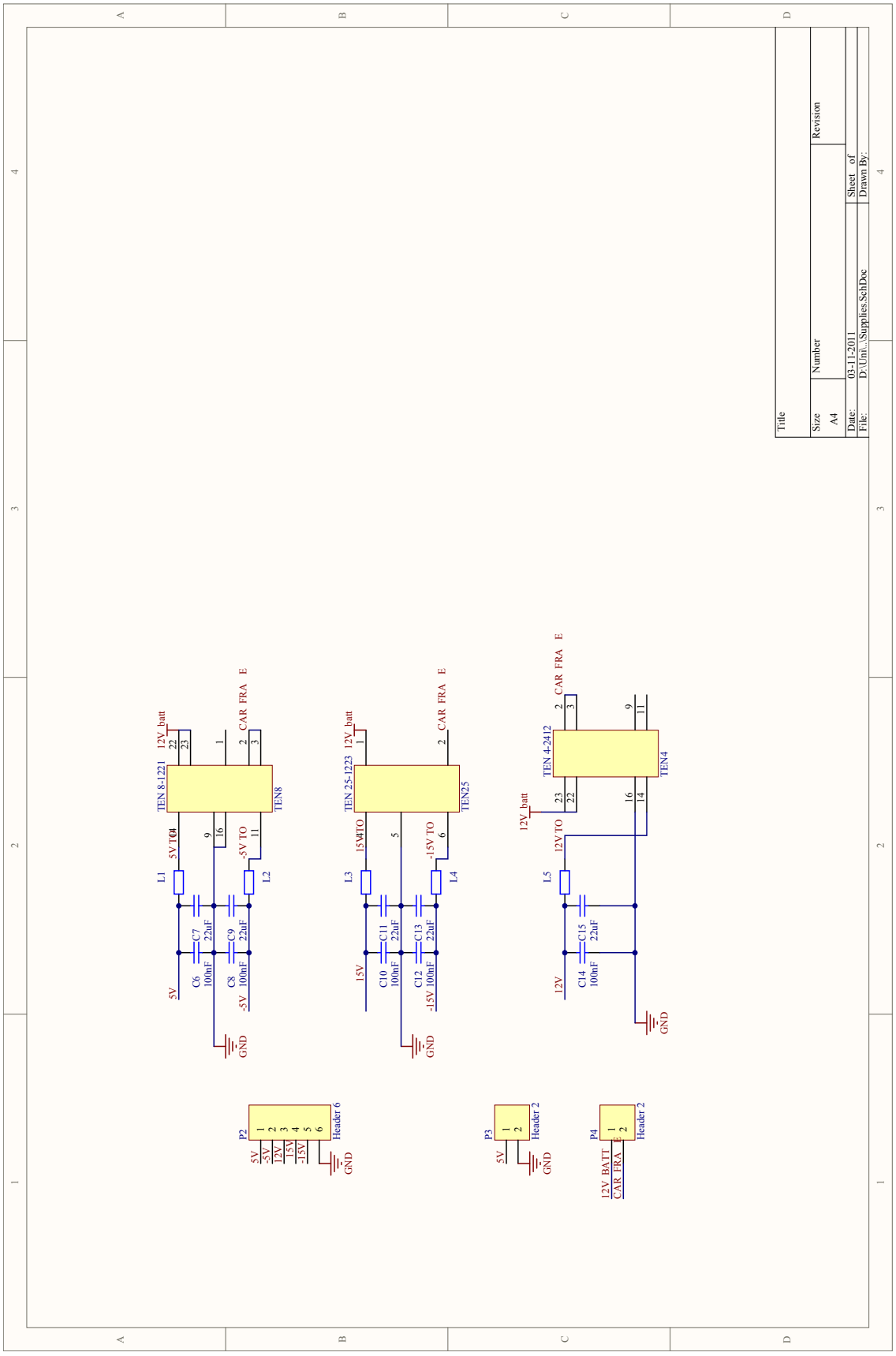

Figure H.7: *Schematic of supply board.*

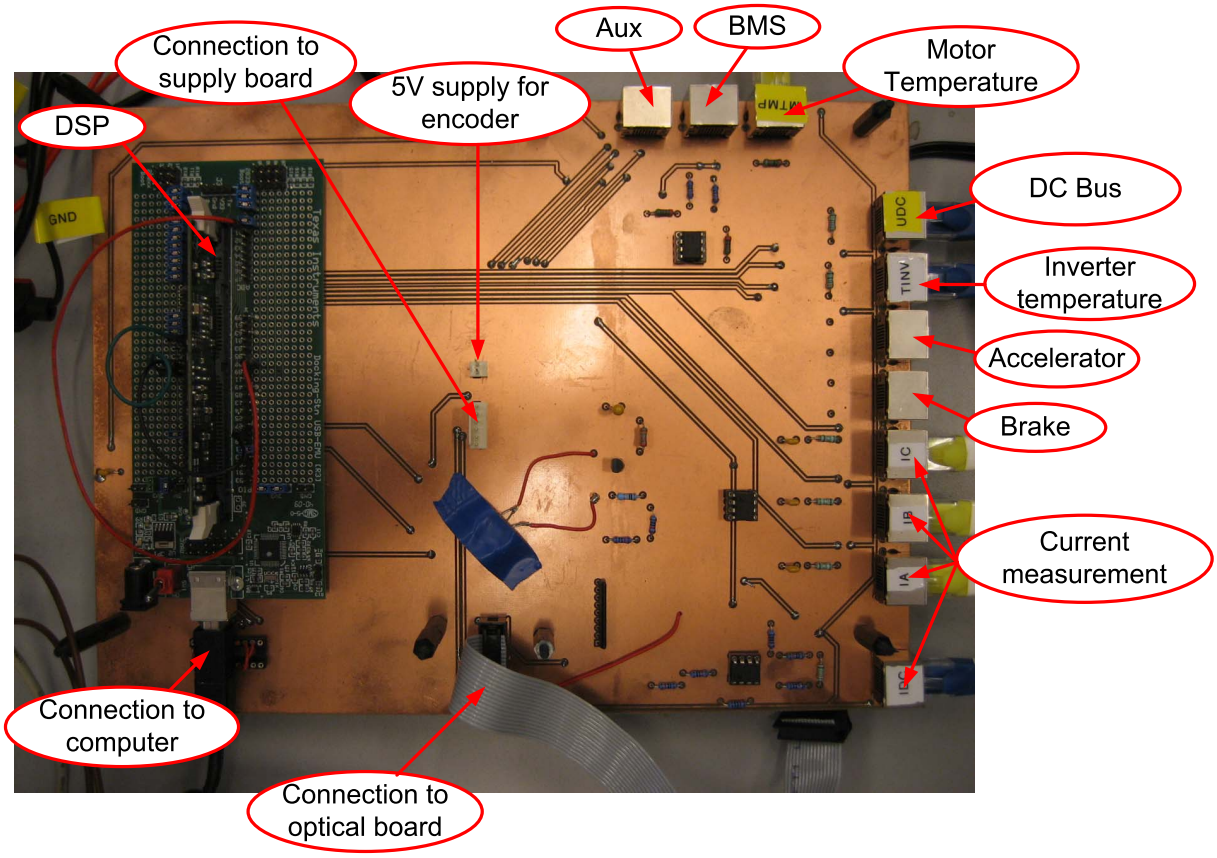

Figure H.8: *Main DSP board.*

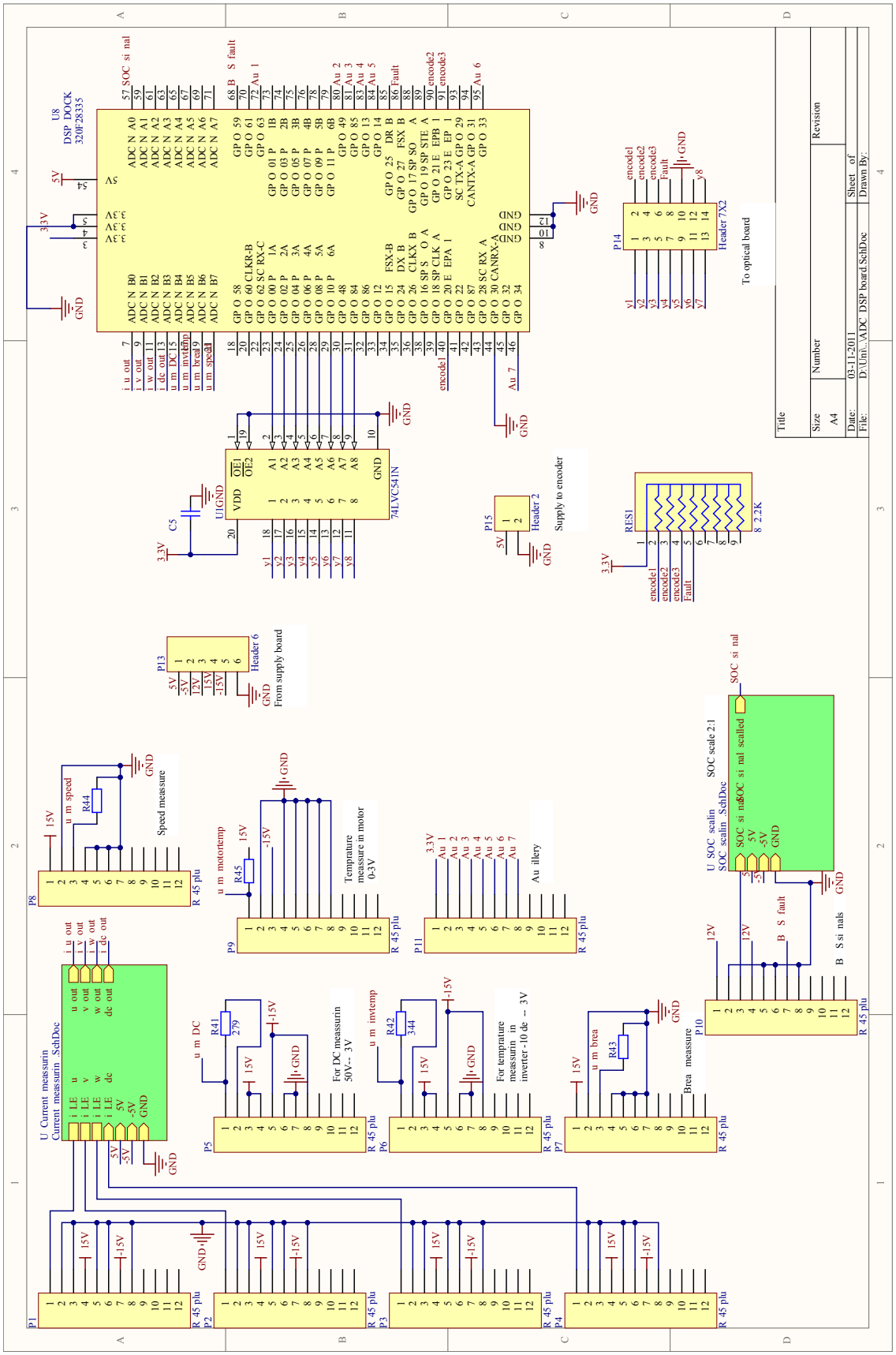

Figure H.9: *Schematic of main DSP board (1/3).*

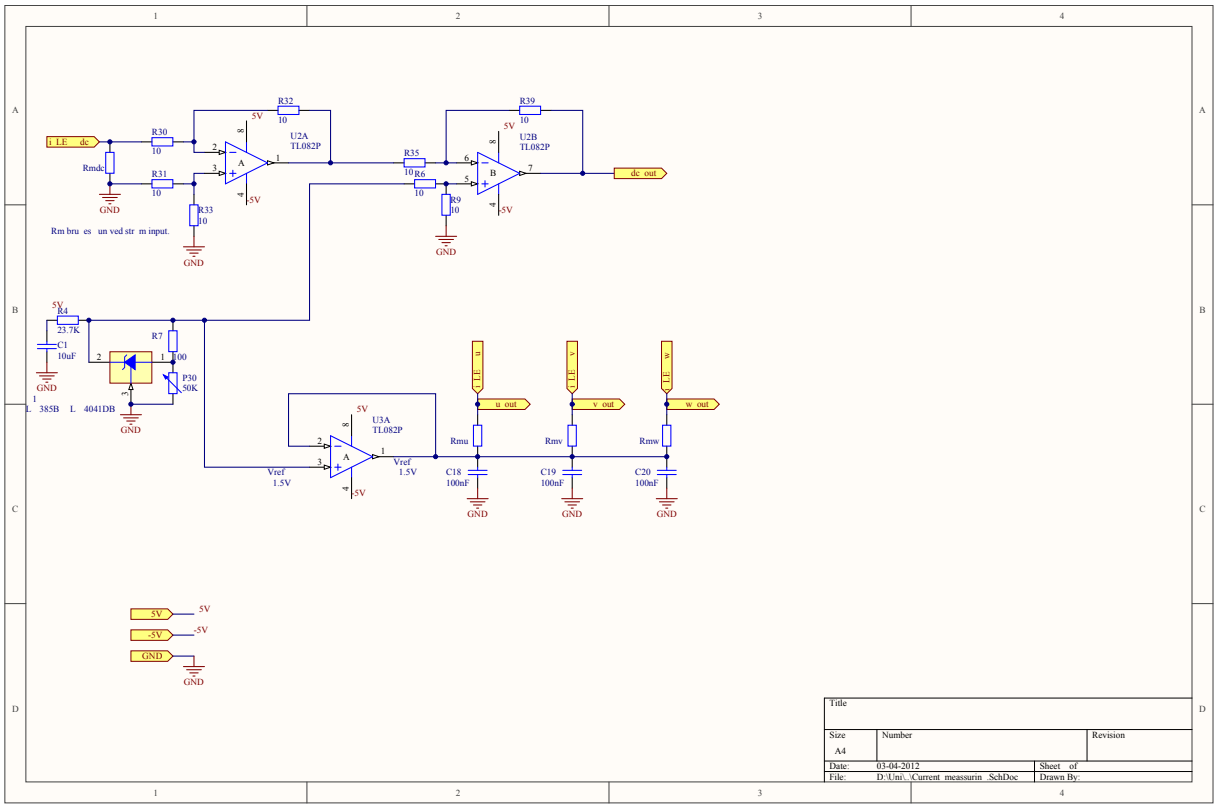

Figure H.10: *Schematic of main DSP board (2/3).*

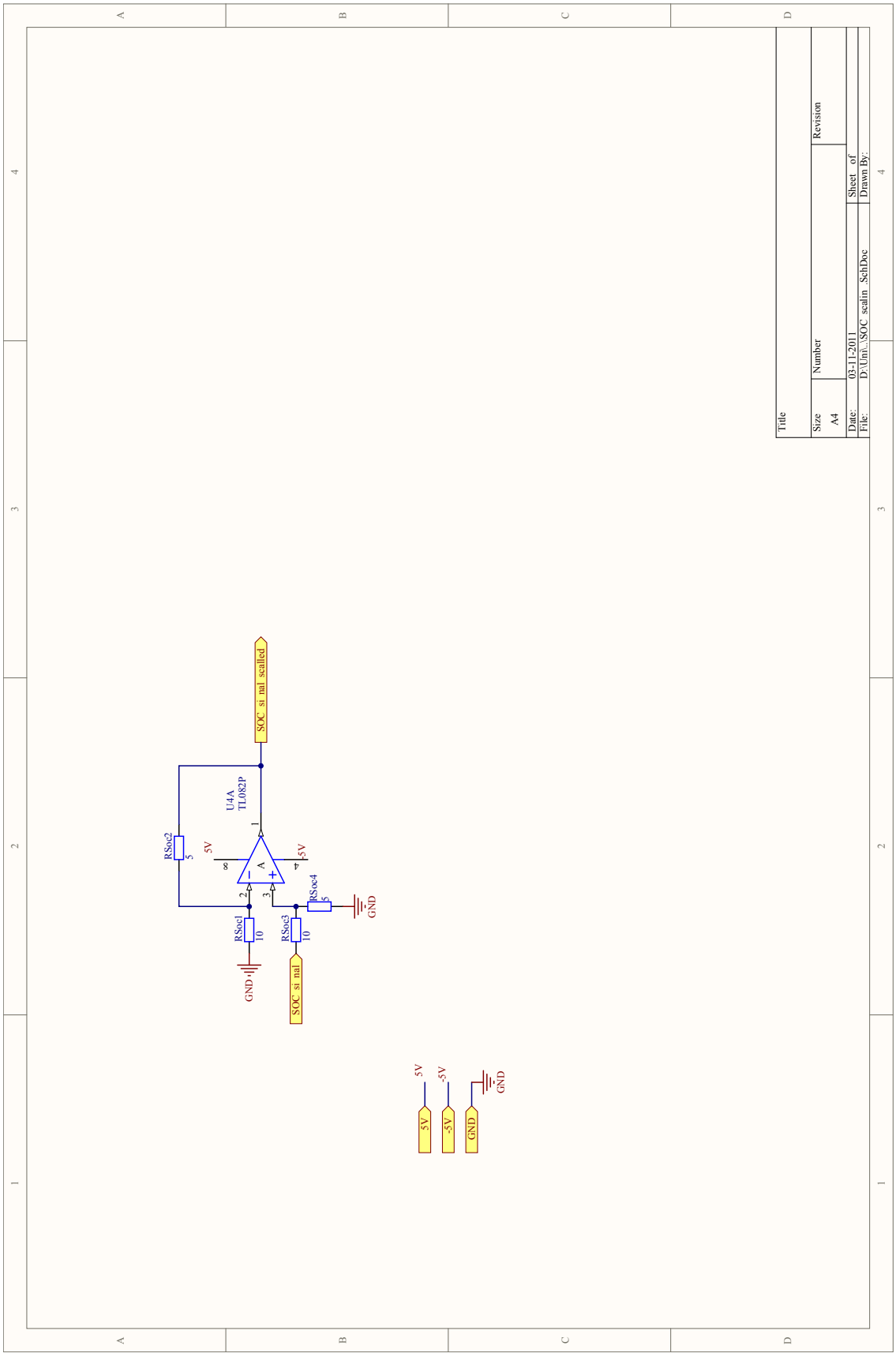

Figure H.11: *Schematic of main DSP board (3/3).*

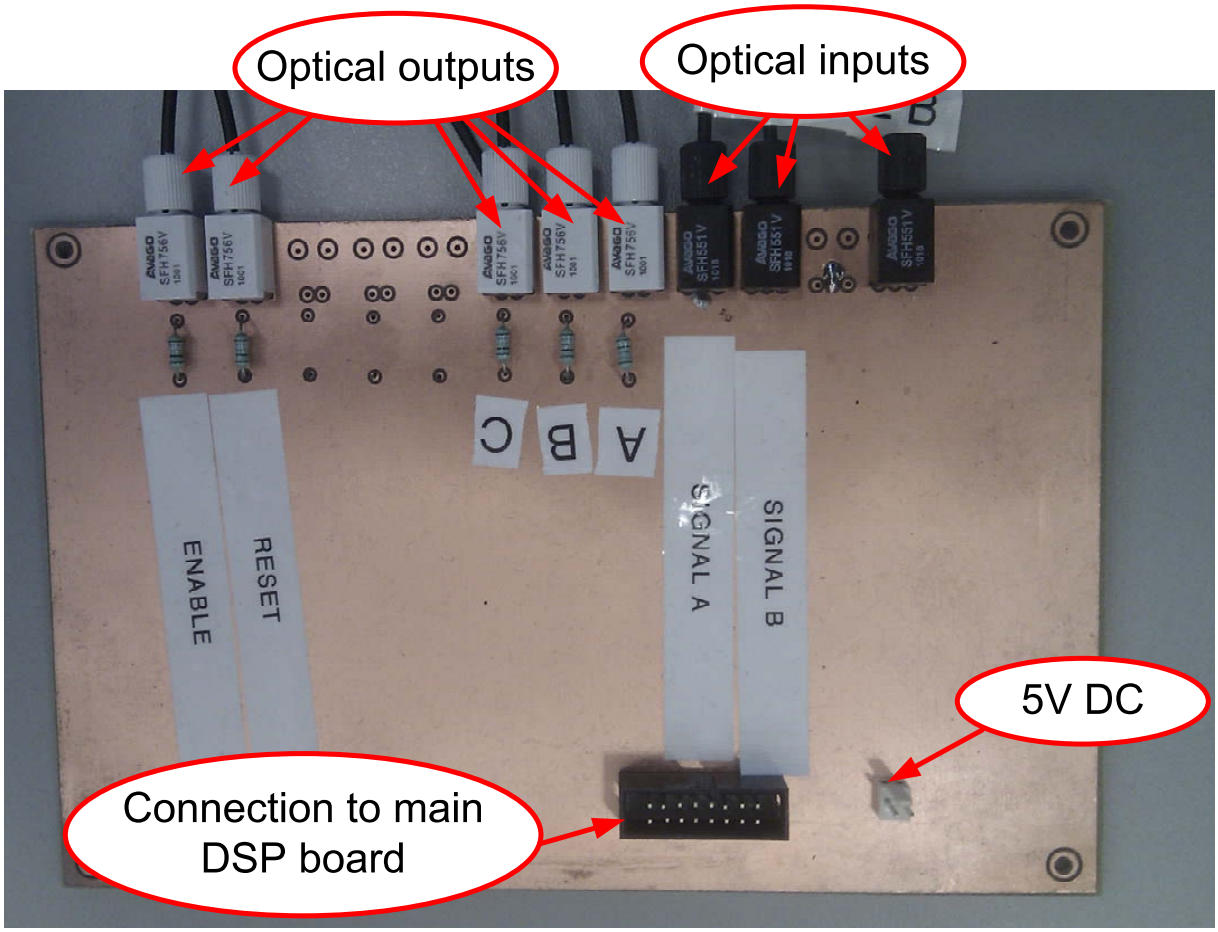

Figure H.12: *Optical board.*

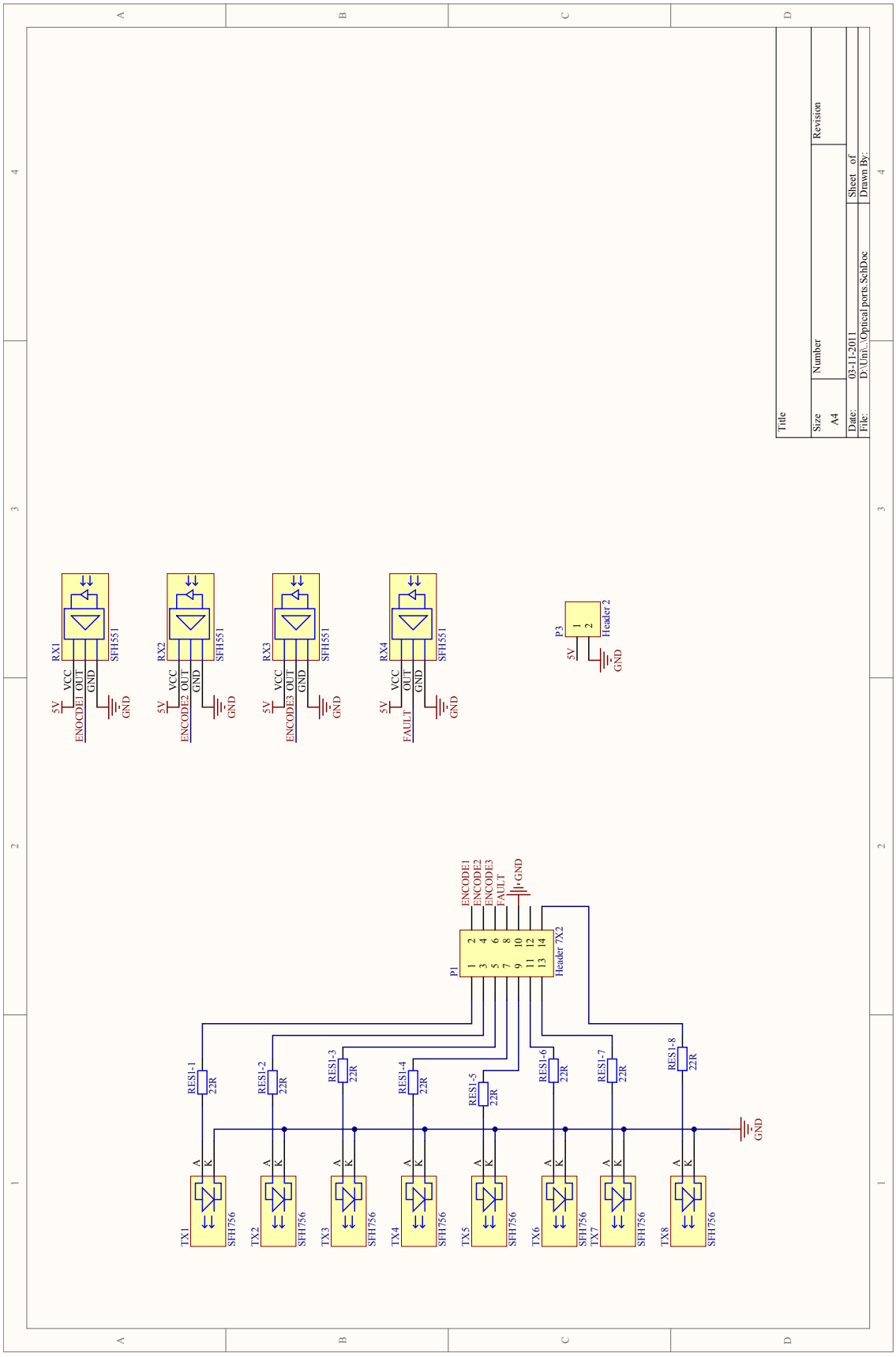

Figure H.13: *Schematic of optical board.*

H.3 VHDL Code For the FPGA

The VHDL-code for the FPGA written by Torben N. Matzen is seen in figure H.14, H.15, H.16, H.17, H.18 and H.19.

Sep 20, 11 16:31 **bpi_cpld.vhd** Page 1/3

```
----------------------------------------------------------------------------------
-- Company:
-- Engineer:
--
-- Create Date:    September 2011
-- Design Name:
-- Module Name:    Sauer Danfoss Interface Card CPLD - Behavioral
-- Project Name:
-- Target Device:
-- Tool versions:
-- Description:
--
-- Dependencies:
--
-- Revision:
-- Revision 0.01 - File Created
-- Additional Comments:
--
----------------------------------------------------------------------------------
library IEEE;
use IEEE.STD_LOGIC_1164.ALL;
use IEEE.STD_LOGIC_ARITH.ALL;
use IEEE.STD_LOGIC_UNSIGNED.ALL;

---- Uncomment the following library declaration if instantiating
---- any Xilinx primitives in this code.
--library UNISIM;
--use UNISIM.VComponents.all;

entity bpi_cpld is
    Port (      SW1, SW2, SW3, SW4, SW5, SW6, SW7 : in std_logic;
                                PWM1, PWM2, PWM3, PWM4, PWM5, PWM6 : in std_logi
c;
                                RESET_IN, AUX_IN : in std_logic;
                                FAULT_FROMBPI : in std_logic;
                                CLK : in std_logic;
                                CA, CB, CC, CD, CE, CF, CG, CDP : out std_logic;
                                AUX_OUT, FAULT_OUT : out std_logic;
                                RESET_TOBPI : out std_logic;
                                UH,UL,VH,VL,WH,WL : out std_logic);
end bpi_cpld;

architecture Behavioral of bpi_cpld is
signal HEX: std_logic_vector(3 downto 0); --Opretter en 4-bits signal-ledning
signal LED: std_logic_vector(6 downto 0); --Opretter en 7-bits signal-ledning
signal DTIME: std_logic_vector(6 downto 0);
signal LEGS: std_logic_vector(5 downto 0);
signal SYSTEM_STATE: std_logic_vector(1 downto 0);

component dead_time
   Port (DTlen : in std_logic_vector (6 downto 0);
                        CLK : in std_logic;
                        LEG : in std_logic;
                        HIGH, LOW : out std_logic);
end component;

type STATE_RESET_type is (S_RESET, S_NORMAL);
signal STATE_RESET : STATE_RESET_type;


begin
--DTIME <= SW5 & SW4 & SW3 & SW2 & SW1;
```

Figure H.14: *VHDL code page 1.*

Sep 20, 11 16:31 **bpi_cpld.vhd** Page 2/3

```
--DTIME<= "0100000";
DTIME<=  "0" & SW4 & SW3 & SW2 & SW1 & "11";

--HEX  <= SW4 & SW3 & SW2 & SW1; --Sammenkaeder 4 signaler til en 4-bits vector
                                 --Signaler bliver IKKE ANDed.


SYSTEM_STATE<= FAULT_FROMBPI & AUX_IN;

        with SYSTEM_STATE SELect
   HEX<= "0001" when "00",       --Fault, enabled
         "0000" when "01",       --Fault, disabled
         "0011" when "10",       --OK, enabled
         "0010" when "11",       --OK, disabled
         "1111" when others;


  CA   <= LED(0);  --De enkelte signaler i Led
  CB   <= LED(1);  --forbindes med de oenskede udgange
  CC   <= LED(2);
  CD   <= LED(3);
  CE   <= LED(4);
  CF   <= LED(5);
  CG   <= LED(6);
  CDP  <= SW5 or SW6 or SW7 or not PWM4 or not PWM5 or not PWM6;

   with HEX SELect
   LED<= "0000110" when "0001",   --1
         "1011011" when "0010",   --2
         "1001111" when "0011",   --3
         "1100110" when "0100",   --4
         "1101101" when "0101",   --5
         "1111101" when "0110",   --6
         "0000111" when "0111",   --7
         "1111111" when "1000",   --8
         "1101111" when "1001",   --9
         "1110111" when "1010",   --A
         "1111100" when "1011",   --b
         "0111001" when "1100",   --C
         "1011110" when "1101",   --d
         "1111001" when "1110",   --E
         "1110001" when "1111",   --F
         "0111111" when others;   --0



      LEG_U : dead_time
    port map (DTlen(6 downto 0)=>DTIME(6 downto 0),
              CLK=>CLK,
              LEG=>PWM1,
              HIGH=>LEGS(0),
              LOW=>LEGS(1));

      LEG_V : dead_time
    port map (DTlen(6 downto 0)=>DTIME(6 downto 0),
              CLK=>CLK,
              LEG=>PWM2,
              HIGH=>LEGS(2),
              LOW=>LEGS(3));

      LEG_W : dead_time
```

Figure H.15: *VHDL code page 2.*

Sep 20, 11 16:31 **bpi_cpld.vhd** Page 3/3

```
      port map (DTlen(6 downto 0)=>DTIME(6 downto 0),
                CLK=>CLK,
                LEG=>PWM3,
                HIGH=>LEGS(4),
                LOW=>LEGS(5));

-- AUX_IN allocated to \ENABLE
UH<= not LEGS(0) or AUX_IN; -- or not FAULT_FROMBPI;
UL<= not LEGS(1) or AUX_IN; -- or not FAULT_FROMBPI;
VH<= not LEGS(2) or AUX_IN; -- or not FAULT_FROMBPI;
VL<= not LEGS(3) or AUX_IN; -- or not FAULT_FROMBPI;
WH<= not LEGS(4) or AUX_IN; -- or not FAULT_FROMBPI;
WL<= not LEGS(5) or AUX_IN; -- or not FAULT_FROMBPI;

FAULT_OUT<= not FAULT_FROMBPI;
AUX_OUT <= SW7;



asdf : process(CLK)
        variable reset_cnt : INTEGER range 0 to 7;
        variable RESET_IN_OLD : std_logic;

        begin -- Process

                if CLK'event and CLK = '1' then

                        case STATE_RESET is
                                when S_RESET =>
                                        RESET_TOBPI<= '0';
                                        reset_cnt:= reset_cnt +1;
                                        if (reset_cnt > 6) then
                                                reset_cnt:= 0;
                                                STATE_RESET<= S_NORMAL;
                                        end if;

                                when S_NORMAL =>
                                        if RESET_IN_OLD = '1' and RESET_IN = '0'
 then
                                                STATE_RESET<= S_RESET;
                                        end if;
                                        RESET_TOBPI<= '1';

                                when others =>
                                        null;

                        end case;
                        RESET_IN_OLD:= RESET_IN;
                end if;
        end process; -- Process
end Behavioral;
```

Figure H.16: *VHDL code page 3.*

Oct 24, 05 13:42 **dead_time.vhd** Page 1/2

```
----------------------------------------------------------------------------------
-- Company:
-- Engineer:
--
-- Create Date:    10:45:51 10/21/05
-- Design Name:
-- Module Name:    dead_time - Behavioral
-- Project Name:
-- Target Device:
-- Tool versions:
-- Description:
--
-- Dependencies:
--
-- Revision:
-- Revision 0.01 - File Created
-- Additional Comments:
--
----------------------------------------------------------------------------------
library IEEE;
use IEEE.STD_LOGIC_1164.ALL;
use IEEE.STD_LOGIC_ARITH.ALL;
use IEEE.STD_LOGIC_UNSIGNED.ALL;

---- Uncomment the following library declaration if instantiating
---- any Xilinx primitives in this code.
--library UNISIM;
--use UNISIM.VComponents.all;


entity dead_time is
    Port (      DTlen : in std_logic_vector (6 downto 0);
                        CLK : in std_logic;
                        LEG : in std_logic;
                        HIGH, LOW : out std_logic);
end dead_time;


architecture Behavioral of dead_time is

type Sreg0_type is (S_HIGH, S_LOW, S_WAIT);
-- S0 : HIGH switch on
-- S1 : LOW switch on
-- S3 : Dead time both switches off
signal Sreg0 : Sreg0_type;

begin
        process(CLK)
        variable DTcnt : INTEGER range 0 to 127;

        begin -- Process
                if CLK'event and CLK = '1' then
                        case Sreg0 is
                                when S_HIGH =>
                                        LOW<='0';
                                        if LEG = '1' then
                                          HIGH<='1';
                                        else
                                          HIGH<='0';
                                          Sreg0<=S_WAIT;
                                        end if;
```

Figure H.17: *VHDL code page 4.*

Oct 24, 05 13:42 **dead_time.vhd** Page 2/2

```
                                when S_LOW =>
                                        HIGH<='0';
                                        if LEG = '0' then
                                                LOW<='1';
                                        else
                                                LOW<='0';
                                                Sreg0<=S_WAIT;
                                        end if;

                                when S_WAIT =>
                                        HIGH<='0';
                                        LOW<='0';

                                        if DTcnt = DTlen then
                                                DTcnt:= 0;
                                                if LEG = '0' then
                                                        Sreg0<= S_LOW;
                                                else
                                                        Sreg0<= S_HIGH;
                                                end if;
                                        else
                                                DTcnt:=DTcnt+1;
                                        end if;

                                when others =>
                                        null;

                        end case;
                end if;
        end process; -- Process
end Behavioral;
```

Figure H.18: *VHDL code page 5.*

Oct 24, 05 8:52 **bpi_cpld_connections.ucf** Page 1/1

```
#PACE: Start of Constraints generated by PACE

#PACE: Start of PACE I/O Pin Assignments
NET "AUX_IN"  LOC = "P11"  ;
NET "AUX_OUT"  LOC = "P8"  ;
NET "CA"  LOC = "P7"  ;
NET "CB"  LOC = "P4"  ;
NET "CC"  LOC = "P1"  ;
NET "CD"  LOC = "P44"  ;
NET "CDP"  LOC = "P43"  ;
NET "CE"  LOC = "P2"  ;
NET "CF"  LOC = "P6"  ;
NET "CG"  LOC = "P3"  ;
NET "CLK"  LOC = "P5"  ;
NET "FAULT_FROMBPI"  LOC = "P34"  ;
NET "FAULT_OUT"  LOC = "P9"  ;
NET "PWM1"  LOC = "P22"  ;
NET "PWM2"  LOC = "P20"  ;
NET "PWM3"  LOC = "P18"  ;
NET "PWM4"  LOC = "P19"  ;
NET "PWM5"  LOC = "P14"  ;
NET "PWM6"  LOC = "P13"  ;
NET "RESET_IN"  LOC = "P12"  ;
NET "RESET_TOBPI"  LOC = "P33"  ;
NET "SW1"  LOC = "P42"  ;
NET "SW2"  LOC = "P40"  ;
NET "SW3"  LOC = "P39"  ;
NET "SW4"  LOC = "P38"  ;
NET "SW5"  LOC = "P37"  ;
NET "SW6"  LOC = "P36"  ;
NET "SW7"  LOC = "P35"  ;
NET "UH"  LOC = "P28"  ;
NET "UL"  LOC = "P29"  ;
NET "VH"  LOC = "P24"  ;
NET "VL"  LOC = "P25"  ;
NET "WH"  LOC = "P26"  ;
NET "WL"  LOC = "P27"  ;

#PACE: Start of PACE Area Constraints

#PACE: Start of PACE Prohibit Constraints

#PACE: End of Constraints generated by PACE
```

Figure H.19: *VHDL code page 6.*

APPENDIX I

DATASHEETS

I.1 ABM Induction Machine

The datasheet for the induction machine is seen in figure I.1. Performance characteristics of the ABM induction machine are seen in figure I.2.

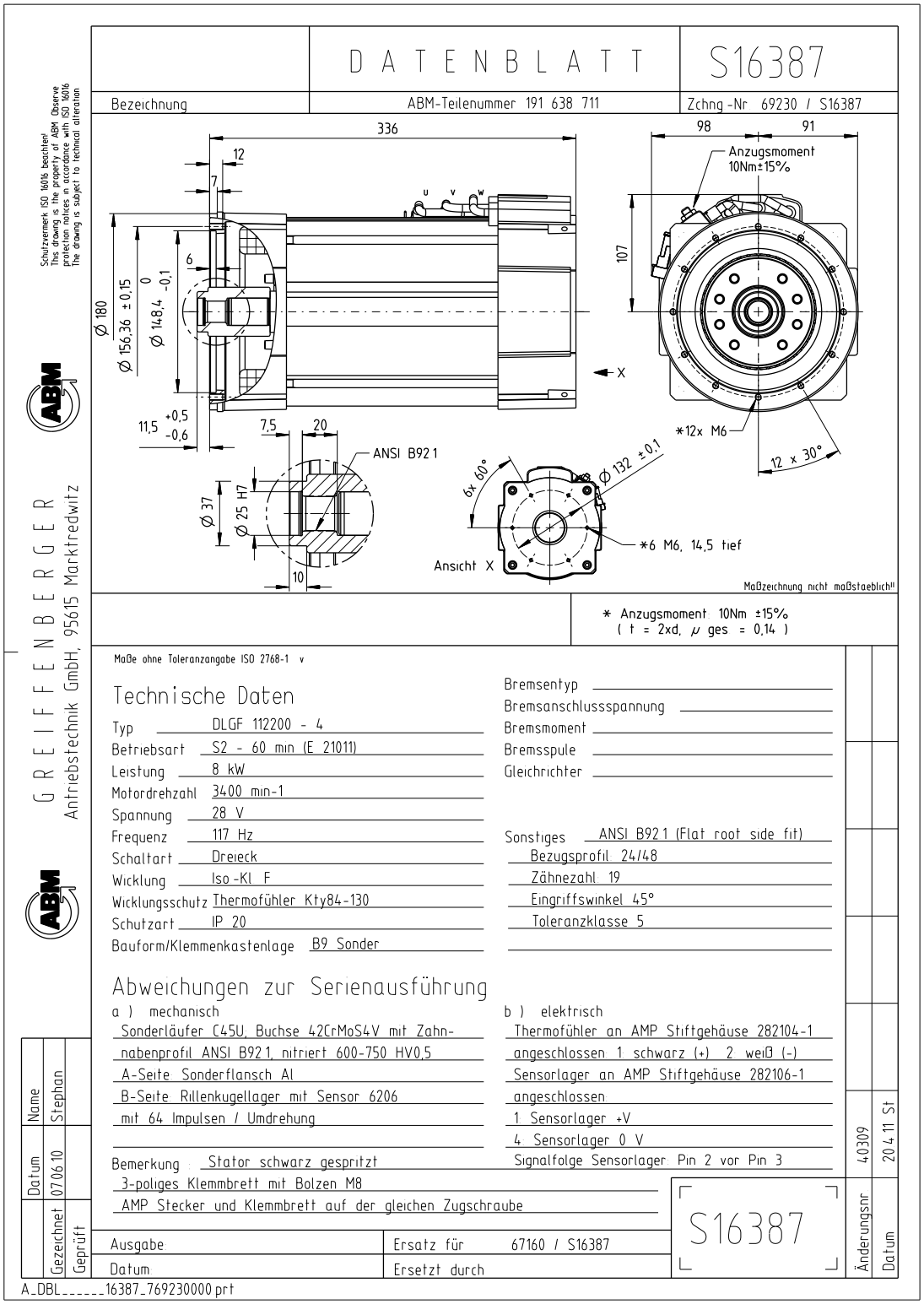

Figure I.1: *Datasheet for induction machine*

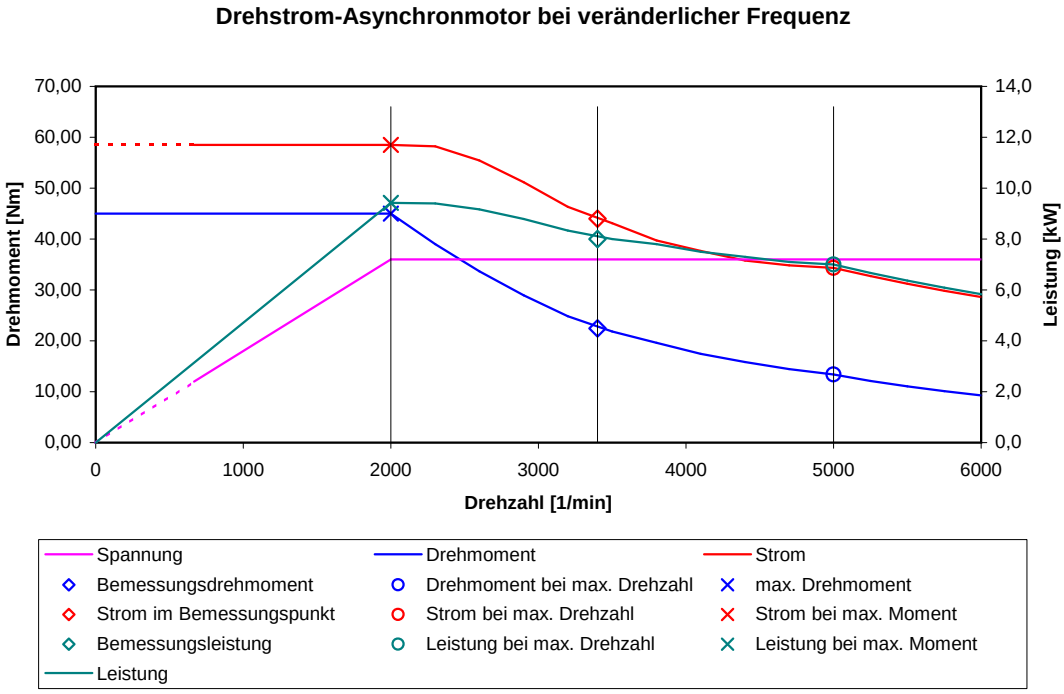

Motortyp:	DLG112200-4	Polzahl:	4
E-Nr.:	21011	Spannung [V]:	28
Typenschild Nr.:		Eckfrequenz [Hz]:	69

Bemerkungen:

max. Drehmoment

Drehzahl [min^{-1}]:	2000	Leistungsfaktor:	0,80	Frequenz [Hz]:	69
Drehmoment [Nm]:	45,00	Wirkungsgrad [%]:	80,0		
Leistung [kW]:	9,42	Betriebsart:	S2-5 min		
Strom [A]:	304,0	Spannung [V]:	28		

Bemessungsleistung

Drehzahl [min^{-1}]:	3400	Leistungsfaktor:	0,83	Frequenz [Hz]:	117
Drehmoment [Nm]:	22,47	Wirkungsgrad [%]:	87,0		
Leistung [kW]:	8,00	Betriebsart:	S2-60 min		
Strom [A]:	228,7	Spannung [V]:	28		

max. Drehzahl

Drehzahl [min^{-1}]:	5000	Leistungsfaktor:	0,90	Frequenz [Hz]:	169
Drehmoment [Nm]:	13,37	Wirkungsgrad [%]:	90,0		
Leistung [kW]:	7,00	Betriebsart:	S2-10 min		
Strom [A]:	178,4	Spannung [V]:	28		

Hinweis: Strom, Leistungsfaktor und Wirkungsgrad sind Schätzwerte

E21011_1.xls BZe 07.04.2009 08.04.2009 09:00

Figure I.2: *Performance characteristics of ABM induction machine.*

BIBLIOGRAPHY

Heinz Willi Van Der Broeck, Hans-Christoph Skudelny, and Georg Viktor Stanke. *Analysis and Realization of a Pulsewidth Modulator Based on Voltage Space Vectors*. IEEE, 1988. URL: http://ieeexplore.ieee.org/stamp/stamp.jsp?tp=&arnumber=87265.

Min Chen and Gabriel A. Rincon-Mora. *Accurate Electrical Battery Model Capable of Predicting Runtime and I-V Performance*. IEEE TRANSACTIONS ON ENERGY CONVERSION, 2006. URL: http://users.ece.gatech.edu/rincon-mora/publicat/journals/tec05_batt_modl.pdf.

J. Duncan Glover, Mulukutla S. Sarma, and Thomas J. Overbye. *Power System*. Cengage Learning, 4 edition, 2010. ISBN 13: 978-0-495-66787-2.

American National Standard Institute. *ANSI B92.1, Involute Splines and Inspection*. 1996.

Paul C. Krause, Oleg Wasynczuk, and Scott D. Sudhoff. *Analysis of electric machinery and drive systems*. John Wiley & Sons, Inc., 2 edition, 2002. ISBN: 047114326x.

J.F. Moreno, F.P. Hidalgo, and M.D. Martinez. *Realisation of tests to determine the parameters of the thermal model of an induction machine*. IEEE, 2001. URL: http://ieeexplore.ieee.org/stamp/stamp.jsp?tp=&arnumber=955372.

Robert L. Norton. *Machine Design An Integrated Approach*. Pearson Prentice Hall, 3 edition, 2006. ISBN: 0-13-202012-2.

D. W. Novotny and T. A. Lipo. *Vector Control And Dynamics of AC Drives*. Oxford Science Publications, 1996. ISBN: 978-0-19-856439-3.

Paresh C. Sen. *Principles of Electric Machines and Power Electronics*. John Wiley & Sons, 2 edition, 1997. ISBN: 978-0-471-02295-4.

ThunderSky. *Thunder Sky battery cell*. URL: http://www.everspring.net/product-battery-LFP160AHA.htm.